

Distribution Agreement

In presenting this thesis or dissertation as a partial fulfillment of the requirements for an advanced degree from Emory University, I hereby grant to Emory University and its agents the non-exclusive license to archive, make accessible, and display my thesis or dissertation in whole or in part in all forms of media, now or hereafter known, including display on the world wide web. I understand that I may select some access restrictions as part of the online submission of this thesis or dissertation. I retain all ownership rights to the copyright of the thesis or dissertation. I also retain the right to use in future works (such as articles or books) all or part of this thesis or dissertation.

Signature:

Brendan Deal

Date

Leveling Up DNA Hybridization Affinity and Specificity Using Heteromultivalent DNA-
Functionalized Particles

By

Brendan Deal
Doctor of Philosophy

Chemistry

Khalid Salaita
Advisor

Jennifer Heemstra
Committee Member

Yonggang Ke
Committee Member

James Kindt
Committee Member

Accepted:

Kimberly Jacob Arriola, Ph.D, MPH
Dean of the James T. Laney School of Graduate Studies

Date

Leveling Up DNA Hybridization Affinity and Specificity Using Heteromultivalent DNA-
Functionalized Particles

By

Brendan Deal
B.S., Davidson University, 2016

Advisor: Khalid Salaita, PhD

An abstract of
A dissertation submitted to the Faculty of the
James T. Laney School of Graduate Studies of Emory University
in partial fulfillment of the requirements for the degree of
Doctor of Philosophy
in Chemistry
2022

Abstract

Leveling Up DNA Hybridization Affinity and Specificity Using Heteromultivalent DNA-Functionalized Particles

By Brendan Deal

Beyond the essential role that DNA hybridization serves in biological processes, it has also been demonstrated to be a powerful tool that enables many biological investigations and transformative applications in diagnostics, therapeutics, and nanotechnology. Despite the success of DNA hybridization-based applications, further enhancements in binding affinity and specificity are obstructed by several fundamental constraints. To bypass these obstacles, multivalent DNA hybridization has emerged as a promising strategy due to its ability to yield highly avid and specific binding. Numerous examples of multivalent DNA hybridization have been exhibited in recent years and have found significant utility in fields ranging from nanoparticle-based sensing to fundamental immunology. This dissertation begins by describing the fundamental parameters that influence multivalent DNA hybridization and highlighting several areas that have greatly benefited from the application of this concept. Following this guide to understanding and applying multivalent DNA hybridization, this dissertation presents two fundamental explorations into designing DNA-functionalized particles capable of high avidity and specificity binding to biologically relevant DNA targets using heteromultivalent DNA hybridization. Finally, essential steps towards further application of multivalent DNA hybridization in nanotechnology, sensing, and gene regulation are outlined.

Leveling Up DNA Hybridization Affinity and Specificity Using Heteromultivalent DNA-
Functionalized Particles

By

Brendan Deal
B.S., Davidson University, 2016

Advisor: Khalid Salaita, PhD

A dissertation submitted to the Faculty of the
James T. Laney School of Graduate Studies of Emory University
in partial fulfillment of the requirements for the degree of
Doctor of Philosophy
in Chemistry
2022

Acknowledgements

I want to first acknowledge everyone who has helped me out with the research projects included in this dissertation. I am sincerely grateful to my advisor, Dr. Khalid Salaita, for the helpful advice, guidance, and ideas he has contributed. I want to also extend my thanks to Dr. James Kindt for his help with the modeling for both projects and really helping us to better understand the fundamental concepts described in this dissertation. I would moreover like to thank Rong for always letting me come to her for help with everything and for coming up with the idea for the specificity project in Chapter 3 with me. She helped me perform many big experiments, troubleshoot unexpected results, and see the value in this work. Furthermore, I would like to express my gratitude to Hiro for helping me with particle characterization and mass spec, Han for synthesizing all of the gold nanoparticles I used for the project in Chapter 2, and Victor for helping me get started with this work in my first year. Finally, I am greatly appreciative to Dr. Tine Curk, Dr. Rosalind Allen, and Dr. Daan Frenkel for meeting with us and providing great insights on multivalent binding.

Next, I want to further extend my gratitude to Dr. Khalid Salaita, my committee, and my friends in the Chemistry department for helping me to grow as a scientist and as a person. Khalid was a great advisor who taught me so much about how to be a better scientist. He was always patient and helpful when I didn't know what I was doing and gave me freedom and put your trust in me when I did. Dr. Jen Heemstra, Dr. Yonggang Ke, and Dr. James Kindt provided an abundance of helpful feedback and advice over the last several years and were always supportive and encouraging. All of my lab mates and friends in the department helped me to learn so much about science, life, and the world and made my PhD a much more enjoyable experience.

I want to further acknowledge Rong, my wonderful girlfriend, travel companion, and lab partner. She was always supportive and thoughtful, and helped me through so many tough times and struggles inside and outside of lab. She constantly showed me how to get the most out of life and how to always dream big.

Lastly, I want to thank my family. My brother Travis, who I followed from school to school including going to the same college, always lead the way for me and showed me that it was possible for me to do well and achieve so much in school. Finally, I want to express the greatest gratitude to my parents for always supporting me through everything and encouraging me to try hard in school even from a young age. They gave me the freedom to go to whatever college I wanted and to keep going as far as I wanted in my education!

Table of Contents

Chapter 1. Overview of the Fundamental Concepts and Applications of Multivalent DNA

Hybridization.....	1
1.1. Introduction.....	2
1.2. Fundamentals of Multivalent DNA Hybridization.....	5
1.2.1. How Does Multivalency Enhance Binding Affinity and Specificity?.....	5
1.2.2. Defining Homomultivalent and Heteromultivalent DNA Hybridization.....	7
1.2.3. The Spatial Arrangement of Oligonucleotides Significantly Impacts Multivalent Hybridization.....	9
1.2.4. The Value of n Dictates Binding Valency of Multivalent Hybridization Interactions.....	13
1.2.5. Individual Oligonucleotide Length and Monovalent Binding Affinity Impacts Binding Avidity and Selectivity.....	16
1.2.6. Linkers and Spacers Increase Reach and Provide Flexibility to Multivalent Hybridization Interactions.....	19
1.2.7. Anchor Orientation and Spacer Length Control the Binding Geometry of Multivalent Hybridization.....	23
1.2.8. Quaternary Level and Higher Multivalent DNA Hybridization.....	26
1.3. Applications of Multivalent DNA Hybridization.....	28
1.3.1. DNA-Based Artificial Motors.....	28
1.3.2. Nucleic Acid Sensing.....	31
1.3.3. Tools to Study Biology.....	33
1.4. Aims and Scope of the Dissertation.....	36

1.5. References.....	38
Chapter 2. Engineering DNA-Functionalized Nanostructures to Bind Nucleic Acid Targets Heteromultivalently with Enhanced Avidity.....	42
2.1. Introduction.....	43
2.2. Results.....	46
2.2.1. Modeling Binding of Random and Patterned HeteroMV SNAs.....	46
2.2.2. Design and Melting Curve Analysis for Random HeteroMV SNAs.....	48
2.2.3. Thermodynamics and Affinity of Random HeteroMV SNA Binding.....	50
2.2.4. Development and Characterization of Patterned HeteroMV SNAs.....	52
2.2.5. Impact of Spatial Patterning on HeteroMV SNA Binding.....	54
2.3. Discussion.....	55
2.4. Materials and Methods.....	58
2.4.1. Oligonucleotides.....	58
2.4.2. Reagents.....	59
2.4.3. Consumables.....	60
2.4.4. Equipment.....	60
2.4.5. Modeling.....	60
2.4.6. Synthesis of Gold Nanoparticles.....	64
2.4.7. Random HeteroMV SNA Synthesis.....	64
2.4.8. Determining Number of Oligos/AuNP.....	65
2.4.9. Melting Curve Measurement for Random HeteroMV SNAs.....	66
2.4.10. Cy5 Conjugation to Target Strands.....	67
2.4.11. van't Hoff Binding Affinity Measurement.....	67

2.4.12. Native PAGE.....	68
2.4.13. Patterned and Mispatterned SNA Synthesis.....	69
2.4.14. Determining Number of Templates/Patterned SNA.....	70
2.4.15. Melting Curve Measurement for Patterned SNAs.....	70
2.5. Appendix.....	72
2.6. References.....	91
Chapter 3. Heteromultivalency Enables Optimization of the Specificity and Cooperativity of DNA Hybridization.....	94
3.1. Introduction.....	95
3.2. Results.....	98
3.2.1. Modeling the Specificity and Cooperativity of HeteroMV Hybridization..	98
3.2.2. Measuring the Specificity and Cooperativity of HeteroMV Hybridization.....	101
3.2.3. Determining the Impact of Spacer Length on HeteroMV Hybridization Specificity and Cooperativity.....	104
3.2.4. Determining the Impact of Binding Orientation on HeteroMV Hybridization Specificity and Cooperativity.....	106
3.2.5. Detecting the Cis/Trans Relationship of Two Mutations Using HeteroMV Hybridization.....	108
3.2.6. Distinguishing Different Strains of SARS-CoV-2 Using HeteroMV Hybridization.....	111
3.3. Discussion.....	113
3.4. Materials and Methods.....	117

3.4.1. Oligonucleotides.....	117
3.4.2. Reagents.....	118
3.4.3. Consumables.....	119
3.4.4. Equipment.....	119
3.4.5. Modeling.....	120
3.4.6. Synthesis of DNA-Functionalized Silica Particles.....	123
3.4.7. Determining Number of Oligos Per Silica Particle.....	124
3.4.8. Atto647N Conjugation to Target Strands.....	125
3.4.9. Flow Cytometry Assay and Analysis to Measure Target Binding.....	125
3.4.10. Fluorescence Microscopy of Atto647N-Labeled Targets Hybridized to Beads.....	126
3.5. Appendix.....	127
3.6. References.....	152
Chapter 4. Summary and Future Outlook.....	155
4.1. Summary.....	156
4.2. Future Outlook for Multivalent DNA Hybridization.....	158
4.2.1. Further Applications for Multivalent DNA Hybridization in Diagnostics.....	158
4.2.2. Investigating HeteroMV DNA Hybridization on a Lipid Surface.....	163
4.2.3. Potential Advantages and Obstacles for Use of HeteroMV DNA Hybridization in Therapeutic Applications.....	165
4.3. References.....	166

List of Figures

Figure 1.1. The tertiary level of multivalent binding in nucleic acid hybridization.....	9
Figure 1.2. Impact of ligand spatial arrangement.....	15
Figure 1.3. Impact of n and binding valency.....	19
Figure 1.4. Impact of individual oligo length and binding affinity.....	22
Figure 1.5. Impact of linkers, spacers, and flexibility.....	25
Figure 1.6. Impact of anchor orientation and binding orientation.....	29
Figure 1.7. Quaternary level and higher multivalent DNA hybridization.....	32
Figure 1.8. Multivalent DNA hybridization enables DNA-based artificial motors.....	34
Figure 1.9. Applying multivalent hybridization for nucleic acid sensing.....	37
Figure 1.10. Using multivalent hybridization as a tool to study biology.....	40
Figure 2.1. Binding of target to random and patterned heteroMV SNAs.....	50
Figure 2.2. Effect of random heteromultivalency on binding valency and binding uniformity...	55
Figure 2.3. Effect of random heteromultivalency on thermodynamics and affinity.....	57
Figure 2.4. Characterization and binding analysis of patterned heteroMV SNAs.....	58
Figure A2.1. Modeling the impact of target concentration and surface occupancy on mean binding valency.....	77
Figure A2.2. Depiction of multivalent DNA binding interaction.....	78
Figure A2.3. Synthesis and characterization of heteroMV SNAs.....	79
Figure A2.4. Raw melts and binding capacity determination for random heteroMV SNAs.....	80
Figure A2.5. Characterization of modified oligonucleotides.....	81
Figure A2.6. Impact of target:SNA ratio on random heteroMV SNAs binding	

thermodynamics.....	82
Figure A2.7. Preparation of template/segments complex and PAGE characterization.....	83
Figure A2.8. Geometric model of template/segments complex attached to surface of AuNP....	84
Figure A2.9. Scheme, raw melts, and characterization for patterned SNAs template melting....	85
Figure A2.10. Preparation of mispatterned SNAs and determination of segment densities for patterned and mispatterned SNAs.....	86
Figure A2.11. Melting characterization of patterned SNAs binding excess targets.....	87
Figure A2.12. Raw melts, ΔH , and $-T\Delta S$ values for patterned, random and mispatterned n=6 heteroMV SNAs.....	88
Figure 3.1. Hypothesized advantages of heteromultivalent DNA hybridization and modeling key applications.....	96
Figure 3.2. Measuring the specificity and cooperativity of heteroMV hybridization using flow cytometry.....	102
Figure 3.3. Determining the impact of spacer length on heteroMV hybridization.....	105
Figure 3.4. Determining the impact of binding orientation on heteroMV hybridization specificity and cooperativity.....	107
Figure 3.5. Detecting the cis/trans relationship of two mutations using heteroMV hybridization.....	109
Figure 3.6. Distinguishing different strains of SARS-CoV-2 using heteroMV hybridization...	112
Figure A3.1. Modeling the specificity of homoMV particles for single mutant targets.....	127
Figure A3.2. Modeling the specificity of heteroMV particles for single mutant targets.....	128
Figure A3.3. Modeling the specificity of heteroMV particles for double mutant targets.....	129

Figure A3.4. Description of targets and Nupack predictions of target secondary structure.....	130
Figure A3.5. Synthesis and purification of Atto647N-labeled targets.....	132
Figure A3.6. Mass spectrometry characterization of Atto647N-labeled targets.....	133
Figure A3.7. Synthesis of DNA-functionalized silica particles.....	139
Figure A3.8. Characterization of DNA-functionalized silica particles.....	140
Figure A3.9. Flow cytometry gating strategy to isolate singlet beads for analysis.....	141
Figure A3.10. Representative histograms for all bead combinations binding the no spacer targets.....	142
Figure A3.11. Fluorescence microscopy images of beads hybridized to target.....	143
Figure A3.12. Impact of spacer length and type on binding of 8T, 8S, and 8T-8S beads.....	144
Figure A3.13. Impact of linker orientation on $n=1$ bead binding and representative histograms for $n=2$ beads binding WT targets.....	145
Figure A3.14. Representative histograms and results for all bead combinations binding the SNP ₁ /SNP ₂ , WT ₁ /SNP ₂ , SNP ₁ /WT ₂ , and WT ₁ /WT ₂ targets.....	146
Figure A3.15. Representative histograms and results for all bead combinations binding the model SARS-CoV-2 targets.....	147
Figure 4.1. Polymerase-mediated methods to detect unlabeled targets.....	159
Figure 4.2. Potential methods to enhance specificity for a target with a single SNP using multivalent hybridization.....	162
Figure 4.3. Three potential approaches to create patterned heteroMV lipid particles.....	164

List of Tables

Table A2.1. List of oligonucleotides used in Chapter 2.....	63
Table A2.2. T_m values for random heteroMV SNAs from van't Hoff melting assay.....	89
Table A2.3. Thermodynamic values for random heteroMV SNAs.....	90
Table A2.4. Affinity values for random heteroMV SNAs.....	91
Table A2.5. T_m values for random heteroMV SNAs from 5:1 and 10:1 target:SNA ratio van't Hoff melting assays.....	92
Table A2.6. Thermodynamic and affinity values for random heteroMV SNAs from 5:1 and 10:1 target:SNA ratio assays.....	93
Table A2.7. T_m values for patterned SNAs from van't Hoff melting assay.....	94
Table A2.8. Thermodynamic and affinity values for patterned SNAs.....	95
Table A3.1. List of oligonucleotides used in Chapter 3.....	117
Table A3.2. Average median fluorescence intensity \pm standard error of the mean values for all bead combinations binding no spacer G12C target.....	148
Table A3.3. Average median fluorescence intensity \pm standard error of the mean values for all bead combinations binding no spacer WT target.....	149
Table A3.4. Average discrimination factor \pm standard error of the mean values for all bead combinations binding no spacer targets.....	150
Table A3.5. Average cooperativity factor \pm standard error of the mean values for all bead combinations binding no spacer G12C target.....	151

List of Abbreviations

ACN	acetonitrile
ANOVA	analysis of variance
AuNP	gold nanoparticle
bp	base pair
C_{eff}	effective concentration
CF	cooperativity factor
Cy5	cyanine 5
DI	deionized
DF	discrimination factor
DMSO	dimethyl sulfoxide
DNA	deoxyribonucleic acid
DTT	dithiothreitol
EDTA	ethylenediaminetetraacetic acid
ESI-MS	electrospray ionization- mass spectrometry
FDA	United States Food and Drug Administration
FRET	Förster resonance energy transfer
fwhm	full width at half maximum
heteroMV	heteromultivalent
homoMV	homomultivalent
HFIP	1,1,1,3,3,3-hexafluoro-2-propanol
HPA	hydroxypicolinic acid
HPLC	high pressure liquid chromatography

HRP	horse radish peroxidase
KCN	potassium cyanide
K_d	dissociation constant
K_{eq}	equilibrium constant
KRAS	Kirsten rat sarcoma virus
MALDI-TOF-MS	matrix-assisted laser desorption ionization time-of-flight- mass spectrometry
MFI	median fluorescence intensity
MM	mismatch factor
mRNA	messenger ribonucleic acid
NHS	N-Hydroxysuccinimide
NP	nanoparticle
NSET	nanoparticle-surface energy transfer
nt	nucleotide
PAGE	polyacrylamide gel electrophoresis
PAINT	point accumulation in nanoscale topology
PBS	phosphate-buffered saline
PCR	polymerase chain reaction
PEG	polyethylene glycol
qPCR	quantitative polymerase chain reaction
rcf	relative centrifugal force
rpm	revolutions per minute
RNA	ribonucleic acid

RT	room temperature
SARS-CoV-2	Severe acute respiratory syndrome coronavirus 2
SDS	sodium dodecyl sulfate
SEM	standard error of the mean
SLB	supported lipid bilayer
SMCC	succinimidyl-4-(N-maleimidomethyl)cyclohexane-1-carboxylate
SNA	spherical nucleic acid
SNP	single nucleotide polymorphism
ss	single-stranded
SSC	saline-sodium citrate
TCEP	tris(2-carboxyethyl)phosphine
TE	tris-EDTA
TEM	transmission electron microscopy
TFA	trifluoroacetic acid
T_m	melting temperature
T_{tol}	tension tolerance
WT	wild type

Chapter 1

Overview of the Fundamental Concepts and Applications of Multivalent DNA

Hybridization

1.1. Introduction

Since elucidation of the structure of the DNA duplex in 1954 by Franklin, Watson, and Crick, nucleic acids have emerged as an enabling material outside of cell biology in a diverse array of disciplines, including diagnostics, therapeutics, and nanotechnology. The power of nucleic acids as a material is widely attributed to its easy chemical synthesis, high customizability, compatibility with enzymes, and particularly its simple base-pairing rules that allow straightforward binding known as hybridization. Nucleic acid duplexes are held together through the collective strength of many individual binding interactions, including hydrogen bond-mediated base pairing and van der Waals force-mediated base stacking. DNA, which is more commonly used due to its higher stability compared to RNA, first forms A-T and G-C base pairs through 2 or 3 individual hydrogen bonds, respectively. However, the primary stabilizing force for DNA hybridization is the base stacking that occurs between neighboring nucleotides on the same oligonucleotide strand following duplex formation.¹ These cooperative binding interactions enable stable duplex structures while maintaining highly selective binding of an oligonucleotide for its complement.

Despite the sequence-dependent specificity and high affinity of DNA hybridization, limitations exist which hinders further improvements in biotechnology applications. As the length of complementary oligonucleotide increases, the free energy of hybridization and the thermal melting temperature of the duplex will increase. Though high binding affinity is generally desired in many assays, there is a fundamental tradeoff between affinity and specificity. As affinity increases, discrimination between perfect match targets and single nucleotide mismatch or partial complement targets becomes more difficult.² Another limitation is that when oligonucleotides becomes longer and more flexible, they are more likely to contain significant intramolecular secondary structure. This secondary structure can hinder the affinity and kinetics of hybridization

occurring in solution as well as on a 2D or 3D surface.³ Therefore, to avoid these well documented problems of secondary structure and loss of specificity, finding alternate approaches to increase the affinity of hybridization is desirable.

To overcome these limitations, researchers have attempted to incorporate the concept of multivalent binding in DNA hybridization-based technologies. Multivalent binding occurs when two molecules or structures are bound through multiple individual binding interactions, such as ligand-receptor pairs. Biology has evolved to use a variety of multivalent interactions to enable higher affinity and higher specificity binding. For example, viral particles express trivalent hemagglutinin on their surface to allow high affinity multivalent binding to multiple sialic acid receptors on cell surfaces simultaneously, leading to increased infectivity.⁴ Multivalent interactions are also essential in carbohydrate binding as it allows glycan molecules that individually form weak and low specificity interactions with their receptors to bind cooperatively to achieve enhanced overall binding affinity and specificity.⁵ Mimicking these natural multivalent interactions, examples of artificial multivalent binders are now abundant. Recently, Xu *et al.* engineered self-assembling vesicles that exhibited enhanced multivalent binding to inhibit the growth of amyloid peptides fibrils.⁶ Kwon *et al.* demonstrated the ability of precisely designed DNA-based nanostructures to bind tightly to viral particles and aid in sensing and inhibition of the viruses.⁷

Inspired by these examples of multivalency, a number of fundamental concepts, new molecular designs, and related applications of multivalent DNA hybridization have emerged recently and are the focus of this chapter. Herein, multivalent DNA hybridization is defined as a binding interaction that is mediated by the hybridization of multiple pairs of complementary oligonucleotide sequences presented on two structures (**Figure 1.1A**). Moreover, we classify these

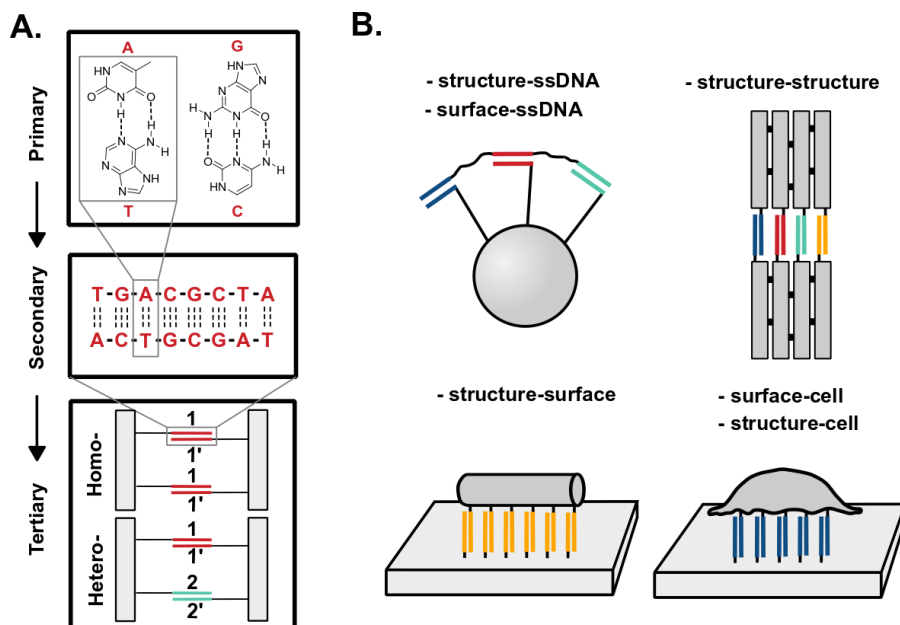


Figure 1.1. The tertiary level of multivalent binding in nucleic acid hybridization. (a) Scheme describing the primary, secondary, and tertiary levels of multivalent binding in DNA hybridization. (b) Examples of tertiary level multivalent binding interactions between different probe and target structures and materials.

interactions as tertiary level multivalent binding to distinguish them from the two existing levels of multivalent binding present in a standard DNA duplex. Specifically, the 2-3 distinct hydrogen bonds that link pair two nucleotides together can be considered the primary level, while the multiple individual base pairs that link two oligonucleotides together can be regarded as the secondary level of multivalent binding. Finally, we will use the terms “probe” and “target” to describe the multivalent structures that present the complementary oligonucleotide “ligands” and “receptors”, respectively. However, in some cases the probe and target are physically identical structures, such as two nanoparticles with the same diameter, and thus probe and target can be used interchangeably.

Examples of this tertiary level of multivalency, often simply referred to as multivalent DNA hybridization in this thesis, explored thus far include binding between a DNA-coated structure (nanomaterial or particle) or surface and a complementary single-stranded target,⁸⁻⁹ two

DNA-coated structures,¹⁰⁻¹¹ a DNA-coated structure and a DNA-coated surface,¹²⁻¹⁴ and a DNA-coated structure or surface and a cell presenting DNA on its outer membrane (**Figure 1.1B**).¹⁵⁻¹⁶ Furthermore, investigations of multivalent DNA hybridization have explored both homomultivalent interactions, where each oligonucleotide duplex is identical, and heteromultivalent interactions, with multiple oligonucleotide pairs with unique sequences (**Figure 1.1A**). Successful multivalent interactions between structures of varying material, shape, and size often require careful design of a multivalent probe for the desired multivalent target to achieve optimal overall binding. Important design parameters include the positioning of each ligand on the probe and receptor on the target, the number of ligands and receptors presented (n), as well as the individual affinity between each binding partner. Additionally, the length of the spacer between binding regions on a single stranded target or of the linker connecting oligos to a multivalent structure can significantly impact the effectiveness of the multivalent hybridization. Finally, the anchoring orientation and binding geometry of oligos can further tune multivalent binding properties and applications. Implementing this tertiary level of homo- or heteromultivalent binding, offers more tunable binding parameters that has enhanced the utility of polynucleotide hybridization in nanotechnology, sensing, and biological investigations.

1.2. Fundamentals of Multivalent DNA Hybridization

1.2.1. How Does Multivalency Enhance Binding Affinity and Specificity?

Multivalent binding interactions can achieve collective affinities, or avidities, that are much stronger than a monovalent binding interaction. Often, multivalent interactions are thought to be stronger simply because they are the combination of many individual monovalent binding interactions. However, the multivalent binding free energy is not equal to the sum of the individual

monovalent binding free energies. Instead, the degree of the binding enhancement from multivalent binding depends on many other parameters. To better understand these parameters that determine the multivalent binding avidity, we will describe a simple bivalent binding event, where linked ligands A and B bind multivalently to linked receptors A' and B'. Each individual binding event involved in a multivalent interaction takes place sequentially. Thus, we will begin with A binding A', although it is equally likely that B could bind B' first. This initial binding event mimics a typical monovalent interaction where the amount of binding at equilibrium is influenced by the concentration of each binding molecule, i.e., the number of molecules in a solution with a fixed volume. After A is bound to A', the next interaction can then take place. Unlike ligand A which had to locate its receptor A' from anywhere in the entire solution volume, ligand B is constrained within a drastically smaller volume as it is physically linked to ligand A, which has already bound the target. The volume that ligand B can occupy through diffusion is now based on the length of the linker connecting it to A, rather than the total volume of the solution. If designed properly, receptor B' will also be located within this reduced volume and thus have a higher local or effective concentration. To account for this higher effective concentration, B then binds B' with an enhanced affinity, $K_{eq, B, multi}$, according to the following equation:

$$K_{eq, B, multi} = K_{eq, B, mono} * c_{eff} \quad (1)$$

where $K_{eq, B, mono}$ is the monovalent binding affinity and c_{eff} is a factor to account for the effective concentration. The total affinity term for the bivalent interaction, $K_{eq, A-B, multi}$ is thus:

$$K_{eq, A-B, multi} = K_{eq, A, mono} * K_{eq, B, mono} * c_{eff} \quad (2)$$

Several factors can influence c_{eff} in the multivalent binding affinity equation above, but it can be approximated as the total concentration of receptor B' molecules located in the volume that B can reach after A has bound A'. To maximize c_{eff} , the multivalent interaction should thus be

designed such that there are as many B' molecules as possible within as small of a volume as possible. In the case where there is only one copy of B' on the target, the length of the linker can be increased to ensure that B' is located within the diffusion volume of B. However, ideally the linker will be just long enough for B to reach B' as any length longer would increase the volume without offering additional access to B' receptors. Alternatively, if the linker is too short and B can't interact with B' then c_{eff} becomes 0 and thus the total multivalent binding avidity is 0 as well. Beyond the factors that impact c_{eff} , the individual binding affinity terms for A binding A' and B binding B' can also change in several instances. For example, strain experienced by the linker, interactions between the linker and the target, and cooperative interactions where one binding event has a significant impact on subsequent binding events can all further tune the overall binding avidity. For further discussion on the impact of linkers and the effective concentration model, see section **1.2.6. Linkers and Spacers Increase Reach and Provide Flexibility to Multivalent Hybridization Interactions**. In addition to enhancing the affinity, multivalent binding can also lead to more specific binding events. For example, if A binds A' with an affinity 10x stronger than its affinity to C', then the total affinity between a bivalent molecule A-A and a bivalent target A'-A' will be 100x greater than between A-A and C'-C'. These enhancements in avidity and specificity for a bivalent interaction, can potentially be even greater when the binding valency is further increased, though effective design becomes more difficult. For further discussion on the avidity and specificity of multivalent interactions, see **Chapters 2 and 3**, respectively.

1.2.2. Defining Homomultivalent and Heteromultivalent DNA Hybridization

All tertiary level multivalent DNA hybridization interactions can be divided into two main categories: homomultivalent (homoMV) hybridization and heteromultivalent (heteroMV)

hybridization. In homoMV hybridization interactions, each individual ligand and individual receptor have the same sequence, resulting in the formation of multiple identical duplexes. The most common type of homoMV hybridization occurs between two homoMV DNA nanostructures or DNA-functionalized structures, such as nanoparticles, microparticles, or surfaces. In the many examples of this class of homoMV hybridization described in recent years, a large variety of materials have been used as the scaffold linking the oligonucleotides. For example, Estirado *et al.* demonstrated homoMV binding between a 1-D rod-like polymer presenting a homomultivalent DNA display and a DNA duplex with identical short single-stranded overhangs.¹⁰ Bazrafshan *et al.* showed also that homoMV-binding DNA origami rods can bind and roll along a surface densely coated with the complementary RNA strand.¹⁴ Meanwhile, Kern *et al.* investigated homoMV binding occurring between DNA origami-coated silica beads and protein-linked DNA receptors studding the surface of a cell.¹⁶ Though less common, multivalent binding between homoMV DNA-functionalized structures and single-stranded DNA containing multiple repeating sections has also been explored. Curk *et al.* demonstrated the concept by computationally modeling homoMV binding between a DNA-functionalized surface and a full-length bacterial genome target.⁹ Due to the length of the bacterial genome target used in this work many sections contain significant complementarity to a single oligonucleotide sequence and thus could form many individual duplexes with the surface. However, detection of shorter sequences, which are less likely to possess significant repetitions, is often more desirable, and therefore homoMV binding is not appropriate for such targets.

Alternatively, in heteroMV hybridization interactions, multiple distinct ligand and receptor sequences are involved, yielding multiple non-identical duplexes. Like homoMV hybridization, heteroMV hybridization can occur between two DNA nanostructures or DNA-functionalized

structures. For instance, Nangreave *et al.* investigated heteroMV binding between two DNA tile nanostructures that formed heterodimers through the interaction of several sticky end-mediated hybridization events.¹¹ In addition to being able to bind other heteroMV structures, heteroMV structures are able to bind single-stranded targets with non-repetitive sequences, and therefore have expanded target options compared to homoMV structures. We characterized the properties of heteroMV binding to ssDNA using gold nanoparticles functionalized with up to 6 distinct oligo sequences (**Chapter 2**).⁸ The six oligos were designed to bind consecutively along a ~100mer ssDNA sequence that was based on a common drug target's transcript. Beyond the increased targeting capabilities, heteroMV structures can simultaneously present ligands with different lengths or G/C contents which allows more control over the thermodynamics and kinetics of the multivalent binding. Moreover, Schueder *et al.*, as well as our own work discussed in **Chapter 3**, demonstrated that heteroMV binding can be used to detect the proximity of two unique oligo sequences, or oligo-linked proteins, in "AND" logic gate type assays.¹⁷

1.2.3. The Spatial Arrangement of Oligonucleotides Significantly Impacts Multivalent Hybridization

For both homoMV and heteroMV hybridization, an important design parameter is the spatial arrangement of individual ligands and receptors at the probe-target interface. Forming an effective multivalent hybridization interaction requires each ligand to physically interact and hybridize with each receptor. For example, if a probe presents two ligands spaced 5 nm apart it

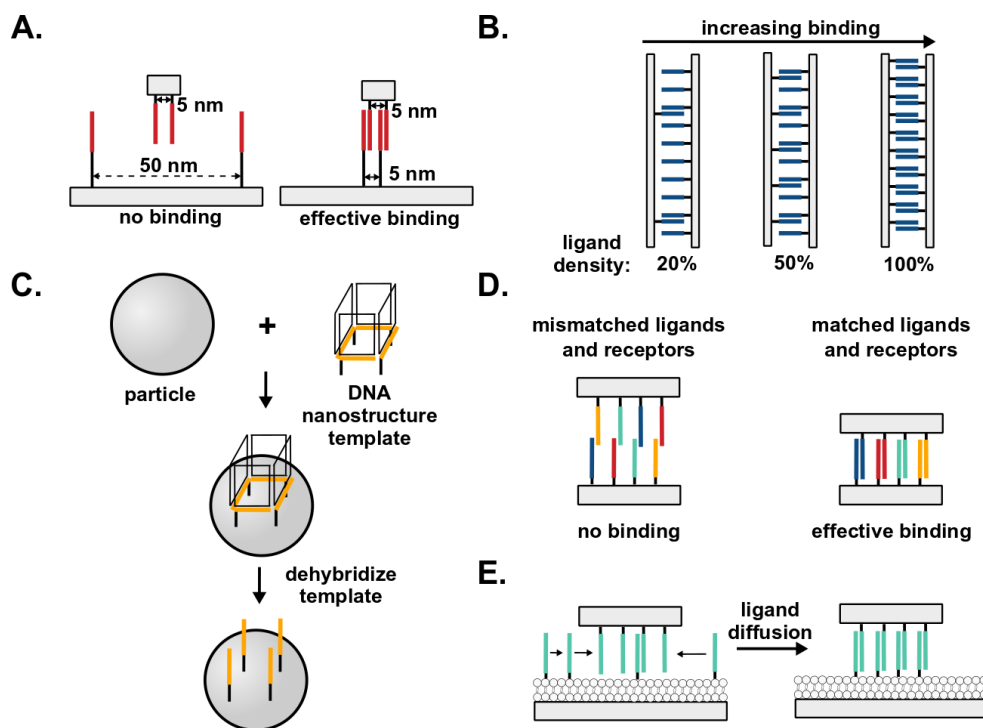


Figure 1.2. Impact of ligand spatial arrangement. (a) Example of how the distance between ligands can impact the effectiveness of multivalent binding to a target that presents receptors with a specific distance between them. (b) Scheme describing how ligand density can be optimized to maximize total binding to a densely functionalized target. (c) One method for controlling the position and spacing of DNA ligands on a particle or surface, adapted from Edwardson *et al.*²² (d) In heteroMV binding, ligands and receptors must have matching positions to allow multivalent binding. (e) Structures with ligands on a fluid surface, such as a supported lipid bilayer, can allow ligand diffusion to form more effective multivalent binding.

will suffer from a large energetic penalty if it were to bind bivalently to a target that presents two receptors spaced 50 nm apart, or instead not be able to form the multivalent interaction at all (**Figure 1.2A**). One approach to achieve proper ligand spacing is to use DNA nanostructures or DNA origami structures to precisely position each oligo ligand. Nangreave *et al.* demonstrated that binding between two DNA tile structures that each positioned oligos with identical inter-oligo distance resulted in an approximately 2-fold greater change in free energy when increasing valency from 1 to 4.¹¹ However, precise control of the spacing between ligands on a surface coated randomly with a layer of DNA is more challenging. In this case, the spacing between each ligand

can be approximately controlled by adjusting the oligo concentration incubated with the scaffold to tune the oligo density on the surface. In many cases, the density of DNA on the surface can simply be maximized to ensure that individual oligos are close enough to form as many duplexes as possible with the target (**Figure 1.2B**). Scheepers *et al.* measured binding between two colloidal particles presenting complementary oligos and found that hybridization-mediated aggregation rates were highly sensitive to the density of DNA on each particle as minimal aggregation occurred with 4×10^3 ligands/ μm^2 and maximum aggregation occurred with 2.2×10^4 ligands/ μm^2 .¹⁸ Other studies also observed this “super-selectivity”, where binding selectivity is based on the number of interactions formed rather than the presence or absence of a target.⁹⁻¹⁰ However, though not directly quantified in multivalent binding systems, Pinheiro *et al.*'s findings in monovalent binding systems suggest that high density and steric crowding can decrease hybridization on-rates by as much as ~20%.¹⁹ Moreover, Randeria *et al.* suggests that higher density leads to more stable monovalent hybridization for the first few targets that bind a DNA-coated surface due to a higher local salt concentration, but finds that each additional duplex formed makes binding less favorable.²⁰

Alternatively, to control more precisely the spacing of ligands on a surface, several approaches have been described that make use of DNA nanostructures to transfer DNA ligands to the surface of the material in a controlled fashion. For example, Suzuki *et al.* created a 1D DNA template-based method to deposit two oligos on a gold nanoparticle with precise spacing.²¹ Later, Edwardson *et al.* instead demonstrated patterning of oligos in 2D shapes on a gold nanoparticle surface using simple DNA nanostructure templates (**Figure 1.2C**).²² Finally, Xie *et al.* encapsulated gold nanoparticles inside 3D DNA lattices to transfer a 3D arrangement of oligos onto the gold nanoparticle.²³ These template-based approaches all enabled highly controlled oligo

spacing and patterning, though the multivalent binding capabilities of the resulting patterned DNA-particles were not explored.

Additionally, heteroMV-hybridizing structure design must consider the order or arrangement of each individual ligand on the structure in order to match the positions of their complements on the target (**Figure 1.2D**). For example, Nangreave *et al.* used DNA tile nanostructures to ensure that each pair of complementary oligos were presented in a specific order directly across from each other.¹¹ We instead used a different approach to match the order of oligos on the surface of a particle with a ssDNA target (**Chapter 2**).⁸ Specifically, we first bound each oligo ligand monovalently to the target sequence to arrange the oligos in the correct position relative to each other. Then excess of the target-ligand complex was incubated with gold nanoparticles to deposit many series of the ligands on the surface of the particle while still bound to the target. In this way, the oligo ligands were positioned with appropriate spacing and ordering to then efficiently re-bind the same target sequence heteromultivalently. This method resulted in a ~15 order of magnitude enhancement in binding affinity for particles with controlled instead of random ligand positioning.

Beyond simply matching ligand spacing on the probe with receptor spacing on the target, ligand spatial arrangement can also impact multivalent binding in other ways. Nangreave *et al.* revealed that when two sticky end associations were on adjacent helices, the multivalent binding based-increase in $-\Delta H$ was ~30 kcal/mol, while two binding pairs spaced further apart instead reduced $-\Delta H$ by ~3 kcal/mol relative to monovalent binding.¹¹ Moreover, Bazrafshan *et al.* showed that DNA origami motors moved more linearly and processively when ligands were located in the middle of the motor instead of at the two ends.¹⁴ However, in the case of ligands on a fluid surface, such as DNA attached to a supported lipid bilayer, spacing between ligands is less important than

the total ligand density due to lateral mobility. Dubacheva *et al.* showed in a host-guest binding multivalent system that when ligand density is moderate, total binding is higher and more selective on a fluid surface because more ligands are able to diffuse into the binding region and stabilize the interaction (**Figure 1.2E**).²⁴ However, when ligand density is high, total binding was observed to be lower experimentally and computationally on a fluid surface because surface bound-targets recruited too many nearby ligands and resulted in a global depletion of ligands on the surface. An additional approach to overcome energetic penalties due to uneven ligand-receptor spacings in multivalent hybridization is to include flexible linkers and spacers (**See section 1.2.6. Linkers and Spacers Increase Reach and Provide Flexibility to Multivalent Hybridization Interactions for this discussion**). Taken together, controlling the spatial arrangement in multivalent systems is critical in tuning multivalent binding properties and dictating the effectiveness of the desired function.

1.2.4. The Value of n Dictates Binding Valency of Multivalent Hybridization Interactions

Another critical parameter in multivalent hybridization is the binding valency, or the number of individual duplexes formed in a multivalent interaction. In well controlled systems where the probe or target has a specific number of ligands or receptors (n), the binding valency of homoMV and heteroMV binding interactions should be equal to the smaller n value, assuming proper spacing and positioning (**Figure 1.3A**). This was shown by Estirado *et al.* where the target was converted from $n=1$ to $n=6$ through the addition of ssDNA overhangs, leading to a linear decrease in ΔG and >4 order of magnitude increase in binding affinity, suggesting increased binding valency (**Figure 1.3B**).¹⁰ Similarly, Nangreave *et al.* generally observed more

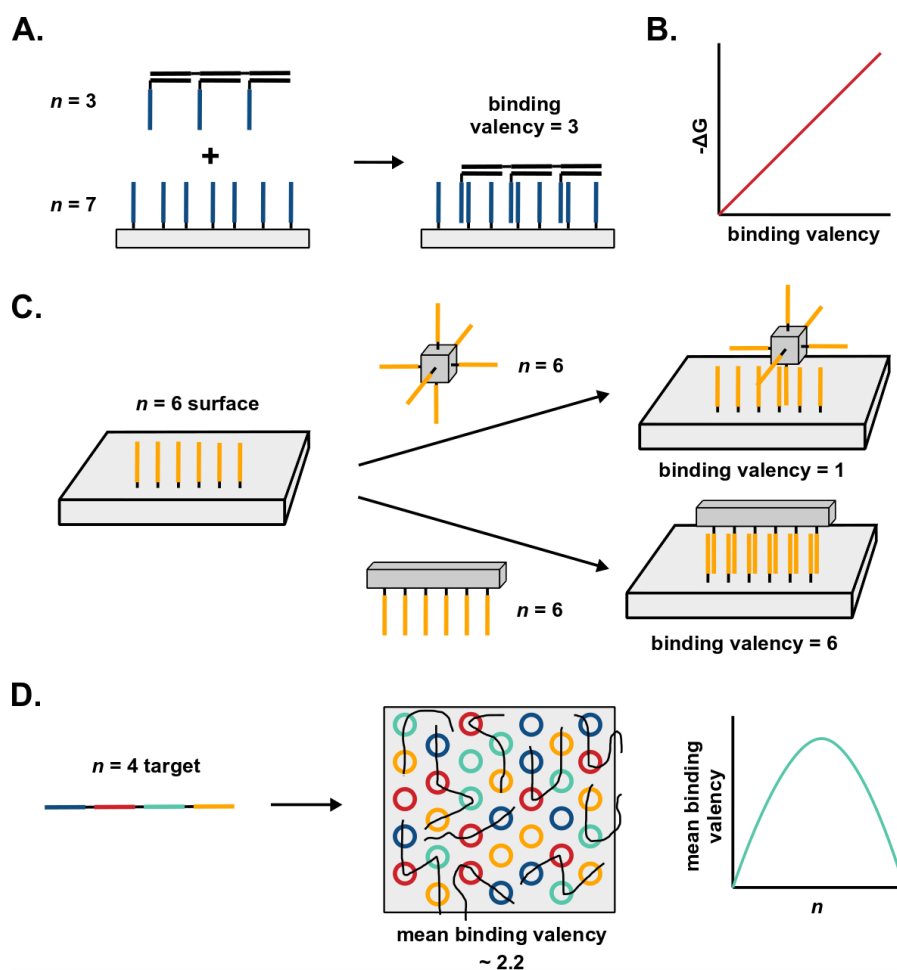


Figure 1.3. Impact of n and binding valency. (a) Scheme illustrating how the probe or target with the smaller value of n determines the maximum binding valency. (b) Idealized plot describing the positive linear relationship between binding valency and $-\Delta H$ of the multivalent interaction. (c) 3D shape of the probe and target can determine overall binding valency. (d) Mean binding valency of a heteroMV binding interaction between a surface with random ligand arrangement and a target peaks and then decreases as n increases due to probability of ligands being positioned correctly decreases, adapted from Deal *et al.*⁸

energetically favorable binding and increasing melting temperatures with a $\sim 25^\circ\text{C}$ higher T_m when n was increased from 1 to 4.¹¹ However, in both homoMV and heteroMV binding if the spacing or positioning is mismatched, then valency will be less than n and instead be equal to the number of ligands that can bind simultaneously as discussed in the previous section **1.2.3. The Spatial Arrangement of Oligonucleotides Significantly Impacts Multivalent Hybridization (Figure 1.2B and 1.2D)**. Similarly, if the shapes of the target and probe are not compatible then the valency

can be limited as well. For example, in the case of a cube binding a 2D surface, it is not possible for all of the ligands on the probe to bind the target simultaneously as some ligands are located too far away from the contact area of the two structures (**Figure 1.3C**).¹⁸ Relatedly, when spheres or cylinders hybridize to surfaces, there is a discrete contact area at the interface of the two DNA-coated scaffolds, thus resulting in binding valencies less than n . Yet, when engineering DNA-based artificial motors, these unbound oligos away from the initial binding interaction were coupled with enzymatic activity to power processive rolling of the structure across the surface.¹³⁻

14

For heteroMV binding where either the probe or the target has a random ligand arrangement, the relationship between n and binding valency is more complicated. We showed that if the ligands are arranged randomly, binding valency saturates once n reaches a certain value, which varied between $n=4$ and $n=6$ based on assay conditions and individual oligo binding affinities, and then decreases (**Figure 1.3D and Chapter 2**).⁸ This observation is based on the probability that each ligand is positioned in the right location, which decreases as n increases. Thus, when n is low, the impact of ordering and spacing on binding valency is less significant.

Ultimately, the binding valency of multivalent hybridization can greatly impact binding thermodynamics and kinetics. One straightforward effect is that increasing binding valency leads to increased collective binding affinity, referred to as avidity, as described in section **1.2.1. How Does Multivalency Enhance Binding Affinity and Specificity?**.^{8, 10} Therefore, when aiming to increase assay sensitivity, it is desirable to increase binding valency as much as possible to maximize avidity. Similarly, Scheepers *et al.* showed experimentally and computationally that increasing receptor density, and thus increasing binding valency, led to sharp increases in particle-particle binding rates.¹⁸ However, as binding valency increased, particles presenting higher affinity

ligands lost selectivity, whereas the selectivity of particles with low affinity ligands increased (see **section 1.2.5. Individual Oligonucleotide Length and Monovalent Binding Affinity Impacts Binding Avidity and Selectivity for further discussion**). Recently, the impact of higher binding valency has been further investigated in the context of DNA-based artificial motors by Kowalewski *et al.* through simulations. It was found that increasing multivalency (up to $n=16$) allows the motors to travel longer on the surface before detaching, though the translocation speed of the motors was actually reduced.²⁵ These examples demonstrate that while increasing valency is often desirable, there are also instances when lower valency binding might be more advantageous depending on the desired outcomes.

1.2.5. Individual Oligonucleotide Length and Monovalent Binding Affinity Impacts Binding Avidity and Selectivity

The binding strength of each distinct nucleic acid duplex, often dictated by the number of base pairs and G/C content in the duplex, can tune the overall properties of multivalent hybridization interactions including avidity (**Figure 1.4A**). Estirado *et al.* demonstrated that presenting ssDNA overhangs with 5 complementary nucleotides instead of 4 resulted in two orders of magnitude higher binding avidity.¹⁰ However, many works have observed that increasing individual oligonucleotide binding affinity can result in worse cooperativity as a single duplex becomes strong enough to form a stable monovalent interaction (see **Chapter 3 for further discussion**). On the contrary, shorter length or lower affinity ligands can give rise to strong cooperative binding that results in super-selective binding (**Figure 1.4B**). As discussed in the **section 1.2.3. The Spatial Arrangement of Oligonucleotides Significantly Impacts Multivalent Hybridization**, super-selective binding is characterized by a strong dependence on the receptor

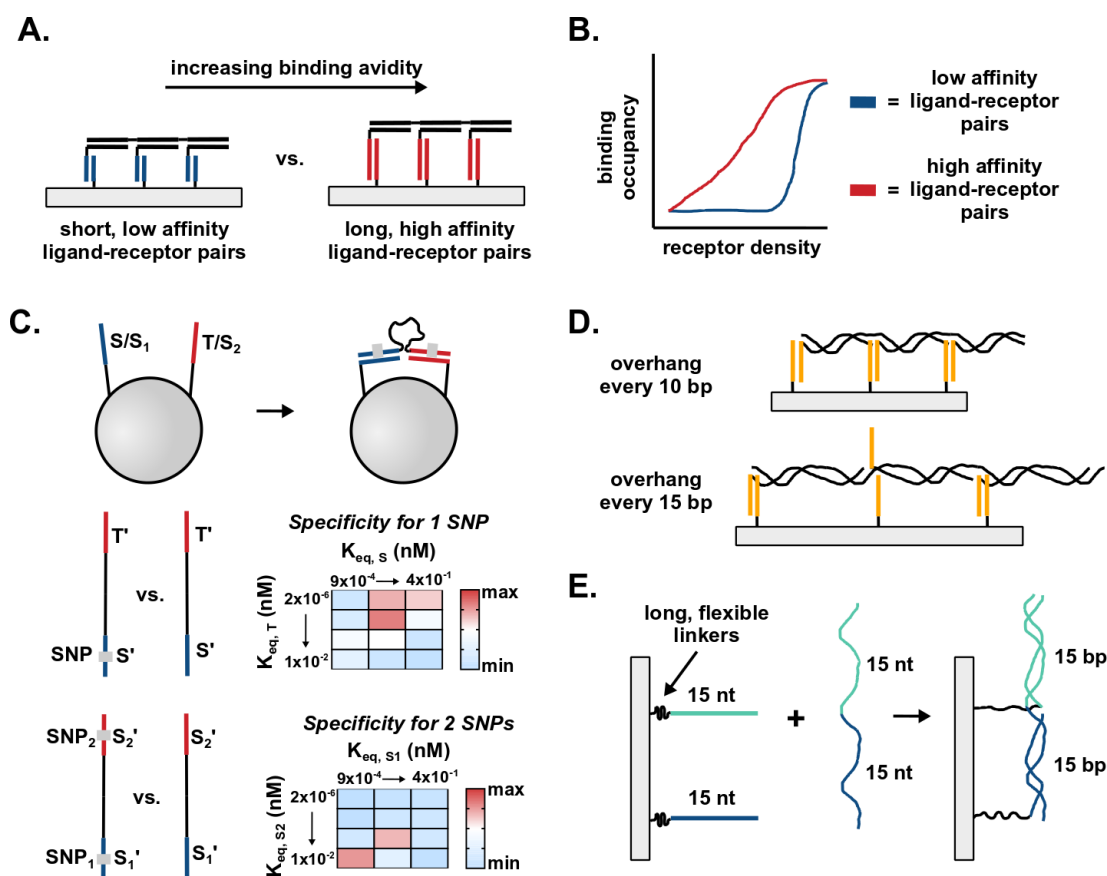


Figure 1.4. Impact of individual oligo length and binding affinity. (a) Longer or higher affinity ligands increases maximum binding avidity. (b) Use of shorter or lower affinity ligands can lead to “super-selective” binding that is highly sensitive to density of receptors on the target. (c) Computational data predicting how the affinity of each ligand presented on a bivalent probe impacts the specificity of binding a ssDNA target with 1 or 2 SNPs. Top, specificity for a target with a SNP in the S’ region is calculated as (SNP-containing target binding) / (non-SNP-containing target binding). Bottom, specificity for a target with a SNP in the S1’ and in the S2’ regions is calculated as (double SNP-containing target binding) / (non-SNP-containing target binding). Adapted from **Chapter 3**. (d) Positioning ssDNA overhangs every 10 bp on a duplex scaffold to match helicity of DNA duplexes ensures that all ligands extend from the same side of the duplex. (e) Long, flexible linkers allow ligands to reach the opposite side of a duplex to allow 15 nt ligands to bind ssDNA targets without exhibiting strain.

density or total binding valency, where higher valencies yield strong binding and lower valencies yield weak binding.⁹ Scheepers *et al.* demonstrated that 9-15 bp duplexes between DNA-coated particles resulted in a linear dependence between particle binding events and receptor density, whereas 5-8 bp duplexes resulted in measured binding rates that increased nearly quadratically

with receptor density.¹⁸ Similarly, Estirado *et al.* showed in their 1D binding system that 5 bp duplexes demonstrated “super-selective” binding, while binding of 7-8 bp duplexes with stronger affinities did not depend significantly on binding valency or density.¹⁰ Similar trends were observed in our studies, where decreasing the affinity of each oligo by reducing the ionic strength of the buffer, resulted in more stable and higher valency binding to the target, with up to 5°C higher melting temperatures when $n=6$ (**Chapter 2**).⁸

The individual oligonucleotide binding affinity or length can significantly impact the specificity of multivalent hybridization in addition to avidity. Curk *et al.* showed that when binding homomultivalently to a ssDNA target, if the binding oligo is shorter, it is more likely to encounter completely overlapping off-target sequences, resulting in lower discrimination between the genomes of similar bacterial strains.⁹ Alternatively, if the oligo is longer, it is unlikely to find a complete overlapping sequence but is more likely to form undesired binding interactions with partial overlapping sequences. This is one of the reasons why probes designed to detect single nucleotide polymorphisms (SNPs) typically fall in a narrow range of lengths, such as ~25 nucleotide probes commonly used in microarray sensing assays.²⁶ We also showed the importance of oligo affinity on heteroMV binding specificity in detecting single mutant and double mutation targets (**Chapter 3**). For single mutant targets, presenting a short tuning oligo (T) alongside a SNP-binding oligo (S) allows more precise tuning of total binding affinity, thus allowing improved specificity (**Figure 1.4C, top**). For double mutant targets, cooperativity and specificity are both important and therefore two weak affinity oligos that bind cooperatively with strong discrimination for SNPs can result in enhanced binding specificity (**Figure 1.4C, bottom**). In this case, specificity was enhanced because each oligo is complementary to a SNP and thus can be easily distinguished from the wildtype target, which forms two mismatches with the probe. Important applications of

this include distinguishing heterozygous cis mutations from heterozygous trans mutations and discriminating between similar viral strains (**Figure 1.9B, Chapter 3**).²⁷⁻²⁹

The length of binding ligands when binding ssDNA or dsDNA targets is also significant due to the fundamental structure of a DNA duplex. A beta-form DNA duplex contains ~10 bp for every rotation of the double helix and thus every 10th nucleotide is approximately on the same side of the duplex. When binding to ssDNA overhangs off of a dsDNA target, Estirado *et al.* ensured that each overhang extended in the same direction by using 10-11 nt duplexes in the dsDNA scaffold (**Figure 1.4D**).¹⁰ Similarly, when a DNA-functionalized structure binds a ssDNA target, using 10 nucleotide long ligands guarantees that the linker connecting each ligand to the structure spans as short of a distance as possible. However, previously we demonstrated effective heteroMV binding to ssDNA using 12-15 nt binding oligos (**Chapter 2**).⁸ In this case, the observed effective multivalent binding is likely a result of the use of flexible T10 linkers to attach the binding oligos to the particle surface, potentially allowing the binding oligos to bind their complementary target region without enthalpic cost due to straining (**Figure 1.4E**). Moreover, the presence of gaps between binding regions on the target can further minimize strain when using binding oligos that are not 10-11 nt long. The following section will further explain how linkers and spacers can be used to minimize enthalpic strain and enhance overall efficacy of multivalent hybridization.

1.2.6. Linkers and Spacers Increase Reach and Provide Flexibility to Multivalent Hybridization Interactions

In all multivalent structures, individual ligands are connected to each other through spacers or to a scaffold through linkers. Spacers and linkers can vary greatly in length, ranging from long polymers to several covalent bonds. In general, both spacers and linkers can be used to increase

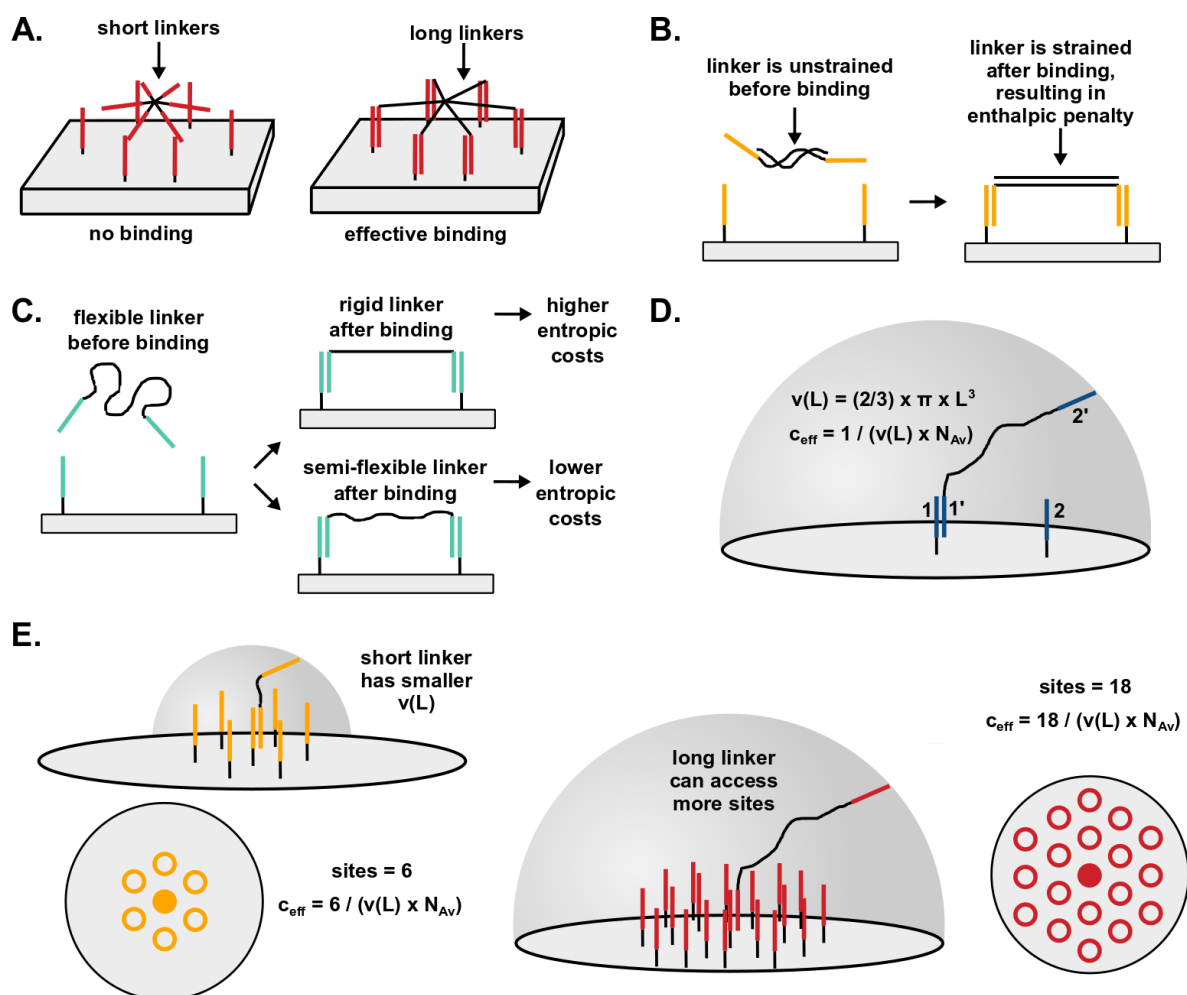


Figure 1.5. Impact of linkers, spacers, and flexibility. (a) Illustration of using long linkers to allow ligands to span greater distances to bind their receptors. (b) Short linkers that must stretch to allow for multivalent binding can experience strain that results in enthalpic penalties. (c) Scheme describing the impact of loss of conformational entropy that flexible linkers experience after binding. If the linker maintains some flexibility after binding, then entropic costs are lower. (d) Effective concentration, c_{eff} , model suggests that increasing linker length results in a larger maximum diffusion volume, $v(L)$, for the unbound ligand and a lower c_{eff} for the unbound receptor on the target. (e) For maximum c_{eff} when binding a target with many receptors, such as a dense surface, there is a trade-off when increasing linker length. A shorter linker has smaller $v(L)$ but can access fewer receptors, whereas a longer linker has increased $v(L)$ but has more accessible receptors.

the span, the distance that an oligo can reach, of multivalent probes and targets in order to form an effective interaction. If several ligands on a probe are positioned closer together than their receptors on the target, then the length of the linker that connects the ligands to each other or to

the probe can be tuned. Importantly, if the linker is too short, the ligands will not be able to bind multivalently at all (**Figure 1.5A**) or the linker will experience enthalpic strain as it stretches to allow the ligands to reach the receptors, thus lowering the stability of the binding interaction (**Figure 1.5B**). Schueder *et al.* demonstrated this concept well by showing that target binding could be tuned by increasing the linker length to approximate the spacing between two short DNA ligands.¹⁷

Despite the increased span offered by linkers, initial studies assumed that flexible linkers become completely rigid after binding, even when longer than the distance between ligands, and thus will result in loss of conformational entropy upon binding (**Figure 1.5C, top**).³⁰ Specifically, this would result in an entropic cost of binding due to loss in conformational freedom of 0.7 kcal mol⁻¹ per freely rotating single bond of the linker. However, more recently, others found that linkers often maintain flexibility after binding and that the impact of flexible linkers is relatively minimal with a less severe penalty per linker bond (**Figure 1.5C, bottom**).³¹⁻³² One possible explanation of the impact of the linker length is the effective concentration (c_{eff}) model (**equation 2**). The c_{eff} is defined as the ratio of the binding constants for the second ligand-receptor interaction (intramolecular) and first ligand-receptor interaction (intermolecular) formed between a multivalent probe and target.³³ Essentially, c_{eff} is proportional to the probability that two binding ligands on either end of a linker are located at a certain distance from each other (**Figure 1.5D**).³² This probability is determined by the linker length and the corresponding diffusion volume, i.e., the volume that a tethered ligand can diffuse.³⁴ When linker length increases, the unbound ligand can diffuse further from its receptor and thus the probability of successful binding and c_{eff} decreases. Krishnamurthy *et al.* found that the stability of binding with long, flexible linkers is only 8-fold lower than when linker length is approximately equal to the ligand spacing.³²

The impact of a high-density coating of DNA ligands on a 2D or 3D surface has also been explored using the effective concentration model. In this case, there are two opposing parameters that impact c_{eff} : linker length and number of accessible ligands.³³ As described previously, c_{eff} decreases as linker length increases, but when multiple ligands are present, c_{eff} increases due to the increasing number of accessible ligands (**Figure 1.5E**), partially canceling out the negative impact of linker length. Therefore, the diminished c_{eff} values due to linker length are less significant in multivalent binding when ligand density is high. In fact, we observed increasing total binding of a spacer-containing DNA target to a DNA-coated silica bead as spacer length increased (**Chapter 3**). Mathematical simulations by Curk *et al.* predicts that multivalent binding will still be effective when a DNA-functionalized surface hybridizes multivalently to distant sites throughout a genomic DNA target.⁹ Additionally, with a computational method, Kowalewski *et al.* showed that increasing the linker length between the body and legs of a “molecular spider”, allowing each leg to reach more DNA ligands, leads to diffusion speeds that increase proportionally to the length of the linker squared.²⁵

In multivalent hybridization, the linker material can also have a significant impact on the binding avidity. Despite the convenience of using ssDNA as linkers to connect each binding region or to attach to the scaffold, it can lead to undesirable interactions such as binding between the ssDNA linker and other oligonucleotides in the system or forming linker secondary structures. Thus, the sequence of the DNA linker must be carefully designed. For example, poly-T or poly-A linkers are commonly used as they do not form any secondary structure and only bind strongly to poly-A or poly-T oligos. Alternatively, non-DNA linkers can be used, such as polyethylene glycol, which have minimal interactions with DNA. When binding multivalently to ssDNA targets containing a spacer between binding sites, such as two distant sites in a transcript or genome, it is

possible that the spacer regions can form weak interactions with the ligands, and the likelihood increases as the spacer region increases in length. In this scenario, neither the material nor sequence of the spacer region can be changed and thus these undesirable interactions are sometimes inevitable.

1.2.7. Anchor Orientation and Spacer Length Control the Binding Geometry of Multivalent Hybridization

One parameter that is specific to multivalent DNA hybridization is the binding orientation of each oligo with the target. The two strands in a nucleic acid duplex are antiparallel, where the 5' end of one strand is bound to the 3' end of the complementary strand and vice versa. Because of this feature in DNA hybridization, the terminus that is used to attach the ligand to the probe will impact the orientation that the oligo binds the target. For example, when two particles are functionalized with complementary oligos that are each anchored to the particle through their 5' terminus, the resulting homoMV duplexes can form a different geometry compared to when one of the oligos is attached through its 3' end (**Figure 1.6A**).³⁵ Particularly when the linkers are short or less flexible and ignoring particle curvature effects, duplexes with two 5' anchored oligos can form perpendicular to the surface of the particles whereas duplexes with one 5' and one 3' anchored oligo can form parallel to the surface.³⁶ One important consequence of this is the distance between two particles bound by DNA duplexes. When binding in the perpendicular orientation, the distance between the particles will be approximately equal to the sum of the lengths of the DNA duplex and the two linker groups. Thus, if the duplex length increases, then the particles will be distanced further apart from each other. However, when binding in the parallel orientation, the distance between the particles will instead be approximately equal to sum of the width of a DNA

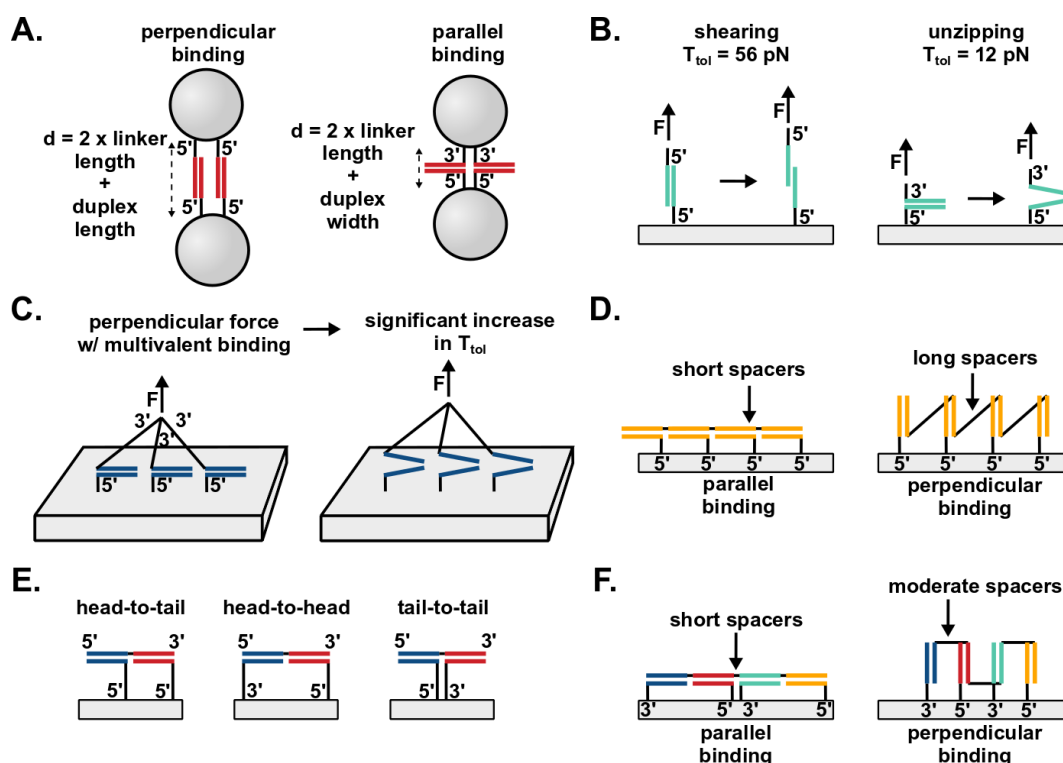


Figure 1.6. Impact of anchor orientation and binding orientation. (a) Anchoring ligands and receptors through the same termini can result in perpendicular binding and an interparticle distance equal to two times the linker length plus the duplex length. Anchoring ligands and receptors through opposite termini can result in parallel binding and an interparticle distance equal to two times the linker length plus the duplex width. (b) Perpendicular binding results in a shearing geometry with a higher tension tolerance (T_{tol}) while parallel binding results in an unzipping geometry with a lower T_{tol} . (c) Multivalent hybridization can significantly increase T_{tol} when a pulling force perpendicular to the surface is applied, adapted from Blanchard *et al.*³⁸ (d) The length of the spacer between binding regions on a homoMV ssDNA target determines if binding is parallel or perpendicular to the probe. Spacers must be able to reach from bottom of one duplex to top of neighbor duplex and vice versa to yield perpendicular binding. (e) For heteroMV binding, anchor orientation impacts geometry of target binding. (f) The length of the spacer between binding regions on a heteroMV ssDNA target determines if binding to a surface with alternating oligo anchoring termini is parallel or perpendicular to the probe. Spacers must be able to reach from top of one duplex to top of neighbor duplex and vice versa to yield perpendicular binding.

duplex ($\sim 2 \text{ nm}$) and the two linker groups. Therefore, even when the duplex length increases, the distance between the particles can remain constant. This is significant in sensing techniques that rely on detecting the distance between a probe and a target, such as gold nanoparticle aggregation assays or potentially FRET based assays.³⁶ Moreover, binding orientation

has significant impacts on the mechanical stability of the DNA duplex. It has been shown that shifting the binding orientation from the parallel geometry, referred to as unzipping mode, to the perpendicular geometry, referred to as shearing mode, can increase the tensile force that a duplex can tolerate (T_{tol}) from 12 pN to 56 pN (**Figure 1.6B**).³⁷ Blanchard *et al.* further showed that T_{tol} can increase ~5-fold through parallel or perpendicular multivalent hybridization when the force is applied perpendicular to the surface (**Figure 1.6C**).³⁸

When binding to ssDNA targets homomultivalently with each ligand anchored through the same terminus, binding orientation is instead controlled by the length of the spacer between each binding region on the target. For example, when the spacer length is short, each binding oligo will be forced to bend and allow parallel binding to occur (**Figure 1.6D**). However, when binding regions are separated by a longer spacer, perpendicular binding becomes possible whenever the spacer is at least as long as the distance between opposite ends of neighboring duplexes. As heteroMV binding allows different oligos to be anchored through opposite termini on the same surface, relative binding orientations can be controlled by each oligo's anchor group. For instance, an $n=2$ heteroMV particle can bind through several different orientations that we refer to as head-to-head, head-to-tail, and tail-to-tail, where head refers to the non-anchored end of the oligo and tail refers to the linker (**Figure 1.6E and Chapter 3**). Schueder *et al.* used the tail-to-tail orientation for binding the ssDNA target in their proximity PAINT method.¹⁷ They found low cooperativity binding even with increased linker length and instead took advantage of the tail-to-tail orientation to form a supporting duplex using the proximal linkers of the oligos. We further demonstrated that the relative binding orientation improves the binding stability and cooperativity by 6-fold for the head-to-head orientation compared to the tail-to-tail when there is no spacer region between binding sites (**Chapter 3**). For a probe with $n > 2$, it is only possible to design

multivalent binding interactions with each ligand anchored through the same terminus,⁸ as described in **Chapter 2**, or with some combination of multiple orientations, such as alternating between the head-to-head and tail-to-tail orientations. This alternating method should potentially allow perpendicular target binding to targets with shorter spacer lengths, as the requirement for spacer length is based on the distance between oligos on the surface instead of the duplex length (**Figure 1.6F**). Therefore, the choice of anchor orientation when designing a multivalent binding interaction to a ssDNA target depends on both the spacing and the value of n .

1.2.8. Quaternary Level and Higher Multivalent DNA Hybridization

The creation of quaternary level multivalent DNA hybridization interactions is also feasible and has been demonstrated in controlled and random binding systems. Herein, we define the quaternary level of multivalent binding as interactions where a probe composed of 2 or more individual multivalent structures linked together binds a target through multiple distinct tertiary level hybridization events (**Figure 1.7A**). One example of quaternary level multivalent hybridization was demonstrated by Bazrafshan *et al.* when two DNA-functionalized gold nanoparticles that were linked together bound to a surface coated with complementary oligos (**Figure 1.7B**). In this example, each particle-surface connection was mediated by tertiary level multivalent hybridization, and thus the collective binding interaction was composed of two tertiary level binding events.³⁹ Physically linking two gold particles to create a dimer enabled more unidirectional rolling motion across the surface when coupled with an RNase cleavage-mediated mechanism of particle displacement.

While less controlled, quaternary level hybridization can also be observed when DNA-functionalized particles aggregate through many target-mediated or non-target-mediated

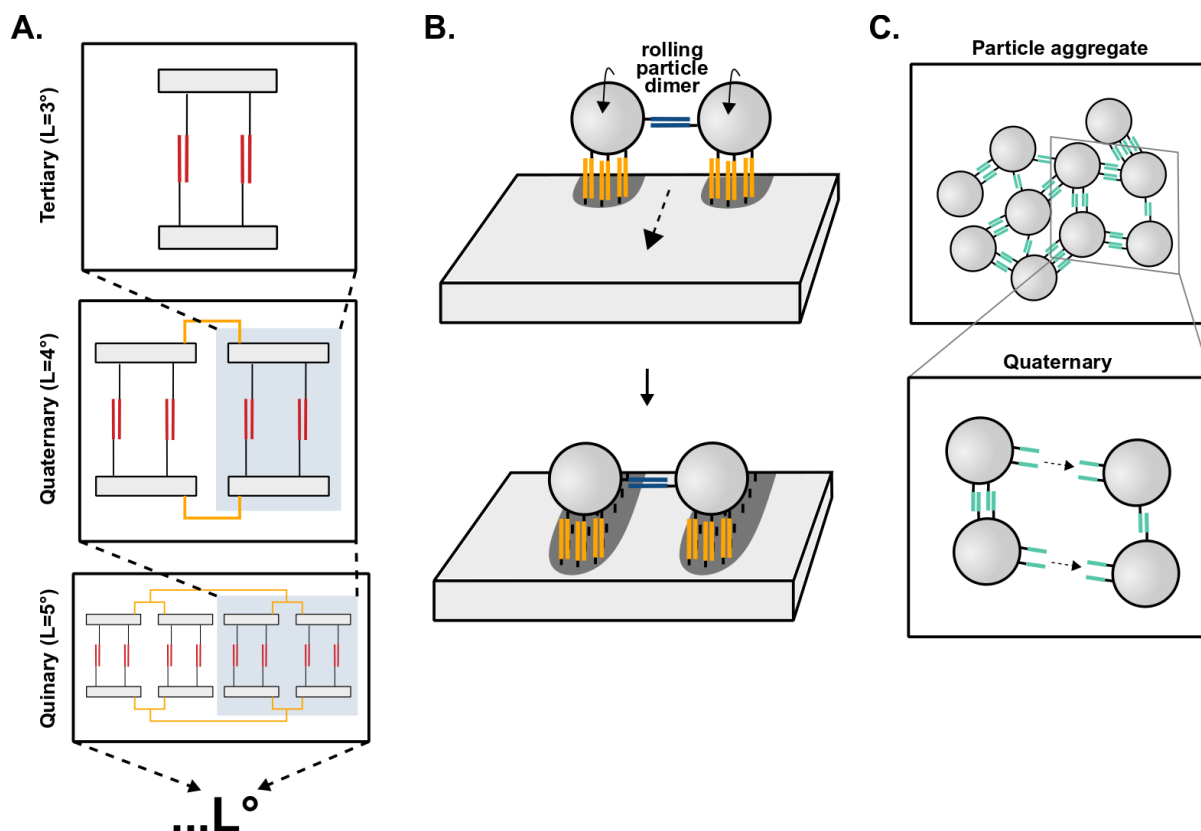


Figure 1.7. Quaternary level and higher multivalent DNA hybridization. (a) Scheme describing theoretical examples of tertiary, quaternary, and quinary level multivalent hybridization. (b) A dimeric DNA-functionalized particle binding to and rolling on a DNA-coated surface exhibits quaternary level multivalent hybridization as demonstrated by Bazrafshan *et al.*³⁹ (c) Quaternary level multivalent hybridization can occur when DNA-functionalized particles aggregate.

dimerization events. Mirkin *et al.* first showed that when two sets of gold nanoparticles functionalized with different oligos are mixed together, the addition of an oligonucleotide that is complementary to the oligos on both particles can lead to large scale aggregation.⁴⁰ This has also been demonstrated in target free systems with particles presenting complementary oligos (**Figure 1.7C**).³⁵ In either case, a single monovalent binding event is able to dimerize two particles, though it is highly probable that a significant number of the dimer linkages are multivalent in nature due to the high density of oligos on the particles. During the process of hybridization-driven random aggregation, 2 or more distinct tertiary level hybridization interactions between two small

aggregates are likely to occur. By extension, continued aggregation also likely results in two sets of quaternary level binding dimers becoming linked and forming multiple quaternary level interactions with another particle aggregate, thus yielding an even higher level of multivalent binding. Each individual multivalent interaction at each level results in additional enhancements to the binding avidity and a rapid, dramatic aggregation results.

1.3. Applications of Multivalent DNA Hybridization

1.3.1. DNA-Based Artificial Motors

One application in the field of nanotechnology that requires the use of multivalent hybridization is DNA-based artificial motors, including DNA walkers and DNA-based rolling motors. Perhaps the simplest of these artificial motors are DNA walkers, which commonly consist of 2-6 DNA legs that can move across a DNA functionalized surface (**Figure 1.8A**). Typically, these motors are deposited onto a surface via multivalent hybridization of their DNA legs, and then powered by dehybridization events for motion. Driven by enzymatic cleavage or external fuel, when one leg dehybridizes from its complement on the surface, it rebinds a new complement on the surface, which powers the motor to take a step. Consequently, the motor relocates to a new position after a series of these events. One key enabling feature of these motors is that through multivalent DNA hybridization, the loss of one leg does not result in the DNA walker detaching from the surface as the remaining hybridized DNA legs are still bound. As a result of the DNA walker remaining attached, the dehybridized DNA is then able to hybridize a new nearby oligo on the surface and pull the DNA walker with it. Many varieties of these artificial motors have been developed that use different techniques to power the dehybridization of each leg. Early examples of dehybridization techniques utilized toehold-mediated strand displacement with an external

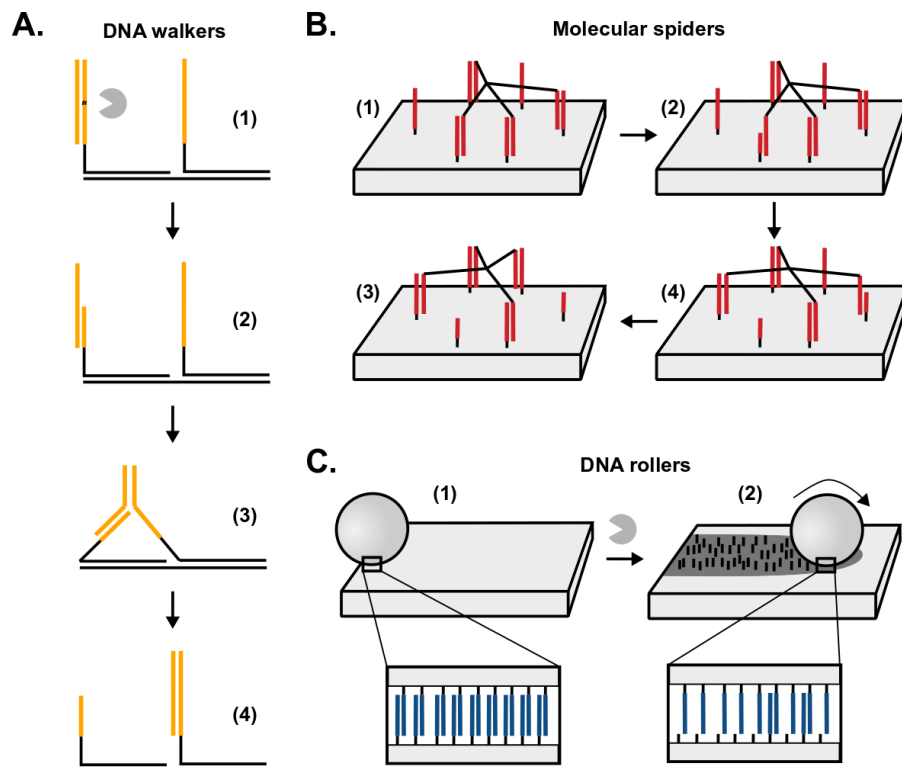


Figure 1.8. Multivalent DNA hybridization enables DNA-based artificial motors (a) A DNA walker taking one step. (1) An enzyme nicks the anchor that the DNA walker is bound too. (2) A toehold is generated as the cleaved anchor dehybridizes. (3) The toehold region on the DNA walker hybridizes to the next anchor position. (4) Toehold-mediated strand displacement occurs and the DNA walker moves to the next anchor, leaving behind a destroyed anchor. (b) A molecular spider moving on a DNA-functionalized surface. (1) Each DNAzyme leg of the spider is hybridized to an anchor. (2) One DNAzyme leg cleaves its anchor. (3) The DNAzyme leg moves to an uncleaved anchor while another leg cleaves its anchor. (4) The DNAzyme leg moves to an uncleaved anchor. (c) A DNA roller moving on an RNA-functionalized surface. (1) Each leg on the DNA roller forms DNA-RNA duplexes with the surface. (2) RNase H enzyme is added to solution to cleave DNA-RNA duplexes and power the rolling of the particle across the surface as each leg continuously hybridizes, dehybridizes following cleavage, and rehybridizes to a new anchor.

DNA fuel, restriction enzymes, nicking enzymes, or DNAzymes.⁴¹⁻⁴⁷ Recently, Li *et al.* designed a ssDNA “acrobat” with two binding regions separated by a linker that cartwheels across a DNA-functionalized surface through a repeating cycle of multivalent hybridization and toehold-mediated strand displacement without external fuel.⁴⁸ To further prevent motor detachment from the surface after the loss of an anchor, Pei *et al.* increased the valency of the DNA walkers by

attaching several of the DNA legs to a streptavidin core, creating “molecular spiders” (**Figure 1.8B**).⁴⁹ Overall, these multivalent artificial DNA walkers are able to yield fast, processive, and controllable motion, that has been used in cargo transport and controlled robot-like motion on a DNA origami surface.^{12, 50}

Another form of DNA-based artificial motors is the rolling motors, which consist of a spherical or rod-like nano-or microparticle that is saturated with DNA legs on all sides (**Figure 1.8C**). These rolling motors undergo a similar mechanism of motion as the walkers, however, since these motors are completely blanketed with DNA legs, they bind with high valency of 100s or more duplexes at a time. As a result of the high degree of multivalency, these motors are capable of highly processive diffusion across the surface. However, as discussed in the section **1.2.4. The Value of n Dictates Binding Valency of Multivalent Hybridization Interactions**, this valency can lead to slower motion as more legs must be cleaved in order for the motor to move. Thus, they rely on rapid RNase-mediated cleavage to overcome the high degree of valency and enable a super diffusive rolling-like mechanism of motion. Different core materials and shapes have been used including silica microparticles, DNA origami rods, and gold nanoparticles.^{13-14, 39} Yehl *et al.* showed that the motors are able to efficiently detect single nucleotide polymorphisms as each additional duplex that binds the particle to the surface increases the total difference in affinity between a surface coated with perfect match complements and mismatched complements.¹³ Piranej *et al.* expanded the power of the DNA-based rolling motors by using them to perform computations involving stalling in the presence of a DNA locking strand or resuming motion with another unlocking strand.⁵¹ Furthermore, Blanchard *et al.* showed that silica microparticle DNA-based rolling motors are able to generate ~100 pN of force as it rolls along the surface, enough to

rupture biotin-streptavidin bonds, which are believed to be the strongest non-covalent bonds in existence.⁵²

1.3.2. Nucleic Acid Sensing

Another notable area that multivalent DNA hybridization has been applied is nucleic acid sensing. One of the first examples of this is using DNA targets to drive the assembly or aggregation of DNA-functionalized gold nanoparticles. Mirkin *et al.* demonstrated this concept by functionalizing 2 solutions of gold nanoparticles with a dense layer of different DNA strands that each were complementary to a part of an oligonucleotide target (**Figure 1.9A**).⁵³ When the target oligonucleotide bound simultaneously to the DNA strands on both particles they became linked together. Importantly, due to the high density of DNA on the particles, multiple targets were able to link two particles at the same time, forming highly cooperative and stable multivalent DNA hybridization interactions. As more and more particles become linked, macroscopic aggregates of a dense web of gold particles can form that are easily visualized by the naked eye (**Figure 1.9A**). Interestingly, this system also exhibits quaternary level multivalent hybridization (see **section 1.2.8. Quaternary Level and Higher Multivalent DNA Hybridization for more information**). As a result of the highly cooperative and multivalent binding, this system displays enhanced binding specificity as each additional duplex formed between two particles or a new linkage to a third particle leads to additional discrimination between a perfect matched or mismatched target.⁵⁴⁻

55

We demonstrate in **Chapter 3** that multivalent DNA hybridization can also be applied towards more effective tuning of the specificity for a ssDNA target with one or multiple SNPs.

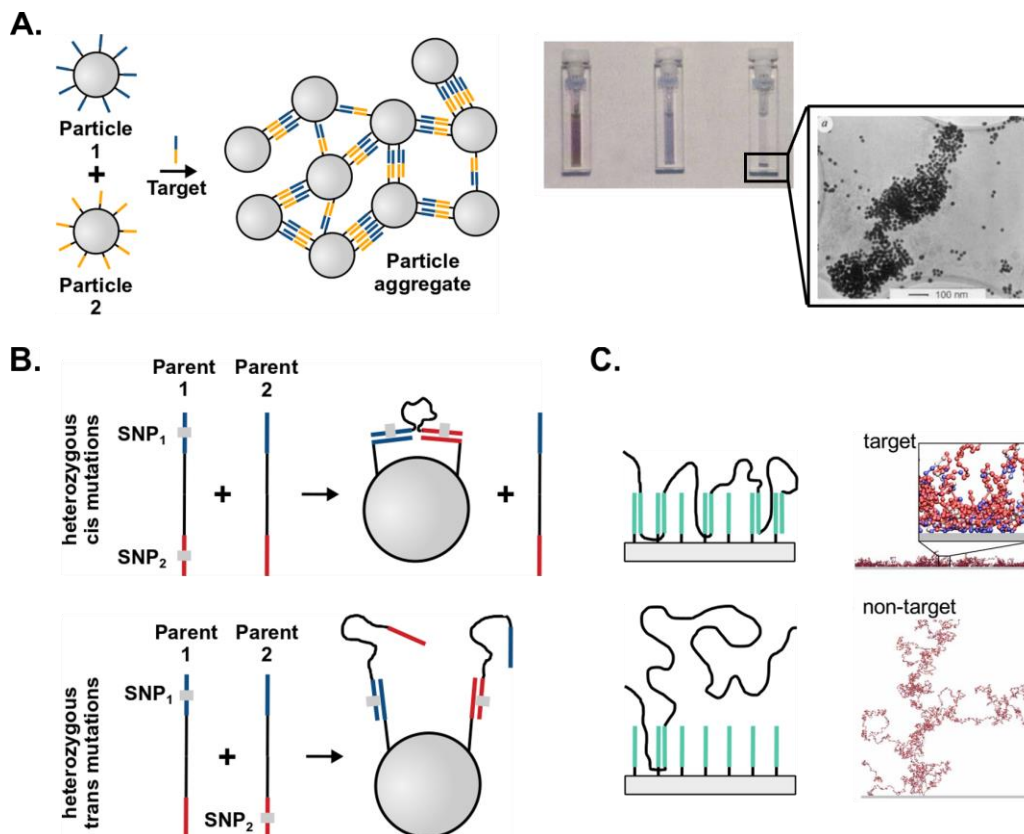


Figure 1.9. Applying multivalent hybridization for nucleic acid sensing. (a) A gold nanoparticle aggregation assay for detection of a nucleic acid target. Particles 1 and 2 are each coated with oligos that are complementary to half of the target to allow the target to bridge two particles together and drive aggregation. The photograph shows the gold nanoparticle solution before target addition (left), after target addition but before sedimentation (middle), and after sedimentation (right). The TEM image shows the aggregated particles after target addition. Adapted from reference 40 by permission from Springer Nature Customer Service Centre GmbH: Springer Nature, Copyright 1996. (b) Scheme showing a method for discriminating between heterozygous cis and trans mutations. When both mutations are on the same target (cis), high affinity multivalent binding to the particle occurs. When only one mutation is present on each target (trans), each target only forms a weak monovalent binding interaction with the bead. (c) Scheme and simulated binding of an *E. coli* genomic target and a non-specific genomic target with a DNA-functionalized surface. The desired target is predicted to form more contacts with the surface as demonstrated by the proximity of each 400 nt target region (sphere) to the surface.⁹

Leveraging the weak binding of a short oligo that is non-complementary to the SNP region, we can fine tune the overall binding affinity by smaller increments compared to adding or subtracting a base pair from a standard duplex. Through this precise tuning of affinity, we show that more

optimal specificity can be achieved than often possible with monovalent binding probes and without altering buffer conditions. Moreover, we demonstrate a >100-fold difference in binding between the double-mutant and non-mutant targets when detecting two SNPs heteromultivalently, even when these SNP sites are separated by >20 nt. This enhanced specificity for multiple mutation targets is useful for determining if multiple mutations are located on the same gene copy (heterozygous cis) or different gene copies (heterozygous trans) (**Figure 1.9B**).

Multivalent DNA hybridization has also been demonstrated as an effective approach to achieve “super-selective” sensing. As discussed previously, multivalent binding can lead to enhanced sensitivity where binding requires a high receptor density as a result of the dramatic enhancements in binding avidity as the binding valency increases. To demonstrate this concept of improved selectivity through multivalent hybridization, Curk *et al.* modeled the multivalent binding of a DNA-functionalized surface to the full-length genome of a specific strain of *E. coli* (**Figure 1.9C**).⁹ They found that a surface presenting 20 nt DNA probes at low density was able to form significantly more binding interactions with the *E. coli* genomic sequence of interest when compared to unrelated bacterial, viral, and mitochondrial genomes. Significantly, selectivity was maintained even when discriminating the desired *E. coli* genome from a food-poisoning inducing strain of *E. coli* that only differs in a few regions of the genome.

1.3.3. Tools to Study Biology

The utility of multivalent DNA hybridization has also been explored in techniques to study biological processes, including investigations into protein-protein interactions, cell mechanobiology, phagocytosis, and immunology. Schueder *et al.* applied bivalent DNA hybridization to measure the spatial proximity of alpha- and beta-tubulin in microtubules with

super-resolution fluorescence microscopy.¹⁷ By binding a primary antibody to each protein on the surface of U2OS cells and then using oligonucleotide-linked secondary antibodies, both proteins of interest were specifically labeled with a unique oligonucleotide docking strand (**Figure 1.10A, left**). Next, a fluorescent imager strand complementary to both docking sites was added that was engineered to only bind when both docking sites were in close proximity and able to bind cooperatively. The fluorescent imager strand binds the pair of docking sites transiently to allow for many binding-unbinding-rebinding events to be imaged over time using fluorescent microscopy. As a result of the cooperative nature of the bivalent DNA hybridization interaction, this approach yielded a super-resolution map of where the alpha- and beta-tubulin proteins contact each other (**Figure 1.10A, right**).

To investigate the molecular level ligand-receptor forces present at a cell-surface interface, Dutta *et al.* used DNA origami tension probes to bridge a cell and a surface through multivalent DNA hybridization at both interfaces (**Figure 1.10B, left**).¹⁵ Specifically, a DNA origami six-helix bundle was interfaced with a cell membrane through presenting two DNA duplexes, each with a receptor-specific peptide at the top. Meanwhile, the DNA origami probe attached to the surface through up to three hybridization interactions between a DNA hairpin and an oligo containing a modification allowing surface attachment. Using this probe, a map of the mechanical events occurring during platelet adhesion and activation was obtained (**Figure 1.10B, right**). Enabled by the precise control over ligand density offered by DNA origami and the ~2-fold higher force threshold due to multivalent DNA hybridization, the impact of ligand density and force-response threshold on platelet function was investigated.

Multivalent DNA hybridization has also enabled precise control over biological processes that are mediated through extracellular binding events. For example, Kern *et al.* engineered

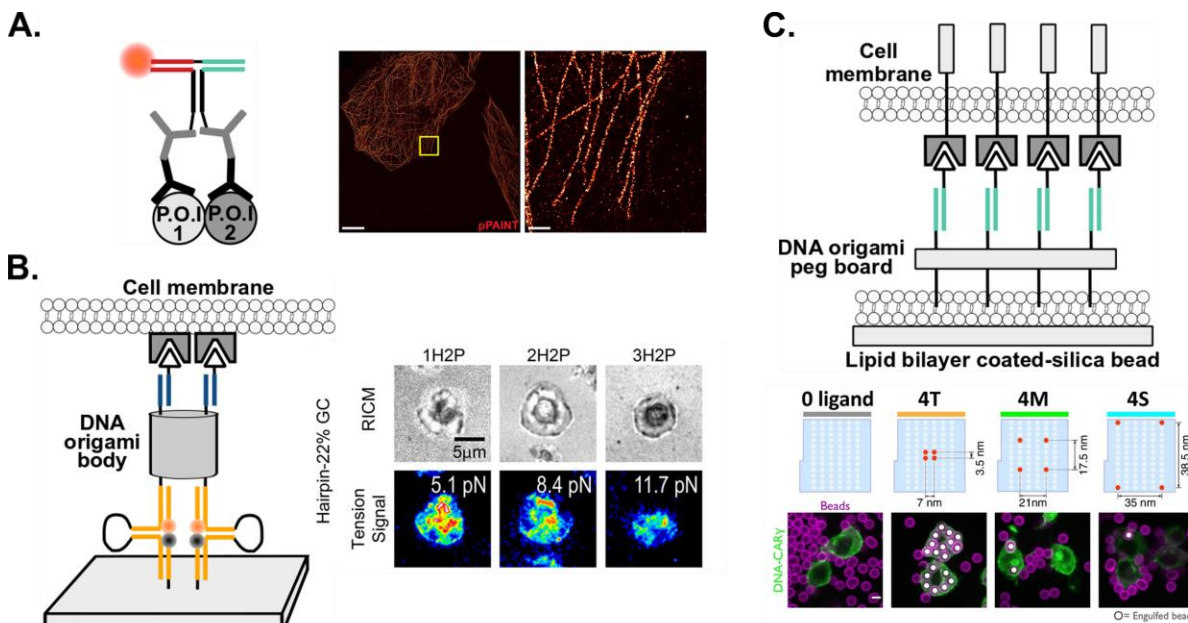


Figure 1.10. Using multivalent hybridization as a tool to study biology. (a) The proximity-PAINT method to detect the proximity of two proteins. Each protein is tagged with a primary antibody and an oligo-labeled secondary antibody. The fluorescent imager strand then binds only when both oligos are close enough to hybridize multivalently. A super resolution fluorescence microscopy map showing the proximity of alpha and beta-tubulin.¹⁷ Zoom-out scale bar is 5 μm and zoom-in scale bar is 500 nm. (b) Scheme showing the use of multivalent DNA origami hairpin tension probes. A DNA origami 6 helix bundle that presents two duplexes with cell-specific ligands on top and one, two, or three DNA hairpins on bottom that bind a surface. When receptors on the cell pull on the ligands, the hairpin probes open and the fluorophore is unquenched. Each additional hairpin that is added increases the pulling force needed to generate fluorescence signal, resulting in less signal when the cell interacts with the surface. Reprinted from reference 15 with permission, Copyright 2018 American Chemical Society. (c) Scheme showing the use of DNA origami-mediated multivalent hybridization to control phagocytosis of lipid bilayer-coated silica beads by cells. When 4 duplexes are close together on the DNA origami peg board, particle uptake is high and when the spacing between the duplexes increases, uptake is reduced.¹⁶ Scale bar is 5 μm .

macrophage cells to present DNA receptors on their surface that were able to bind to DNA origami peg board-functionalized silica microparticles that contained the complementary ligand oligo (Figure 1.10C, top).¹⁶ As a result of the high control over ligand density and spacing afforded by the DNA origami peg board, the impact of ligand density and spacing on engulfment of the silica beads and downstream signaling processes in the macrophages were studied. They found that

increasing the valency of the binding interaction between the cell and the bead by adding more ligands led to increasing bead engulfment that saturated after the max binding valency reached 8. Moreover, by controlling the spacing between each duplex at the cell-bead interface, it was revealed that tighter spacing of 4 ligand-peg boards led to more successful bead engulfment due to enhanced bead-cell binding (**Figure 1.10C, bottom**), as well as enhanced levels of downstream receptor phosphorylation. Using a similar method with DNA origami-cell binding, Dong *et al.* explored the impact of precisely controlled T cell receptor-antigen binding, mediated by multivalent hybridization, on the sensitivity and kinetics of T cell activation.⁵⁶ Interestingly, this work determined that ligand spacing impacts how quickly T cell signaling initiates while binding valency controls the length of the signaling event. Moreover, they found that arranging weak affinity duplexes around a small cluster of high affinity duplexes led to enhanced sensitivity for T cell triggering.

1.4. Aims and Scope of the Dissertation

With careful design and optimization of each binding component, multivalent DNA hybridization has proven its potential to be a powerful technique in artificial motors, sensitive and specific nucleic acid detection, as well as biological investigations. Despite the progress in characterizing and developing this specific variety of multivalent binding, there are many unanswered questions regarding the use of multivalent DNA hybridization to target biologically relevant ssDNA with high avidity and specificity. This dissertation aims to fill these gaps in knowledge by (1) engineering heteroMV structures that are able to bind multivalently to ssDNA targets and characterize the enhancements in avidity offered by ligand spatial patterning; (2) investigate the specificity and cooperativity provided by heteroMV hybridization and the resulting

ability to improve detection of mutant DNA targets; and (3) discuss the future outlook for multivalent hybridization in nanotechnology, diagnostics, and therapeutics.

My exploration into multivalent DNA hybridization began with a simple question: Would a particle that is functionalized with several different oligonucleotide sequences offer improved binding properties when targeting nucleic acids? To fully explore this question and address the stated aims, I devoted my Ph.D. studies into designing heteroMV DNA-functionalized nano- and microparticles, developing new methods to assess their binding properties, and uncovering the potential utilities of heteroMV hybridization in sensing and diagnostics.

In **Chapter 2**, I will describe findings regarding the impact of heteromultivalency and ligand spatial patterning on the binding avidity of DNA-functionalized gold nanoparticles for a long ssDNA target. To fully probe the importance of ligand positioning and spacing, this chapter also presents a new technique that enables control over the spatial arrangement of oligos on a densely functionalized particle. Building on these investigations, **Chapter 3** shows the impact of oligonucleotide length on specific and cooperative heteroMV DNA hybridization. Fundamental examinations of the influence of the distance between two target binding regions as well as the oligonucleotide anchoring orientation revealed the ability for heteroMV particles to bind with high cooperativity to two sites of a target that are separated by up to 15 nucleotides. Through these explorations, it was ultimately demonstrated that precisely tuned heteroMV hybridization allows specific detection of targets with one or two mutations and classification of the genetic inheritance of such mutations. Following the description of these findings, **Chapter 4** provides an overview of remaining questions and expected challenges for the field, and ultimately proposes several next steps for the effective application of multivalent hybridization. Overall, I hope this dissertation can

serve as a handbook to provide insight and guidance for future designs of crucial techniques that aim to apply multivalent DNA hybridization.

1.5. References

1. Yakovchuk, P.; Protozanova, E.; Frank-Kamenetskii, M. D., Base-stacking and base-pairing contributions into thermal stability of the DNA double helix. *Nucleic Acids Res* **2006**, *34* (2), 564-74.
2. Zhang, D. Y.; Chen, S. X.; Yin, P., Optimizing the specificity of nucleic acid hybridization. *Nat Chem* **2012**, *4* (3), 208-14.
3. Gao, Y.; Wolf, L. K.; Georgiadis, R. M., Secondary structure effects on DNA hybridization kinetics: a solution versus surface comparison. *Nucleic Acids Res* **2006**, *34* (11), 3370-7.
4. Bhatia, S.; Dimde, M.; Haag, R., Multivalent glycoconjugates as vaccines and potential drug candidates. *Med. Chem. Commun.* **2014**, *5* (7), 862-878.
5. Tsouka, A.; Hoetzel, K.; Mende, M.; Heidepriem, J.; Paris, G.; Eickelmann, S.; Seeberger, P. H.; Lepenies, B.; Loeffler, F. F., Probing Multivalent Carbohydrate-Protein Interactions With On-Chip Synthesized Glycopeptides Using Different Functionalized Surfaces. *Front Chem* **2021**, *9*, 766932.
6. Xu, Z.; Jia, S.; Wang, W.; Yuan, Z.; Jan Ravoo, B.; Guo, D. S., Heteromultivalent peptide recognition by co-assembly of cyclodextrin and calixarene amphiphiles enables inhibition of amyloid fibrillation. *Nat Chem* **2019**, *11* (1), 86-93.
7. Kwon, P. S.; Ren, S.; Kwon, S. J.; Kizer, M. E.; Kuo, L.; Xie, M.; Zhu, D.; Zhou, F.; Zhang, F.; Kim, D.; Fraser, K.; Kramer, L. D.; Seeman, N. C.; Dordick, J. S.; Linhardt, R. J.; Chao, J.; Wang, X., Designer DNA architecture offers precise and multivalent spatial pattern-recognition for viral sensing and inhibition. *Nat Chem* **2020**, *12* (1), 26-35.
8. Deal, B. R.; Ma, R.; Ma, V. P.; Su, H.; Kindt, J. T.; Salaita, K., Engineering DNA-Functionalized Nanostructures to Bind Nucleic Acid Targets Heteromultivalently with Enhanced Avidity. *J Am Chem Soc* **2020**, *142* (21), 9653-9660.
9. Curk, T.; Brackley, C. A.; Farrell, J. D.; Xing, Z.; Joshi, D.; Direito, S.; Bren, U.; Angioletti-Uberti, S.; Dobnikar, J.; Eiser, E.; Frenkel, D.; Allen, R. J., Computational design of probes to detect bacterial genomes by multivalent binding. *Proc Natl Acad Sci U S A* **2020**, *117* (16), 8719-8726.
10. Magdalena Estirado, E.; Aleman Garcia, M. A.; Schill, J.; Brunsveld, L., Multivalent Ultrasensitive Interfacing of Supramolecular 1D Nanoplatfoms. *J Am Chem Soc* **2019**, *141* (45), 18030-18037.
11. Nangreave, J.; Yan, H.; Liu, Y., Studies of thermal stability of multivalent DNA hybridization in a nanostructured system. *Biophys J* **2009**, *97* (2), 563-71.
12. Lund, K.; Manzo, A. J.; Dabby, N.; Michelotti, N.; Johnson-Buck, A.; Nangreave, J.; Taylor, S.; Pei, R.; Stojanovic, M. N.; Walter, N. G.; Winfree, E.; Yan, H., Molecular robots guided by prescriptive landscapes. *Nature* **2010**, *465* (7295), 206-10.
13. Yehl, K.; Mugler, A.; Vivek, S.; Liu, Y.; Zhang, Y.; Fan, M.; Weeks, E. R.; Salaita, K., High-speed DNA-based rolling motors powered by RNase H. *Nat Nanotechnol* **2016**, *11* (2), 184-90.

14. Bazrafshan, A.; Meyer, T. A.; Su, H.; Brockman, J. M.; Blanchard, A. T.; Piranej, S.; Duan, Y.; Ke, Y.; Salaita, K., Tunable DNA Origami Motors Translocate Ballistically Over μm Distances at nm/s Speeds. *Angew Chem Int Ed Engl* **2020**.
15. Dutta, P. K.; Zhang, Y.; Blanchard, A. T.; Ge, C.; Rushdi, M.; Weiss, K.; Zhu, C.; Ke, Y.; Salaita, K., Programmable Multivalent DNA-Origami Tension Probes for Reporting Cellular Traction Forces. *Nano Lett* **2018**, *18* (8), 4803-4811.
16. Kern, N.; Dong, R.; Douglas, S. M.; Vale, R. D.; Morrissey, M. A., Tight nanoscale clustering of Fc γ receptors using DNA origami promotes phagocytosis. *Elife* **2021**, *10*.
17. Schueder, F.; Lara-Gutierrez, J.; Haas, D.; Beckwith, K. S.; Yin, P.; Ellenberg, J.; Jungmann, R., Super-Resolution Spatial Proximity Detection with Proximity-PAINT. *Angew Chem Int Ed Engl* **2021**, *60* (2), 716-720.
18. Scheepers, M. R. W.; van, I. L. J.; Prins, M. W. J., Multivalent weak interactions enhance selectivity of interparticle binding. *Proc Natl Acad Sci U S A* **2020**, *117* (37), 22690-22697.
19. Pinheiro, A. V.; Nangreave, J.; Jiang, S.; Yan, H.; Liu, Y., Steric crowding and the kinetics of DNA hybridization within a DNA nanostructure system. *ACS Nano* **2012**, *6* (6), 5521-30.
20. Randeria, P. S.; Jones, M. R.; Kohlstedt, K. L.; Banga, R. J.; Olvera de la Cruz, M.; Schatz, G. C.; Mirkin, C. A., What controls the hybridization thermodynamics of spherical nucleic acids? *J Am Chem Soc* **2015**, *137* (10), 3486-9.
21. Suzuki, K.; Hosokawa, K.; Maeda, M., Controlling the number and positions of oligonucleotides on gold nanoparticle surfaces. *J Am Chem Soc* **2009**, *131* (22), 7518-9.
22. Edwardson, T. G.; Lau, K. L.; Bousmail, D.; Serpell, C. J.; Sleiman, H. F., Transfer of molecular recognition information from DNA nanostructures to gold nanoparticles. *Nat Chem* **2016**, *8* (2), 162-70.
23. Xie, N.; Liu, S.; Fang, H.; Yang, Y.; Quan, K.; Li, J.; Yang, X.; Wang, K.; Huang, J., Three-Dimensional Molecular Transfer from DNA Nanocages to Inner Gold Nanoparticle Surfaces. *ACS Nano* **2019**, *13* (4), 4174-4182.
24. Dubacheva, G. V.; Curk, T.; Frenkel, D.; Richter, R. P., Multivalent Recognition at Fluid Surfaces: The Interplay of Receptor Clustering and Superselectivity. *J Am Chem Soc* **2019**, *141* (6), 2577-2588.
25. Kowalewski, A.; Forde, N. R.; Korosec, C. S., Multivalent Diffusive Transport. *J Phys Chem B* **2021**, *125* (25), 6857-6863.
26. Jakubek, Y. A.; Cutler, D. J., A model of binding on DNA microarrays: understanding the combined effect of probe synthesis failure, cross-hybridization, DNA fragmentation and other experimental details of affymetrix arrays. *BMC Genomics* **2012**, *13*, 737.
27. Chen, N.; Schrijver, I., Allelic discrimination of cis-trans relationships by digital polymerase chain reaction: GJB2 (p.V27I/p.E114G) and CFTR (p.R117H/5T). *Genet Med* **2011**, *13* (12), 1025-31.
28. Zhuang, X.; Lee Yu, H. L.; Hsing, I. M., Toehold probe-based interrogation for haplotype phasing of long nucleic acid strands. *Anal Methods* **2020**, *12* (34), 4185-4190.
29. Lee Yu, H. L.; Fan, T. W.; Hsing, I. M., Oligonucleotide hybridization with magnetic separation assay for multiple SNP phasing. *Anal Chim Acta X* **2020**, *5*, 100050.
30. Mammen, M.; Choi, S. K.; Whitesides, G. M., Polyvalent Interactions in Biological Systems: Implications for Design and Use of Multivalent Ligands and Inhibitors. *Angew Chem Int Ed Engl* **1998**, *37* (20), 2754-2794.
31. Kane, R. S., Thermodynamics of multivalent interactions: influence of the linker. *Langmuir* **2010**, *26* (11), 8636-40.

32. Krishnamurthy, V. M.; Semetey, V.; Bracher, P. J.; Shen, N.; Whitesides, G. M., Dependence of effective molarity on linker length for an intramolecular protein-ligand system. *J Am Chem Soc* **2007**, *129* (5), 1312-20.
33. Huskens, J.; Mulder, A.; Auletta, T.; Nijhuis, C. A.; Ludden, M. J.; Reinhoudt, D. N., A model for describing the thermodynamics of multivalent host-guest interactions at interfaces. *J Am Chem Soc* **2004**, *126* (21), 6784-97.
34. Sorensen, C. S.; Kjaergaard, M., Effective concentrations enforced by intrinsically disordered linkers are governed by polymer physics. *Proc Natl Acad Sci U S A* **2019**, *116* (46), 23124-23131.
35. Lee, J. S.; Seferos, D. S.; Giljohann, D. A.; Mirkin, C. A., Thermodynamically controlled separation of polyvalent 2-nm gold nanoparticle-oligonucleotide conjugates. *J Am Chem Soc* **2008**, *130* (16), 5430-1.
36. Guo, L.; Xu, Y.; Ferhan, A. R.; Chen, G.; Kim, D. H., Oriented gold nanoparticle aggregation for colorimetric sensors with surprisingly high analytical figures of merit. *J Am Chem Soc* **2013**, *135* (33), 12338-45.
37. Wang, X.; Ha, T., Defining single molecular forces required to activate integrin and notch signaling. *Science* **2013**, *340* (6135), 991-4.
38. Blanchard, A. T.; Salaita, K., Multivalent molecular tension probes as anisotropic mechanosensors: concept and simulation. *Phys Biol* **2021**, *18* (3), 034001.
39. Bazrafshan, A.; Kyriazi, M. E.; Holt, B. A.; Deng, W.; Piranej, S.; Su, H.; Hu, Y.; El-Sagheer, A. H.; Brown, T.; Kwong, G. A.; Kanaras, A. G.; Salaita, K., DNA Gold Nanoparticle Motors Demonstrate Processive Motion with Bursts of Speed Up to 50 nm Per Second. *ACS Nano* **2021**, *15* (5), 8427-8438.
40. Mirkin, C. A.; Letsinger, R. L.; Mucic, R. C.; Storhoff, J. J., A DNA-based method for rationally assembling nanoparticles into macroscopic materials. *Nature* **1996**, *382* (6592), 607-9.
41. Shin, J. S.; Pierce, N. A., A synthetic DNA walker for molecular transport. *J Am Chem Soc* **2004**, *126* (35), 10834-5.
42. Omabegho, T.; Sha, R.; Seeman, N. C., A bipedal DNA Brownian motor with coordinated legs. *Science* **2009**, *324* (5923), 67-71.
43. Yin, P.; Yan, H.; Daniell, X. G.; Turberfield, A. J.; Reif, J. H., A unidirectional DNA walker that moves autonomously along a track. *Angew Chem Int Ed Engl* **2004**, *43* (37), 4906-11.
44. Bath, J.; Green, S. J.; Turberfield, A. J., A free-running DNA motor powered by a nicking enzyme. *Angew Chem Int Ed Engl* **2005**, *44* (28), 4358-61.
45. Tian, Y.; He, Y.; Chen, Y.; Yin, P.; Mao, C., A DNzyme that walks processively and autonomously along a one-dimensional track. *Angew Chem Int Ed Engl* **2005**, *44* (28), 4355-8.
46. Sherman, W. B.; Seeman, N. C., A Precisely Controlled DNA Biped Walking Device. *Nano Lett* **2004**, *4* (7), 1203-1207.
47. Tomov, T. E.; Tsukanov, R.; Glick, Y.; Berger, Y.; Liber, M.; Avrahami, D.; Gerber, D.; Nir, E., DNA Bipedal Motor Achieves a Large Number of Steps Due to Operation Using Microfluidics-Based Interface. *ACS Nano* **2017**, *11* (4), 4002-4008.
48. Li, J.; Johnson-Buck, A.; Yang, Y. R.; Shih, W. M.; Yan, H.; Walter, N. G., Exploring the speed limit of toehold exchange with a cartwheeling DNA acrobat. *Nat Nanotechnol* **2018**, *13* (8), 723-729.
49. Pei, R.; Taylor, S. K.; Stefanovic, D.; Rudchenko, S.; Mitchell, T. E.; Stojanovic, M. N., Behavior of polycatalytic assemblies in a substrate-displaying matrix. *J Am Chem Soc* **2006**, *128* (39), 12693-9.

50. Thubagere, A. J.; Li, W.; Johnson, R. F.; Chen, Z.; Doroudi, S.; Lee, Y. L.; Izatt, G.; Wittman, S.; Srinivas, N.; Woods, D.; Winfree, E.; Qian, L., A cargo-sorting DNA robot. *Science* **2017**, *357* (6356).
51. Piranej, S. B., A; Salaita, K, Chemical-to-mechanical molecular computation using DNA-based motors with onboard logic. *Nat Nanotechnol* **2022**.
52. Blanchard, A. T.; Bazrafshan, A. S.; Yi, J.; Eisman, J. T.; Yehl, K. M.; Bian, T.; Mugler, A.; Salaita, K., Highly Polyvalent DNA Motors Generate 100+ pN of Force via Autochemophoresis. *Nano Lett* **2019**, *19* (10), 6977-6986.
53. Mirkin, C. A.; Letsinger, R. L.; Mucic, R. C.; Storhoff, J. J., A DNA-based method for rationally assembling nanoparticles into macroscopic materials. *Nature* **1996**, *382*, 607-609.
54. Taton, T. A.; Mirkin, C. A.; Letsinger, R. L., Scanometric DNA array detection with nanoparticle probes. *Science* **2000**, *289* (5485), 1757-60.
55. Park, S. J.; Taton, T. A.; Mirkin, C. A., Array-based electrical detection of DNA with nanoparticle probes. *Science* **2002**, *295* (5559), 1503-6.
56. Dong, R.; Aksel, T.; Chan, W.; Germain, R. N.; Vale, R. D.; Douglas, S. M., DNA origami patterning of synthetic T cell receptors reveals spatial control of the sensitivity and kinetics of signal activation. *Proc Natl Acad Sci U S A* **2021**, *118* (40).

Chapter 2

Engineering DNA-Functionalized Nanostructures to Bind Nucleic Acid Targets Heteromultivalently with Enhanced Avidity

Adapted with permission from Brendan R. Deal, Rong Ma, Victor Pui-Yan Ma, Hanquan Su, James T. Kindt, and Khalid Salaita. Engineering DNA-functionalized nanostructures to bind nucleic acid targets heteromultivalently with enhanced avidity. *J. Am. Chem. Soc.* April 27, 2020, 142 (21), 9653–9660. Copyright 2020 American Chemical Society

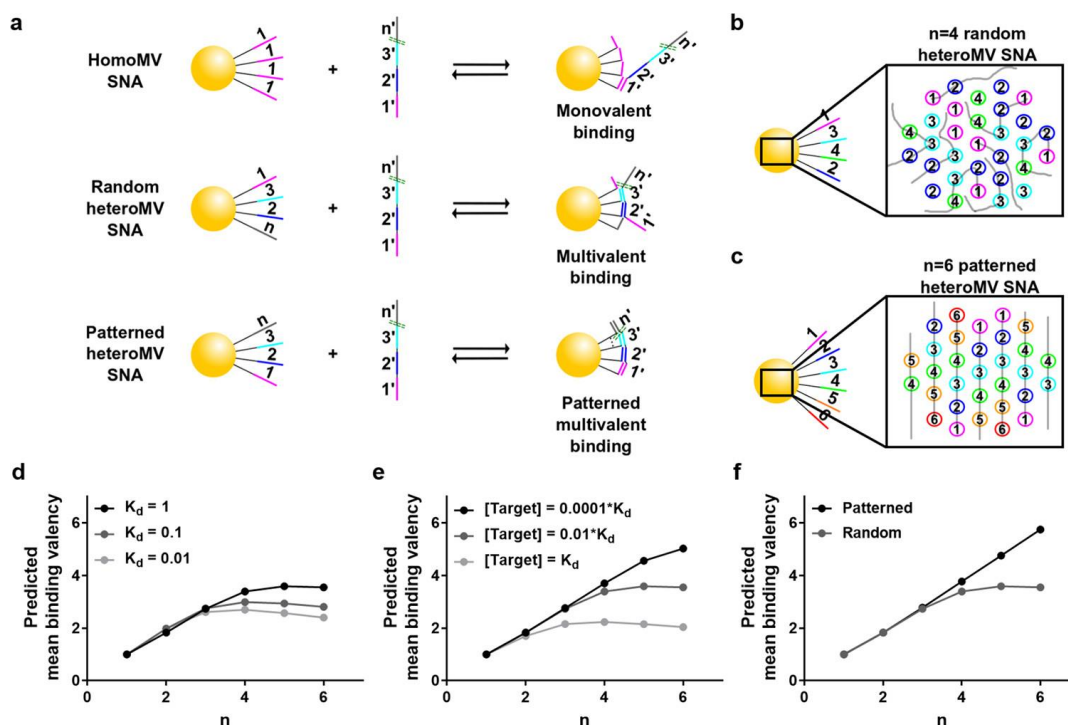
2.1. Introduction

A multivalent interaction occurs when a multivalent ligand binds a multivalent receptor through several individual ligand–receptor pairs.¹ Such interactions commonly offer an enhanced collective affinity, or avidity, and thus, Nature has evolved to utilize multivalent interactions to aid in many biological and chemical processes. For example, uptake of influenza viral particles into cells is aided by the avid multivalent interaction between a trivalent hemagglutinin molecule and multiple sialic acid molecules on the cell membrane.² Inspired by such natural multivalent interactions, many synthetic multivalent interactions have been engineered to tightly bind a receptor, such as a peptide or a viral particle, for improved sensing and therapeutics.³⁻⁴ An especially noteworthy example of a multivalent binding interaction utilized both naturally and synthetically is nucleic acid hybridization. Polynucleotide hybridization occurs through two distinct levels of multivalent binding. The primary level of multivalent binding is the 2–3 hydrogen bonds formed between each nucleobase pair, whereas the secondary level is the concurrent base stacking and binding of a series of nucleobases to their complementary bases on another polynucleotide. These multivalent interactions result in high specificity and affinity binding that is fundamental in genetics and gene expression across all organisms, as well as antisense oligonucleotide therapeutics and DNA nanotechnology.

Interestingly, within the field of DNA nanotechnology, a tertiary level of multivalency in DNA hybridization has emerged with the ability to further strengthen and tune binding affinity. This tertiary level of multivalency in DNA hybridization occurs when multiple oligonucleotides that are anchored on a scaffold bind a target simultaneously. Tertiary multivalent nucleic acid interactions have been explored between two one-dimensional scaffolds bound together by identical pairs of oligonucleotides.⁵ The affinity of this homomultivalent (homoMV) interaction

was found to increase linearly with the number of oligonucleotides displayed. Moreover, many copies of an oligonucleotide have been arranged on a particle or nanomaterial surface to multivalently bind an oligocoated surface or another oligocoated particle.⁶⁻¹⁰ These homoMV tertiary multivalent interactions, as well as those found in some DNA origami structures, display a heightened affinity, allowing for useful applications in sensing, DNA motors, and supramolecular assembly.¹¹ However, many desirable applications, including gene regulation and mRNA sensing, require binding with high affinity to single-stranded polynucleotides hundreds of bases long and with a nonrepeating sequence, which homoMV structures are unable to bind multivalently. To multivalently bind such targets, it is necessary to engineer heteromultivalent (heteroMV) structures that present a series of unique oligonucleotide sequences, each able to bind a distinct stretch of the target. Currently, little is known about the multivalent interaction between nanostructures presenting heteroMV DNA and a nucleic acid target. Therefore, the goal of this work is to investigate and quantify heteroMV nucleic acid binding to provide insight into designing nanostructures that bind single-stranded polynucleotides with improved affinity.

One prominent DNA-functionalized nanostructure that can be used as a model system to explore multivalent binding interactions is the spherical nucleic acid (SNA).¹²⁻¹³ SNAs are typically comprised of many copies of an oligonucleotide arranged around a spherical core, such as a gold nanoparticle. SNAs presenting a highly dense layer of oligonucleotides are able to bind monovalently to their target sequence with enhanced affinity that can be more than 2 orders of magnitude greater than that of linear sequences (**Figure 2.1A**).¹⁴⁻¹⁶ This high-affinity interaction has allowed SNAs' utility in many applications, most notably RNA sensing-based diagnostics and gene regulation.¹⁷⁻²⁰ Herein, we adapt the SNA platform to display a heteroMV layer of short



oligos attached to a gold nanoparticle (AuNP). We hypothesize that heteroMV SNAs can form tertiary multivalent interactions with a single-stranded nucleic acid target (**Figure 2.1A**). Recognizing the importance of ligand positioning in multivalency,^{1, 21} we tested a second hypothesis that spatial patterning of the DNA oligos on the particle surface can lead to further enhancement in target affinity. This prediction was studied by developing a new facile strategy to create spatially positioned oligonucleotides, where the target nucleic acid templates the molecular deposition of oligos on the nanoparticle surface (**Figure 2.1A**).

Specifically, we investigate heteroMV SNAs comprised of up to six unique oligo sequences designed to bind a ~ 90 nucleotide (nt) DNA target. Through modeling and experiments, we reveal that the binding valency of heteroMV SNAs with randomly anchored oligos increases with the inclusion of each additional unique oligosequence (n) but eventually decreases due to the random arrangement. Moreover, we determined the thermodynamic parameters governing multivalent binding and found that random heteromultivalency leads to an increase in affinity of up to ~ 50 orders of magnitude compared to the corresponding homoMV SNA as a result of increasing the enthalpic benefits from binding. Next, we show that spatial patterning of the oligos on heteroMV SNAs results in a further ~ 15 order-of-magnitude enhancement in the affinity of binding relative to heteroMV SNAs with random oligo positioning. Overall, the incorporation of heteromultivalency and spatial patterning into the SNA platform offers a general and simple approach for exploring and fine-tuning the multivalent binding affinity of DNA-functionalized nanostructures, thus improving their diagnostic and therapeutic potential and utility in DNA nanotechnology.

2.2. Results

2.2.1. Modeling Binding of Random and Patterned HeteroMV SNAs

A mathematical model was first developed in order to predict the effective strength of an interaction between a target and a heteroMV SNA that is randomly arranged (**Figure 2.1B**) or spatially patterned (**Figure 2.1C**). Briefly, assuming a random arrangement of oligos with n unique sequences (sequence $x, x + 1, \dots, n - 1, n$) on the AuNP surface, the probability of sequence x being located next to sequence $x + 1$, which is next to $x + 2$, etc., was calculated mathematically (**Figure 2.1B**). Then using Langmuir adsorption-type kinetics, the predicted mean binding valency, or

average number of segments bound to a single target, was used as a proxy to estimate the strength of binding (see **methods for a detailed description**). This was obtained after varying n and the K_d of the interaction between a single segment and its complementary region on the target. Significantly, the results of the model predict that as n increases, the mean binding valency will increase, plateau around $n = 4$, and then decrease as the probability of sequence x being neighbored by $x - 1$ or $x + 1$ decreases with increasing n (**Figure 2.1D**). Therefore, the model suggests that the probability of a random heteroMV SNA forming a maximum binding valency interaction drops as n increases. However, the model also predicts that the binding valency, as well as the value of n that leads to maximum binding valency, can be enhanced by decreasing the affinity of each segment (**Figure 2.1D**). This is because weak or labile segments allow for extensive sampling of conformational space to avoid trapping at kinetic intermediates that do not maximize binding. Alternatively, the model further reveals that decreasing the concentration of the target sequence in solution will yield higher valency binding as the probability of a target binding to a sequential series of segments ($x, x + 1$, etc.) increases (**Figure 2.1E, Figure A2.1**). The impact of spatial patterning on heteroMV SNA multivalent binding was also predicted by assuming each sequence x is located next to $x - 1$ and $x + 1$ (**Figure 2.1C**). The modeling results show that spatial patterning offers minimal advantage over random SNAs when n is low. However, as n increases, spatial patterning leads to higher mean binding valency compared to random heteroMV SNAs (**Figure 2.1F**). Overall, the results of the mathematical model show that a random orientation of segments will form the most efficient multivalent interaction with shorter, less stable segments or when hybridization is performed in stringent conditions (low salt, low target concentration, presence of surfactant), whereas the effects of spatial patterning will be most impactful when there are more unique segments (higher values of n).

2.2.2. Design and Melting Curve Analysis for Random HeteroMV SNAs

To test the predictions of the modeling, six oligonucleotides (segments 1–6) between 12 and 15 nucleotides (nt) in length with similar melting temperatures were designed to bind sequentially along a 91 nt DNA target based on a region of an mRNA transcript (**Figure A2.2**). To offer additional flexibility, a 2 nt spacer region was included between each segment's binding location on the target sequence, resulting in the formation of single-stranded gaps in the binding complex (see **Figure A2.2 for further detail**). Additionally, segments 1–6 each contain a T10 polynucleotide linker terminated with a thiol group at the 5' end to allow conjugation to a ~13 nm AuNP core. A series of SNAs were then synthesized with increasing number of distinct sequences (n) using the salt-aging method, beginning with a traditional homoMV SNA containing only segment 1 ($n = 1$ SNA) and ending with a heteroMV SNA incubated with equimolar concentrations of segments 1–6 ($n = 6$ SNA). The total number of oligos per AuNP for $n = 1$ and 6 SNAs was measured to be 162 ± 11 and 168 ± 6 , respectively (**Figure A2.3**).

In order to determine if heteroMV SNAs form efficient multivalent interactions with the target sequence, melting curves were measured for the SNA–target complex. First, $n = 1–6$ SNAs were incubated for 1 h with a 25-fold excess of the target sequence labeled with FAM in $1 \times$ PBS (**Figure 2.2A**). Following hybridization, unbound targets were removed through washing, and the samples were heated to 80 °C. As the SNA:target complex was heated, the fluorescence increased due to dehybridization and subsequent dequenching of the FAM-tagged target as the efficiency of the nanosurface energy transfer (NSET) decreased.²² From the melting curves we determined the melting temperature (T_m), the full width at half-maximum (fwhm) of the transition, and maximum fluorescence intensity following melting. As n increased, the T_m increased by up to ~12 °C, suggesting that multiple segments were able to bind the target simultaneously (**Figure 2.2B**).

However, when $n > 4$ a drop in T_m was observed, supporting the predicted limitations of random heteroMV SNAs (**Figure 2.1F**). Note that one would not normally see a decrease in T_m as the duplex lengthens for conventional linear oligonucleotides. Furthermore, the fwhm of the first derivative plots of each melting curve was determined. It was found that as n increased, the fwhm increased as well, indicating that the melting transition was less uniform (**Figure 2.2C**). This suggests that as n increased there was a wider range of binding valencies present. By incubating with a 25 molar excess of targets, we were able to also determine the number of targets bound per particle (**Figure A2.4**). Generally, as n increased, fewer targets bound each SNA, likely due to each target occupying more segments on the particle surface and the inherent reduction in maximum binding capacity as the total number of each unique oligo decreases when n increases. Next, we tested the modeling prediction that increased stringency, resulting in a lower affinity for each segment, would lead to higher valency binding. The same series of melting experiments was repeated, with the exception of performing the hybridization in a more stringent buffer, $0.1 \times$ SSC (saline sodium citrate), 0.2% Tween20 (~ 15 mM Na⁺). Note, the washing buffer and buffer in which the melting curves were measured are identical in the two sets of experiments. Indeed, it was observed that the T_m 's for $n = 1-6$ SNAs increased by up to ~ 4 °C when hybridization stringency increased (**Figure 2.2D**). The value of n giving the highest T_m also increased to $n = 6$, a similar result to that predicted with modeling (**Figure 2.1D**). The noticeable ~ 2 °C lower T_m for the $n = 1$ SNA after hybridizing in less stringent conditions is consistent with previous observations of a negative cooperativity in SNA binding as an increasing number of targets are bound to the surface.¹⁵ Furthermore, in more stringent hybridization conditions we see reversing of the trends for binding uniformity and capacity, with $n = 4$ resulting in the most uniform binding and the most targets bound (**Figure 2.2E and A2.4**).

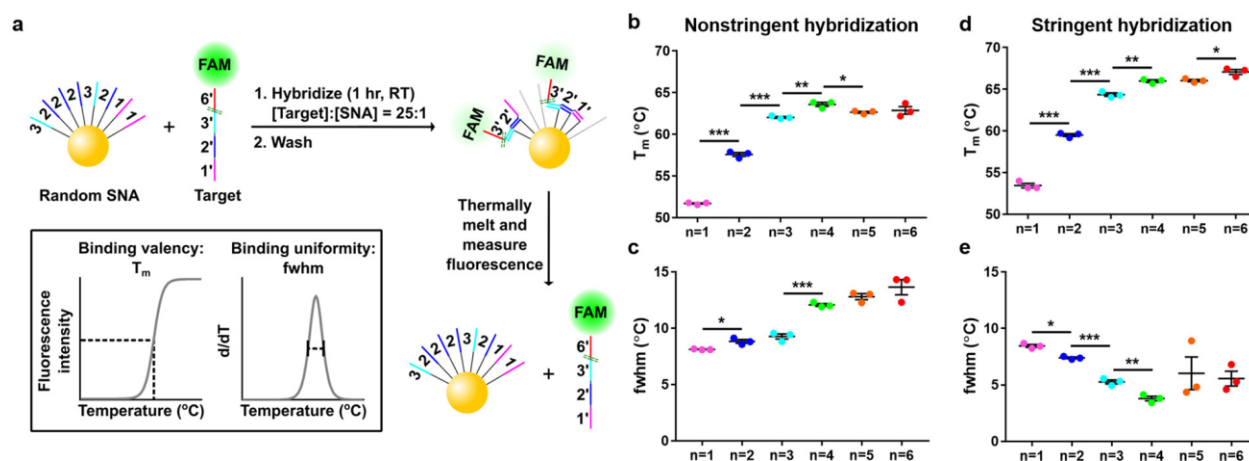


Figure 2.2. Effect of random heteromultivalency on binding valency and binding uniformity. (a) Schematic illustration describing the melting experiment where excess FAM-labeled target was hybridized to random $n = 1-6$ SNAs and fluorescence was measured as the complex was thermally melted. Inset illustrates how the melting temperature (T_m) and the full width at half-maximum (fwhm) were calculated. (b and c) Impact of increasing n on T_m (b) and fwhm (c) after hybridizing target to SNA in nonstringent buffer ($1 \times$ PBS). (d and e) Impact of increasing n on T_m (d) and fwhm (e) after hybridizing target to SNA in stringent buffer ($0.1 \times$ SSC, 0.2% Tween20). Both sets of melting curves were measured in $4 \times$ SSC, 0.2% Tween20 buffer. Error bars represent standard error of the mean. Values from sequential groups were compared using unpaired student t tests (* $P < 0.05$; ** $P < 0.01$; *** $P < 0.001$). No statistical differences were observed between unmarked sequential groups.

2.2.3. Thermodynamics and Affinity of Random HeteroMV SNA Binding

We next measured the thermodynamic binding parameters of randomly organized $n = 1-6$ heteroMV SNAs binding to the target. In these studies, the particles were incubated at a 1:1 ratio of SNA to target for 1 h (**Figure 2.3A**). The concentration of SNA was varied from 1.75 to 15 nM, and the T_m for the complex was measured as the Cy5-labeled target was thermally dehybridized (**Figure A2.5, Table A2.2**). For each SNA, ~ 20 thermal melting curves were used to populate the van't Hoff plot showing $\ln(C_T)$ versus $1/T_m$ (**Figure 2.3B**). Note that C_T is the sum of the SNA and target concentrations. The following equation was then applied, using 1.986×10^{-3} kcal $K^{-1} \text{ mol}^{-1}$ for the gas constant R , to calculate the ΔH and ΔS of binding (**Table A2.3**)

$$\frac{1}{T_m} = \frac{R}{\Delta H} \ln C_T + \frac{\Delta S - R \ln 4}{\Delta H}$$

From these values, the ΔG of binding was then derived.¹⁵ First, consistent with the melting studies shown in **Figure 2.2**, T_m plateaued for SNAs with $n > 4$. The flattening slopes as n increases (**Figure 2.3B**) correspond to a more favorable enthalpy of binding (**Figure 2.3C**), suggesting that each target is binding more segments. On the other hand, the entropic cost of binding increased with increasing n as less of the target remained unbound and flexible (**Figure 2.3D**). Nonetheless, the enthalpic benefits outweighed the entropic costs, resulting in a dramatic enhancement in ΔG (~ 50 kcal/mol) as n increases from 1 to 6 (**Figure 2.3E**). The decrease in ΔG corresponds to a ~ 40 order-of-magnitude enhancement in binding affinity (K_{eq}) (**Figure 2.3E**) and a multivalent enhancement value, β ($\beta = K_{eq}^{multi}/K_{eq}^{mono}$), of 7×10^{38} as n increased from 1 to 6 (**Table A2.4**). Similar results were obtained when random heteroMV SNAs bound an identical target with no spacers between segment binding regions, with a total ~ 50 order-of-magnitude enhancement in avidity (**Table A2.4**). Consistent with the modeling predictions (**Figure 2.1E**), the decreased target:SNA ratio (1:1 instead of 25:1 in **Figure 2.2**) resulted in a more linear relationship between n and binding affinity, with the $n = 6$ heteroMV SNAs exhibiting the highest affinity. However, when the target:SNA ratio was increased to 5:1 or 10:1, the affinity of each heteroMV SNA decreased and affinity appears to saturate after $n = 5$ (**Figure A2.6**, **Table A2.5**, **Table A2.6**). The fwhm values also increased, suggesting that binding becomes less uniform as the target:SNA ratio increases (**Figure A2.6**).

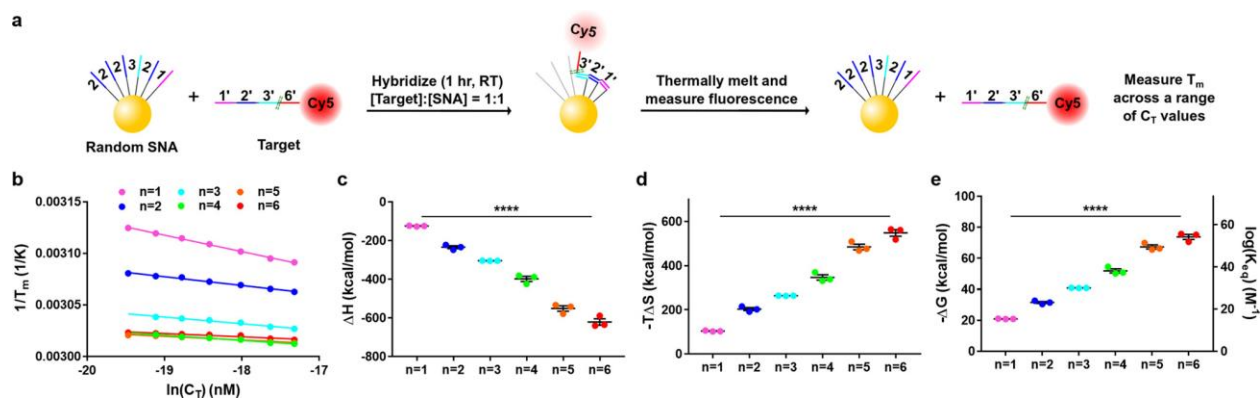


Figure 2.3. Effect of random heteromultivalency on thermodynamics and affinity. (a) Schematic illustration describing the experiment to obtain thermodynamic parameters and affinity values. Random $n = 1-6$ SNAs were bound to Cy5-labeled target in $1 \times$ SSC, 0.2% Tween20 and the T_m was measured across a range of [SNA + target] (C_T) values. (b) Linear van't Hoff plots from which thermodynamic values were extracted. (c–e) ΔH (c), $-T\Delta S$ (d), and $-\Delta G$ and $\log(K_{eq})$ (e) values of random $n = 1-6$ SNAs binding to target. Error bars represent standard error of the mean. Values were compared using one-way ANOVA (**** $P < 0.0001$).

2.2.4. Development and Characterization of Patterned HeteroMV SNAs

Here, we hypothesized that spatial patterning of SNAs could boost target affinity compared to that of heteroMV SNAs with random oligo positioning. To test this hypothesis, we first developed a molecular printing method to create patterned heteroMV SNAs (**Figure 2.4A**). Briefly, segments 1–6 were first hybridized to a ssDNA template, identical to the no-spacer containing target sequence, forming an 81mer duplex with a “nick” located between each segment binding region. A native PAGE gel was performed to confirm the successful binding of the six segments to the template (**Figure A2.7**). The segment/template complex was then incubated with the AuNP, forming up to six thiol linkages in a sequential array on the NP surface (as shown in **Figure 2.4A and Figure A2.8**). The single-strand nicks help accommodate the local curvature of the spherical nanoparticle surface.²³ Next, salt aging was performed to increase the packing density of the complex on the particle. The template was then removed by dehybridization with a series of washes in DI water at RT. After template dehybridization, segments 1–6 remain on the particle surface

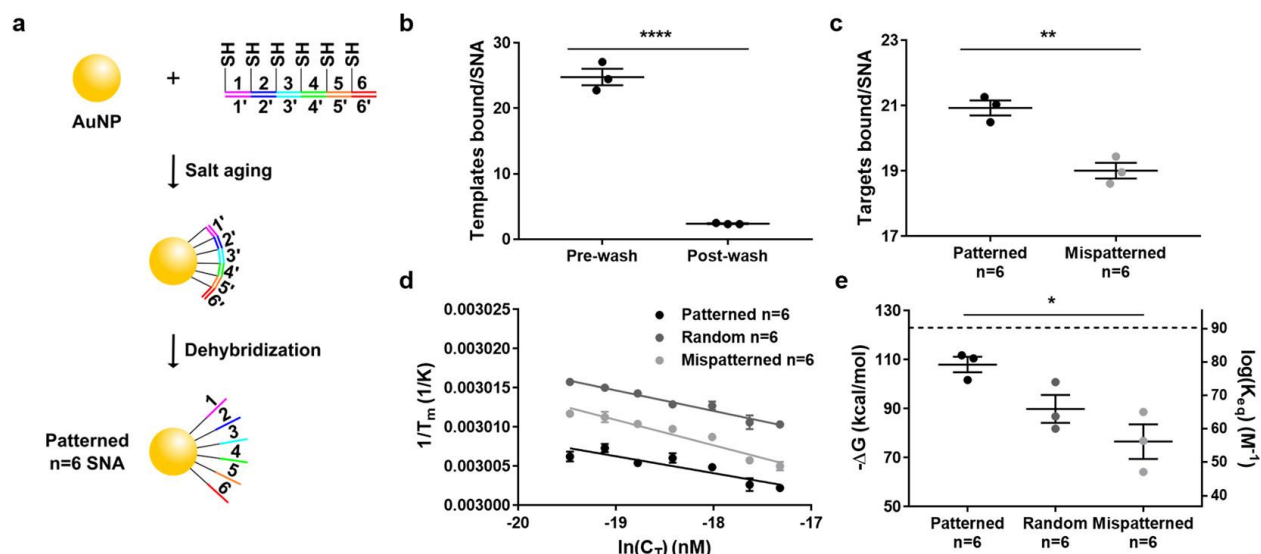


Figure 2.4. Characterization and binding analysis of patterned heteroMV SNAs. (a) Schematic illustration depicting the synthesis of patterned SNAs. After preannealing segments 1–6 to the template, the complex was incubated with the AuNP. Next, salt aging was performed, and then the template was dehybridized. (b) Quantifying templates bound per SNA before and after dehybridizing. (c) Targets bound per AuNP for patterned and mispatterned SNAs after high-stringency washes. (d and e) van't Hoff plots (d) and $-\Delta G$ and $\log(K_{eq})$ (e) for patterned, random, and mispatterned $n = 6$ SNAs binding the no-spacer target. Dashed line in e represents the predicted $-\Delta G$ value (123 kcal/mol) for the non-nicked 81 bp duplex binding in solution. Error bars represent standard error of the mean. Templates/targets bound values were compared using an unpaired student t test, and $-\Delta G$ and $\log(K_{eq})$ values were compared using one-way ANOVA (* $P < 0.05$; ** $P < 0.01$; **** $P < 0.0001$).

because of the strong thiol–gold association, with controlled position and spacing, yielding a spatially patterned heteroMV SNA with $n = 6$. Note that while we could create patterned SNAs with fewer unique segments, these structures were less desirable as the modeling suggested a maximum affinity enhancement for the $n = 6$ particles (**Figure 2.1F**).

Because patterned heteroMV SNAs have not been reported in past literature, we began by characterizing the DNA–AuNP conjugate. First, the number of complexes loaded to each particle was quantified by detecting release of a FAM-labeled template following heating (**Figure A2.9**). This melting assay revealed that ~ 25 templates were bound to each SNA (**Figure 2.4B**). Next, we validated template dehybridization and found that $\sim 90\%$ of templates were removed (**Figure 2.4B**). Moreover, the total number of binding ligands (segments 1–6) per particle was quantified to be

~135 (**Figure A2.10**). This indicates that each template was bound to ~5.5 segments, offering further evidence of successful hybridization and loading onto the particle.

2.2.5. Impact of Spatial Patterning on HeteroMV SNA Binding

To characterize target binding by patterned heteroMV SNAs, we obtained thermal melting curves and also applied the van't Hoff relation to determine the thermodynamic binding constants. For these assays, we created mispatterned heteroMV SNAs using a template with shuffled binding regions to serve as an additional control. The mispatterned $n = 6$ SNAs are chemically identical to patterned SNAs (same total number of segments 1–6, **Figure A2.10**) except for the relative positioning of the oligos on the NP surface, allowing the role of spatial patterning to be properly elucidated. First, the two particle types were incubated with an excess amount of the no-spacer target labeled with FAM, which is identical to the template used for patterning, and washed with high-stringency buffer ($0.1 \times$ SSC, 0.2% Tween20). Thermal melting curves were then obtained by measuring the fluorescence increase while heating. While the patterned and mispatterned SNAs demonstrated a similar melting temperature (<1 °C difference), patterned SNAs were able to bind a few more targets than their mispatterned counterparts (**Figure 2.4C**, **Figure A2.11**). To more sensitively examine the effects of spatial patterning, the thermodynamics and affinity of the patterned binding interaction were quantified using the van't Hoff relation as described above and compared to the random SNAs (**Figure A2.12**, **Table A2.7**, **Table A2.8**). These experiments revealed a strong impact of oligo positioning on the binding enthalpy, as the dependence of T_m on concentration became less dramatic when going from intentionally mispatterned to random to patterned oligo positioning (**Figure 2.4D**). This enthalpic enhancement with spatial patterning is likely the result of more segments binding each target and reduced strain on the binding entities.

As before, the enthalpic benefits exceeded the entropic costs, leading to a significantly more favorable binding free energy and a ~ 23 order-of-magnitude enhancement in K_{eq} for patterned SNAs over mispatterned (**Figure 2.4E**). Notably, the predicted ΔG for the same duplex containing no nicks is approximately -123 kcal/mol (dashed line in **Figure 2.4E**), which is only $\sim 10\%$ greater than the ΔG of the patterned SNA (-108 ± 3.2 kcal/mol) to the same target. The patterned SNAs were also able to bind the spacer-containing target with a ~ 15 order-of-magnitude higher avidity relative to the mispatterned SNAs (**Table A2.8**). These results demonstrate that proper positioning of the binding ligands on the NP surface is critical for forming a highly effective multivalent interaction.

2.3. Discussion

In this report, heteroMV SNAs were created to bind a nucleic acid target multivalently. By including multiple unique oligosequences, each complementary to a specific region of a ssDNA target, multiple oligo segments bind the target simultaneously. Aided by this multivalent binding, we observed a dramatic enhancement in the melting temperature and binding affinity relative to homoMV SNAs. Thus, the enhanced binding avidity to an oligotarget presented herein has the potential to heighten the efficacy of SNAs and other similar nanostructures in many important applications. We also identify a trade-off between maximizing the binding capacity of a nanoparticle and its binding affinity (quantity versus quality of binding). For example, we found that under stringent hybridization conditions, fewer targets bind a particle, but these few targets display a greater binding valency. In other words, under stringent conditions, the target can sample a wider range of binding geometries to overcome kinetic barriers and maximize the number of segments bound, thus reaching a thermodynamic minimum. On the basis of this conclusion, we

expect that by shortening the length of each segment we can further increase the binding valency for random heteroMV SNAs.

Importantly, we demonstrate a 15 order-of-magnitude enhancement in binding affinity when six complementary oligonucleotides are spatially organized on the particle surface instead of randomly positioned. This massive enhancement is the result of a templating-based strategy to control the relative position of each oligo on the surface of the nanoparticle. To spatially pattern DNA one can use top-down or bottom-up strategies.²⁴⁻²⁷ Bottom-up self-assembly of DNA nanostructures, such as the DNA origami technique, is clearly advantageous when the desired pattern is at the sub-100 nm length scale. Indeed, through careful template design, a variety of 2D and 3D multivalent receptors have been created to target virus capsids, proteins, and other biologically relevant molecules.^{4, 28-29} Our spatial patterning simply utilizes a conventional DNA oligonucleotide template and several shorter thiolated oligos. This has important advantages in terms of maximizing the yield of synthesis since DNA origami is often limited by low yields and low synthesis scale.³⁰ We note several reports showing the feasibility of generating a variety of DNA patterns on gold nanoparticle scaffolds.³¹⁻³³ These methods have created interesting geometries that are focused on generating nanoparticles with a discrete number of oligonucleotides with specific position and spacing. The materials have been investigated in the context of controlling material synthesis. However, the impact of spatially patterning oligonucleotides on binding affinity to a DNA target has not been characterized previously. Moreover, only by maximizing DNA density on the particle surface is it possible to achieve maximum enhancement in binding affinity.¹⁶ We anticipate that this simple yet efficacious spatial patterning technique developed in this work can be broadly utilized in supramolecular chemistry and nanotechnology.

In conclusion, we demonstrated a simple approach to boost the affinity of DNA–nanoparticle conjugates by many orders of magnitude without making any chemical changes to its composition. Further optimization of patterned heteroMV SNAs is likely possible by considering the three-dimensional topology of the DNA duplex and positioning each segment’s linker at every turn of the DNA double helix. For example, positioning the thiol group on the multivalent complex with 10–11 nucleotide intervals will likely relieve potential enthalpic strain as all of the T10 linkers should extend from the complex in the same approximate direction. However, 10–11mer segments could lower the total affinity of the heteroMV SNA for its target when compared to the longer 12–15mer segments described herein. Additionally, in this work, the binding segments are all anchored to the NP through a T10 linker. Given the importance of linker rigidity in tuning avidity, trimming the 10-nucleotide spacer may offer further enhancements in binding affinity by lowering the entropic costs of binding.¹ One limitation of the present study is that the thermodynamic parameters quantified were determined for one model target, and when this approach is applied toward designing potent binders in different biomedical or diagnostic applications, it is likely that noncanonical secondary structures may modulate the predicted avidity. To further demonstrate the general applicability of the techniques presented here, additional target sequences and the impact of the target spacer length should be investigated. A potential limitation of patterned SNAs is the labile nature of the thiol–gold bond which is highly sensitive to time, temperature, and pH.³⁴⁻³⁵ This may be addressed by using the more stable chelating thiols anchors such as lipoic acid.³⁶ SNAs and other DNA-presenting nanostructures have already made their way into FDA-approved diagnostics and potential human therapies, and thus, heteromultivalent binding, both patterned and nonpatterned, holds important promise for biomedical sensing and antagonism of transcripts.

2.4. Materials and Methods

2.4.1. Oligonucleotides

All oligonucleotides were custom synthesized by Integrated DNA Technologies (Coralville, IA).

Table A2.1. includes the names and sequences for all oligonucleotides used in this work.

Structures of the modifications are shown in **Figure A2.5**. Note that segment 6 has an 11T spacer instead of 10T. However, we do not expect that this will impact any findings from this work.

Table A2.1. List of oligonucleotides used in Chapter 2.

Name	Sequence (5' to 3')
segment 1	/5ThioMC6-D/TTTTTTTTTTACTCTACCACATATA
segment 2	/5ThioMC6-D/TTTTTTTTTTTCCTTGGGAACC
segment 3	/5ThioMC6-D/TTTTTTTTTTTGACAGTAAATGCG
segment 4	/5ThioMC6-D/TTTTTTTTTTTCAGCAAATGCCA
segment 5	/5ThioMC6-D/TTTTTTTTTTTAGGTCATGAATATAA
segment 6	/5ThioMC6-D/TTTTTTTTTTTACAGCAAATATCCT
amine-labeled target	AGGATATTTGCTGTCTTTATATTCATGACCT ACTGGCATTGCTGAACGCATTTACTGTC ACGGTCCCAAGGACCTATATGTGGTAGAGT/3AmMO/
amine-labeled target- no spacers	AGGATATTTGCTGTTTATATTCATGACCT TGGCATTGCTGCGCATTTACTGTC GGTCCCAAGGATATATGTGGTAGAGT/3AmMO/
patterned template	AGGATATTTGCTGTTTATATTCATGACCT TGGCATTGCTGCGCATTTACTGTC GGTCCCAAGGATATATGTGGTAGAGT
mispatterned template	TGGCATTGCTGAGGATATTTGCTGT GGTCCCAAGGATTATATTCATGACCT TATATGTGGTAGAGTCGCATTTACTGTC
FAM-labeled target	AGGATATTTGCTGTCTTTATATTCATGACCT ACTGGCATTGCTGAACGCATTTACTGTC ACGGTCCCAAGGACCTATATGTGGTAGAGT/36-FAM/
FAM-labeled target- no spacers	AGGATATTTGCTGTTTATATTCATGACCT TGGCATTGCTGCGCATTTACTGTC GGTCCCAAGGATATATGTGGTAGAGT/36-FAM/
T10	/5ThioMC6-D/TTTTTTTTTTT

2.4.2. Reagents

Nitric acid (Cat# BDH3044500MLPC) was purchased from VWR (Radnor, PA). Hydrochloric acid (Cat# HX0603-3), sodium phosphate monobasic monohydrate (Cat# SX0710), sodium chloride (Cat# SX0420, GR ACS), potassium chloride (Cat# 1049360500), monopotassium phosphate (Cat# PX1565-1), and Dri-solv methylsulfoxide (Cat# MX1457-7) were purchased from EMD Millipore (Burlington, MA). Gold (III) chloride trihydrate (Cat# 520918-1G), sodium citrate tribasic dihydrate (Cat# S4641-25G), dithiothreitol (DTT) (Cat# 10197777001), sodium dodecyl sulfate (SDS) (Cat# L3771), 3-hydroxypicolinic acid (3-HPA) (Cat# 56197), potassium cyanide (Cat# 60178), potassium hydroxide (Cat# 221473), sodium bicarbonate (Cat# S6014), acetonitrile (Cat# 34998), and tetramethylethylenediamine (TEMED) (Cat# T9281) were purchased from Sigma-Aldrich (St. Louis, MO). Sodium phosphate dibasic was purchased from (Cat# 470302-660) Ward's Science (Rochester, NY). 20x TE buffer (Cat# 42020325-2) was purchased from bioWORLD (Dublin, OH). Quant-IT Oligreen ssDNA reagent (Cat# O7582), Tween20 (Cat# BP337), 6x DNA loading dye (Cat# R0611), ammonium persulfate (APS) (Cat# BP179-25), and SYBR Gold nucleic acid gel stain (Cat# S11494) were purchased from Thermo Fisher Scientific (Waltham, MA). Saline sodium citrate (SSC) buffer (Cat# AM9763) was purchased from Ambion (Austin, TX). Cyanine 5 NHS ester (Cat# 23020) was purchased from Lumiprobe (Hunt Valley, MD). Triethylammonium acetate (Cat# 60-4110-57) and trifluoroacetic acid (Cat# 60-4040-57) were purchased from Glen Research (Sterling, VA). Ammonium citrate (Cat# 09831) was purchased from Fluka Analytical (Charlotte, NC). Tris(2-carboxyethyl)phosphine hydrochloride (TCEP) (Cat# T1656) was purchased from Tokyo Chemical Industry (Tokyo, Japan). 30% Acrylamide/Bis Solution 29:1 (Cat# 1610156) was purchased from Bio-Rad (Hercules, CA).

2.4.3. Consumables

200-mesh carbon coated copper grids (Cat# CF200-Cu) were purchased from Electron Microscopy Sciences (Hatfield, PA). Illustra-NAP 25 columns (Cat# 17085201) were purchased from GE healthcare (Pittsburg, PA). 96-well white flat bottom polystyrene microplates (Cat# 3912) were purchased from Corning (Corning, NY). P2 size exclusion gel (Cat# 1504118) was purchased from Bio-Rad (Hercules, CA). LightCycler 480 Multiwell Plate 96 qPCR plates (white) (Cat# 04729692001) were purchased from Roche (Penzberg, Upper Bavaria, Germany). Amicon Ultra-0.5 mL centrifugal filters (30,000 NMWL) (Cat# UFC503024) were purchased from EMD Millipore (Burlington, MA).

2.4.4. Equipment

The major equipment that was used in this study includes: H-7500 transmission electron microscope (TEM) (Hitachi), Nanodrop 2000 UV-Vis Spectrophotometer (Thermo Scientific), Barnstead nanopure water purifying system (Thermo Fisher), SB3D1020 3D Nutation Mixer orbital shaker (Southwest Science), ultrasonic cleaner bath sonicator (Cat# 97043-968) (VWR), 5424 R centrifuge (Eppendorf), Synergy H1 plate reader (Biotek), Dual-Fl-UV-800 fluorometer (Horiba) with cuvette (105-251-15-40) (Hellma Analytics), high-performance liquid chromatography 1100 (Agilent) with AdvanceBio Oligonucleotide C18 column (653950-702, 4.6 x 150 mm, 2.7 μ m) (Agilent), Matrix-assisted laser desorption/ionization time-of-flight mass spectrometer (MALDI-TOF-MS) (Voyager STR), LightCycler 96 qPCR instrument (Roche), and Amersham Typhoon gel imager (GE Healthcare).

2.4.5. Modeling

Statistics of association of oligos to SNAs with patterned or randomly distributed complements with varying segment number (n) were calculated using a mean-field lattice kinetic model, based on the Langmuir adsorption isotherm. Binding is assumed to take place through the initial binding of a single segment to an unoccupied complement site, at a rate proportional to the bulk solution oligo concentration c_{bulk} ([Target]), followed by sequential binding of adjacent segments (if an unoccupied complementary neighbor site exists) at a rate proportional to some higher effective local concentration c_{eff} . Desorption of a lone single segment or of a bound segment on either end of a sequence of bound segments is treated using the same rate constant; desorption from the interior of a sequence of bound segments is assumed negligible.

For a patterned heteroMV SNA, with n segments each templated sequence of n segments is assumed to equilibrate with the bath of oligos independently, as if all templates were on parallel tracks with no crossover possibility. Oligos are assumed to bind a track in a contiguous series of segments; the possibility of unbound internal loops is neglected. The fraction of tracks having an oligo bound at all segments from i to j with $i \leq j \leq n$ is designated f_{ij} , leading to $\frac{1}{2} n \times (n+1)$ distinct binding arrangements to track. To express the rates of all possible adsorption and desorption events, it is useful to define individual site occupancies,

$$\Theta_i = \sum_{i' \leq i, j' \geq i} f_{i'j'}$$

as well as the occupancies by lower and upper border segments,

$$\Theta_{i,low} = \sum_{j' \geq i} f_{ij'} ; \Theta_{j,up} = \sum_{i' \leq j} f_{i'j}$$

(For i, j out of the range from 1 to n we can define $\Theta_i, \Theta_{i,low}, \Theta_{j,up} = 1$.)

Equations for the rates of the elementary processes then become:

Rates for binding the first and subsequent segments depend on the bulk or effective concentration and the fractional occupations of the complementary sites. The rate of the elementary process of adsorption at a single segment i follows the Langmuir model:

$$r_{on,i} = k_{on}c_{bulk}(1 - \Theta_i)$$

The rates of binding of segments with higher or lower indices depend on the effective concentration and the probability that the adjacent site will be occupied. Noting that the complementary site at the next higher segment may either be free, with probability $1 - \Theta_{j+1}$, or occupied by the lowest bound segment of a different oligo, with probability $\Theta_{j+1,low}$, the fraction of bound oligos that have a free site at $j+1$ is incorporated into the elementary step rate as:

$$r_{i,j \rightarrow i,j+1} = k_{on}c_{eff}f_{i,j} \frac{(1 - \Theta_{j+1})}{(1 - \Theta_{j+1} + \Theta_{j+1,low})}$$

Similarly,

$$r_{i,j \rightarrow i-1,j} = k_{on}c_{eff}f_{i,j} \frac{(1 - \Theta_{i-1})}{(1 - \Theta_{i-1} + \Theta_{i-1,up})}$$

The rates of full desorption of oligos bound at a single segment i , or of lowering the valency by 1 segment at the lower or upper end, all have the same simple form:

$$r_{off,i} = k_{off}f_{ii}$$

$$r_{i,j \rightarrow i+1,j} = k_{off}f_{i,j}$$

$$r_{i,j \rightarrow i,j-1} = k_{off}f_{i,j}$$

From these elementary steps, master equations for all occupancies f_{ij} can be written and were integrated numerically to give kinetics of binding assuming constant and well-mixed c_{bulk} .

Random heteroMV SNAs with n segments were treated in an analogous manner, with the introduction of a distribution of track lengths created through this random deposition. Again, we neglect the possibility of crossover across tracks, assuming that the addition of a new path will be

cancelled out by the disruption of another path. To determine this distribution, we define a nearest neighbor number m , which represents how many sites are within range of a bound site. Assuming random distribution of oligos, the probability that *no* sites within range will have the correct sequence to bind one of n total segments is

$$x = \left(\frac{n-1}{n}\right)^m$$

This expression gives the fraction of all sites with a track length of 1. The probability that the track will end in each successive step is $\left(\frac{n-1}{n}\right)^{m-1}$, as the “backward” option is eliminated. The mean-field probability of finding a track corresponding to each i,j starting and ending segment is calculated using this approach; in the end, only the length $n'=j-i+1$ is used. Kinetic trajectories for each subset of tracks of length n' are calculated in parallel exactly as for templated systems, and the results are weighted according to the number of tracks of different length.

For both types of systems, the kinetic trajectories were calculated at fixed c_{bulk} ([Target]) until converged at an equilibrium. The results at equilibrium depend on the following parameters in dimensionless units: c_{bulk} , K_d (individual segment binding affinity, equal to k_{off}/k_{on}), c_{eff} , and m . For the data in **Figure 2.1D**, c_{bulk} was held constant at a value of 0.01 while K_d was varied with values of 1, 0.1, and 0.01. For **Figure 2.1E**, K_d was held constant at a value of 1 while c_{bulk} was varied with values of 0.0001, 0.01, and 1. For **Figure 2.1F**, both parameters were held constant with $c_{bulk} = 0.01$ and $K_d = 1$. Finally, all modeling results presented herein were generated with $c_{eff} = 10$ and $m = 6$. The mean valency was calculated as:

$$valency = \frac{\sum_{i,j}(i-j+1)f_{ij}}{\sum_{i,j}f_{ij}}$$

It was assumed that each bound site had six nearest neighbors ($m = 6$) based on the hexagonal packing of Au atoms on the nanoparticle surface.³⁷

2.4.6. Synthesis of Gold Nanoparticles

The synthesis protocol was adapted from a published protocol from Mirkin and colleagues.³⁸ Briefly, the glassware was cleaned with aqua regia ($\text{HNO}_3 + 3\text{HCl}$) and washed with nanopure water at least 5 times. Then, 250 ml of 1 mM gold (III) chloride trihydrate solution was transferred into a 500 ml round-bottom flask coupled to a reflux condenser (water flowing through the condenser). Next, the solution was heated and rigorously stirred till the refluxing rate reached ~1 drip/s. While the gold solution was refluxing, 25 ml of 38.8 mM sodium citrate tribasic dihydrate solution was rapidly injected into the flask (one injection within 1 sec). The flask was resealed. The solution was kept stirring and turned to clear, to black, and then to wine-red. 15 mins after adding citrate solution, the heat was removed to allow the reaction to cool to room temperature (usually takes 2-4 hours). Lastly, the cool AuNP solution was filtered through a 0.45 μm acetate filter and stored at 4°C. The concentration of the AuNPs were determined by UV-Vis by measuring the absorbance at 520 nm with the Nanodrop instrument. The size of AuNPs was characterized by transmission electron microscopy (TEM). TEM measurements were acquired on a Hitachi H-7500 transmission electron microscope at an accelerating voltage of 80 kV in the Robert P. Apkarian Integrated Electron Microscopy Core at Emory University. Briefly, 5 ml of gold solution was deposited on a 200-mesh carbon coated copper grid (Electron Microscopy Sciences) for 10 mins. Excess liquid was then wicked away and AuNPs were imaged without further negative staining using the TEM.

2.4.7. Random HeteroMV SNA Synthesis

Thiolated segment strands were treated with 0.1 M DTT in disulfide cleavage buffer (170 mM phosphate buffer, pH = 8.0) for 2-3 hours at room temperature to reduce the disulfide protecting

group to thiol. For heteroMV SNAs with n unique segments, the concentration of each segment in the mixture incubated with DTT is equal to total $[\text{DNA}]/n$. These reduced segment strands were purified using a NAP 25 size exclusion column. The oligo concentration was determined by UV-Vis. Then, $\sim 3 \mu\text{M}$ (final concentration) thiolated oligonucleotides were mixed with $\sim 7 \text{ nM}$ AuNPs (final concentration) in nanopure water and incubated on an orbital shaker overnight in the dark at room temperature. Next, phosphate adjustment buffer (100 mM phosphate buffer, pH = 7.0) and SDS (10% w/v in nanopure water) were added to make a DNA-AuNP mixture with 10 mM phosphate and 0.1% w/v SDS. This mixture was incubated on an orbital shaker for another 30 min at RT. Salting buffer (10 mM phosphate buffer and 2 M NaCl, pH 7.0) was then added in eight increments, increasing total NaCl concentration stepwise as follows: 0.05, 0.1, 0.2, 0.3, 0.4, 0.5, 0.6, and 0.7 M. After each addition, the SNAs were sonicated in a bath sonicator 20–30 s and incubated on an orbital shaker for 20 min. Following salt aging to 0.7 M NaCl final concentration, SNAs were left overnight on an orbital shaker and then stored in 0.7 M NaCl at 4°C until use.

2.4.8. Determining Number of Oligos/AuNP

Salted particles (random SNAs and patterned SNAs) were washed three times by centrifugation at 13,000 rpm for 20 min at 22°C. After each spin, particles were resuspended in nanopure water. The particles were then diluted to a concentration of 0.2, 0.4, 0.6, and 0.8 nM to yield a 320 μL solution in 1x TE buffer using a stock of 20x TE Buffer (0.2 M Tris-HCl and 20 mM EDTA, pH = 7.5) and nanopure water. To dissolve the gold core and release the oligonucleotides, the particles were incubated in 10 mM KCN (using a 200 mM KCN stock buffered in KOH) for 30 min. From each sample, 100 μL was added to three wells of a 96 well plate and incubated with 100 μL of 1x Oligreen reagent for ~ 5 min before measuring fluorescence using the Biotek plate reader. To

generate a standard curve of fluorescence vs. [DNA], 320 μL of 0, 0.1, 0.2, 0.5, 1, 1.5, and 2 $\text{ng}/\mu\text{L}$ samples of unreduced DNA (mixture of same segments as the particles being measured) were first prepared in 1x TE buffer. DNA was then incubated with 10 mM KCN for 30 min to remain consistency with particle samples. From each sample, 100 μL was added to three wells of a 96 well plate and incubated with 100 μL of 1x Oligreen reagent for ~ 5 min before measuring fluorescence using the plate reader. Using the standard curve, the concentration of DNA in particle samples was determined and then divided by initial AuNP concentration to determine the number of oligos per AuNP.

2.4.9. Melting Curve Measurement for Random HeteroMV SNAs

Salted random heteroMV SNA particles were washed three times by centrifugation at 13,000 rpm for 20 min at 22°C. After the first two spins, particles were resuspended in nanopure water. After the third spin, particles were resuspended in 1x PBS or 0.1x SSC, 0.2% Tween20 and concentrated to ~ 4 nM. Particles were then incubated for 1 hour with 100 nM of FAM-labeled target strand at room temperature with shaking. Following template strand hybridization, particles were washed three times at 13,000 rpm for 20 min to remove any unbound target. After the first two spins, particles were resuspended in 1x SSC and after the third spin, particles were resuspended in 4x SSC, 0.2% Tween20. A melting curve was obtained by heating the particles from 25°C to 80°C and measuring the fluorescence every 5°C using the Horiba fluorometer. Melting curves were fit on GraphPad Prism using the function: log(agonist) vs. response – variable slope equation. This fit provided a T_m for each melting curve. Normalized melting curves were obtained by plugging each data point x into the equation: $(\text{maximum fluorescence} - x)/(\text{maximum fluorescence} - \text{minimum fluorescence})$. The first derivative plot of each fitted curve was also plotted and fit to a

gaussian distribution, and the standard deviation was multiplied by 2.355 to obtain the full width at half-maximum value (fwhm). The fluorescence intensity at 80°C was used as the maximum fluorescence intensity value after melting. To determine how many targets bound to each SNA, a calibration curve was generated by measuring fluorescence intensity at 80°C of FAM-labeled target at a range of concentrations (0.1-80 nM) incubated with 4 nM T10-conjugated SNAs to control for AuNP quenching effects. T10-conjugated SNAs were prepared by adding 3 nmol of Thiol-T10 DNA to 1 mL of 10 nM AuNP, incubating at -30°C for > 2 hours, and then thawing and washing 3x in nanopure water.³⁹ The calibration curve was then used to convert maximum fluorescence intensity values after melting to concentration of target. Concentration of target values were then divided by 4 nM (SNA concentration) to determine targets bound per SNA.

2.4.10. Cy5 Conjugation to Target Strands

Excess NHS-Cy5 (250 µg) was dissolved in 10 µL of fresh DMSO and then added to 10 nmol of amine-labeled target strands in 1x PBS with 0.1 M NaHCO₃. The reaction was left for > 4 hs at room temperature. After incubation, unreacted NHS-Cy5 and salts were removed by P2 gel filtration and purified using an analytical-scale reverse-phase HPLC with an Agilent AdvanceBio Oligonucleotide C18 column. Product was eluted in Solvents A: 0.1 M TEAA and B: ACN with a linear gradient of 10-100% Solvent B over 45 min at 0.5 mL/min flow rate. The desired product was characterized by MALDI-TOF-MS. 3-HPA was dissolved in 50% ACN/H₂O containing 0.1% TFA and 5 mg/mL ammonium citrate as matrix to acquire MALDI-TOF-MS spectra. The concentration of the strands was determined by UV-Vis using a Nanodrop instrument.

2.4.11. van't Hoff Binding Affinity Measurement

Salted particles were centrifuged three times at 13,000 rpm for 20 min and after each centrifugation the supernatant was removed and replaced with fresh nanopure water. In a qPCR plate, 20 μ L solutions of SNAs and Cy5-labeled targets at a 1:1, 5:1, or 10:1 target:SNA ratio were prepared in 1x SSC, 0.2% Tween20 buffer. The targets were labeled with Cy5 rather than FAM due to its enhanced brightness allowing for more sensitive fluorescence detection. The total concentration of SNA and Cy5-targets (C_T) was varied, while maintaining a 1:1, 5:1, or 10:1 target:SNA ratio, to prepare a series of C_T values from 3.5 to 30, 10.5 to 90, or 19.25 to 165 nM, respectively. Samples were left to hybridize at RT for one hour to hybridize before measurement of T_m . Using the qPCR instrument (LightCycler 96), the plate was incubated at 40°C for 5 min before heating to 65°C at a rate of 2.4°C/minute with 25 fluorescent measurements obtained per °C. Melting curves were fit using the GraphPad Prism log(agonist) vs. response- variable slope function, providing a T_m for each melting curve. Triplicate T_m values for each sample at each C_T value were obtained. Based on equation 1, $\ln(C_T)$ vs. $1/T_m$ was then plotted and fit to a linear curve with slope equal to $R/\Delta H$ and y-intercept equal to $(\Delta S - R \ln 4)/(\Delta H)$. A value of $1.986 \times 10^{-3} \text{ kcal K}^{-1} \text{ mol}^{-1}$ was used for R.

$$\text{Equation 1: } \frac{1}{T_m} = \frac{R}{\Delta H} \ln C_T + \frac{\Delta S - R \ln 4}{\Delta H}$$

From the values of ΔH and ΔS , values for ΔG and K_{eq} were obtained using equation 2 and equation 3, respectively, and extrapolating data to 298 K.

$$\text{Equation 2: } \Delta G = \Delta H - T\Delta S$$

$$\text{Equation 3: } K_{eq} = e^{-\Delta G/RT}$$

2.4.12. Native PAGE

Segment strands (120 μM each) were annealed to template strand (100 μM) in 0.1x PBS, 0.1x Phosphate Adjustment Buffer (10 mM phosphate buffer). For the purified complex in lane 9, hybridized DNA was then incubated with 100x TCEP for ~ 30 min to remove thiol protecting groups. Hybridized DNA was then purified with a 30k amicon filter by centrifuging 3x at 14,000 rcf for 30 min, removing flow-through (containing non-hybridized segments, excess TCEP, and thiol protecting group), and adding ~ 500 μL of 1x SSC to the concentrated sample after each centrifugation. 10 pmol of segments 1-6 mixture (lane 1) and 5 pmol of template (lane 2) or annealed complex (lanes 3-9) in 1x TBE with 1x DNA loading dye were added to a 6% native PAGE gel and run for an hour at 60 V. Gels were stained with 1x SYBR Gold reagent for 10 min and imaged on the Amersham Typhoon gel imager.

2.4.13. Patterned and Mispatterned SNA Synthesis

Non-reduced thiolated segment strands (120 μM each) were annealed to the template strand (100 μM) in 0.1x PBS, 0.1x Phosphate Adjustment Buffer (10 mM phosphate buffer). Hybridized DNA was then incubated with 100x TCEP for ~ 30 min to remove thiol protecting groups. Hybridized and reduced DNA was then purified with a 30k amicon filter by centrifuging 3x at 14,000 rcf for 30 min, removing flow-through (containing non-hybridized segments, excess TCEP, and thiol protecting group), and adding ~ 500 μL of 1x SSC to the concentrated sample after each centrifugation. 500 nM (final concentration) of annealed DNA was then added to ~ 10 nM AuNPs suspended in 10 mM phosphate buffer with 0.1% w/v SDS and 10 mM NaCl to maintain DNA hybridization and shook on an orbital shaker for one hour at room temperature. Particles were then salt-aged to 0.7 M NaCl as described above and backfilled with ~ 3 μM thiol-T10 DNA (final concentration) 20 min after the last salt addition to ensure complete saturation of the AuNP surface

with DNA. Particles were left overnight on an orbital shaker at room temperature and then stored at 4°C until ready for use.

2.4.14. Determining Number of Templates/Patterned SNA

Salted particles were centrifuged three times at 13,000 rpm for 20 min and after each centrifugation the supernatant was removed. After the first two spins, particles were resuspended in 1x SSC (pre-dehybridization measurement) or nanopure water (post-dehybridization measurement). After the third spin, particles were resuspended in 4x SSC, 0.2% Tween20 and concentrated to ~4 nM. Particles were then heated from 25°C to 80°C and the fluorescence was measured every 5°C using the fluorometer. The maximum fluorescence intensity value was then converted to templates bound per SNA using the calibration curve and method presented above.

2.4.15. Melting Curve Measurement for Patterned SNAs

Salted particles (patterned and mispatterned SNAs) were washed three times by centrifugation at 13,000 rpm for 20 min at 22°C. After the first two spins, particles were resuspended in nanopure water. After the third spin, particles were resuspended in 1x PBS and concentrated to ~4 nM. Particles were then incubated for 1 hour with 100 nM of FAM-labeled no-spacer target strand at room temperature with shaking. Following template strand hybridization, particles were washed three times at 13,000 rpm for 20 min to remove any unbound target. After the first two spins, particles were resuspended in 0.1x SSC, 0.2% Tween20 and after the third spin, particles were resuspended in 4x SSC, 0.2% Tween20. Using the qPCR instrument (Light cycler 96), the plate was incubated at 40°C for 5 min before heating to 71°C at a rate of 2.4°C/minute with 25 fluorescent measurements obtained per °C. Melting curves were fit using the GraphPad Prism

log(agonist) vs. response- variable slope function, providing a T_m for each melting curve. The first derivative plot of each fitted curve was also plotted and fit to a gaussian distribution and the standard deviation was multiplied by 2.355 to obtain the full width at half-maximum value (fwhm). To determine how many targets bound to each SNA, a calibration curve was generated by measuring fluorescence intensity at 80°C of FAM-labeled target at a range of concentrations (0.1-80 nM) incubated with 4 nM T10-conjugated SNAs to control for AuNP quenching effects. T10-conjugated SNAs were prepared by adding 3 nmol of Thiol-T10 DNA to 1 mL of 10 nM AuNP, incubating at -30°C for > 2 hours, and then thawing and washing 3x in nanopure water.³⁹ The calibration curve was then used to convert maximum fluorescence intensity values after melting to concentration of target. Concentration of target values were then divided by 4 nM (SNA concentration) to determine targets bound per SNA.

2.5. Appendix

Figure A2.1. Modeling the impact of target concentration and surface occupancy on mean binding valency. (a-b) Modeling results predicting the mean binding valency of random $n=1-6$ SNAs as the target concentration (a) and the fraction of binding sites on the surface bound to a target (b) increases, assuming the K_d of each individual segment binding to the particle equals 1. (c-d) Modeling results predicting the mean binding valency of random $n=1-6$ SNAs as the target concentration (c) and the fraction of binding sites on the surface bound to a target (d) increases, assuming the K_d of each individual segment binding to the particle equals 0.01. The target concentrations and K_d values used for these modeling results are of arbitrary units (a.u.).

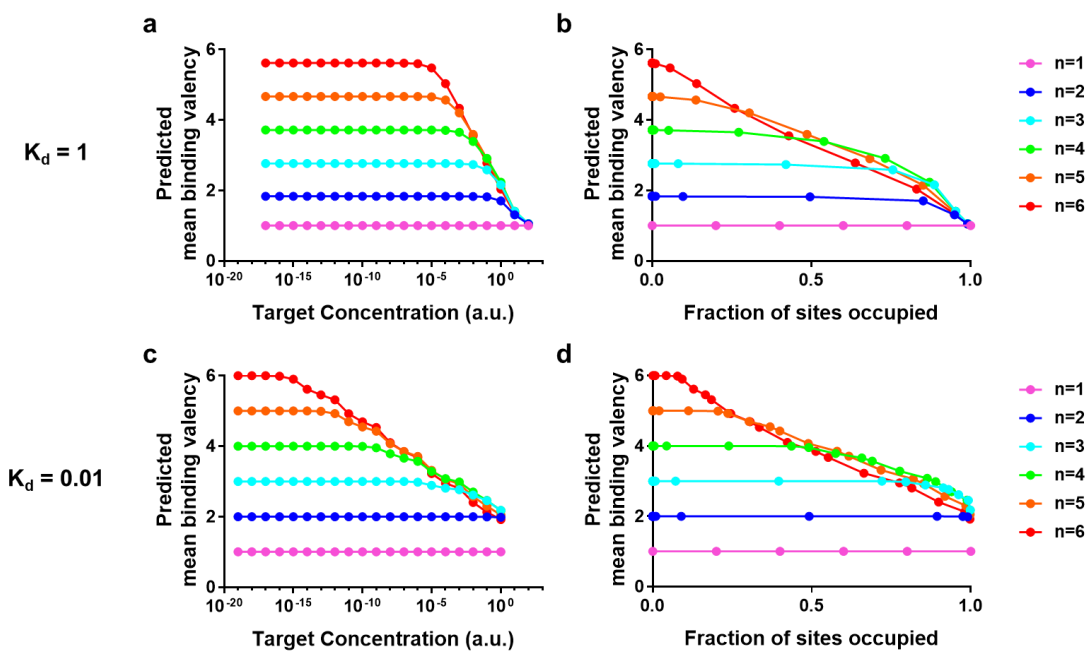


Figure A2.2. Depiction of multivalent DNA binding interaction. (a) Table showing binding sequences for segments 1-6 as well as the spacer-containing (underlined) target and the template/target with no spacers. The melting temperature was determined using the nearest neighbor thermodynamic estimate on the *OligoAnalyzer* software package available on IDT's website. For predicted T_m 's, the following conditions were used: oligonucleotide concentration = 250 nM, Na^+ = 150 mM, and Mg^{2+} = 0 mM. (b) Schematic depicting the binding interaction between segments 1-6 with the target and with the template/no-spacer target. Based on data not shown, adenine bases in the spacer region of the spacer-containing target are depicted hybridizing the thymine bases at the 3' end of the T10 linker, resulting in the likely formation of a 1 nt gap between segments 2 and 3 and between segments 4 and 5 and a single-strand nick between segments 3 and 4. Alternatively, the no-spacer target/template forms a single-strand nick between each binding interaction.

a

Name	Sequence (5' to 3')	T_m (°C)
segment 1	ACTTACCACATATA	37
segment 2	TCCTGGGAACC	41
segment 3	GACAGTAAATGCC	38.4
segment 4	CAGCAAATGCCA	40.3
segment 5	AGGTCATGAATATAA	35
segment 6	ACAGCAAATATCCT	38.5
target	AGGATATTGCTGCTTTATATTCATGACCT ACGGCATTGCTGAAAGCGCATTACTGTC ACGGTCCCAAGGACCTATATGTTGGTAGAGT	-
template/ target- no spacers	AGGATATTGCTGTTTATATTCATGACCT TGGCATTGCTGCGCATTACTGTC GGTCCCAAGGATATATGTTGGTAGAGT	79

b

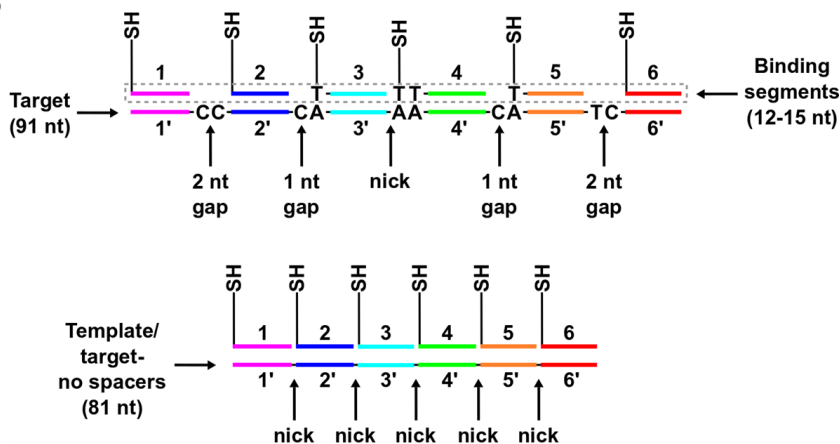


Figure A2.3. Synthesis and characterization of heteroMV SNAs. (a) Representative TEM image of citrate stabilized AuNPs used in this work. (b) Histogram plotting the particle diameter based on analysis of 326 AuNPs imaged using TEM. (c) Schematic showing synthesis of heteroMV SNAs. Equimolar concentrations of thiolated-T10-segments 1-6 were added to 13 nM AuNPs and then salt-aged to yield heteroMV SNAs with n unique oligos ($n \leq 6$). (d) Schematic illustrating the protocol for determining the number of oligos per AuNP. HeteroMV SNAs were incubated with 10 mM KCN for 30 min to dissolve the AuNP core. Released oligos were then incubated with Quant-iT OliGreen reagent for ~ 5 min before measuring fluorescence. (e) Calibration curves for $n=1$ and $n=6$ SNAs were generated by incubating a range of concentrations of segments 1 or segments 1-6 (for $n=1$ and $n=6$ SNAs, respectively) with Quant-iT OliGreen reagent (mean \pm SEM). Each data point represents the mean value of triplicate fluorescence values for each sample at each concentration. Each curve was linearly fit to obtain a conversion factor between fluorescence intensity and [DNA]. (f) Plots showing the DNA density (DNA/AuNP) for $n=1$ and $n=6$ SNAs (mean \pm SEM). Each data point represents the mean value from 4 samples prepared at 0.2, 0.4, 0.6, and 0.8 nM initial AuNP concentration, with triplicate fluorescence values for each sample at each concentration. An unpaired student t test showed no statistical difference ($P > 0.05$) for DNA/AuNP between $n=1$ and $n=6$ SNAs.

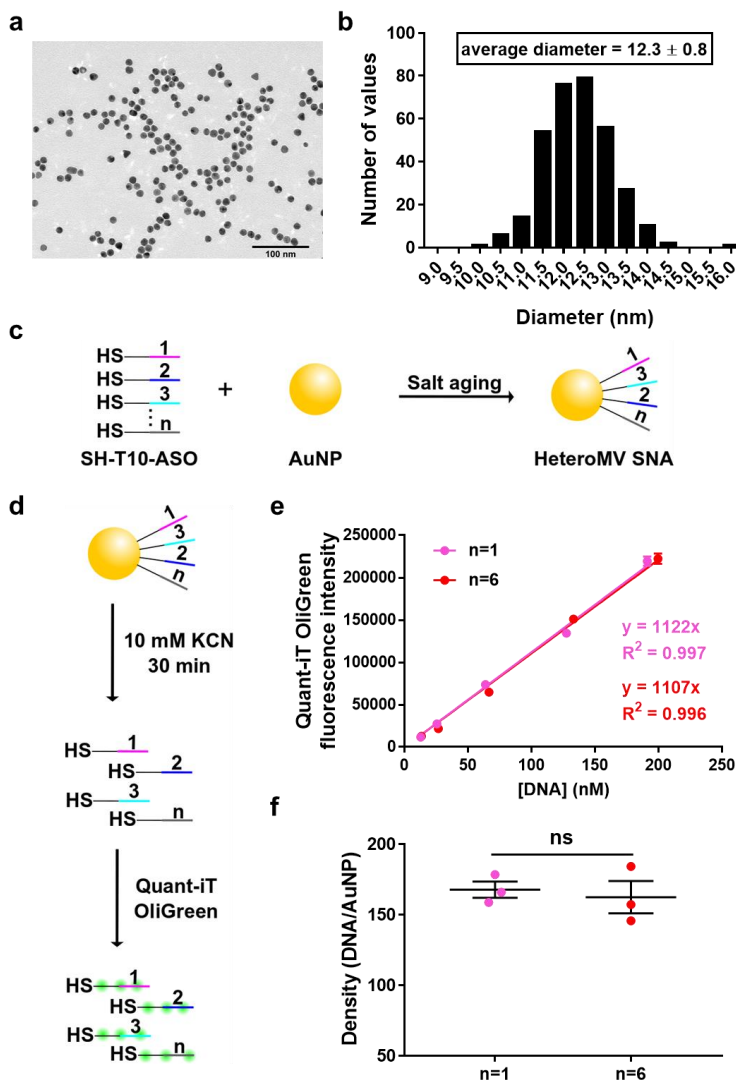


Figure A2.4. Raw melts and binding capacity determination for random heteroMV SNAs.

(a-b) Raw melting curves for $n=1-6$ SNAs after hybridizing in (a) 1x PBS or (b) 0.1x SSC, 0.2% Tween20. (c-d) Normalized melting curves for $n=1-6$ SNAs after hybridizing in (c) 1x PBS or (d) 0.1x SSC, 0.2% Tween20. Each data point represents the mean and SEM of triplicate measurements. (e) Scheme showing how to calculate number of targets bound per AuNP from fluorescence intensity value after melting using a calibration curve. (f) Calibration curve generated by measuring fluorescence intensity at 80°C of target at different concentrations incubated with T10 AuNPs. (g-h) The impact of increasing n on targets bound per SNA after hybridizing target to SNA in 1x PBS (g) or in 0.1x SSC, 0.2% Tween20 (h). Error bars represent standard error of the mean. Values were compared using unpaired student t tests (* $P < 0.05$; ** $P < 0.01$; *** $P < 0.001$).

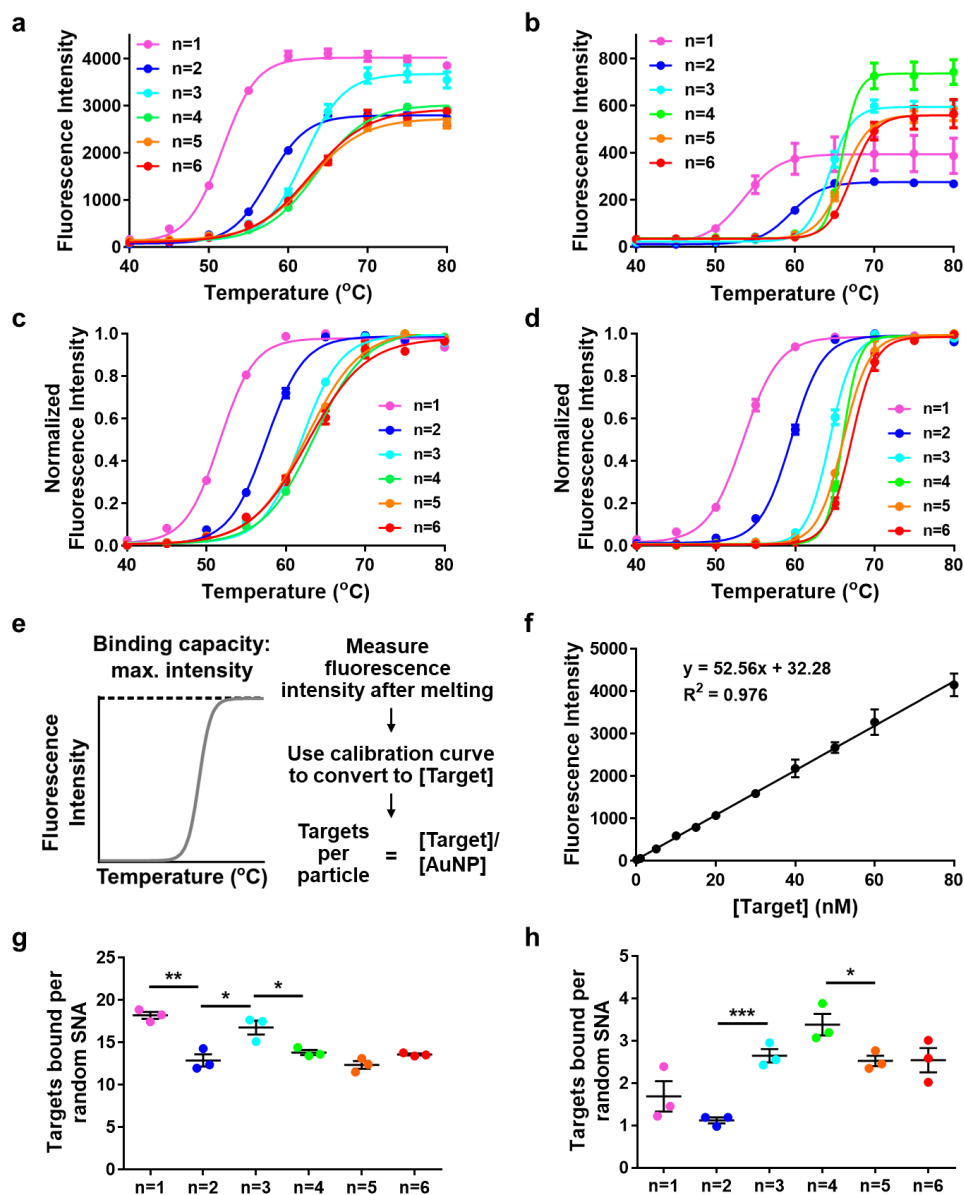


Figure A2.5. Characterization of modified oligonucleotides. (a) Structure of oligonucleotide modifications used in the current work. (b-c) HPLC traces and MALDI-TOF-MS of the (b) no-spacer Cy5-labeled target and the (c) Cy5-labeled target after reacting the corresponding amine targets with NHS-Cy5. Arrows represent the material collected from HPLC. (d) Table of calculated masses, measured m/z values found, and percent error of starting materials and Cy5-labeled products.

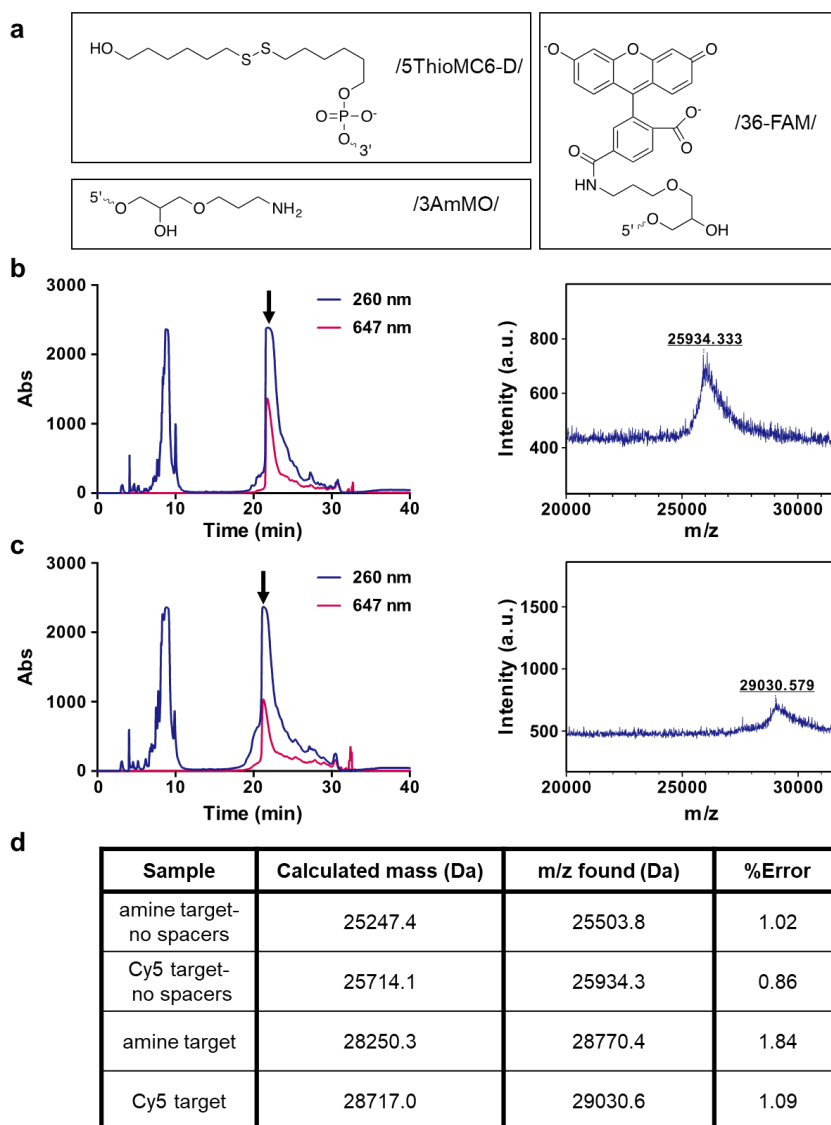


Figure A2.6. Impact of target:SNA ratio on random heteroMV SNAs binding thermodynamics. (a-b) T_m (a) and fwhm (b) values in triplicate of 5 nM random $n=1-6$ SNAs incubated with Cy5-labeled target at 1:1, 5:1, or 10:1 target:SNA ratios. (c-e) ΔH (c), $-T\Delta S$ (d), and $\log(K_{eq})$ (e) values for $n=1-6$ random SNAs incubated with Cy5-labeled target at 1:1, 5:1, or 10:1 target:SNA ratios. Data represents mean values of three replicates and error bars correspond to SEM. The complete set of T_m values from which ΔH and $-T\Delta S$ were calculated are shown in **Table A2.2** for the 1:1 target:SNA ratio data and **Table A2.5** for the 5:1 and 10:1 target:SNA ratio data. ΔH and $-T\Delta S$ values are shown in **Table A2.3** for the 1:1 target:SNA ratio data and **Table A2.6** for the 5:1 and 10:1 target:SNA ratio data. Finally, $\log(K_{eq})$ values are shown in **Table A2.4** for the 1:1 target:SNA ratio data and **Table A2.6** for the 5:1 and 10:1 target:SNA ratio data.

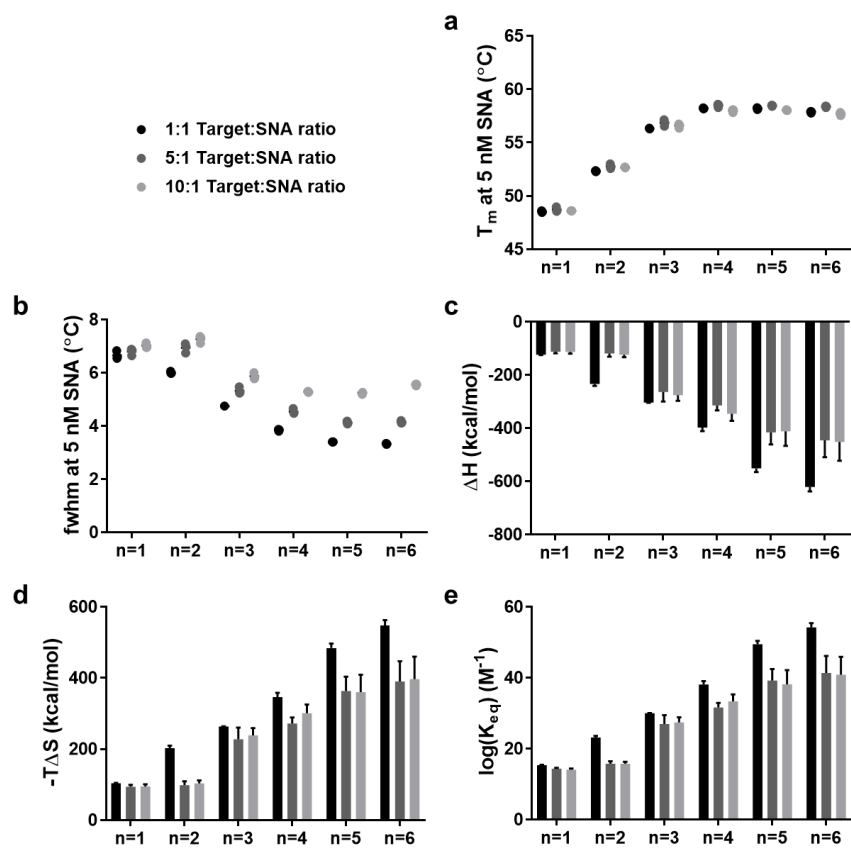


Figure A2.8. Geometric model of template/segments complex attached to surface of AuNP.

2D geometric model (drawn to scale) of the hybridized template/segments 1-6 complex attached to the surface of a 13 nm gold nanoparticle. The AuNP has a radius of ~6.5 nm and a circumference of ~40.8 nm. When assuming the T10 spacer on segments 1-6 adds an additional 6.3 nm between particle surface and complex lying tangential to surface, the particle and T10 has a radius of 12.8 nm (80.4 nm circumference).⁴⁰ If we assume the template/segments complex is ~27.5 nm long (length of 81mer duplex), then we can calculate that the complex will wrap around 34% of the particle surface. Moreover, since segments 1-6 are not connected, there will be “single stranded nicks” that will allow the complex to accommodate for the local curvature of the gold nanoparticle.

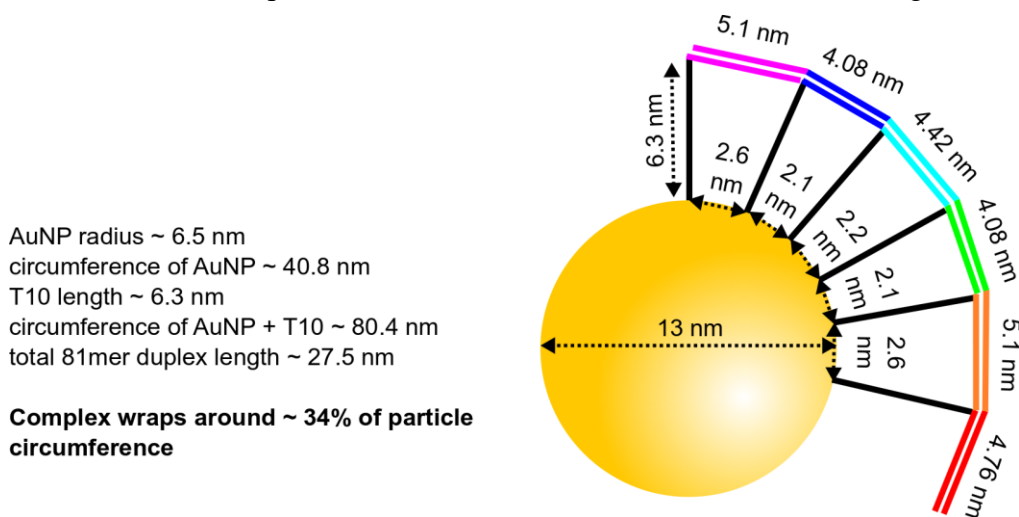


Figure A2.9. Scheme, raw melts, and characterization for patterned SNAs template melting.

(a) Schematic for thermal melting assay for determining templates bound to patterned SNAs before and after dehybridization of the template. Salted patterned SNAs were either washed 3x with 1x SSC (pre-dehybridization) or 3x with nanopure water (post-dehybridization) (mean \pm SEM from three triplicate melting curves). (b) Raw melting curves for patterned SNAs pre-dehybridization and post-dehybridization. (c) Table of T_m values, fwhm values, and number of targets bound from melting curves in (b) (mean \pm SEM).

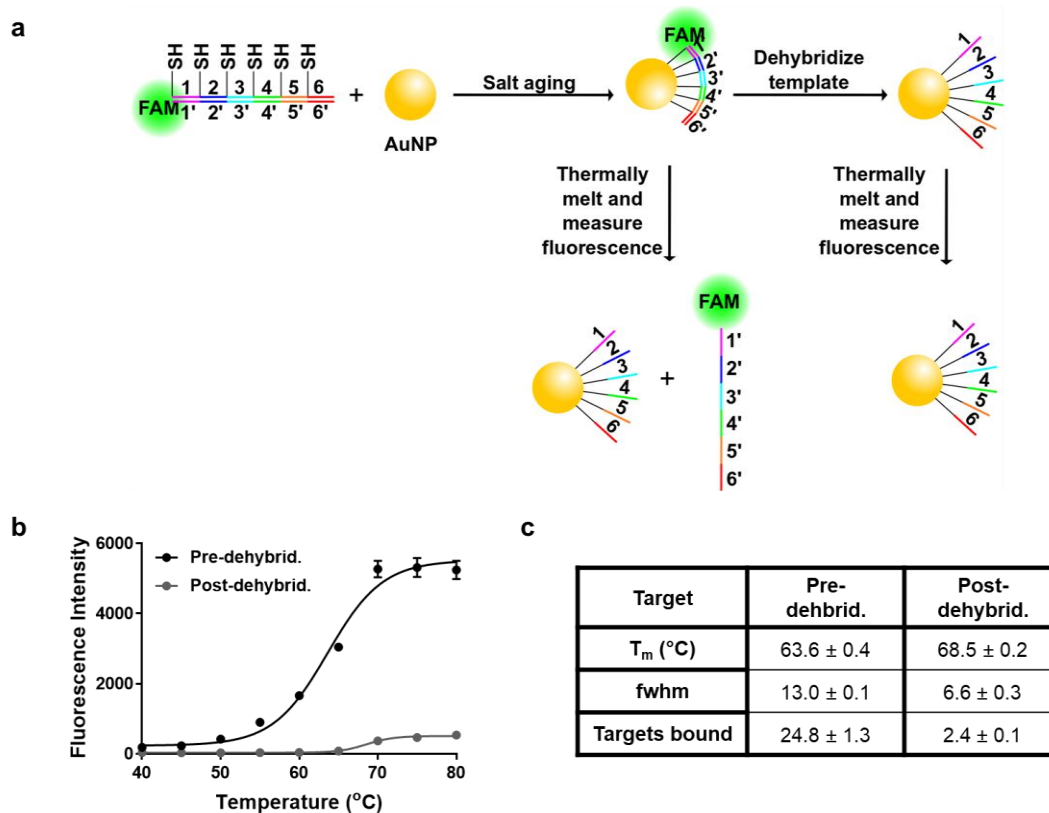


Figure A2.10. Preparation of mispatterned SNAs and determination of segment densities for patterned and mispatterned SNAs. (a) Schematic for synthesis of $n=6$ mispatterned SNAs. Segments 1-6 were hybridized to the shuffled mispatterned template before incubation with particle. Particle was then salt-aged and washed with water to dehybridize mispatterned template, yielding mispatterned heteroMV SNA. (b) Table including patterned and mispatterned template sequences. The melting temperature was determined using the nearest neighbor thermodynamic estimate on the *OligoAnalyzer* software package available on IDT's website. For predicted T_m 's, the following conditions were used: oligonucleotide concentration = 250 nM, Na^+ = 150 mM, and Mg^{2+} = 0 mM. (c) Plots showing the DNA density (DNA/AuNP) for $n=6$ patterned and mispatterned SNAs (mean \pm SEM). Each data point represents the mean value from 4 samples prepared at 0.2, 0.4, 0.6, and 0.8 nM initial AuNP concentration, with triplicate fluorescence values for each sample at each concentration. An unpaired student t test showed no statistical difference ($P > 0.05$) for the number of DNA/AuNP between patterned and mispatterned SNAs.

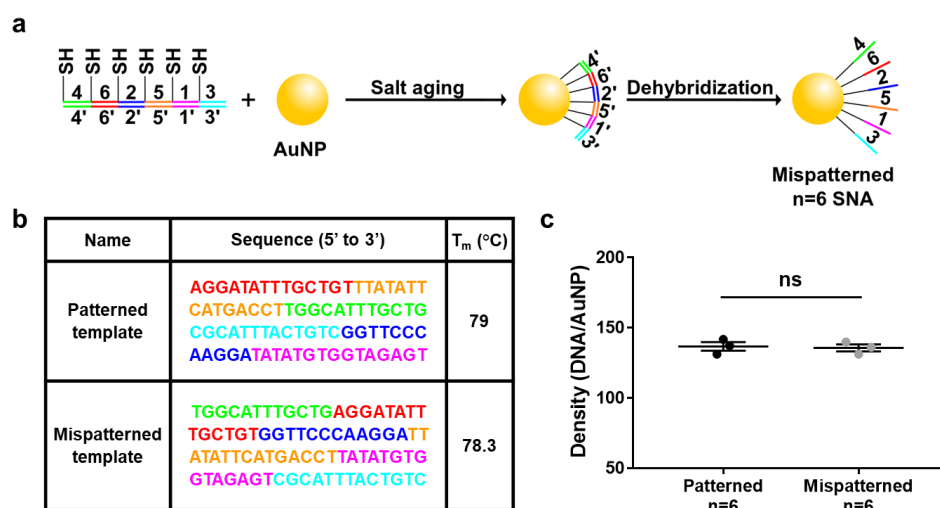


Figure A2.11. Melting characterization of patterned SNAs binding excess targets. (a) Triplicate raw melting curves for patterned and mispatterned $n=6$ SNAs after hybridizing to the no-spacer target at a 25:1 target:SNA ratio in 1x PBS and washing with 0.1x SSC, 0.2% Tween20 buffer. Each data point represents a single fluorescence reading. (b-c) Melting temperature (T_m) (b) and full width at half-maximum (fwhm) (c) values (mean \pm SEM) for patterned and mispatterned SNAs after fitting data raw data in (a). Values were compared using an unpaired student t test ($^{ns}P > 0.05$; $^{**}P < 0.01$). The larger fwhm value for patterned SNAs suggests patterned SNAs bind some targets with higher valencies that are less achievable for mispatterned SNAs, while both particle types form lower valency interactions as well due to the high target concentration that saturates the surface, resulting in a broader melting transition. (d) Calibration curve generated by measuring fluorescence intensity at 80°C of target at different concentrations incubated with T10 AuNPs.

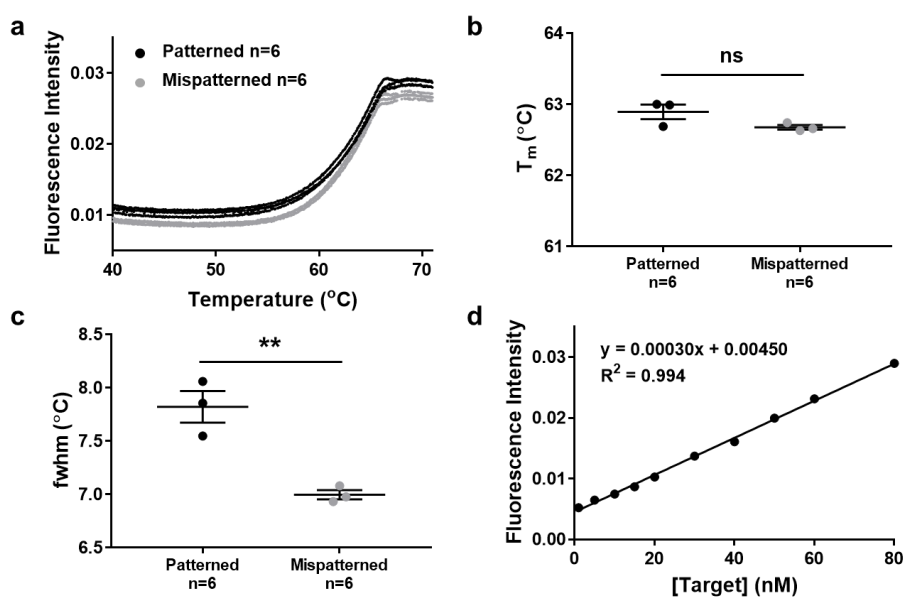


Figure A2.12. Raw melts, ΔH , and $-T\Delta S$ values for patterned, random and mispatterned $n=6$ heteroMV SNAs. (a) Triplicate raw thermal melting curves for patterned, random, and mispatterned $n=6$ SNAs binding the no-spacer Cy5-labeled target. For melting curves shown: $[SNA] = 3.5$ nM, $[target] = 3.5$ nM, $C_T = 7$ nM. Each melting curve was fit as described in the methods section and a T_m for each curve was calculated. (b-c) ΔH (b) and $-T\Delta S$ (c) values for patterned, random, and mispatterned $n=6$ SNAs binding the no-spacer Cy5-labeled target. Error bars represent mean \pm SEM from three replicate measurements. T_m values for random $n=6$ SNAs are shown in **Table A2.2** and T_m values for patterned and mispatterned SNAs are shown in **Table A2.7**.

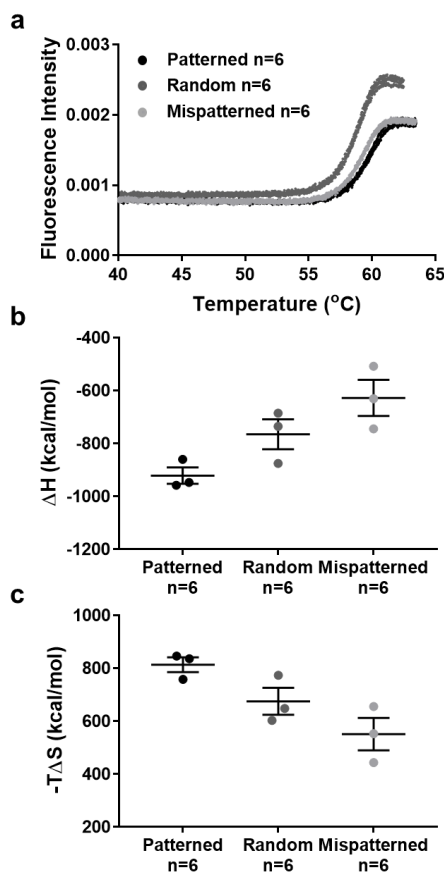


Table A2.2. T_m values for random heteroMV SNAs from van't Hoff melting assay. T_m values (mean \pm SEM) from three individual melting curves (3 separate hybridizations and melts) for $n=1$ -6 SNAs binding to Cy5-labeled targets at a 1:1 ratio ($C_T = [SNA] + [Target]$). Targets were hybridized to SNAs in 1x SSC, 0.2% Tween20 buffer for 1 hour at room temperature. Thermal melting curves were obtained by reading fluorescence increase with a qPCR instrument as Cy5-target dehybridizes from SNA.

Target	C_T (nM)	T_m ($^{\circ}C$)					
		$n=1$	$n=2$	$n=3$	$n=4$	$n=5$	$n=6$
target	3.5	46.89 \pm 0.04	51.47 \pm 0.04	-	-	57.91 \pm 0.02	57.65 \pm 0.02
	5	47.43 \pm 0.00	51.75 \pm 0.05	56.00 \pm 0.04	57.85 \pm 0.03	57.98 \pm 0.03	57.72 \pm 0.02
	7	47.92 \pm 0.08	51.88 \pm 0.01	56.16 \pm 0.02	58.09 \pm 0.04	58.11 \pm 0.03	57.80 \pm 0.02
	10	48.52 \pm 0.04	52.32 \pm 0.03	56.33 \pm 0.02	58.21 \pm 0.03	58.19 \pm 0.05	57.87 \pm 0.05
	15	49.25 \pm 0.06	52.66 \pm 0.04	56.59 \pm 0.05	58.39 \pm 0.03	58.35 \pm 0.02	57.94 \pm 0.04
	22	49.95 \pm 0.06	53.07 \pm 0.03	57.02 \pm 0.03	58.74 \pm 0.07	58.65 \pm 0.02	58.28 \pm 0.02
	30	50.35 \pm 0.07	53.37 \pm 0.03	57.24 \pm 0.01	58.83 \pm 0.02	58.73 \pm 0.07	58.41 \pm 0.03
target- no spacers	3.5	47.38 \pm 0.02	52.03 \pm 0.01	-	-	58.58 \pm 0.03	58.45 \pm 0.01
	5	47.90 \pm 0.02	52.32 \pm 0.06	56.51 \pm 0.05	58.25 \pm 0.02	58.62 \pm 0.02	58.53 \pm 0.00
	7	48.53 \pm 0.02	52.60 \pm 0.03	56.74 \pm 0.03	58.42 \pm 0.03	58.79 \pm 0.02	58.61 \pm 0.02
	10	49.09 \pm 0.03	52.86 \pm 0.05	56.93 \pm 0.04	58.61 \pm 0.07	58.90 \pm 0.04	58.76 \pm 0.03
	15	49.85 \pm 0.01	53.22 \pm 0.02	57.17 \pm 0.03	58.73 \pm 0.04	58.98 \pm 0.01	58.78 \pm 0.06
	22	50.58 \pm 0.03	53.77 \pm 0.04	57.51 \pm 0.03	59.07 \pm 0.03	59.27 \pm 0.04	59.01 \pm 0.10
	30	51.04 \pm 0.09	54.14 \pm 0.02	57.66 \pm 0.05	59.20 \pm 0.01	59.35 \pm 0.08	59.04 \pm 0.03

Table A2.3. Thermodynamic values for random heteroMV SNAs. ΔH , ΔS , and ΔG values (mean \pm SEM) from linear fits of three $\ln(C_T)$ vs. $1/T_m$ curves for $n=1-6$ SNAs binding to Cy5-labeled targets. $\ln(C_T)$ vs. $1/T_m$ curves were obtained from T_m values in **Table A2.2**. ΔG values were calculated using a temperature value of 298 K.

Target	Parameter	$n=1$	$n=2$	$n=3$	$n=4$	$n=5$	$n=6$
target	ΔH (kcal/mol)	-124.64 \pm 1.26	-234.39 \pm 7.28	-304.37 \pm 0.37	-398.16 \pm 13.24	-551.71 \pm 13.95	-621.61 \pm 16.47
	ΔS (kcal/mol*K)	-0.348 \pm 0.004	-0.681 \pm 0.022	-0.884 \pm 0.001	-1.162 \pm 0.040	-1.625 \pm 0.042	-1.838 \pm 0.050
	ΔG (kcal/mol)	-20.91 \pm 0.08	-31.51 \pm 0.63	-40.88 \pm 0.05	-51.86 \pm 1.34	-67.34 \pm 1.34	-73.86 \pm 1.64
target- no spacers	ΔH (kcal/mol)	-118.81 \pm 1.58	-217.90 \pm 1.07	-333.47 \pm 5.94	-412.38 \pm 16.42	-584.19 \pm 24.58	-765.03 \pm 56.78
	ΔS (kcal/mol*K)	-0.329 \pm 0.005	-0.629 \pm 0.003	-0.971 \pm 0.018	-1.204 \pm 0.049	-1.720 \pm 0.074	-2.266 \pm 0.171
	ΔG (kcal/mol)	-20.67 \pm 0.11	-30.50 \pm 0.09	-44.18 \pm 0.56	-53.72 \pm 1.71	-71.64 \pm 2.50	-89.84 \pm 5.70

Table A2.4. Affinity values for random heteroMV SNAs. $\log(K_{eq})$ (mean \pm SEM) from triplicate ΔG values (Table A2.3) and β values ($\beta = K_{eq}^{multi (n>1)}/K_{eq}^{mono (n=1)}$) for $n=1-6$ SNAs binding to Cy5-labeled targets.

Target	Parameter	$n=1$	$n=2$	$n=3$	$n=4$	$n=5$	$n=6$
target	$\log(K_{eq}) (M^{-1})$	15.35 ± 0.06	23.12 ± 0.46	30.00 ± 0.04	38.06 ± 0.98	49.41 ± 0.98	54.20 ± 1.20
	β		6.0×10^7	4.5×10^{14}	5.1×10^{22}	1.2×10^{34}	7.1×10^{38}
target- no spacers	$\log(K_{eq}) (M^{-1})$	15.17 ± 0.08	22.38 ± 0.07	32.42 ± 0.41	39.42 ± 1.25	52.57 ± 1.83	65.92 ± 4.18
	β		1.6×10^7	1.8×10^{17}	1.8×10^{24}	2.5×10^{37}	5.7×10^{50}

Table A2.5. T_m values for random heteroMV SNAs from 5:1 and 10:1 target:SNA ratio van't Hoff melting assays. T_m values (mean \pm SEM) from three individual melting curves (3 separate hybridizations and melts) for $n=1-6$ SNAs binding to the Cy5-labeled target at a 5:1 or 10:1 target:SNA ratio ($C_T = [SNA] + [Target]$). Targets were hybridized to SNAs in 1x SSC, 0.2% Tween20 buffer for 1 hour at room temperature. Thermal melting curves were obtained by reading fluorescence increase with a qPCR instrument as Cy5-target dehybridizes from SNA.

Target:SNA ratio	C_T (nM)	T_m ($^{\circ}$ C)					
		$n=1$	$n=2$	$n=3$	$n=4$	$n=5$	$n=6$
5:1	10.5	47.07 \pm 0.07	51.57 \pm 0.03	56.06 \pm 0.09	57.83 \pm 0.10	57.95 \pm 0.12	57.96 \pm 0.21
	15	47.51 \pm 0.14	51.88 \pm 0.08	56.29 \pm 0.13	58.07 \pm 0.12	58.26 \pm 0.11	58.07 \pm 0.11
	21	48.15 \pm 0.09	52.23 \pm 0.09	56.57 \pm 0.09	58.29 \pm 0.14	58.31 \pm 0.08	58.21 \pm 0.15
	30	48.73 \pm 0.12	52.77 \pm 0.12	56.85 \pm 0.18	58.48 \pm 0.09	58.46 \pm 0.03	58.37 \pm 0.04
	45	49.55 \pm 0.18	53.62 \pm 0.19	57.19 \pm 0.24	58.77 \pm 0.18	58.76 \pm 0.14	58.54 \pm 0.13
	66	50.13 \pm 0.21	54.37 \pm 0.22	57.46 \pm 0.24	59.03 \pm 0.12	58.85 \pm 0.14	58.69 \pm 0.15
	90	50.86 \pm 0.12	55.27 \pm 0.25	57.85 \pm 0.22	59.32 \pm 0.11	59.18 \pm 0.14	59.08 \pm 0.08
10:1	19.25	46.91 \pm 0.08	51.28 \pm 0.06	55.82 \pm 0.09	57.42 \pm 0.11	57.36 \pm 0.06	57.18 \pm 0.09
	27.5	47.45 \pm 0.04	51.60 \pm 0.03	56.00 \pm 0.12	57.64 \pm 0.10	57.68 \pm 0.16	57.42 \pm 0.11
	38.5	48.08 \pm 0.05	52.14 \pm 0.07	56.31 \pm 0.13	57.95 \pm 0.12	57.81 \pm 0.07	57.60 \pm 0.16
	55	48.60 \pm 0.00	52.67 \pm 0.02	56.58 \pm 0.11	57.99 \pm 0.09	58.05 \pm 0.02	57.68 \pm 0.08
	82.5	49.36 \pm 0.05	53.54 \pm 0.05	56.85 \pm 0.16	58.36 \pm 0.11	58.30 \pm 0.16	57.91 \pm 0.19
	121	49.94 \pm 0.04	53.99 \pm 0.03	57.15 \pm 0.20	58.58 \pm 0.19	58.26 \pm 0.09	57.99 \pm 0.15
	165	50.75 \pm 0.04	54.77 \pm 0.13	57.47 \pm 0.08	58.77 \pm 0.05	58.59 \pm 0.12	58.33 \pm 0.09

Table A2.6. Thermodynamic and affinity values for random heteroMV SNAs from 5:1 and 10:1 target:SNA ratio assays. ΔH , ΔS , and ΔG values (mean \pm SEM) from linear fits of three $\ln(C_T)$ vs. $1/T_m$ curves for $n=1-6$ SNAs binding to the Cy5-labeled target at a 5:1 or 10:1 target:SNA ratio. $\ln(C_T)$ vs. $1/T_m$ curves were obtained from T_m values in **Table A2.5**. ΔG values were calculated using a temperature value of 298 K. $\log(K_{eq})$ (mean \pm SEM) from triplicate ΔG values and β values ($\beta = K_{eq}^{\text{multi}(n>1)}/K_{eq}^{\text{mono}(n=1)}$) for $n=1-6$ SNAs binding to the Cy5-labeled target.

Target:SNA ratio	Parameter	$n=1$	$n=2$	$n=3$	$n=4$	$n=5$	$n=6$
5:1	ΔH (kcal/mol)	-113.15 \pm 5.87	-119.47 \pm 12.12	-264.35 \pm 36.02	-315.06 \pm 18.37	-416.53 \pm 44.87	-446.39 \pm 63.49
	ΔS (kcal/mol*K)	-0.314 \pm 0.018	-0.329 \pm 0.037	-0.764 \pm 0.110	-0.913 \pm 0.056	-1.219 \pm 0.136	-1.309 \pm 0.191
	ΔG (kcal/mol)	-19.51 \pm 0.38	-21.41 \pm 0.98	-36.70 \pm 3.37	-43.06 \pm 1.76	-53.37 \pm 4.46	-56.30 \pm 6.53
	$\log(K_{eq})$ (M ⁻¹)	14.31 \pm 0.28	15.71 \pm 0.72	26.93 \pm 2.47	31.59 \pm 1.29	39.16 \pm 3.27	41.31 \pm 4.79
	β		2.49 $\times 10^1$	4.14 $\times 10^{12}$	1.91 $\times 10^{17}$	7.10 $\times 10^{24}$	9.99 $\times 10^{26}$
10:1	ΔH (kcal/mol)	-113.67 \pm 6.54	-124.51 \pm 9.28	-276.25 \pm 21.66	-346.01 \pm 27.07	-412.28 \pm 54.48	-452.66 \pm 70.32
	ΔS (kcal/mol*K)	-0.317 \pm 0.020	-0.346 \pm 0.029	-0.802 \pm 0.066	-1.009 \pm 0.082	-1.209 \pm 0.165	-1.332 \pm 0.213
	ΔG (kcal/mol)	-19.14 \pm 0.47	-21.40 \pm 0.78	-37.29 \pm 2.01	-45.43 \pm 2.63	-51.99 \pm 5.42	-55.66 \pm 6.86
	$\log(K_{eq})$ (M ⁻¹)	14.05 \pm 0.35	15.70 \pm 0.57	27.36 \pm 1.48	33.33 \pm 1.93	38.15 \pm 3.98	40.84 \pm 5.03
	β		4.54 $\times 10^1$	2.06 $\times 10^{13}$	1.94 $\times 10^{19}$	1.26 $\times 10^{24}$	6.24 $\times 10^{26}$

Table A2.7. T_m values for patterned SNAs from van't Hoff melting assay. T_m values (mean \pm SEM) from three individual melting curves (3 separate hybridizations and melts) for $n=6$ patterned and mispatterned SNAs binding to Cy5-labeled targets at 1:1 ratio ($C_T = [\text{SNA}] + [\text{target}]$). Targets were hybridized to SNAs in 1x SSC, 0.2% Tween20 buffer for 1 hour at room temperature. Thermal melting curves were obtained in the same buffer solution by reading fluorescence increase with a qPCR instrument as Cy5-target dehybridizes from SNA.

Target	C_T (nM)	T_m ($^{\circ}\text{C}$)	
		patterned	mispatterned
target- no spacers	3.5	59.50 \pm 0.07	58.89 \pm 0.04
	5	59.38 \pm 0.06	58.94 \pm 0.07
	7	59.59 \pm 0.04	59.04 \pm 0.02
	10	59.52 \pm 0.07	59.11 \pm 0.05
	15	59.65 \pm 0.03	59.22 \pm 0.02
	22	59.89 \pm 0.09	59.55 \pm 0.04
	30	59.94 \pm 0.05	59.63 \pm 0.06
target	3.5	58.92 \pm 0.03	58.67 \pm 0.03
	5	58.88 \pm 0.04	58.66 \pm 0.02
	7	59.01 \pm 0.04	58.85 \pm 0.06
	10	59.01 \pm 0.02	58.88 \pm 0.06
	15	59.08 \pm 0.04	59.03 \pm 0.01
	22	59.38 \pm 0.06	59.38 \pm 0.03
	30	59.64 \pm 0.05	59.63 \pm 0.06

Table A2.8. Thermodynamic and affinity values for patterned SNAs. ΔH , ΔS , ΔG , $\log(K_{eq})$, and β ($K_{eq}^{multi (n>1)}/K_{eq}^{mono (n=1)}$) values (mean \pm SEM) from linear fits of three $\ln(C_T)$ vs. $1/T_m$ curves for $n=6$ patterned and mispatterned SNAs binding to Cy5-labeled targets. $\ln(C_T)$ vs. $1/T_m$ curves were obtained from T_m values in **Table A2.7**. ΔG values were calculated using a temperature value of 298 K.

Target	Parameter	patterned	mispatterned
target- no spacers	ΔH (kcal/mol)	-921.56 \pm 31.10	-627.52 \pm 68.35
	ΔS (kcal/mol*K)	-2.730 \pm 0.094	-1.849 \pm 0.206
	ΔG (kcal/mol)	-107.99 \pm 3.18	-76.54 \pm 7.05
	$\log(K_{eq})$ (M ⁻¹)	79.25 \pm 2.33	56.16 \pm 5.18
	β	1.19 $\times 10^{64}$	9.88 $\times 10^{40}$
target	ΔH (kcal/mol)	-688.07 \pm 34.45	-495.17 \pm 15.78
	ΔS (kcal/mol*K)	-2.031 \pm 0.104	-1.451 \pm 0.048
	ΔG (kcal/mol)	-82.73 \pm 3.56	-62.63 \pm 1.59
	$\log(K_{eq})$ (M ⁻¹)	60.70 \pm 2.61	45.96 \pm 1.17
	β	2.26 $\times 10^{45}$	4.04 $\times 10^{30}$

2.6. References

1. Mammen, M.; Choi, S. K.; Whitesides, G. M., Polyvalent Interactions in Biological Systems: Implications for Design and Use of Multivalent Ligands and Inhibitors. *Angew Chem Int Ed Engl* **1998**, *37* (20), 2754-2794.
2. Bhatia, S.; Dimde, M.; Haag, R., Multivalent glycoconjugates as vaccines and potential drug candidates. *Med. Chem. Commun.* **2014**, *5* (7), 862-878.
3. Xu, Z.; Jia, S.; Wang, W.; Yuan, Z.; Jan Ravoo, B.; Guo, D. S., Heteromultivalent peptide recognition by co-assembly of cyclodextrin and calixarene amphiphiles enables inhibition of amyloid fibrillation. *Nat Chem* **2019**, *11* (1), 86-93.
4. Kwon, P. S.; Ren, S.; Kwon, S. J.; Kizer, M. E.; Kuo, L.; Xie, M.; Zhu, D.; Zhou, F.; Zhang, F.; Kim, D.; Fraser, K.; Kramer, L. D.; Seeman, N. C.; Dordick, J. S.; Linhardt, R. J.; Chao, J.; Wang, X., Designer DNA architecture offers precise and multivalent spatial pattern-recognition for viral sensing and inhibition. *Nat Chem* **2020**, *12* (1), 26-35.
5. Magdalena Estirado, E.; Aleman Garcia, M. A.; Schill, J.; Brunsveld, L., Multivalent Ultrasensitive Interfacing of Supramolecular 1D Nanoplatfoms. *J Am Chem Soc* **2019**, *141* (45), 18030-18037.
6. Lee, J. S.; Seferos, D. S.; Giljohann, D. A.; Mirkin, C. A., Thermodynamically controlled separation of polyvalent 2-nm gold nanoparticle-oligonucleotide conjugates. *J Am Chem Soc* **2008**, *130* (16), 5430-1.
7. Liu, B.; Huang, Z.; Liu, J., Polyvalent Spherical Nucleic Acids for Universal Display of Functional DNA with Ultrahigh Stability. *Angew Chem Int Ed Engl* **2018**, *57* (30), 9439-9442.
8. Yehl, K.; Mugler, A.; Vivek, S.; Liu, Y.; Zhang, Y.; Fan, M.; Weeks, E. R.; Salaita, K., High-speed DNA-based rolling motors powered by RNase H. *Nat Nanotechnol* **2016**, *11* (2), 184-90.
9. Blanchard, A. T.; Bazrafshan, A. S.; Yi, J.; Eisman, J. T.; Yehl, K. M.; Bian, T.; Mugler, A.; Salaita, K., Highly Polyvalent DNA Motors Generate 100+ pN of Force via Autochemophoresis. *Nano Lett* **2019**, *19* (10), 6977-6986.
10. Bazrafshan, A.; Meyer, T. A.; Su, H.; Brockman, J. M.; Blanchard, A. T.; Piranej, S.; Duan, Y.; Ke, Y.; Salaita, K., Tunable DNA Origami Motors Translocate Ballistically Over μm Distances at nm/s Speeds. *Angew Chem Int Ed Engl* **2020**.
11. Ke, Y.; Ong, L. L.; Shih, W. M.; Yin, P., Three-dimensional structures self-assembled from DNA bricks. *Science* **2012**, *338* (6111), 1177-83.
12. Mirkin, C. A.; Letsinger, R. L.; Mucic, R. C.; Storhoff, J. J., A DNA-based method for rationally assembling nanoparticles into macroscopic materials. *Nature* **1996**, *382* (6592), 607-9.
13. Cutler, J. I.; Auyeung, E.; Mirkin, C. A., Spherical nucleic acids. *J Am Chem Soc* **2012**, *134* (3), 1376-91.
14. Lytton-Jean, A. K. R.; Mirkin, C. A., A Thermodynamic Investigation into the Binding Properties of DNA Functionalized Gold Nanoparticle Probes and Molecular Fluorophore Probes. *J Am Chem Soc* **2005**, *127*, 12754-12755.
15. Randeria, P. S.; Jones, M. R.; Kohlstedt, K. L.; Banga, R. J.; Olvera de la Cruz, M.; Schatz, G. C.; Mirkin, C. A., What controls the hybridization thermodynamics of spherical nucleic acids? *J Am Chem Soc* **2015**, *137* (10), 3486-9.
16. Fong, L. K.; Wang, Z.; Schatz, G. C.; Luijten, E.; Mirkin, C. A., The Role of Structural Enthalpy in Spherical Nucleic Acid Hybridization. *J Am Chem Soc* **2018**, *140* (20), 6226-6230.

17. Giljohann, D. A.; Seferos, D. S.; Prigodich, A. E.; Patel, P. C.; Mirkin, C. A., Gene Regulation with Polyvalent siRNA–Nanoparticle Conjugates. *J Am Chem Soc* **2009**, *131*, 2072-2073.
18. Alhasan, A. H.; Kim, D. Y.; Daniel, W. L.; Watson, E.; Meeks, J. J.; Thaxton, C. S.; Mirkin, C. A., Scanometric microRNA array profiling of prostate cancer markers using spherical nucleic acid-gold nanoparticle conjugates. *Anal Chem* **2012**, *84* (9), 4153-60.
19. Seferos, D. S.; Giljohann, D. A.; Hill, H. D.; Prigodich, A. E.; Mirkin, C. A., Nano-flares: probes for transfection and mRNA detection in living cells. *J Am Chem Soc* **2007**, *129* (50), 15477-9.
20. Rosi, N. L.; Giljohann, D. A.; Thaxton, C. S.; Lytton-Jean, A. K.; Han, M. S.; Mirkin, C. A., Oligonucleotide-modified gold nanoparticles for intracellular gene regulation. *Science* **2006**, *312* (5776), 1027-30.
21. Kane, R. S., Thermodynamics of multivalent interactions: influence of the linker. *Langmuir* **2010**, *26* (11), 8636-40.
22. Liu, Y.; Yehl, K.; Narui, Y.; Salaita, K., Tension sensing nanoparticles for mechano-imaging at the living/nonliving interface. *J Am Chem Soc* **2013**, *135* (14), 5320-3.
23. Vologodskii, A.; Frank-Kamenetskii, M. D., Strong bending of the DNA double helix. *Nucleic Acids Res* **2013**, *41* (14), 6785-92.
24. Veneziano, R.; Ratanalert, S.; Zhang, K.; Zhang, F.; Yan, H.; Chiu, W.; Bathe, M., Designer nanoscale DNA assemblies programmed from the top down. *Science* **2016**, *352* (6293), 1534.
25. Demers, L. M.; Ginger, D. S.; Park, S. J.; Li, Z.; Chung, S. W.; Mirkin, C. A., Direct patterning of modified oligonucleotides on metals and insulators by dip-pen nanolithography. *Science* **2002**, *296* (5574), 1836-8.
26. Rothmund, P. W., Folding DNA to create nanoscale shapes and patterns. *Nature* **2006**, *440* (7082), 297-302.
27. Jun, H.; Zhang, F.; Shepherd, T.; Ratanalert, S.; Qi, X.; Yan, H.; Bathe, M., Autonomously designed free-form 2D DNA origami. *Sci Adv* **2019**, *5* (1), eaav0655.
28. Rinker, S.; Ke, Y.; Liu, Y.; Chhabra, R.; Yan, H., Self-assembled DNA nanostructures for distance-dependent multivalent ligand-protein binding. *Nat Nanotechnol* **2008**, *3* (7), 418-22.
29. Han, X.; Jiang, Y.; Li, S.; Zhang, Y.; Ma, X.; Wu, Z.; Wu, Z.; Qi, X., Multivalent aptamer-modified tetrahedral DNA nanocage demonstrates high selectivity and safety for anti-tumor therapy. *Nanoscale* **2018**, *11* (1), 339-347.
30. Praetorius, F.; Kick, B.; Behler, K. L.; Honemann, M. N.; Weuster-Botz, D.; Dietz, H., Biotechnological mass production of DNA origami. *Nature* **2017**, *552* (7683), 84-87.
31. Suzuki, K.; Hosokawa, K.; Maeda, M., Controlling the number and positions of oligonucleotides on gold nanoparticle surfaces. *J Am Chem Soc* **2009**, *131* (22), 7518-9.
32. Edwardson, T. G.; Lau, K. L.; Bousmail, D.; Serpell, C. J.; Sleiman, H. F., Transfer of molecular recognition information from DNA nanostructures to gold nanoparticles. *Nat Chem* **2016**, *8* (2), 162-70.
33. Xie, N.; Liu, S.; Fang, H.; Yang, Y.; Quan, K.; Li, J.; Yang, X.; Wang, K.; Huang, J., Three-Dimensional Molecular Transfer from DNA Nanocages to Inner Gold Nanoparticle Surfaces. *ACS Nano* **2019**, *13* (4), 4174-4182.
34. Wu, X. A.; Choi, C. H.; Zhang, C.; Hao, L.; Mirkin, C. A., Intracellular fate of spherical nucleic acid nanoparticle conjugates. *J Am Chem Soc* **2014**, *136* (21), 7726-33.

35. Bhatt, N.; Huang, P. J.; Dave, N.; Liu, J., Dissociation and degradation of thiol-modified DNA on gold nanoparticles in aqueous and organic solvents. *Langmuir* **2011**, *27* (10), 6132-7.
36. Dougan, J. A.; Karlsson, C.; Smith, W. E.; Graham, D., Enhanced oligonucleotide-nanoparticle conjugate stability using thioctic acid modified oligonucleotides. *Nucleic Acids Res* **2007**, *35* (11), 3668-75.
37. Lobo Maza, F.; Grumelli, D.; Carro, P.; Vericat, C.; Kern, K.; Salvarezza, R. C., The role of the crystalline face in the ordering of 6-mercaptopurine self-assembled monolayers on gold. *Nanoscale* **2016**, *8* (39), 17231-17240.
38. Hill, H. D.; Mirkin, C. A., The bio-barcode assay for the detection of protein and nucleic acid targets using DTT-induced ligand exchange. *Nat Protoc* **2006**, *1* (1), 324-36.
39. Liu, B.; Liu, J., Freezing Directed Construction of Bio/Nano Interfaces: Reagentless Conjugation, Denser Spherical Nucleic Acids, and Better Nanoflares. *J Am Chem Soc* **2017**, *139* (28), 9471-9474.
40. Murphy, M. C.; Rasnik, I.; Cheng, W.; Lohman, T. M.; Ha, T., Probing single-stranded DNA conformational flexibility using fluorescence spectroscopy. *Biophys J* **2004**, *86* (4), 2530-7.

Chapter 3

Heteromultivalency Enables Optimization of the Specificity and Cooperativity of DNA Hybridization

3.1. Introduction

Specific hybridization between complementary nucleic acids enables many sensing and diagnostic methods.¹⁻⁴ For example, PCR assays rely on specific hybridization between primers and templates. However, there is often a fundamental trade-off between maximizing specificity and sensitivity.⁵ High binding affinity results in improved sensitivity, allowing the detection of lower concentration oligonucleotides, but also leads to enhanced off-target binding and decreased discrimination between similar targets. Conversely, lowering target affinity can enhance specificity but lowers the sensitivity of an assay. Thus, there is an affinity “sweet spot” that maximizes the ratio between on- and off-target binding.⁶ Unfortunately, this optimized affinity is difficult to achieve, often resulting in poor discrimination for targets containing mismatches, such as single nucleotide polymorphisms (SNPs).^{5, 7-8} SNPs are implicated in genetic disorders and cancer, and thus rapid and simple detection is highly desirable. Tuning the affinity to maximize specificity can be achieved by changing the probe length. However, the problem with this strategy is that adding or removing a single base pair drastically changes affinity, resulting in low-precision affinity tuning.^{6, 9} Adjusting hybridization conditions such as temperature or ionic strength can also optimize affinity for detecting targets with a single SNP, but this approach fails when detecting multiple mutations simultaneously in a multiplexed or microarray-type assay.¹⁰ Therefore, a fundamental problem in the field pertains to developing facile strategies to fine tune target affinity to optimize specificity of binding.

To overcome this challenge, we tested the hypothesis that multivalent binding can be used to optimize the specificity of hybridization and hence boost the performance of nucleic acid sensing assays. In such assays, target binding often occurs on DNA-functionalized surfaces or particles to allow a more rapid and simple readout.¹¹⁻¹⁴ These structures, which we refer to as

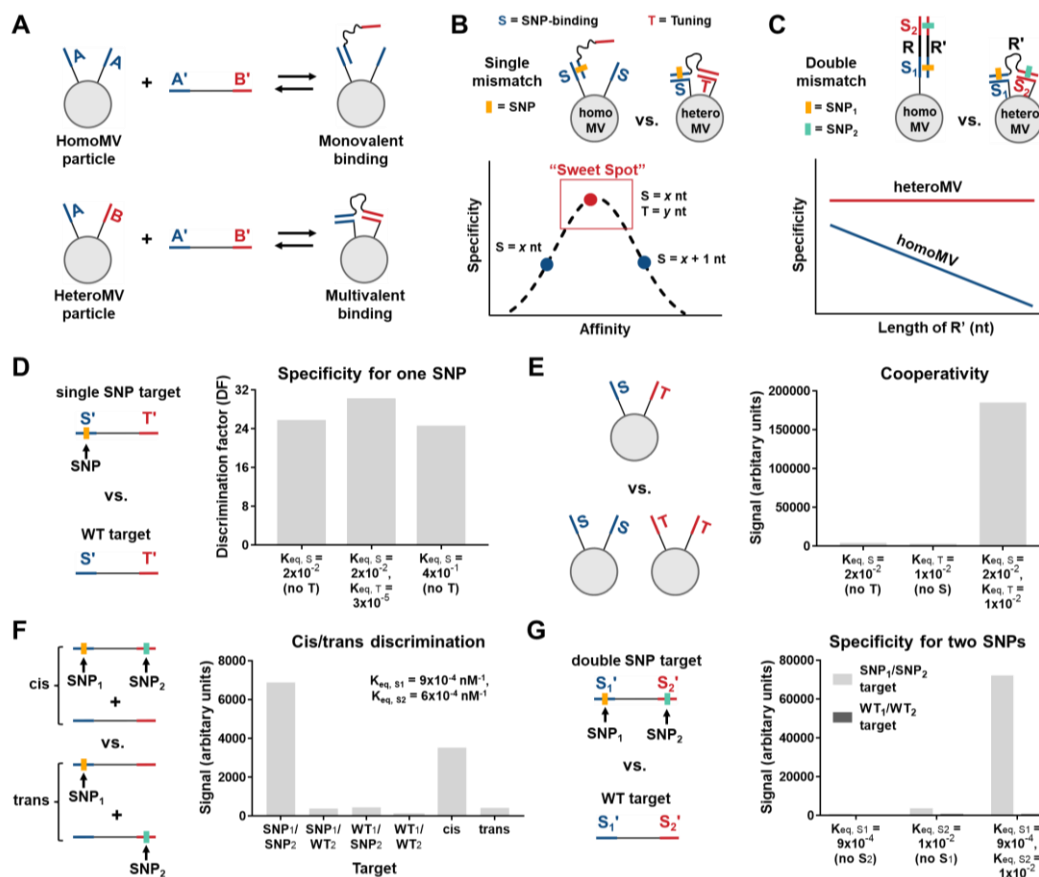


Figure 3.1. Hypothesized advantages of heteromultivalent DNA hybridization and modeling key applications. (a) General illustration of a homoMV DNA-coated structure containing only one unique oligonucleotide sequence (A) and a heteroMV DNA-coated structure containing two unique oligonucleotide sequences (A and B). (b) Scheme illustrating the difficulty in tuning binding affinity by adding an additional base pair to a homoMV binding interaction and the hypothesized ability of a heteroMV structure to more precisely tune the binding affinity of hybridization to achieve maximum specificity. (c) Scheme illustrating the effect of distance between two SNPs on homoMV and heteroMV hybridization specificity. (d-g) Schemes and modeling predictions describing the specificity for one SNP (d), cooperativity (e), cis/trans discrimination (f), and specificity for two SNPs (g) of heteroMV particles presenting two oligos with K_{eq} (M^{-1}) values that are optimal for each application.

homomultivalent (homoMV) DNA-coated structures (**Figure 3.1A, top**), typically hybridize “monovalently”, forming a single duplex with each target. There are a few examples of homoMV structures binding targets multivalently, however this approach is only applicable for repetitive targets.¹⁵⁻¹⁶ We recently demonstrated that heteromultivalent (heteroMV) structures presenting multiple distinct oligonucleotide sequences (**Figure 3.1A, bottom**) can bind multivalently to non-

repetitive targets with high avidity.¹⁷ Motivated by this work, we investigated if presenting a tuning oligo (T) alongside a SNP-binding oligo (S) can precisely tune target binding affinity and achieve high specificity for a single mismatch without relying on buffer optimization (**Figure 3.1B**).

Specificity is also important in applications that require detecting multiple mutations in a single target. For example, haplotype phasing analyses involve distinguishing “cis” and “trans” mutations located on the same or different chromosomal copy.¹⁸⁻¹⁹ Identifying the strain of a rapidly evolving virus also requires specificity for the unique mutations present. However, detecting two mutations on a target is difficult to achieve, as monovalent binding probes bind either both sites and the region in between (R) with low specificity (**Figure 3.1C**), or bind each mutation separately with no cooperativity. To address this challenge, we engineered heteroMV binding to hybridize cooperatively to two mutations with a non-complementary spacer in between (**Figure 3.1C**). With this approach, overall affinity for a desired target is enhanced while maintaining low affinity for single mutant or wildtype targets, similar to “AND” logic gates and proximity assays.²⁰⁻²² Moreover, due to the additive effect of each mismatch, we hypothesized that specificity significantly increases two mutations are targeted through heteromultivalent binding.

In this work, we studied heteroMV DNA-coated silica microparticles presenting two unique oligo sequences ($n=2$) of different length that bind to single stranded targets containing a complementary region to each oligo. The two oligos bind single or double mutant targets in several different orientations while the complementary target regions are directly adjacent or separated by a spacer. Through mathematical modeling and a flow cytometry-based assay that allows rapid measurement of target binding to each microparticle, we reveal that heteroMV binding boosts discrimination for a SNP by a factor of up to 10 over monovalent binding when the length of T < S. Moreover, we demonstrate that cooperativity is maximized when the T and S oligos are tuned

such that they bind with similar, yet weak affinities. This high cooperativity persists when binding to two sites of a target separated by an up to 15 nucleotides (nt) long spacer region and can be further improved by modifying the binding orientation of the two oligos. Through precise tuning of both specificity and cooperativity we display the ability to easily distinguish model heterozygous cis and trans mutations. Finally, we apply heteroMV hybridization towards discriminating model SARS-CoV-2 targets corresponding to the original, alpha, or omicron strains and observe ~800-fold binding enhancements for the omicron target. Overall, heteroMV binding greatly expands the potential of DNA hybridization-based assays and DNA nanotechnology by offering highly tunable specificity and cooperativity.

3.2. Results

3.2.1. Modeling the Specificity and Cooperativity of HeteroMV Hybridization

To predict the impact of heteroMV binding on hybridization specificity and cooperativity, we focused on a particle modified with 50% S and 50% T oligos. Binding of the target to the particle was modeled as a two-step reversible reaction where S and T bind their complements with binding constants $K_{eq, S}$ and $K_{eq, T}$, respectively. The particle-target complex can form three distinct binding states where only S binds, only T binds, or where both segments bind (**Figure A3.2**). The equilibrium constant for the target bound to both segments can be described as:

$$K_{eq} = K_{eq, S} * K_{eq, T} * c_{eff} \quad (1)$$

where c_{eff} is the effective concentration of the unbound second oligo within the volume accessible to the target after binding the first oligo. Thus, the total affinity of all three states for the particle binding a complementary SNP-containing target is:

$$K_{eq, S + T, SNP} = K_{eq, S} + K_{eq, T} + K_{eq, S} * K_{eq, T} * C_{eff} \quad (2)$$

To incorporate specificity into the model, we also derived a binding constant for a wildtype target (WT) containing a mismatch in S' (**Figure 3.1D**). To account for the decreased affinity of the mismatched S oligo-WT target duplex, a mismatch factor (MM) is multiplied to each $K_{eq, S}$ term. Alternatively, the T oligo is non-complementary to the SNP, and thus MM is not applied to the $K_{eq, T}$ terms. Therefore, the total binding affinity for the particle binding the WT target is:

$$K_{eq, S + T, WT} = MM * K_{eq, S} + K_{eq, T} + MM * K_{eq, S} * K_{eq, T} * C_{eff} \quad (3)$$

We next derived an equation to calculate the equilibrium binding occupancy, θ , of the particle-functionalized oligos and converted θ to an arbitrary assay signal, I , using inputted maximum and background assay signals (**see 3.4.5. Modeling**). By calculating I when the particles bound the SNP target or the WT target, the discrimination factor (DF) was calculated using the equation:

$$DF = I_{SNP} / I_{WT} \quad (4)$$

Moreover, by calculating I when a particle with only the S oligo, only the T oligo, or both oligos bound the SNP target (**Figure 3.1E**), the cooperativity factor (CF) was calculated using the equation:

$$CF = 2 * I_{S+T} / (I_S + I_T) \quad (5)$$

To predict the impact of $K_{eq, S}$ and $K_{eq, T}$ on DF and CF, a series of affinities for each oligo were chosen with values spanning many orders of magnitude. The incremental change in affinity between each binding constant roughly approximated the impact of adding one additional base pair to a DNA duplex. Mock values of I , DF, and CF were then generated for each combination of $K_{eq, S}$ and $K_{eq, T}$ (**Figure A3.2**). As described previously for monovalent hybridization,⁶ the relationship between DF and K_{eq} follows a Gaussian distribution, where a specific K_{eq} value ($K_{eq, optimal}$) maximizes DF (DF_{max}) and any K_{eq} value less than or greater than $K_{eq, optimal}$ results in a

diminished DF (**Figure A3.1**). For example, our modeling predicts that for an S only particle, increasing $K_{eq, S}$ from 20 to 400 pM^{-1} (representing the addition of one base pair to the duplex) overshoots $K_{eq, optimal}$ and thus DF_{max} is not achieved. However, adding a T oligo with $K_{eq, T} = 0.03 \text{ pM}^{-1}$ instead precisely increases the total affinity from 20 to 40 pM^{-1} and yields a DF greater than that of any of the $n=1$ particles in the series (**Figure 3.1D**). Note that the model predicts that the T oligo will not enhance DF_{max} and also that if $K_{eq, T}$ is too large (regardless of $K_{eq, S}$), then DF_{max} will decrease (**Figure A3.2**). The second major prediction from the modeling is that CF will be greatest when $K_{eq, S} \approx K_{eq, T}$. Specifically, when $K_{eq, S} = 20 \text{ pM}^{-1}$ and $K_{eq, T} = 10 \text{ pM}^{-1}$ the model predicts that the $n=2$ particle will bind $\sim 50x$ more targets than the average of the two corresponding $n=1$ particles (**Figure 3.1E**).

We next sought to predict whether heteroMV DNA-coated structures can be used to determine if two mutations are located on the same or different chromosome copies. Of the 10 unique combinations of two mutations on two chromosome copies (see **3.4.5. Modeling**), heterozygous cis trans mutations are the most difficult to distinguish (**Figure 3.1F**).²³⁻²⁴ To predict the ability to differentiate two cis or trans mutations, the model was modified so that both oligos are complementary to a SNP by applying a MM factor to $K_{eq, S1}$ and $K_{eq, S2}$ when binding a target lacking the corresponding SNPs. This modification then yields equations for total affinity to the SNP_1/SNP_2 , SNP_1/WT_2 , WT_1/SNP_2 , and WT_1/WT_2 targets (see **3.4.5. Modeling**). Equal mixtures of SNP_1/SNP_2 and WT_1/WT_2 targets or SNP_1/WT_2 and WT_1/SNP_2 targets were used to represent heterozygous cis or trans mutations, respectively. Cis/trans DF values were then calculated using the equation:

$$DF_{cis/trans} = I_{cis} / I_{trans} \quad (6)$$

Using the same individual oligo binding affinities as used in **Fig. 3.1D and 3.1E**, the $DF_{\text{cis/trans}}$ values were generated for each combination of $K_{\text{eq}, S1}$ and $K_{\text{eq}, S2}$ (**Figure A3.3**). These modeling calculations predicted that two oligos with roughly equal binding affinities, slightly weaker than those predicted to give the best CF, will result in the highest $DF_{\text{cis/trans}}$ (**Figure 3.1F**). Alternatively, to maximize $DF_{\text{SNP1+SNP2}}$ ($I_{\text{SNP1/SNP2}} / I_{\text{WT1/WT2}}$) to ~ 300 , our calculations suggest that a total affinity between the affinities that yielded the best CF and $DF_{\text{cis/trans}}$ values is optimal (**Figure 3.1G and A3.3**). Note that $DF_{\text{SNP1+SNP2}}$ is significantly enhanced due to both binding interactions being impacted by the presence of SNPs. Overall, the mathematical model predicts that a T oligo with lower affinity than the S oligo will give the highest specificity for a single mismatch, a T oligo with similar affinity to the S oligo will maximize cooperativity, and two S oligos with equal but weak affinity will offer the highest cis/trans discrimination or specificity for targets containing two mutations.

3.2.2. Measuring the Specificity and Cooperativity of HeteroMV Hybridization

To test the modeling predictions, we designed five S oligos (7-11 nt long, 7S-11S) and seven T oligos (4-10 nt long, 4T-10T) complementary to a 25 nt region of the KRAS genetic sequence that contains the G12C mutation (**Figure 3.2A and Figure A3.4**). We focused on this target because KRAS is an important oncogene and a driver of lung, pancreatic, and colorectal cancers when mutated.²⁵ The G12C target containing the mutation was designed to be perfectly complementary to both the S and T oligos, whereas the WT target lacking the mutation binds the S oligos with a single base mismatch and the T oligos with no mismatches. Both targets were modified at their 3' termini with an Atto647N fluorophore using NHS chemistry (**Figure A3.5 and Figure A3.6**). Each of the S and T oligos contained a T10 polynucleotide linker and a 5' thiol

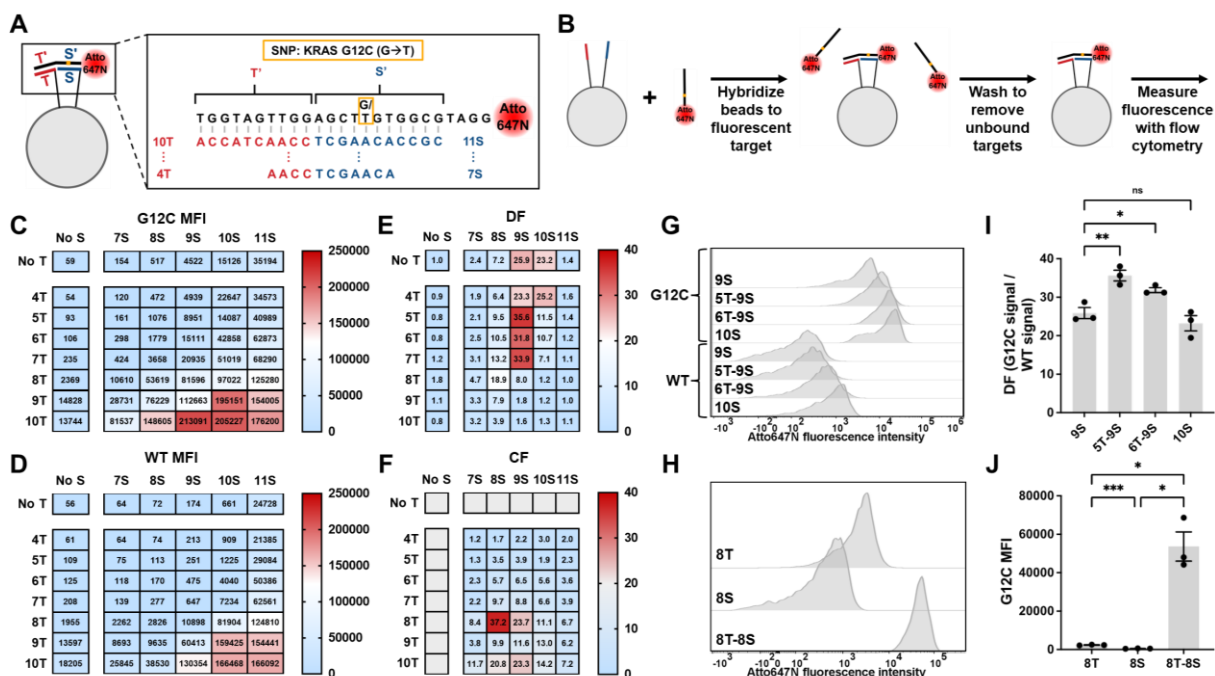


Figure 3.2. Measuring the specificity and cooperativity of heteroMV hybridization using flow cytometry. (a) Design of the oligonucleotides included in the screen to maximize discrimination factor and best cooperativity factor. Yellow box indicates the position of the SNP in the target sequence. (b) Scheme describing the flow cytometry-based assay used to quantify target binding to 5 μ m DNA-coated silica particles. (c and d) Heatmaps showing the median fluorescence intensity of each bead included in the screen when incubated with the G12C target (c) and the WT target (d). (e and f) Heatmaps showing the discrimination factor (e) and cooperativity factor (f) of each bead included in the screen. The cooperativity factor is shown for beads incubated with the G12C target. (g) Representative histograms for 9S, 5T-9S, 6T-9S, and 10S beads binding the G12C and WT targets. (h) Representative histograms for 8T, 8S, and 8T-8S beads binding the G12C target. (i) Measured discrimination factors for 9S, 5T-9S, 6T-9S, and 10S beads. (j) Measured median fluorescence intensity values for 8T, 8S, and 8T-8S beads binding the G12C target. Error bars represent standard error of the mean. Values were compared using paired one-way ANOVA with multiple comparisons follow-up tests ($^{ns}P > 0.05$, $^*P < 0.05$, $^{**}P < 0.01$, $^{***}P < 0.001$).

group to enable conjugation to silica beads using a heterobifunctional linker named SMCC (**Figure A3.7**). Beads were modified with each possible combination of the S and T oligos, giving a total library of 48 different DNA-coated silica beads. The density of the oligos on the beads were measured by first dissolving the beads in 0.1 M KOH as demonstrated previously²⁶ and then using Oligreen reagent to quantify the amount of DNA in solution. These measurements revealed that

the average distance between each oligo on the bead surface was ~5 nm, allowing S and T oligos to bind multivalently to the same target (**Figure A3.8**).

To measure relative binding of the two targets to each of the 48 beads, a flow cytometry-based assay was designed. In this assay, the DNA-coated beads were incubated with 1 nM of target in 1x SSC, 0.1% Tween20 buffer, after which unbound targets were removed through centrifugation and the fluorescence intensity of each individual bead was measured using a flow cytometer (**Figure 3.2B and Figure A3.9**). Median fluorescence intensities (MFI) were measured for each of the 48 beads when they bound the G12C target and the WT target. As expected, MFIs generally increased when the S and/or the T oligo increased in length, confirming that increasing binding affinity results in higher surface occupancy, (θ) (**Figure 3.2C, 3.2D, and A3.10**). To quantify specificity, DF values were calculated for each bead mixture by dividing the G12C and WT MFIs (**Figure 3.2E**). Similar to the modeling predictions, the beads presenting the 9S oligo alongside the 5T, 6T, or 7T oligo had the highest DFs. Specifically, the 5T-9S beads yielded 37% higher specificity compared to the 9S beads (**Figure 3.2I**), which had the highest DF of the homoMV beads tested. Importantly, this enhancement was enabled by precise fine-tuning of K_{eq} as the 5T-9S and 6T-9S beads yielded MFIs between that of the 9S and 10S beads (**Figure 3.2G**). In further agreement with the modeling, the screen showed that the 8T-8S beads bound most cooperatively to the G12C target, with almost 40x greater target binding than the average of the 8T and 8S $n=1$ beads (**Figure 3.2F, 3.2H, and 3.2J**). Fluorescence microscopy was also used to image targets hybridized to the beads and confirmed homogeneous binding across the bead surface (**Figure A3.11**).

3.2.3. Determining the Impact of Spacer Length on HeteroMV Hybridization Specificity and Cooperativity

Next, to assess the ability of heteroMV beads to bind with high cooperativity to two non-adjacent regions of a target, several spacer-containing targets were designed and tested. Previously, the impact of long, flexible spacers/linkers on multivalent binding avidity has been a controversial topic. Some studies reported that flexibility leads to poor cooperativity due to loss of conformational entropy upon binding,²⁷ while others noted minimal impacts of spacer length on avidity and cooperativity.^{15, 28} Hence these experiments were designed to test whether hybridization cooperativity and specificity are maintained when the spacer length increases. We therefore introduced a tri-ethylene glycol (short) or a hexa-ethylene glycol (long) modification between the T' and S' binding regions (internal) or, as a negative control, at the 5' terminus of the target (terminal) (**Figure 3.3A**). Thus, a total of 10 targets were tested with the 8T-8S beads using the flow cytometry-based assay.

The results showed that as internal spacer length increased, more G12C targets bound the beads (**Figure 3.3B**). Inserting a short spacer also enhanced binding to the WT target though the long spacer did not lead to a further increase in binding (**Figure 3.3C and Figure A3.12**). As expected, the terminal spacers did not impact binding to the G12C or WT targets, confirming that the poly-ethylene glycol (PEG) polymer does not chemically influence target binding. The CF of the 8T-8S beads for the G12C targets with different spacer lengths was also calculated by dividing the 8T-8S beads' MFI by the average of the 8T and 8S beads' MFIs when binding the no spacer target. These calculations revealed significant increases in cooperativity as a function of increasing spacer length (**Figure 3.3D**). The impact of spacer length on specificity was also assessed by

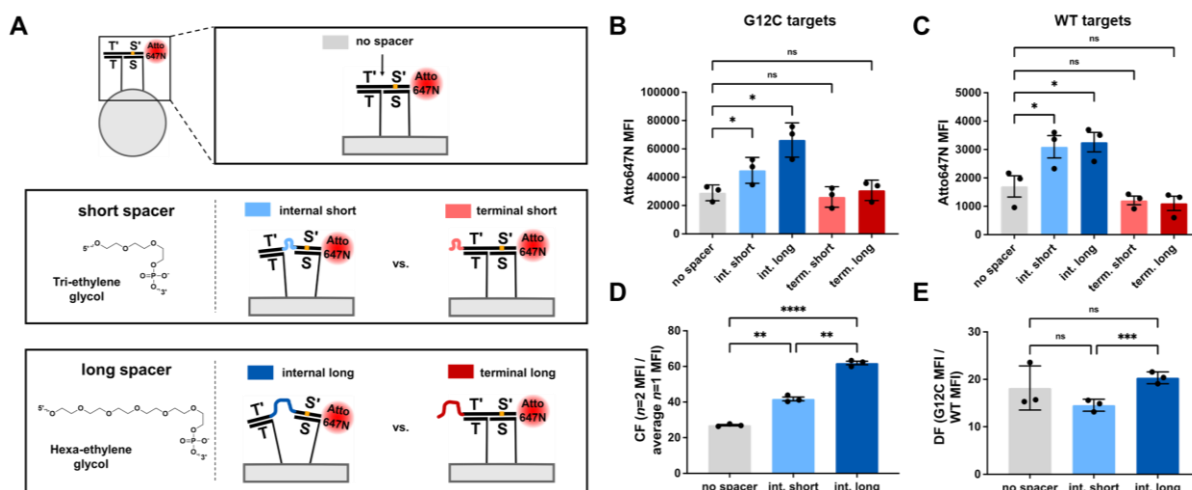


Figure 3.3. Determining the impact of spacer length on heteroMV hybridization. (a) Scheme describing the design of the no spacer target, the internal and terminal short spacer targets, and the internal and terminal long spacer targets including the chemical structures of the PEG spacer molecules. (b and c) Measured median fluorescence intensity values for 8T-8S beads binding the G12C (b) and the WT (c) no spacer, internal short spacer, internal long spacer, terminal short spacer, and terminal long spacer targets. (d and e) Measured cooperativity factors (d) and discrimination factors (e) for the 8T-8S beads binding the G12C target containing no spacer, the internal short spacer, or the internal long spacer. Error bars represent standard error of the mean. Values were compared using paired one-way ANOVA with multiple comparisons follow-up tests (^{ns}P > 0.05, *P < 0.05, **P < 0.01, ***P < 0.001, ****P < 0.0001).

calculating the DF of the 8T-8S beads for each target. Interestingly, the internal spacers did not lead to a strong effect on specificity, though there was a significant difference in DF between the short and long spacer targets (**Figure 3.3E**). Surprisingly, 8T and 8S only beads also showed increased binding to the internal spacer-containing targets, potentially due to weak binding between S' and T as well as T' and S (**Figure A3.12**). Overall, the investigations into the effect of target spacer length revealed that heteroMV hybridization allows binding to two spacer-separated regions of a target with increased cooperativity and no loss in specificity compared to a target with no spacer. These results will provide guidance in potential designs of proximity or “AND” logic gate style-assays as well as in diagnostic assays when it is desirable for the tuning oligo to bind a domain (T') that is not proximal to the SNP site.

3.2.4. Determining the Impact of Binding Orientation on HeteroMV Hybridization Specificity and Cooperativity

Due to the antiparallel nature of DNA hybridization, the choice of terminus (5' or 3') for the anchoring group of the S and T oligos impacts the direction that the oligo binds the target. Therefore, based on the terminus used for each anchor, the two oligos can bind the target in a head-to-tail, head-to-head, or tail-to-tail orientation (**Figure 3.4A**). In this case, head corresponds to the end of the oligo not attached to the particle and tail corresponds to the linker connecting the oligo to the particle. To understand how binding orientation can potentially impact the properties of the binding interaction, 8T-8S beads that bind in the three different orientations were compared. Moreover, to investigate how each orientation is influenced by spacer length, the no spacer, short spacer, and long spacer targets were tested with each binding orientation.

Using the flow cytometry-based binding assay, the MFI of the head-to-tail, head-to-head, and tail-to-tail binding 8T-8S beads was measured for each target (**Figure 3.4B and 3.4C**). When binding the G12C no spacer target, significant differences were observed between the three binding orientations. Specifically, the head-to-head binding orientation yielded the highest binding, while the tail-to-tail orientation resulted in a >3-fold reduction in binding compared to the head-to-tail orientation. However, when binding the short or long spacer G12C targets, the tail-to-tail orientation yielded binding approximately equal to the head-to-tail orientation, while the head-to-head orientation still offered slight improvements in total binding. Relatedly, the head-to-head orientation beads had a significant >2-fold increase in CF relative to the head-to-tail orientation beads and a >6-fold increase relative to the tail-to-tail orientation beads when binding the no spacer G12C target (**Figure 3.4D and 3.4E**). Interestingly, the higher average CF for the head-to-head orientation was maintained for the spacer-containing targets, though the enhancement was not

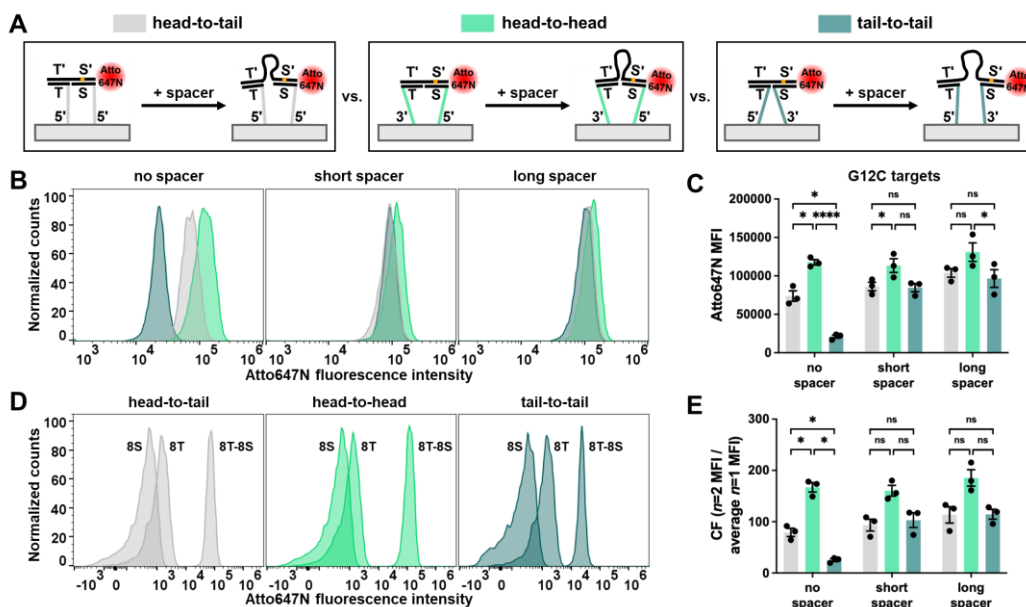


Figure 3.4. Determining the impact of binding orientation on heteroMV hybridization specificity and cooperativity. (a) Scheme describing $n=2$ beads with head-to-tail, head-to-head, or tail-to-tail orientation binding to targets with or without a spacer region. (b) Representative histograms for 8T-8S beads with each orientation binding the G12C no spacer, short spacer, and long spacer targets. (c) Measured median fluorescence intensity values for 8T-8S beads with each orientation binding the G12C target with no spacer, short spacer, and long spacer targets. (d) Representative histograms for 8T, 8S, and 8T-8S beads with each orientation binding the G12C no spacer target. (e) Measured cooperativity factors for 8T-8S beads with each orientation binding the G12C no spacer, short spacer, and long spacer targets. Error bars represent standard error of the mean. Values were compared using paired one-way ANOVA with multiple comparisons follow-up tests ($^{ns}P > 0.05$, $^{*}P < 0.05$, $^{****}P < 0.0001$).

significant. The results for the WT target echoed those of the G12C target, and as expected, the oligo's anchoring terminus did not have a significant effect on $n=1$ beads binding the G12C no spacer target (**Figure A3.13**). Overall, these results validate the importance of binding orientation in tuning binding affinity and cooperativity.

Together, these results can be explained by considering the effects of both the spacing between segments on the bead surface and the base stacking interactions at the interface of the T-T' and S-S' duplexes. Based on the distance between the T and S oligos on the surface, different binding orientations can minimize energetic strain during binding depending on linker length and

duplex length. For example, if T and S are far apart, then binding the no spacer target in the tail-to-tail orientation might result in significant strain on the T10 linkers. Moreover, prior studies showed that base stacking at a nick site results in strong enthalpic contributions to overall binding stability.²⁹⁻³² This is consistent with the head-to-head orientation yielding the most avid binding as it binds with only a nick between the two duplexes. In contrast, in the other orientations, the T10 linkers likely interfere with this base-stacking interaction and hence reduce binding affinity and cooperativity.

3.2.5. Detecting the Cis/Trans Relationship of Two Mutations Using HeteroMV Hybridization

We next tested the modeling prediction that heteroMV binding can be used to distinguish cis and trans heterozygous mutations (**Figure 3.1F and 3.5A**). This challenging task is significant in medical diagnostics as the presence of two mutations on the same gene copy can alter protein function, while one mutation on each gene copy can yield cells with no functional gene copies.^{18, 23-24} Moreover, cis/trans discrimination is significant in genetic counseling in order to track the inheritance of mutations.¹⁸ As a proof-of-concept, 8 and 9 nt S₁ and S₂ oligos were designed to hybridize in the head-to-tail or head-to-head orientation to a complementary to a 31 nt target corresponding to a region of the KRAS gene which contains the G12C mutation (SNP₁) in the S₁' region and the L19F mutation (SNP₂) in the S₂' region (**Figure 3.5B and Figure A3.4**). Between the S₁' and S₂' regions there are 13-15 non-complementary nt (**Figure A3.14**). L19F is a non-canonical mutation that has been found to cause increased tumor proliferation and transforming potential over WT KRAS.³³ We chose to use this mutation in our assay due to its proximity to the

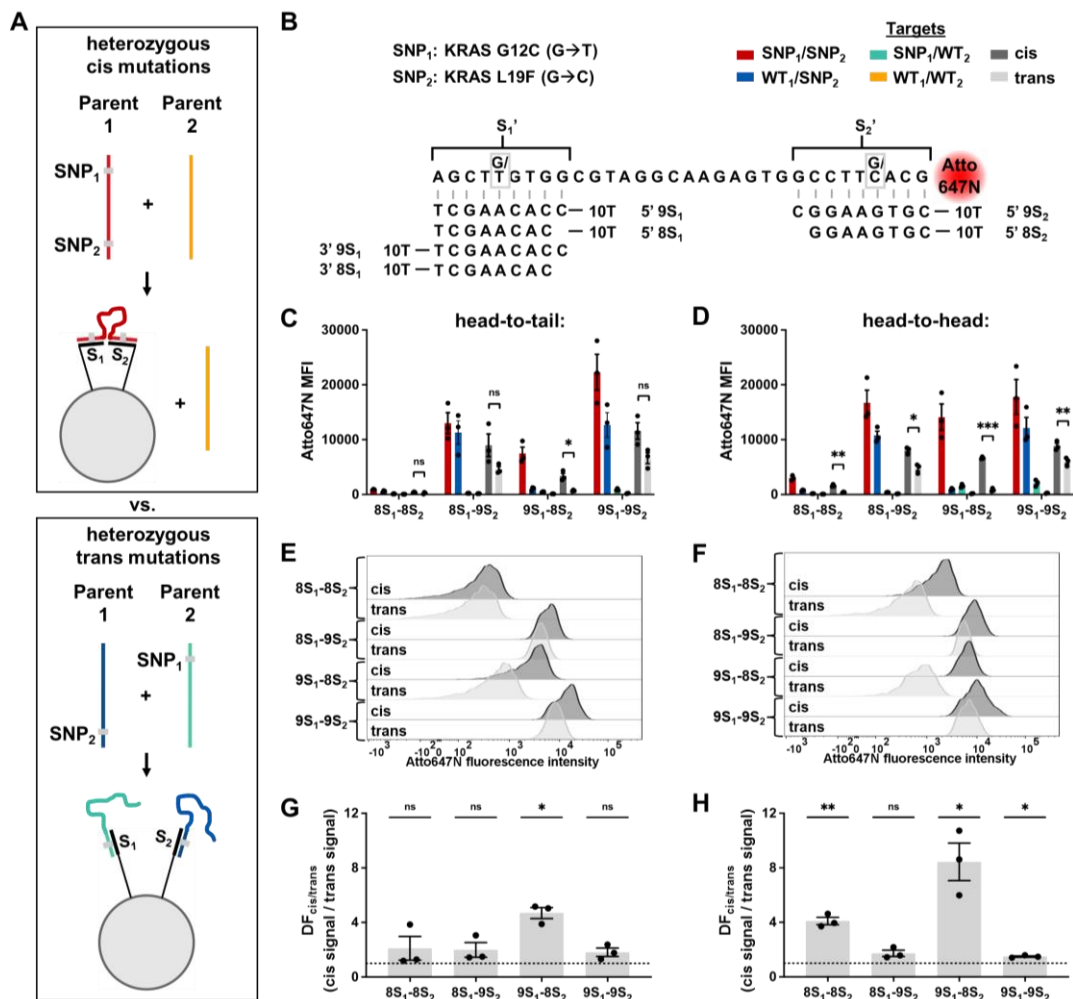


Figure 3.5. Detecting the cis/trans relationship of two mutations using heteroMV hybridization. (a) Scheme illustrating the use of heteromultivalent DNA-coated beads to distinguish the heterozygous cis mutation mixture (red and yellow targets) from the heterozygous trans mutations mixture (blue and green targets). Ideally, the double mutant target (red) will bind the beads multivalently with high affinity, the single mutant targets (blue and green) bind monovalently with low affinity, and the no mutant target (yellow) shows negligible binding. (b) Scheme describing the sequence of the binding oligos, identity of the two SNPs, and the two binding orientations tested. (c and d) Measured median fluorescence intensity values for each bead with head-to-tail orientation (c) or head-to-head orientation (d) binding each of the targets or target combinations in the legend. Values were compared using paired student t tests (^{ns}P > 0.05, *P < 0.05, **P < 0.01, ***P < 0.001). (e and f) Representative histograms for each bead with head-to-tail orientation (e) or head-to-head orientation (f) binding the cis or trans target combinations. (g and h) Measured cis/trans discrimination factors for each bead with head-to-tail orientation (g) or head-to-head orientation (h). Values were compared to baseline value of 1 (dotted black line) using one-sample t tests (^{ns}P > 0.05, *P < 0.05, **P < 0.01). Error bars represent standard error of the mean.

G12C mutation, though we anticipate binding two mutations that are further apart will still be effective.

Using each combination of the binding oligos, 8 heteroMV beads were synthesized and flow cytometry was used to measure their binding to 1 nM of the four targets, as well as to a 0.5 nM of SNP₁/SNP₂ + 0.5 nM of WT₁/WT₂ target mixture (cis) or a 0.5 nM of SNP₁/WT₂ + 0.5 nM of WT₁/SNP₂ target mixture (trans) (**Figure 3.5C, 3.5D, and A3.14**). As expected, all the bead combinations bound the SNP₁/SNP₂ target with the greatest affinity and the WT₁/WT₂ target with the weakest affinity. Moreover, the 9S₁-8S₂ beads with either binding orientation had weak and approximately equal binding to both single mutant targets while showing strong binding to the SNP₁/SNP₂ target, yielding DF values ~10 for both mutations. Due to this specificity for both mutations and strong binding cooperativity, both the head-to-tail and head-to-head 9S₁-8S₂ beads bound the cis target combination significantly more than the trans with DF_{cis/trans} values of 4.7 and 8.4, respectively (**Figure 3.5E-H**). Interestingly, beads containing the 8S₂ oligo showed stronger binding to the SNP₁/SNP₂ target and higher DF_{cis/trans} values when binding in the head-to-head instead of head-to-tail orientation. Alternatively, beads containing the 9S₂ oligo bound the SNP₁/SNP₂ and WT₁/SNP₂ targets similarly, resulting in poor specificity for SNP₁, and had similar DF_{cis/trans} values in both orientations. This suggests that the 9S₂ oligo's affinity for the target is too high resulting in low cooperativity binding that is not impacted by a mismatch in the S₁' region. These results offer further evidence that the head-to-head orientation can yield higher binding, particularly when the two immobilized oligos are binding cooperatively. Overall, this screen reveals that heteroMV hybridization enables strong discrimination between cis and trans heterozygous mutations and demonstrates the importance of precisely tuned binding specificity

and cooperativity. This result is important as it establishes a hybridization-based approach to distinguish cis/trans mutations without using enzymes or magnetic separation techniques.^{24, 34-36}

3.2.6. Distinguishing Different Strains of SARS-CoV-2 Using HeteroMV Hybridization

We next tested our hypothesis that heteroMV hybridization could lead to dramatic enhancements in specificity for targets containing two mutations (**Figure 3.1G**). We thus designed three model targets corresponding to a 29 nt region of the SARS-CoV-2 spike protein gene that contains three mutations (Q498R, N501Y, AND Y505H) in the omicron strain, one mutation in the alpha strain (N501Y), and no mutations in the original strain (**Figure 3.6A**). To hybridize specifically to the omicron strain, two S_1 (8 S_1 and 9 S_1) and two S_2 (8 S_2 and 9 S_2) oligos, complementary to the Q498R site and the Y505H site respectively, were designed so that neither overlap with the N501Y mutation shared by the alpha strain (**Figure 3.6B**). Using these oligos, four $n=2$ beads were synthesized that bound the target in the head-to-head orientation with an 11-13 nt spacer region (**Figure A3.15**). As a negative control, $n=1$ beads functionalized with a 29 nt oligo that is perfectly complementary to the omicron target were also tested (**Figure 3.6B**). Flow cytometry was then performed for each bead when binding the three targets. The results showed that each of the $n=2$ beads tested bound to the omicron target with similarly high affinity and showed minimal binding to the alpha and original targets (**Figure A3.15**). Meanwhile, compared to the 8 S_1 -9 S_2 $n=2$ beads, the $n=1$ beads yielded an approximately equal MFI when binding the omicron target but bound to significantly more alpha and original targets (**Figure 3.6C and 3.6D**). Significantly, the $n=2$ beads offered dramatically enhanced specificity for the omicron strain, with the 8 S_1 -9 S_2 combination bead giving a $DF_{SNP1 + SNP2}$ value of ~ 800 compared to either of the other

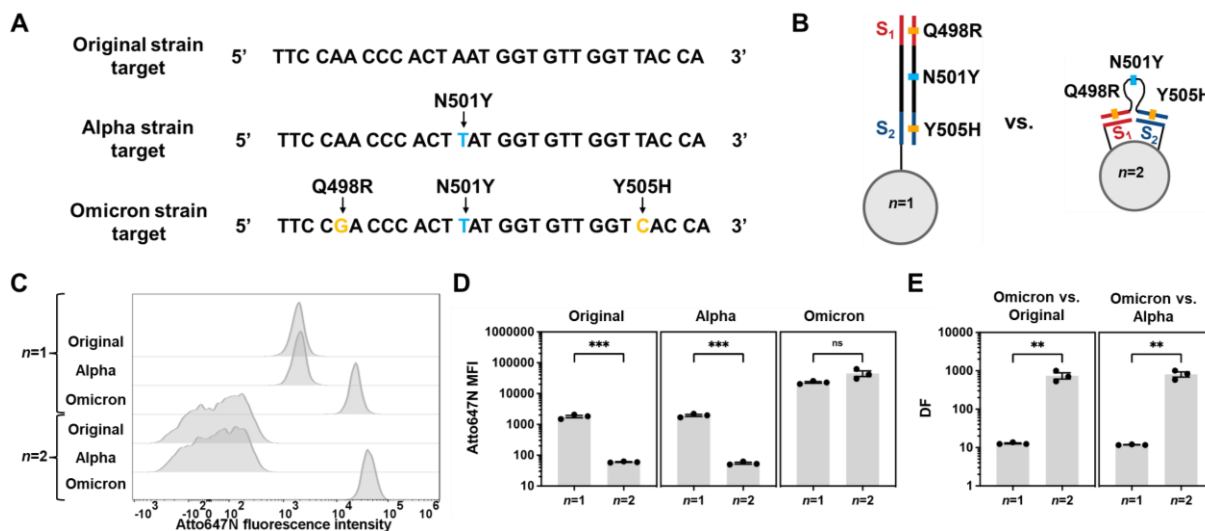


Figure 3.6. Distinguishing different strains of SARS-CoV-2 using heteroMV hybridization. (a) Sequences of targets based on the original, alpha, and omicron strains of SARS-CoV-2 spike protein, with the mutations in each target indicated with arrows. (b) Scheme describing the binding of an $n=1$ bead functionalized with an oligo that is fully complementary to the omicron target and the binding of an $n=2$ bead functionalized with S_1 and S_2 oligos that are complementary to the regions of the target containing the Q498R and Y505H mutations but not the N501Y mutation (c-d) Representative histograms (c) and measured median fluorescence intensity values (d) for the $n=1$ and $8S_1$ - $9S_2$ $n=2$ beads binding each target. (e) Measured discrimination factors for the $n=1$ and $8S_1$ - $9S_2$ $n=2$ beads binding the omicron target vs. the original target or the omicron target vs. the alpha target. Values were compared using unpaired student t tests ($^{ns}P > 0.05$, $^{**}P < 0.01$, $^{***}P < 0.001$). Error bars represent standard error of the mean.

targets (**Figure 3.6E**). The $n=1$ bead had much lower specificity for the omicron target with $DF_{SNP1+SNP2}$ values of ~ 12 .

As the $n=1$ bead has more total complementarity with the target, it was surprising that the $n=1$ and $n=2$ beads yielded approximately equal omicron target binding. Potential explanations include increased secondary structure, reduced K_{on} rates, and reduced DNA density for the $n=1$ bead as has been previously observed for materials functionalized with longer oligos,³⁷⁻³⁸ though these hypotheses were not tested herein. This highlights a general advantage for heteroMV hybridization where each oligo can be shorter in length and therefore less likely to be impacted by these issues. Moreover, the stark differences in specificity between the $n=1$ and $n=2$ beads would

likely become even greater as the inter-SNP distance increases (**Figure 3.1C**). In this case, the length of the oligo on the $n=1$ bead would have to become longer to bind to both SNPs, while the oligos on the $n=2$ beads would not need to be altered, and instead potentially exhibit stronger and more cooperative binding as shown in **Figure 3.4**. Interestingly, the $DF_{\text{SNP1} + \text{SNP2}}$ values obtained were even higher than predicted (**Figure 3.1G**), possibly a result of increased secondary structure for the original and alpha targets relative to the omicron target (**Figure A3.4**). This demonstration of rapid and effective identification of the strain of model viral targets using heteroMV hybridization has the potential to significantly impact the fields of diagnostics, medicine, and public health.

3.3. Discussion

In this report, it was demonstrated that heteromultivalency can be used to precisely tune the properties of a binding interaction between a DNA-coated structure and a single stranded nucleic acid target. Densely coating a microparticle with two distinct oligonucleotide sequences allowed customizable multivalent binding with highly tunable affinity, yielding several important capabilities. By first optimizing each oligo's length, we show that heteroMV binding can control binding strength more precisely than monovalent binding, enabling near-maximum discrimination of perfect match and mismatch targets. Thus, heteroMV offers an approach to optimizing the performance of hybridization-based mutation detection tools while maintaining compatibility with multiplex assays. While different mutations and assay conditions will still require optimization of the oligo lengths to tune specificity, the results herein will accelerate future screening processes. Moreover, heteroMV binding can be combined with other approaches that are commonly used to

enhance binding specificity, such as molecular beacon, toehold-mediated hybridization, and competition/sink probes.^{3,5-8}

In addition to adjusting the oligo length, customizing the spacer length and binding orientation allowed demonstration of highly cooperative binding to two unique regions of a target. Both parameters are thus critical for applications that necessitate selective hybridization only when two receptors are present.²¹ Enhanced cooperativity was also observed as spacer length increased, potentially due to improved ability for a target to reach two adjacent surface oligos. Additionally, as the spacer length increases, the target can span longer distances on the particle surface allowing access to more copies of each binding oligo. These added binding partners, though spread through a larger volume, can result in a higher local concentration of surface-bound oligos.³⁹ This feature is unique to heteroMV structures that are densely functionalized, as opposed to a structure that presents a single copy of each oligo and thus cannot access additional binding sites despite a longer spacer. Cooperative binding was demonstrated with up to 15 nt spacers, though further studies with longer spacers would deepen the investigation. Furthermore, when binding the target lacking a spacer, a 6-fold increase in cooperativity was observed when head-to-head orientation was used instead of tail-to-tail. However, for heteroMV binding where $n > 2$, it is not possible to exclusively use the highly cooperative head-to-head orientation. Instead, each adjacent oligo pair must alternate between binding in the head-to-head and tail-to-tail orientation or each oligo can be anchored through the same terminus, as previously demonstrated.¹⁷

Through the combined benefits of highly tunable affinity and strong cooperativity despite a spacer region in the target, heteroMV binding also resulted in the ability to distinguish heterozygous cis and trans mutations. Through optimization, ~8-fold higher binding was observed when heteroMV particles were incubated with a mixture of double mutant and non-mutant targets

rather than two single mutant targets. Distinguishing between these target mixtures is often achieved through costly and lengthy methods involving complex next-gen sequencing assays, droplet PCR, or single-molecule dilution.¹⁸⁻¹⁹ Alternatively, in monovalent hybridization-based assays either one long probe is used to bind both mutations or a distinct probe binds each mutation. In the first case, specificity and cooperativity diminish due to excessively strong binding, while in the second case each probe binds identically to cis and trans target mixtures.²⁴ For this reason, hybridization-based assays typically rely on a second discriminatory step involving enzymes or separation techniques.^{24, 34-35} Finally, heteroMV hybridization enabled ~800-fold higher binding when targeting two SNPs unique to the omicron strain of the SARS-CoV-2 genome. Standard assays, including rapid antigen tests and PCR do not distinguish different viral strains, and instead whole-genome sequencing is performed for strain identification. Thus, the ability to rapidly determine the strain of the viral sample potentially offers improved monitoring of viral evolution and more complete diagnosis of infections.

The heteroMV hybridization approach presented herein is compatible with many materials used to present oligos in close-proximity, including 1, 2, or 3-dimensional structures. Also, functionalizing the material heteromultivalently is straightforward as oligo spatial patterning does not significantly impact binding affinity when n is low.¹⁷ Moreover, precisely controlling the inter-oligo distance on the surface is not necessary when target binding regions are further apart as such targets can span longer distances without diminished cooperativity. The cooperativity arising from heteroMV binding does however depend on the oligos being pre-linked to a scaffold. Alternatively, “binary” probes have been described, which rely on monovalent binding of two unlinked oligo probes and a separate complex formation step to generate a signal.^{10,40} Additionally, DNA origami nanoswitches have been engineered to switch to a loop conformation upon heteroMV binding to a

target to facilitate detection with gel electrophoresis.^{22, 41} In this work, fluorophore-labeled targets were used to enable a rapid flow cytometry readout but for diagnostic applications requiring unlabeled target sensing, an altered readout method is necessary. In many nucleic acid detection methods, tunable binding affinity that allows highly specific and cooperative binding is essential, and therefore, heteroMV DNA hybridization is a promising method for further advancing biomedical sensing and diagnostics.

3.4. Materials and Methods

3.4.1. Oligonucleotides

All oligonucleotides were custom synthesized by Integrated DNA Technologies (Coralville, IA).

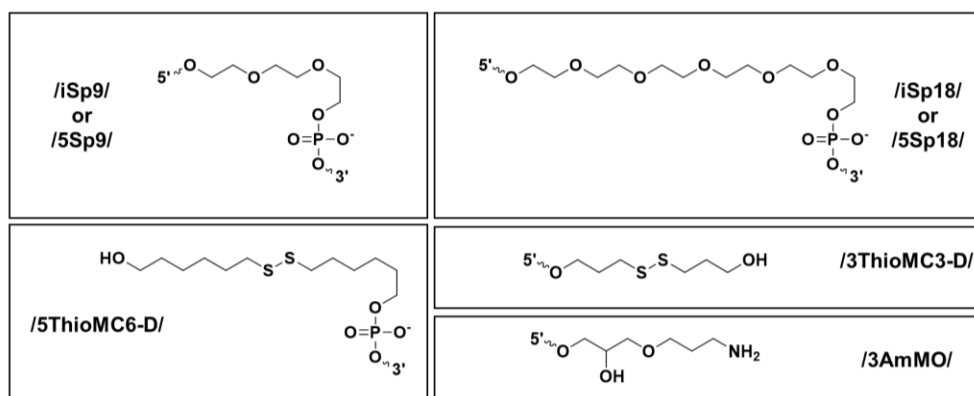
The table below includes the names and sequences for all oligonucleotides used in this work.

Table A3.1. List of oligonucleotides used in Chapter 3.

Name	Sequence (5' to 3')
7S	/5ThioMC6-D/TTTTTTTTTTACAAGCT
8S	/5ThioMC6-D/TTTTTTTTTTCACAAGCT
9S	/5ThioMC6-D/TTTTTTTTTTCCACAAGCT
10S	/5ThioMC6-D/TTTTTTTTTTGCCACAAGCT
11S	/5ThioMC6-D/TTTTTTTTTTTCGCCACAAGCT
4T	/5ThioMC6-D/TTTTTTTTTTCCAA
5T	/5ThioMC6-D/TTTTTTTTTTCCAAC
6T	/5ThioMC6-D/TTTTTTTTTTCCAACT
7T	/5ThioMC6-D/TTTTTTTTTTCCAACTA
8T	/5ThioMC6-D/TTTTTTTTTTCCAACTAC
9T	/5ThioMC6-D/TTTTTTTTTTCCAACTACC
10T	/5ThioMC6-D/TTTTTTTTTTCCAACTACCA
no spacer G12C	TGGTAGTTGGAGCTTGTGGCGTAGG/3AmMO/
no spacer WT	TGGTAGTTGGAGCTGGTGGCGTAGG/3AmMO/
internal short spacer G12C	TGGTAGTTGG/iSp9/AGCTTGTGGCGTAGG/3AmMO/
internal short spacer WT	TGGTAGTTGG/iSp9/AGCTGGTGGCGTAGG/3AmMO/
internal long spacer G12C	TGGTAGTTGG/iSp18/AGCTTGTGGCGTAGG/3AmMO/
internal long spacer WT	TGGTAGTTGG/iSp18/AGCTGGTGGCGTAGG/3AmMO/
terminal short spacer G12C	/5Sp9/TGGTAGTTGGAGCTTGTGGCGTAGG/3AmMO/
terminal short spacer WT	/5Sp9/TGGTAGTTGGAGCTGGTGGCGTAGG/3AmMO/
terminal long spacer G12C	/5Sp18/TGGTAGTTGGAGCTTGTGGCGTAGG/3AmMO/
terminal long spacer WT	/5Sp18/TGGTAGTTGGAGCTGGTGGCGTAGG/3AmMO/
3' thiol 8T	CCAAGCTTTTTTTTTTT/3ThioMC3-D/
3' thiol 8S	CACAAGCTTTTTTTTTTT/3ThioMC3-D/
3' thiol 9S	CCACAAGCTTTTTTTTTTT/3ThioMC3-D/
5' thiol 8S L19F	/5ThioMC6-D/TTTTTTTTTTTCGTGAAGG
5' thiol 9S L19F	/5ThioMC6-D/TTTTTTTTTTTCGTGAAGGC
G12C/L19F	AGCTTGTGGCGTAGGCAAGAGTGCCTTCACG/3AmMO/
WT/L19F	AGCTGGTGGCGTAGGCAAGAGTGCCTTCACG/3AmMO/
G12C/WT	AGCTTGTGGCGTAGGCAAGAGTGCCTTGACG/3AmMO/
WT/WT	AGCTGGTGGCGTAGGCAAGAGTGCCTTGACG/3AmMO/

8S Q498R	GGTCGGAATTTTTTTTTT/3ThioMC3-D/
9S Q498R	GGGTCGGAATTTTTTTTTT/3ThioMC3-D/
8S Y505H	/5ThioMC6-D/TTTTTTTTTTGGTGACC
9S Y505H	/5ThioMC6-D/TTTTTTTTTTGGTGACCA
complement to omicron target	/5ThioMC6D/TTTTTTTTTTGGTGACCAACACCATAAGT GGGTCGGAA
Q498R/N501Y/Y505H target (Omicron)	TTCCGACCCACTTATGGTGTGGTCACCA/3AmMO/
WT/WT/WT target (Original)	TTCCAACCCACTAATGGTGTGGTTACCA/3AmMO/
WT/N501Y/WT target (Alpha)	TTCCAACCCACTTATGGTGTGGTTACCA/3AmMO/

The structures of each of the oligonucleotide modifications in **Table A3.1** are included below.



3.4.2. Reagents

5 μ m aminated silica beads (Cat# SA06N) were purchased from Bangs Laboratory (Fishers, IN). Dri-solv methylsulfoxide (Cat# MX1457-7) was purchased from EMD Millipore (Burlington, MA). Potassium hydroxide (Cat# 221473), sodium bicarbonate (Cat#S6014), acetonitrile (Cat# 34998), and Atto647N NHS ester (Cat#18373-1MG-F) were purchased from Sigma-Aldrich (St. Louis, MO). 20x TE buffer (Cat# 42020325-2) was purchased from bioWORLD (Dublin, OH). Bond-Breaker TCEP (Tris(2-carboxyethyl)phosphine hydrochloride) solution, Neutral pH (Cat#77720), Quant-IT Oligreen ssDNA reagent (Cat# O7582), SMCC (succinimidyl 4-(N-maleimidomethyl)cyclohexane-1-carboxylate) (Cat#22360), sulfo-NHS-acetate (Cat#26777), and Tween20 (Cat# BP337) were purchased from Thermo Fisher Scientific (Waltham, MA). Saline

sodium citrate (SSC) buffer (Cat# AM9763) was purchased from Ambion (Austin, TX). Triethylammonium acetate (Cat# 60-4110-57) was purchased from Glen Research (Sterling, VA).

3.4.3. Consumables

96-well white flat bottom polystyrene microplates (Cat# 3912) were purchased from Corning (Corning, NY). P2 size exclusion gel (Cat#1504118) and P4 size exclusion gel (Cat# #1504124) was purchased from Bio-Rad (Hercules, CA). Nanosep MF centrifugal devices (Cat# ODM02C35) were purchased from Pall Laboratory.

3.4.4. Equipment

The major equipment that was used in this study includes: CytoFLEX flow cytometer (Beckman coulter), Nanodrop 2000 UV-Vis Spectrophotometer (Thermo Scientific), Barnstead nanopure water purifying system (Thermo Fisher), 5424 R centrifuge (Eppendorf), Synergy H1 plate reader (Biotek), high-performance liquid chromatography 1100 (Agilent) with AdvanceBio Oligonucleotide C18 column (653950-702, 4.6x 150 mm, 2.7 μ m) (Agilent), LTQ Orbitrap Velos mass spectrometer (Thermo Scientific), Galaxy mini tabletop centrifuge (VWR), Rebel Brightfield Microscope (ECHO), and Nikon Ti2-E motorized research microscope equipped with SOLA SE II 365 Light Engine, Photometrics Prime 95B-25mm Back-illuminated sCMOS camera, and CF-L AT Cy5/Alexa 647/Draq 5 filter set.

3.4.5. Modeling

In all modeling calculations herein, $c_{\text{eff}} = 50 \text{ uM}$, $\text{MM} = 0.025$, and the ratio of consecutive values for K_{eq} chosen = 20. These values were chosen to most closely reproduce experimental results obtained.

To derive an equation to calculate the equilibrium binding occupancy, θ , of the oligos coating the particle surface using the total binding affinity of the target (K_{eq}), total target concentration ($[\text{target}]$), and total concentration of oligos on the particle surface ($[\text{surface}]$) we began with the standard equation for K_{eq} :

$$K_{\text{eq}} = \frac{[\text{surface}_{\text{bound}}]}{[\text{target}_{\text{unbound}}][\text{surface}_{\text{unbound}}]}$$

This equation is then rearranged into the following form:

$$K_{\text{eq}}[\text{target}_{\text{unbound}}] = \frac{[\text{surface}_{\text{bound}}]}{[\text{surface}_{\text{unbound}}]}$$

$[\text{surface}_{\text{bound}}]$ is then replaced with $[\text{surface}_{\text{total}}] - [\text{surface}_{\text{unbound}}]$ to give the following equation:

$$K_{\text{eq}}[\text{target}_{\text{unbound}}] = \frac{[\text{surface}_{\text{total}}] - [\text{surface}_{\text{unbound}}]}{[\text{surface}_{\text{unbound}}]}$$

As $[\text{surface}_{\text{total}}] - [\text{surface}_{\text{unbound}}] = \theta$ and $[\text{surface}_{\text{unbound}}] = 1 - \theta$, the following equation is then derived.

$$\frac{\theta}{1 - \theta} = K_{\text{eq}}[\text{target}_{\text{unbound}}]$$

In order to solve for θ using only K_{eq} , $[\text{target}]$, and $[\text{target}_{\text{bound}}]$, $[\text{target}_{\text{unbound}}]$ is first replaced with $[\text{target}] - [\text{target}_{\text{bound}}]$:

$$\frac{\theta}{1 - \theta} = K_{\text{eq}}([\text{target}] - [\text{target}_{\text{bound}}])$$

$[\text{target}_{\text{bound}}]$ is replaced with $[\text{surface}]\theta$ to give the following equation:

$$\frac{\theta}{1 - \theta} = K_{eq}([target] - [surface]\theta)$$

This equation is then rearranged into a quadratic form ($\theta = a\theta^2 + b\theta + c$) as follows:

$$\begin{aligned}\theta &= (1 - \theta)(K_{eq}([target] - [surface]\theta)) \\ \theta &= K_{eq}[surface]\theta^2 - K_{eq}[target]\theta - K_{eq}[surface]\theta + K_{eq}[target] \\ 0 &= K_{eq}[surface]\theta^2 - K_{eq}[target]\theta - K_{eq}[surface]\theta - \theta + K_{eq}[target] \\ 0 &= K_{eq}[surface]\theta^2 + (-K_{eq}([target] - [surface]) - 1)\theta + K_{eq}[target]\end{aligned}$$

The equation is then solved for θ using the quadratic formula:

$$\theta = \frac{-b \pm \sqrt{b^2 - 4ac}}{2a}$$

Where $a = K_{eq}[surface]$, $b = -K_{eq}([target] - [surface]) - 1$, and $c = K_{eq}[target]$, giving the final equation for θ :

$$\theta = \frac{K_{eq}([target] + [surface]) + 1 \pm \sqrt{(K_{eq}([target] + [surface]) + 1)^2 - 4K_{eq}^2[surface][target]}}{2K_{eq}[surface]}$$

where the correct value of θ is equal to the root given by subtracting the quadratic portion. For the results shown in Figure 3.1D, E, and G, $[target] = 1$ nM and $[surface] = 1$ nM, and thus the following simplifications can be made:

$$\begin{aligned}\theta &= \frac{2K_{eq} + 1 \pm \sqrt{(2K_{eq} + 1)^2 - 4K_{eq}^2}}{2K_{eq}} \\ \theta &= \frac{1}{2K_{eq}} + 1 \pm \frac{\sqrt{4K_{eq}^2 + 4K_{eq} + 1 - 4K_{eq}^2}}{2K_{eq}} \\ \theta &= \frac{1}{2K_{eq}} + 1 \pm \frac{\sqrt{4K_{eq} + 1}}{2K_{eq}}\end{aligned}$$

For the results shown in Figure 3.1F, $[target_1] = 0.5$ nM and $[target_2] = 0.5$ nM. Therefore, values of θ for $target_1$ and for $target_2$ are calculated and then summed to calculate total θ .

Finally, θ was converted to an arbitrary assay signal, I , using the equation:

$$I = I_{\max} * + I_{bg}$$

where I_{\max} represents the maximum signal and I_{bg} is the background signal when target concentration = 0. In all modeling calculations herein, $I_{\max} = 250000$ and $I_{bg} = 58$.

The 10 possible sequence pairs when considering two mutations (SNP₁ and SNP₂) on two gene copies ($target_1$ and $target_2$) are as follows:

1. $target_1 = \text{SNP}_1/\text{SNP}_2$ and $target_2 = \text{SNP}_1/\text{SNP}_2$ (homozygous double, SNP₁ and SNP₂)
2. $target_1 = \text{SNP}_1/\text{SNP}_2$ and $target_2 = \text{SNP}_1/\text{WT}_2$
3. $target_1 = \text{SNP}_1/\text{SNP}_2$ and $target_2 = \text{WT}_1/\text{SNP}_2$
4. $target_1 = \text{SNP}_1/\text{SNP}_2$ and $target_2 = \text{WT}_1/\text{WT}_2$ (heterozygous cis)
5. $target_1 = \text{SNP}_1/\text{WT}_2$ and $target_2 = \text{SNP}_1/\text{WT}_2$ (homozygous single, SNP₁)
6. $target_1 = \text{SNP}_1/\text{WT}_2$ and $target_2 = \text{WT}_1/\text{SNP}_2$ (heterozygous trans)
7. $target_1 = \text{SNP}_1/\text{WT}_2$ and $target_2 = \text{WT}_1/\text{WT}_2$
8. $target_1 = \text{WT}_1/\text{SNP}_2$ and $target_2 = \text{WT}_1/\text{SNP}_2$ (homozygous single, SNP₂)
9. $target_1 = \text{WT}_1/\text{SNP}_2$ and $target_2 = \text{WT}_1/\text{WT}_2$
10. $target_1 = \text{WT}_1/\text{WT}_2$ and $target_2 = \text{WT}_1/\text{WT}_2$ (wildtype)

The equations for total binding affinity to the SNP₁/SNP₂, SNP₁/WT₂, WT₁/SNP₂, and WT₁/WT₂ targets can be described as:

$$\text{Total } K_{eq, \text{SNP}_1/\text{SNP}_2} = K_{eq, S1} + K_{eq, S2} + K_{eq, S1} * K_{eq, S2} * C_{eff}$$

$$\text{Total } K_{eq, \text{SNP}_1/\text{WT}_2} = K_{eq, S1} + MM_2 * K_{eq, S2} + K_{eq, S1} * MM_2 * K_{eq, S2} * C_{eff}$$

$$\text{Total } K_{eq, \text{WT}_1/\text{SNP}_2} = MM_1 * K_{eq, S1} + K_{eq, S2} + MM_1 * K_{eq, S1} * K_{eq, S2} * C_{eff}$$

$$\text{Total } K_{eq, \text{WT}_1/\text{WT}_2} = MM_1 * K_{eq, S1} + MM_2 * K_{eq, S2} + MM_1 * K_{eq, S1} * MM_2 * K_{eq, S2} * C_{eff}$$

where MM₁ corresponds to a mismatch in S₁' and MM₂ corresponds to a mismatch in S₂'.

3.4.6. Synthesis of DNA-Functionalized Silica Particles

5 μm amine-modified silica particles were suspended in DMSO at a concentration of ~4.4x10⁵ particles/μL. A 100 mg/mL stock of SMCC was then prepared in DMSO and added at a final

concentration of 10 mg/mL to a solution of 4×10^4 particles/ μL suspended in DMSO. The reaction was then incubated at room temperature for 30 min to prepare maleimide-labeled silica beads. During the reaction of SMCC with the amine-modified silica beads, 0.5 μL of 100 μM thiolated DNA (1 μM final), 0.5 μL of 10 mM TCEP (100 μM final), and 49 μL of 1x PBS at pH 6.8 were mixed and incubated at room temperature for 30 min to 1 hour to reduce the thiolated DNA. The maleimide-labeled silica bead solution was then centrifuged on a tabletop mini-centrifuge at 6000 rpm for 1 min and the supernatant was removed and replaced with an equal volume of a 1 mg/mL solution of sulfo-NHS acetate dissolved in DMSO. The reaction was then incubated at room temperature for 30 min to prepare passivated, maleimide-labeled silica beads. Following the 30 min incubation, centrifugation and supernatant removal was performed 4 times. After each of the first three centrifugations, the beads were resuspended in a 2x volume of DMSO. Following the third resuspension, the beads were split into 50 μL aliquots and then centrifuged for the 4th time. After the 4th centrifugation, the supernatant was removed and replaced with the 50 μL solution of 1 μM reduced thiol-DNA and incubated at room temperature overnight or > 8 hours. For $n=2$ beads, a pre-mixed solution containing 500 nM of each oligo was added, resulting in a total concentration of 1 μM of DNA. Following incubation, 50 μL of 1x SSC, 0.1% Tween20 was added to each tube to help with centrifugation. Next, centrifugation and supernatant removal was performed 4 times. After each of the first three centrifugations, the beads were resuspended in 100 μL of 1x SSC, 0.1% Tween20. After the fourth centrifugation, the beads were resuspended in 1 mL of 1x SSC, 0.1% Tween20.

3.4.7. Determining Number of Oligos Per Silica Particle

The approximate concentration of the DNA-coated bead stocks was approximated using four representative stock solutions using a hemacytometer. Then, two volumes containing $\sim 1 \times 10^5$ or $\sim 1.75 \times 10^5$ beads were taken from the four different DNA-coated bead stocks. Centrifugation at 6000 rpm with the tabletop mini-centrifuge and supernatant removal were then performed for each sample, followed by resuspension of the beads in 100 μ L of 0.1 M KOH. The beads were incubated in the KOH solution at room temperature for > 8 hrs. Brightfield microscopy images before and after KOH incubation were obtained using the Rebel Brightfield Microscope (Echo). The bead solution was then centrifuged again, and the supernatant was removed and added to a new tube. The centrifuged bead solution was resuspended in 1x SSC, 0.1% Tween20 and analyzed using flow cytometry to confirm that the beads were etched/dissolved fully. The tube containing the removed supernatant was then filtered using P2 gel filtration to remove KOH from the solution. 20x TE buffer was then added to the solution to give a final 1x concentration of TE buffer. Samples were then transferred to a 96 well plate. Oligreen was then added to the solution at a final concentration of 1x and incubated for ~ 5 min at room temperature before the fluorescence was measured using the Biotek plate reader. To generate a standard curve of fluorescence vs. [DNA], 0, 5, 10, 20, 35, and 50 nM solutions of unreduced thiol DNA were prepared and incubated in a solution of 0.1 M KOH for > 1 hr. Following KOH incubation, the DNA solution was filtered using P2 gel filtration to remove KOH from the solution. 20x TE buffer was then added to the solution to give a final 1x concentration of TE buffer. Samples were then transferred to a 96 well plate. Oligreen was then added to the solution at a final concentration of 1x and incubated for ~ 5 min at room temperature before the fluorescence was measured using the Biotek plate reader. Using the standard curve, the

concentration of DNA in the bead samples was determined and then divided by initial bead concentration to determine the number of oligos per silica bead.

3.4.8. Atto647N Conjugation to Target Strands

Excess NHS-Atto647N (250 μg) was dissolved in 10 μL of fresh DMSO and then added to 10 nmol of amine-labeled target strands in 1x PBS with 0.1 M NaHCO_3 . The reaction was left for > 1 hour at room temperature. After incubation, unreacted NHS-Atto647N and salts were removed by P2 or P4 gel filtration and purified using an analytical-scale reverse-phase HPLC with an Agilent AdvanceBio Oligonucleotide C18 column. Product was eluted in Solvents A: 0.1 M TEAA and B: ACN with a linear gradient of 10-100% Solvent B over 45 min at 0.5 mL/min flow rate. The molecular weight of the products was evaluated with an electron spray ionization (ESI) method using a Thermo Fisher Scientific Orbitrap. The samples were prepared in a mixture of 70% nanopure water and 30% acetonitrile containing 10 μM ethylenediaminetetraacetic acid (EDTA), 0.0375% triethylamine, and 0.75% of 1,1,1,3,3,3-hexafluoro-2-propanol (HFIP) and the spectra were recorded with negative charge mode eluted with the same solution.⁴² The main peak of the obtained ESI-MS spectrum (m/z) was then deconvoluted to obtain the average molecular weight for the oligonucleotides. The concentration of the strands was determined by UV-Vis using a Nanodrop instrument.

3.4.9. Flow Cytometry Assay and Analysis to Measure Target Binding

1 nM Atto647N-labeled target was added to $\sim 2.5 \times 10^4$ DNA-coated silica beads suspended in 1x SSC, 0.1% Tween20 and incubated at room temperature for 1 hour. Following the 1 hour incubation, centrifugation at 6000 rpm with the tabletop mini-centrifuge and supernatant removal

was performed 4 times. After each of the four centrifugations, the beads were resuspended in 100 μL of 1x SSC, 0.1% Tween20. Fully washed beads were then injected into the flow cytometer for final analysis. After performing flow cytometry, FlowJo V10 was used to analyze the data. Singlet beads were isolated from the sample by gating first using forward scatter and side scatter area and second using forward and side scatter height. The median fluorescence intensity of the singlet beads from each sample was then calculated.

3.4.10. Fluorescence Microscopy of Atto647N-Labeled Targets Hybridized to Beads

Wells in a glass bottom 96-well plate were soaked in ethanol for 5 min, rinsed with Nanopure water, and coated in 10% BSA for 15 min and rinsed again prior to imaging. 0 or 1 nM Atto647N-labeled target was added to $\sim 2.5 \times 10^4$ DNA-coated silica beads suspended in 1x SSC, 0.1% Tween20 and incubated at room temperature for >1 hour. Following the incubation, centrifugation at 6000 rpm with the tabletop mini-centrifuge and supernatant removal was performed 4 times. After each of the four centrifugations, the beads were resuspended in 100 μL of 1x SSC, 0.1% Tween20. Fully washed beads were then added to the 96-well microscopy plate and imaged on the fluorescence microscope. Brightfield images were obtained and Atto647N images were acquired using a Cy5 cube. Images were processed using Fiji ImageJ software.

3.5. Appendix

Figure A3.1. Modeling the specificity of homoMV particles for single mutant targets. (a) Scheme showing binding pathway of a homoMV particle binding either a SNP-containing target or a WT target and modification of binding affinity equation with MM factor. (b) Predicted arbitrary signals when a homoMV particle with different affinities binds the SNP target or the WT target. (c) Predicted discrimination factors for a homoMV particle with different affinities. Red dots correspond to discrimination factors for six values of K_{eq} chosen to mimic a series of oligos of length $x, x + 1, \dots, x + 5$ nt. The black dashed curve was generated by fitting the predicted values to a gaussian distribution in GraphPad.

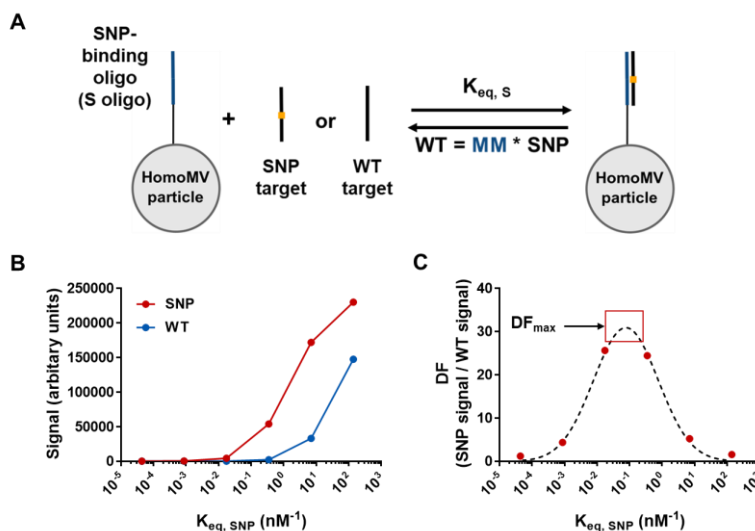


Figure A3.2. Modeling the specificity of heteroMV particles for single mutant targets. (a) Scheme showing the two-step reversible binding pathway of an $n=2$ heteroMV particle binding either a SNP-containing target or a WT target and corresponding equations used to model the binding affinity to each target. (b and c) Heatmap showing the predicted arbitrary signals when binding the SNP target (b) or WT target (c) as the monovalent binding affinities of the S and the R oligo are varied. (d) Predicted discrimination factors for an $n=2$ heteroMV particle as the affinity of R ($K_{eq, R}$ only) is increased (different colors) causing the total affinity for the SNP target ($K_{eq, S + R, SNP}$) to increase (x -axis) for each discrete value of $K_{eq, S}$ only chosen (same color dots). The curves were generated by fitting the predicted values to a gaussian distribution in GraphPad. (e) The maximum DF value predicted from the curve in (d) for each discrete value of $K_{eq, R}$ only. (f) Heatmap showing the predicted discrimination factor when the monovalent binding affinities of the S and the T oligo are varied. Black boxes indicate the $n=1$ and $n=2$ combination with the highest discrimination factors. (g) Heatmap showing the predicted cooperativity factor when the monovalent binding affinities of the S and the T oligo are varied. Black box indicates the $n=2$ combination with the highest cooperativity factor.

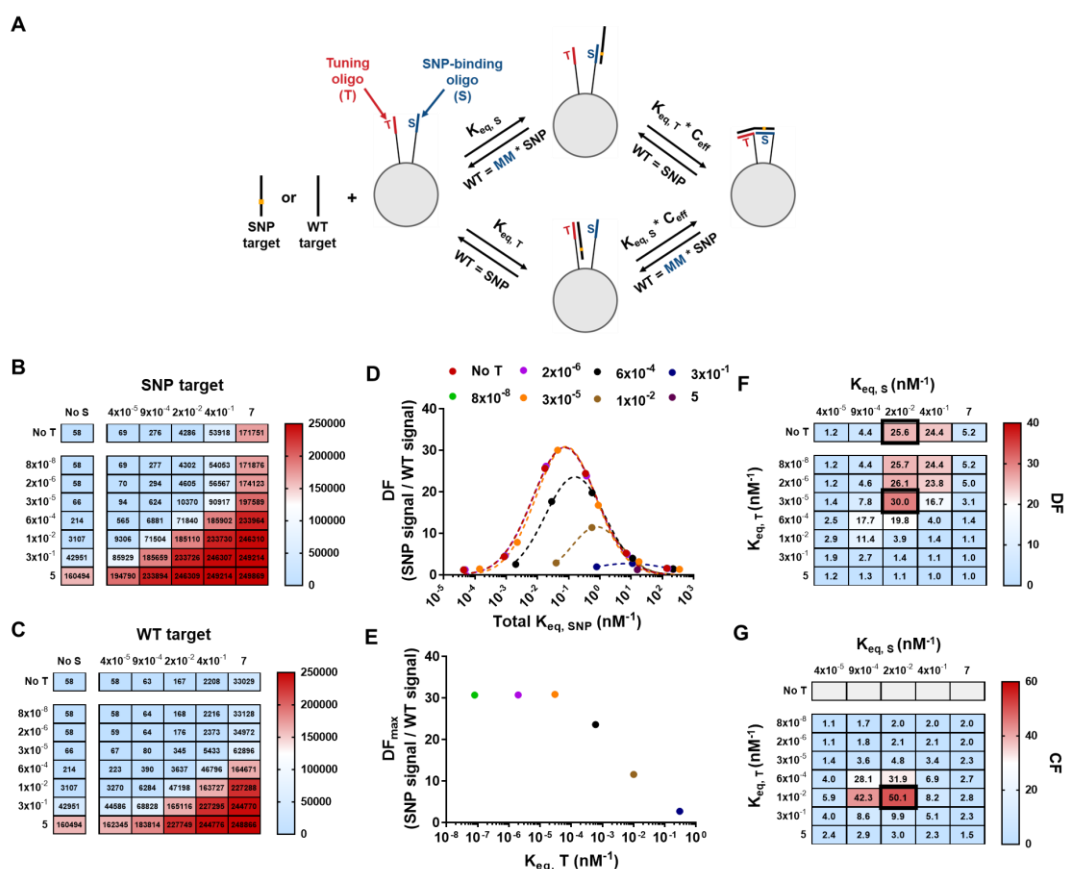


Figure A3.3. Modeling the specificity of heteroMV particles for double mutant targets. (a) Scheme showing the two-step reversible binding pathway of an $n=2$ heteroMV particle binding either a double mutant target or a double WT target and corresponding equations used to model the binding affinity to each target. (b) Heatmap showing the predicted cis/trans discrimination factor when the monovalent binding affinities of the S_1 and the S_2 oligo are varied. Black box indicates the $n=2$ combination with the highest predicted cis/trans discrimination factor. (c) Heatmap showing the predicted double mutant discrimination factor when the monovalent binding affinities of the S_1 and the S_2 oligo are varied. Black box indicates the $n=2$ combination with the highest predicted double mutant discrimination factor.

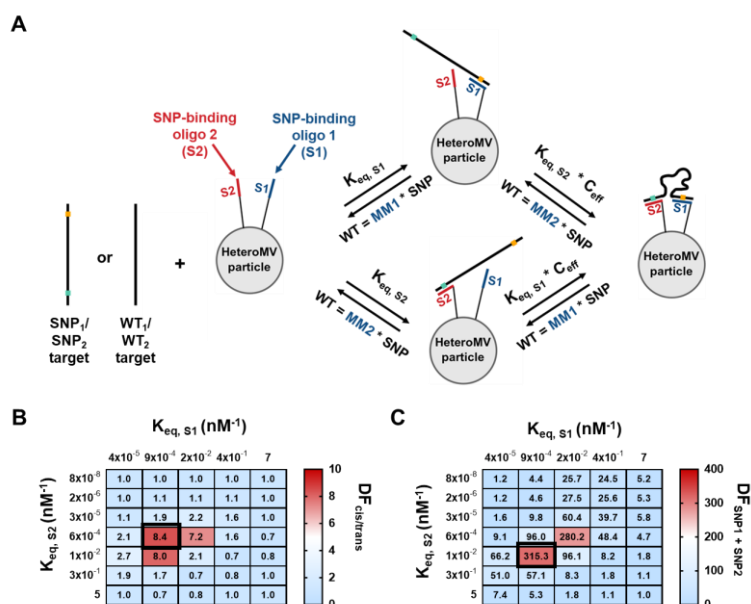


Figure A3.4. Description of targets and Nupack predictions of target secondary structure. (a) Scheme describing the DNA sequence (NCBI Reference Sequence: NG_007524.2) and amino acid sequence (NCBI Reference Sequence: NP_001356715.1) of the first 20 amino acids of human KRAS protein. The location of the no spacer targets used in this work are shown in red, with the G12C mutated codon shown in blue. (b and c) Predictions for the secondary structures of the no spacer G12C (b) and WT (c) targets generated using Nupack. In the illustration on the left, the circle color of each nucleotide refers to the identity of each nucleotide base. In the illustration on the right, the circle color of each nucleotide refers to the probability that each nucleotide is bound at equilibrium if it is shown bound or unbound if it is shown unbound. The black arrows refer to the position of the G12C mutation in the target sequence. (d) The location of the G12C/L19F targets used in this work are shown in red, with the G12C and L19F mutated codons shown in blue. (e, f, g, and h) Predictions for the secondary structures of the G12C/L19F (e), WT/L19F (f), G12C/WT (g), and WT/WT (h) targets generated using Nupack. The black arrows refer to the position of the G12C and L19F mutations in the target sequence. (i) Scheme describing the DNA sequence (NCBI Reference Sequence: NC_045512.2) and amino acid sequence (NCBI Reference Sequence: YP_009724390.1) of amino acids 497-506 of SARS-CoV-2 spike protein. The location of the Omicron/Wuhan/Alpha targets used in this work are shown in red, with the Q498R, N501Y, and Y505H mutated codons shown in blue. (j, k, l) Predictions for the secondary structures of the Omicron (j), Wuhan (k), and Alpha (l) targets generated using Nupack. The black arrows refer to the position of the Q498R, N501Y, and Y505 mutations in the target sequence. All predictions were performed at 0.15 M Na⁺, 0 M Mg²⁺, and 22°C.

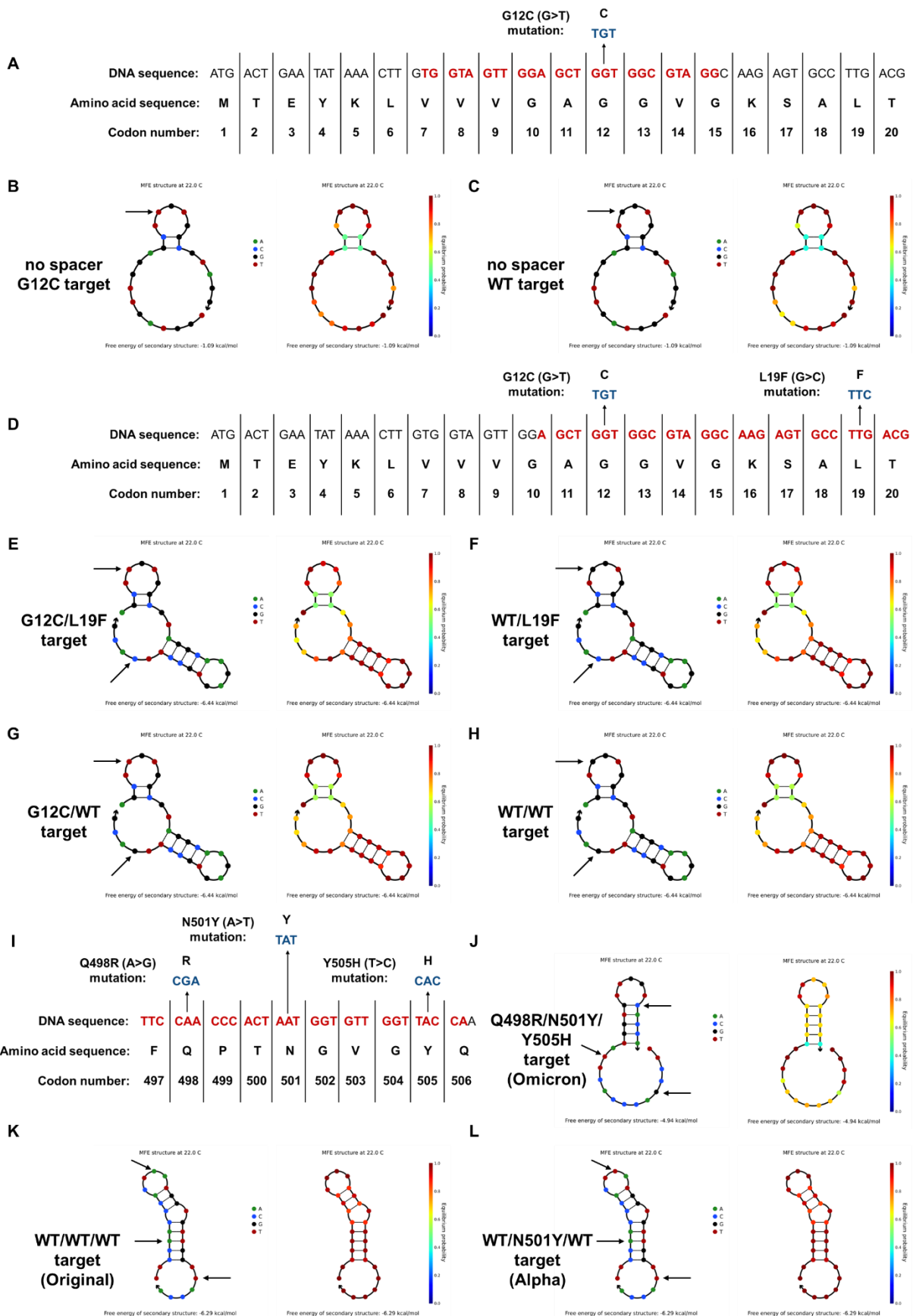


Figure A3.5. Synthesis and purification of Atto647N-labeled targets. (a) Reaction scheme for conjugation of amine-modified oligonucleotides with NHS-Atto647N. (b) HPLC traces of the Atto647N-labeled targets. Arrows represent the material collected from HPLC.

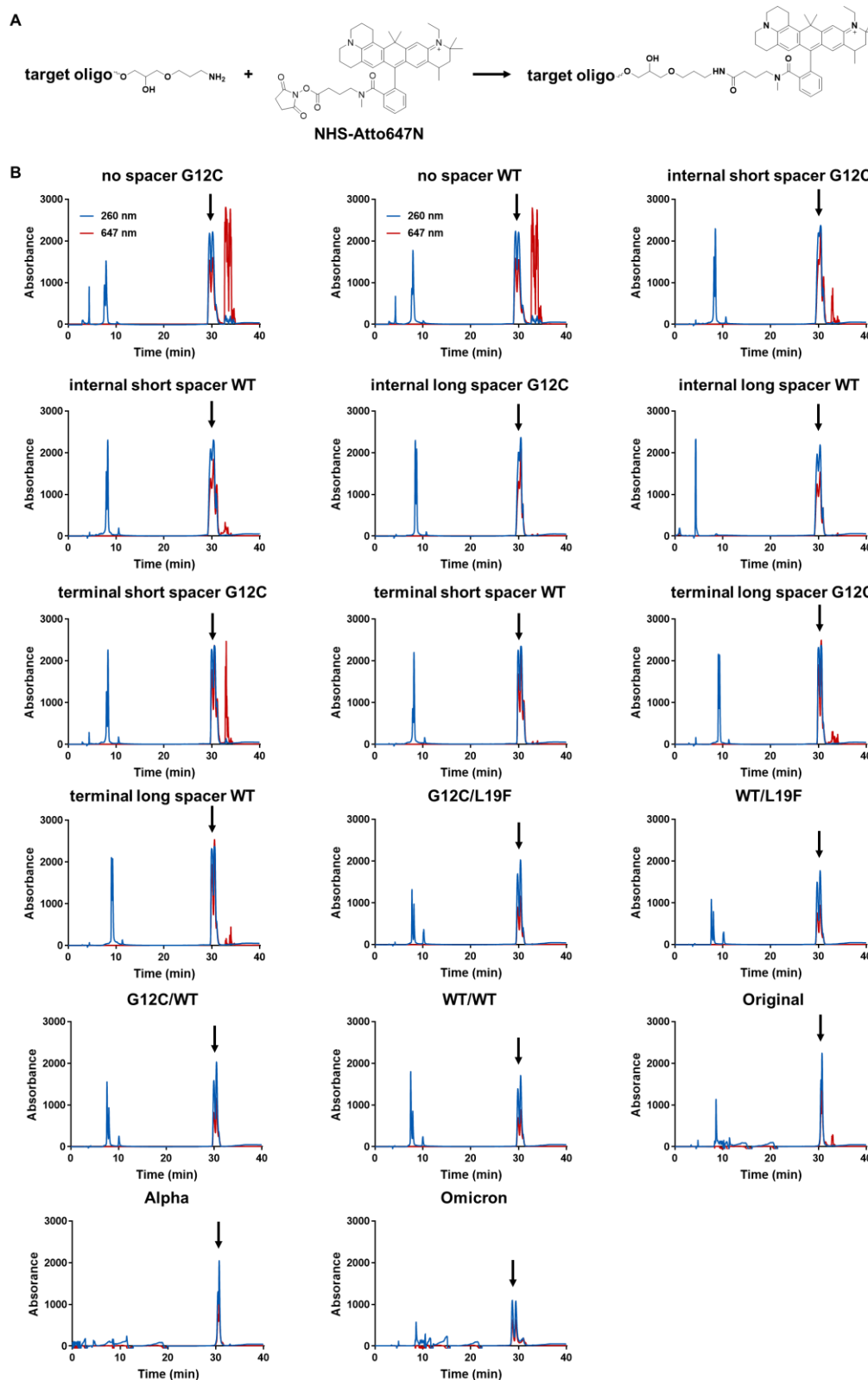
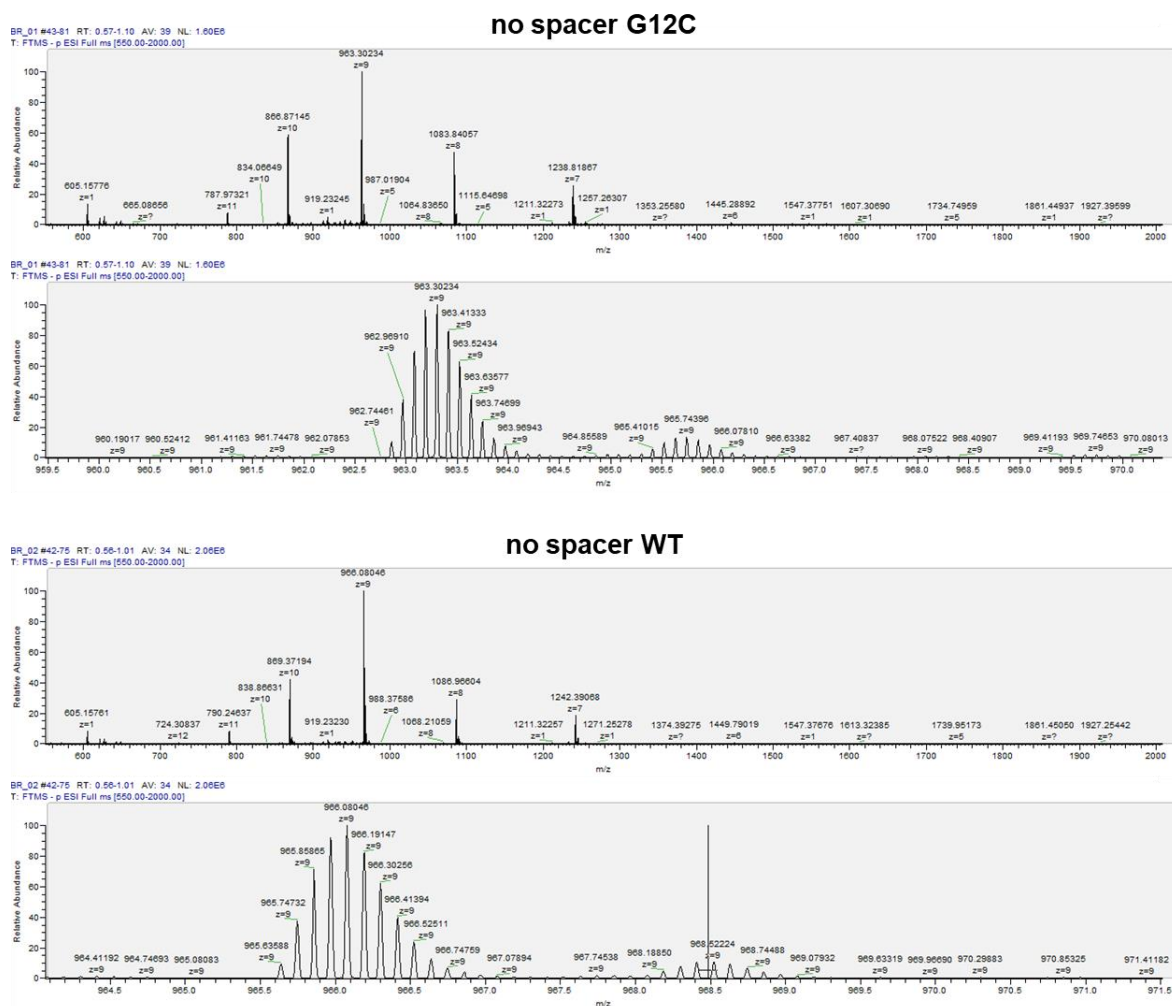


Figure A3.6. Mass spectrometry characterization of Atto647N-labeled targets. (a) Table of calculated masses, measured m/z values found, and difference in mass between calculated and measured masses of Atto647N-labeled targets. (b) Raw ESI mass spectra of Atto647N-labeled targets.

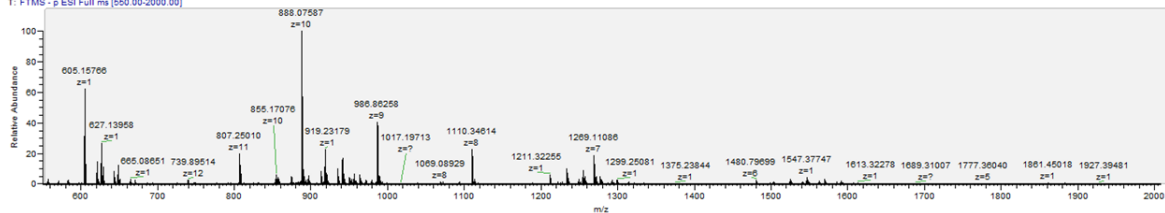
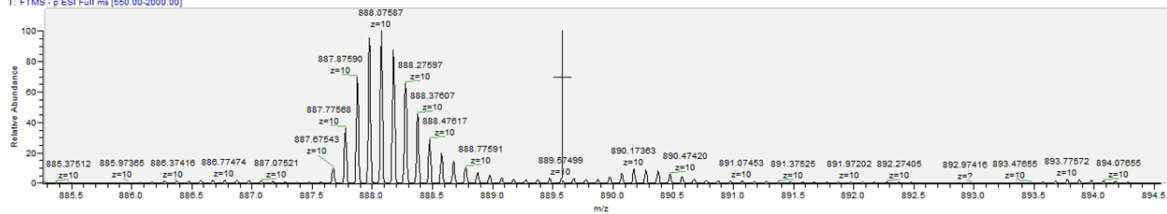
A

Sample	Calculated mass (Da)	m/z found (Da)	Difference (Da)
no spacer G12C	8680.17	8679.72	0.45
no spacer WT	8705.27	8704.72	0.55
internal short spacer G12C	8892.37	8891.76	0.61
internal short spacer WT	8917.37	8916.76	0.61
internal long spacer G12C	9024.47	9023.84	0.63
internal long spacer WT	9049.57	9048.84	0.73
terminal short spacer G12C	8892.37	8891.75	0.62
terminal short spacer WT	8917.37	8916.76	0.61
terminal long spacer G12C	9024.47	9023.83	0.64
terminal long spacer WT	9049.57	9048.84	0.73
G12C/L19F	10432.37	10431.01	1.36
WT/L19F	10457.37	10457.02	0.35
G12C/WT	10472.37	10472.02	0.35
WT/WT	10497.37	10497.03	0.34
Original	9667.87	9667.43	0.44
Alpha	9658.87	9658.41	0.46
Omicron	9659.87	9659.41	0.46

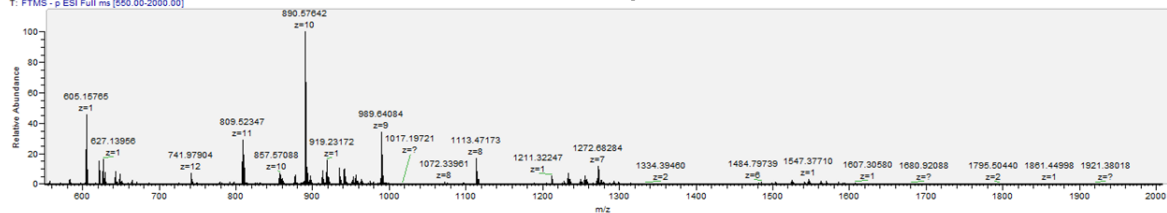
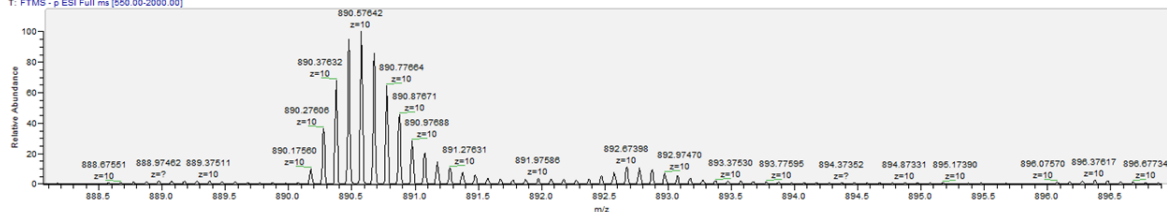
B



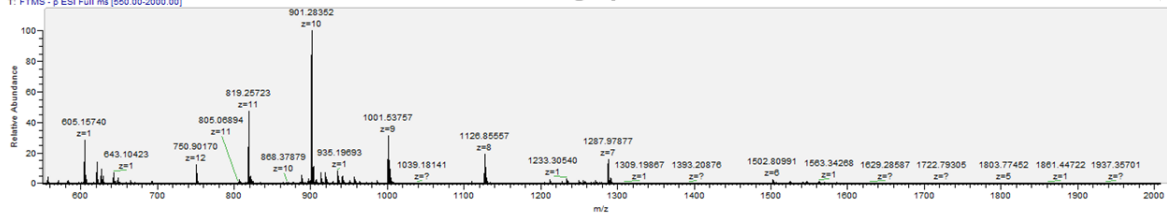
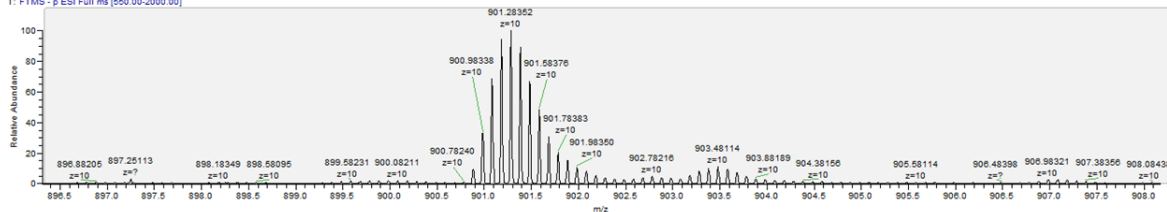
internal short spacer G12C

BR_03 #37-82 RT: 0.48-1.11 Av: 48 NL: 7.46E5
T: FTMS - p ESI Full ms [550.00-2000.00]BR_03 #37-82 RT: 0.48-1.11 Av: 48 NL: 7.46E5
T: FTMS - p ESI Full ms [550.00-2000.00]

internal short spacer WT

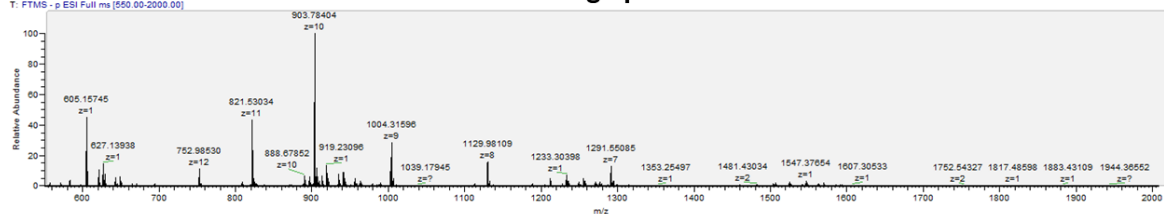
BR_04 #36-82 RT: 0.48-1.11 Av: 47 NL: 9.33E5
T: FTMS - p ESI Full ms [550.00-2000.00]BR_04 #36-82 RT: 0.48-1.11 Av: 47 NL: 9.33E5
T: FTMS - p ESI Full ms [550.00-2000.00]

internal long spacer G12C

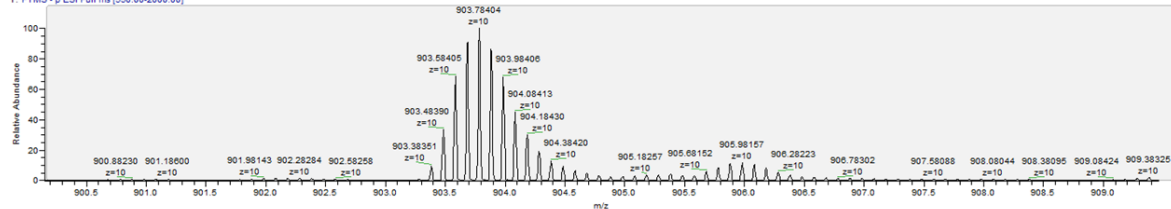
BR_05 #36-82 RT: 0.48-1.11 Av: 47 NL: 1.10E6
T: FTMS - p ESI Full ms [550.00-2000.00]BR_05 #36-82 RT: 0.48-1.11 Av: 47 NL: 1.10E6
T: FTMS - p ESI Full ms [550.00-2000.00]

BR_06 #28-88 RT: 0.37-1.19 AV: 61 NL: 1.04E5
T: FTMS - p ESI Full ms (550.00-2000.00)

internal long spacer WT

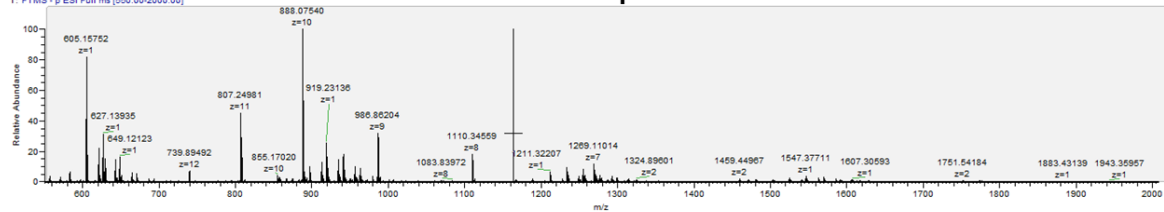


BR_06 #28-88 RT: 0.37-1.19 AV: 61 NL: 1.04E5
T: FTMS - p ESI Full ms (550.00-2000.00)

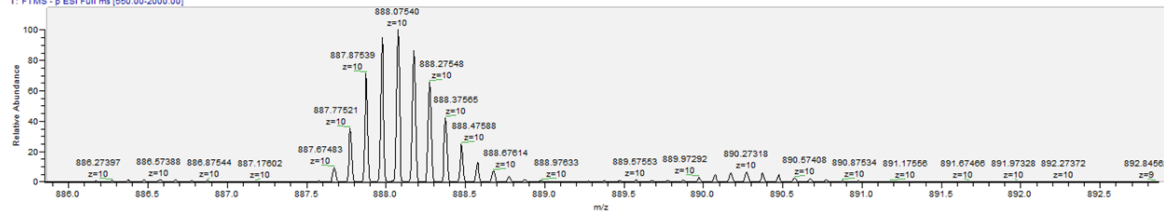


BR_07 #21-59 RT: 0.27-0.93 AV: 49 NL: 4.47E5
T: FTMS - p ESI Full ms (550.00-2000.00)

terminal short spacer G12C

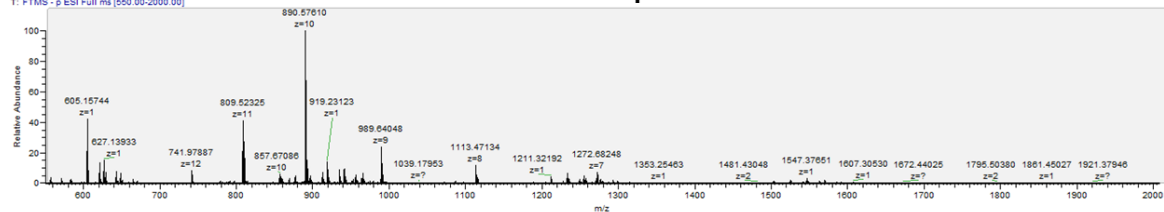


BR_07 #21-59 RT: 0.27-0.93 AV: 49 NL: 4.47E5
T: FTMS - p ESI Full ms (550.00-2000.00)

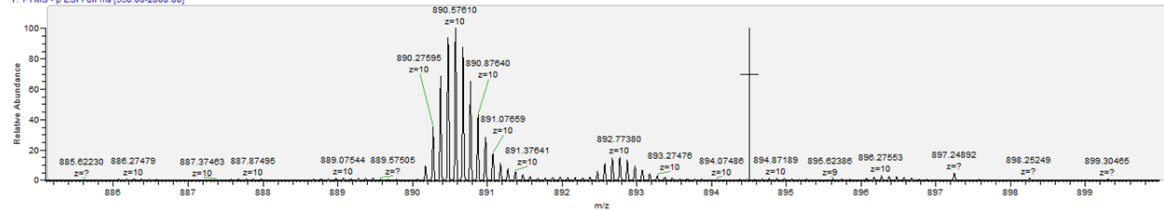


BR_08 #37-91 RT: 0.49-1.23 AV: 55 NL: 8.59E5
T: FTMS - p ESI Full ms (550.00-2000.00)

terminal short spacer WT

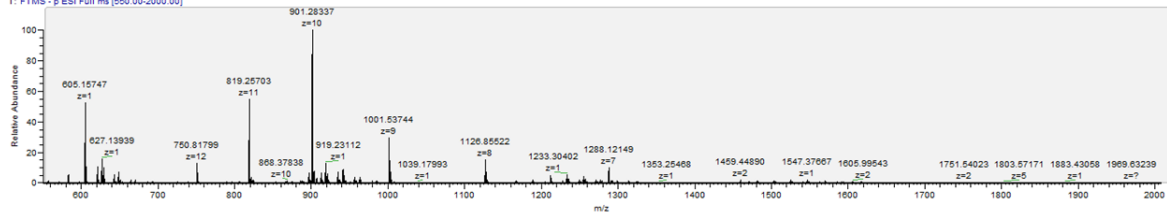


BR_08 #37-91 RT: 0.49-1.23 AV: 55 NL: 8.59E5
T: FTMS - p ESI Full ms (550.00-2000.00)

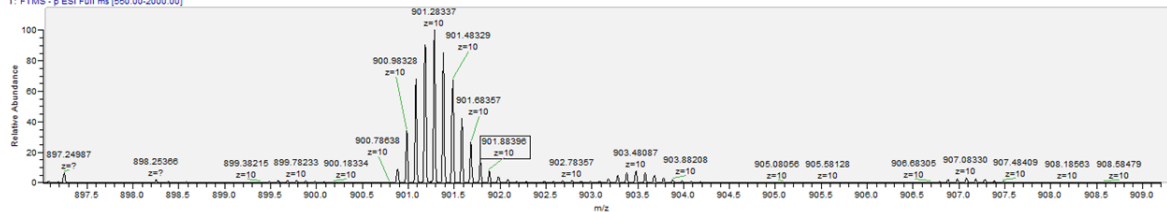


terminal long spacer G12C

BR_09 #26-43 RT: 0.34-0.57 AV: 18 NL: 8.21E5
T: FTMS - p ESI Full ms [550.00-2000.00]

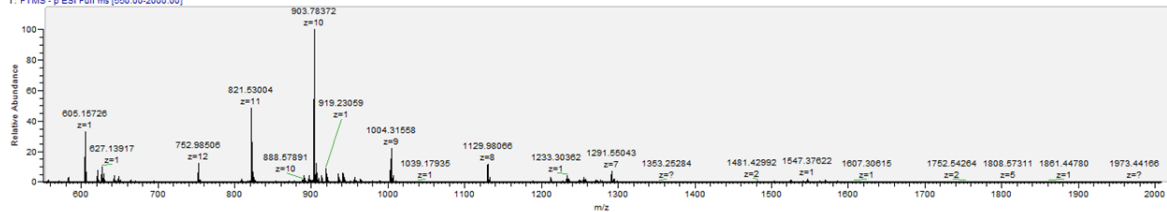


BR_09 #26-43 RT: 0.34-0.57 AV: 18 NL: 8.21E5
T: FTMS - p ESI Full ms [550.00-2000.00]

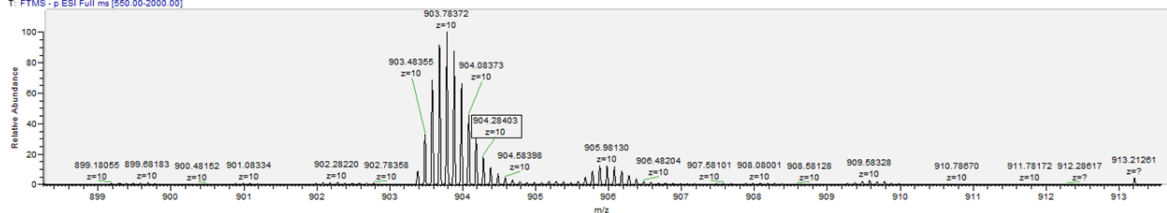


terminal long spacer WT

BR_10 #26-81 RT: 0.34-1.09 AV: 56 NL: 1.32E6
T: FTMS - p ESI Full ms [550.00-2000.00]

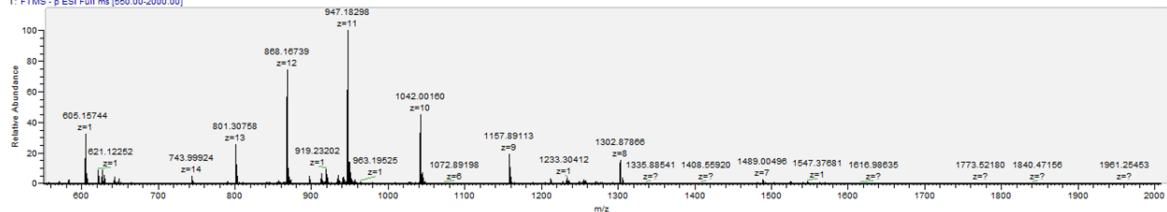


BR_10 #26-81 RT: 0.34-1.09 AV: 56 NL: 1.32E6
T: FTMS - p ESI Full ms [550.00-2000.00]

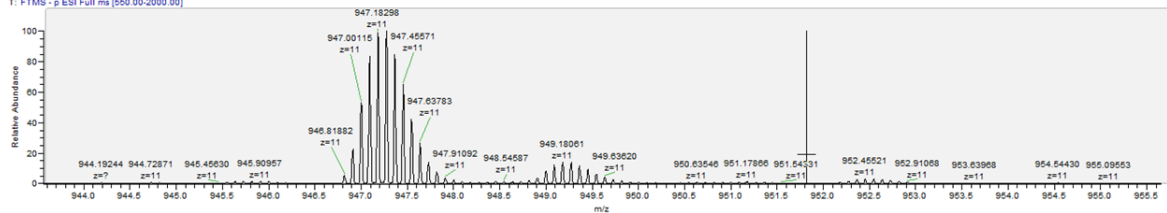


G12C/L19F

BR_11 #32-77 RT: 0.42-1.04 AV: 46 NL: 1.11E6
T: FTMS - p ESI Full ms [550.00-2000.00]

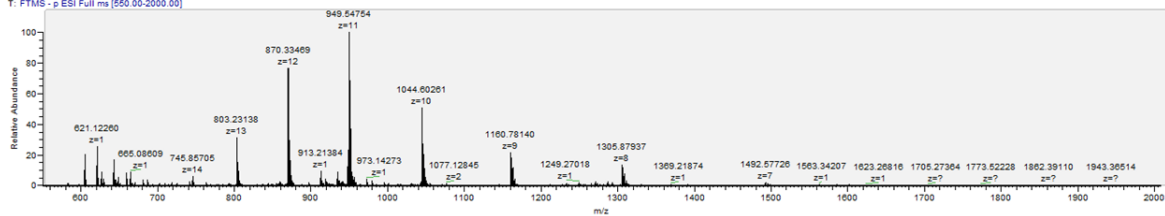


BR_11 #32-77 RT: 0.42-1.04 AV: 46 NL: 1.11E6
T: FTMS - p ESI Full ms [550.00-2000.00]

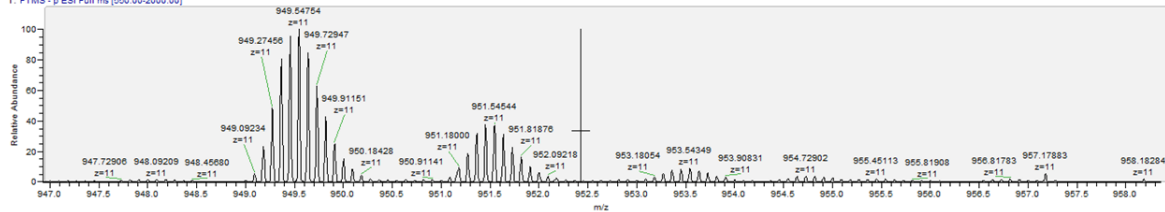


BR_12 #29-80 RT: 0.37-1.08 AV: 53 NL: 0.92E5
T: FTMS - p ESI Full ms [550.00-2000.00]

WT/L19F

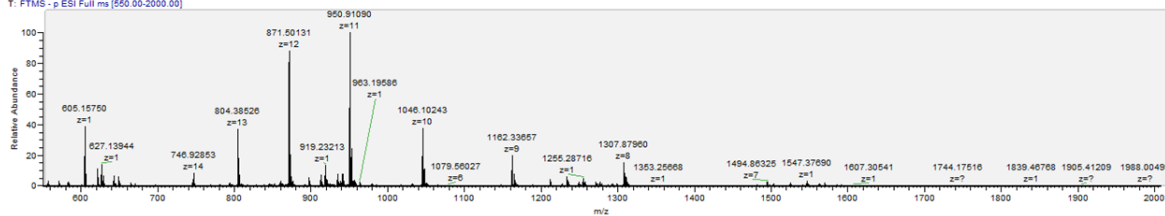


BR_12 #29-80 M1: 0.37-1.08 AV: 53 NL: 0.92E5
T: FTMS - p ESI Full ms [550.00-2000.00]

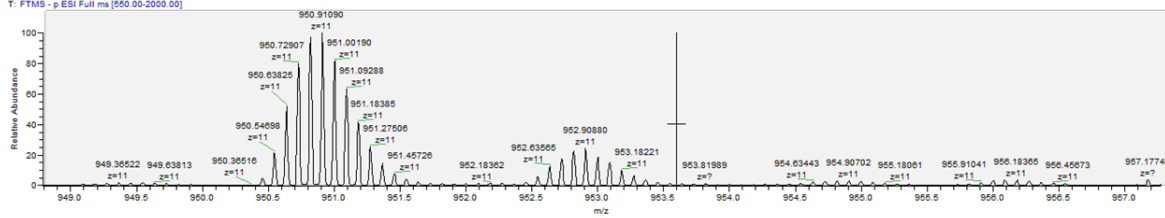


BR_13 #33-95 RT: 0.44-1.29 AV: 63 NL: 1.10E6
T: FTMS - p ESI Full ms [550.00-2000.00]

G12C/WT

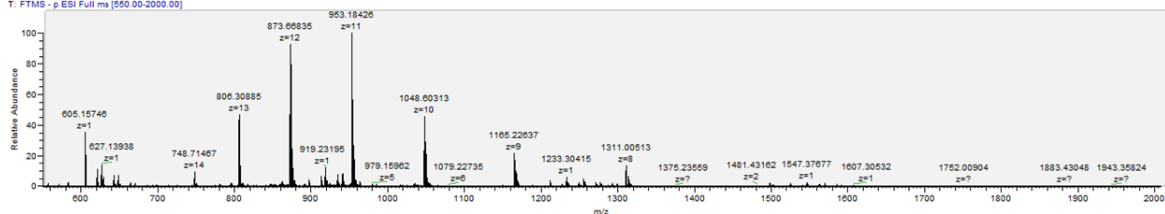


BR_13 #33-95 RT: 0.44-1.29 AV: 63 NL: 1.10E6
T: FTMS - p ESI Full ms [550.00-2000.00]

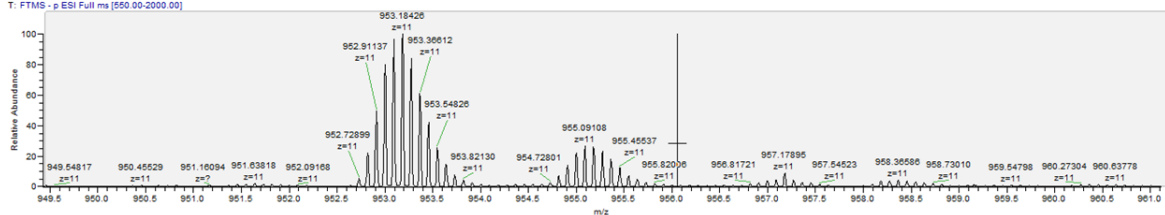


BR_14 #37-85 RT: 0.49-1.15 AV: 49 NL: 1.08E6
T: FTMS - p ESI Full ms [550.00-2000.00]

WT/WT

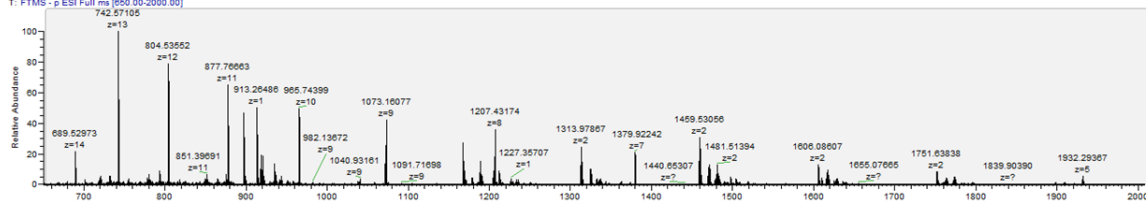


BR_14 #37-85 RT: 0.49-1.15 AV: 49 NL: 1.08E6
T: FTMS - p ESI Full ms [550.00-2000.00]

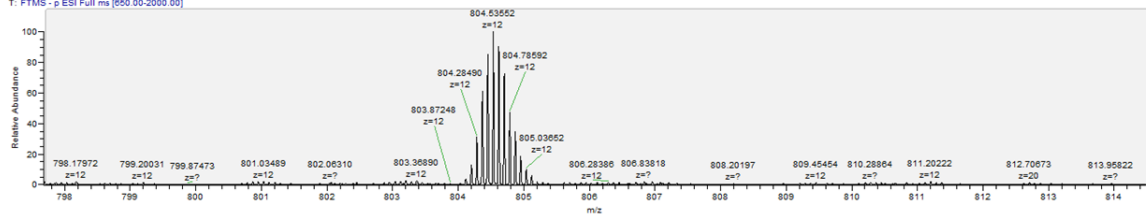


Original

BD1 #97-111 RT: 1.32-1.51 AV: 15 NL: 2.14E5
T: FTMS - p ESI Full ms [650.00-2000.00]

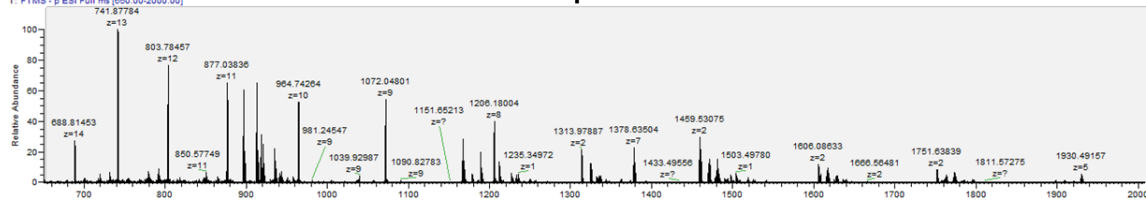


BD1 #97-111 RT: 1.32-1.51 AV: 15 NL: 1.68E5
T: FTMS - p ESI Full ms [650.00-2000.00]

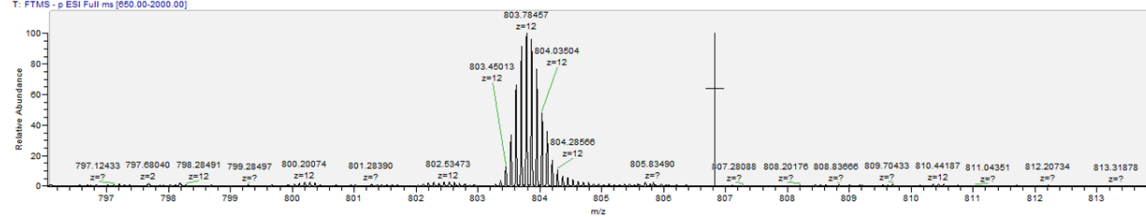


Alpha

BD2 #98-123 RT: 1.33-1.68 AV: 26 NL: 1.86E5
T: FTMS - p ESI Full ms [650.00-2000.00]

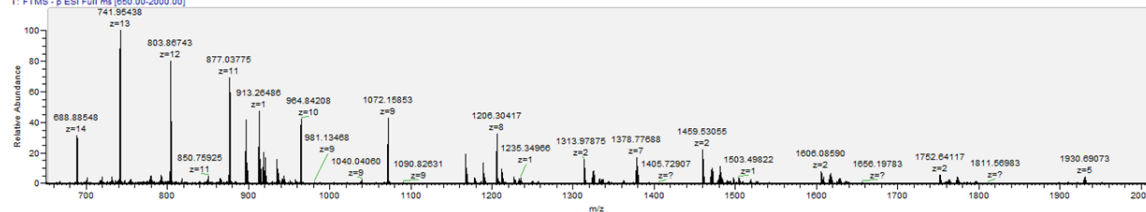


BD2 #98-123 RT: 1.33-1.68 AV: 26 NL: 1.43E5
T: FTMS - p ESI Full ms [650.00-2000.00]



Omicron

BD3 #101-115 RT: 1.38-1.57 AV: 15 NL: 2.60E5
T: FTMS - p ESI Full ms [650.00-2000.00]



BD3 #101-115 RT: 1.38-1.57 AV: 15 NL: 2.08E5
T: FTMS - p ESI Full ms [650.00-2000.00]

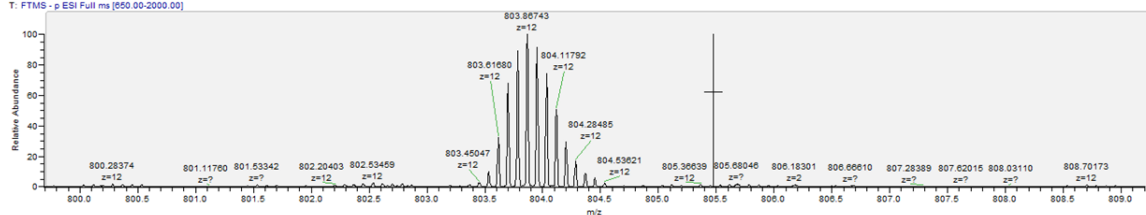


Figure A3.7. Synthesis of DNA-functionalized silica particles. Scheme describing the synthesis of DNA-coated silica particles. On top is a simplified summary of the synthesis, whereas the boxes on the bottom provide further synthetic details and structures of the reagents used. Refer to methods section “Synthesis of DNA-coated silica particles” for a complete description of the synthesis.

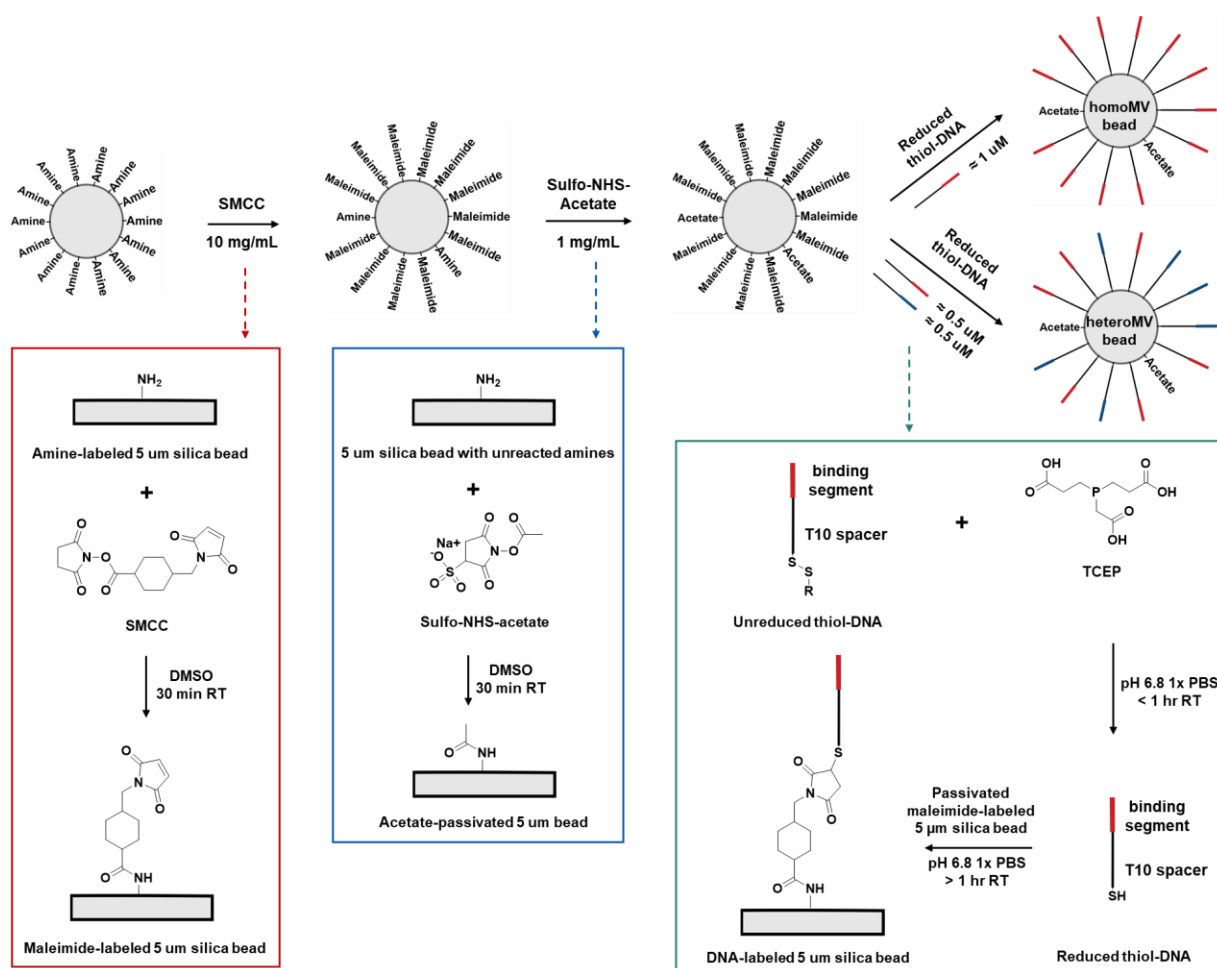


Figure A3.8. Characterization of DNA-functionalized silica particles. (a) Brightfield microscopy images of 5 μm silica beads incubated in 0 M or 0.1 M KOH overnight. (b) Oligreen fluorescence intensity after incubation of 0 or 100 nM of a 20 nt oligo in 0 or 0.1 M KOH for ~6 hours. Following incubation, each sample was split into two tubes, and then Oligreen was added directly to the first tube and added following P2 gel filtration to the second tube. The plot shows that the presence of KOH in solution inhibits Oligreen fluorescence and that removing KOH using a P2 gel before adding Oligreen enables strong Oligreen fluorescence, though some DNA may be lost during filtration. (c) Flow cytometry plot showing side scatter vs forward scatter area of DNA-coated 5 μm silica beads after incubation in 0.1 M KOH for 0, 1, 4, or 8 hrs. The plot shows that over time, the bead size is reduced and the bead structure is damaged following KOH incubation, suggesting that the DNA has been released from the bead surface. (d) Oligreen fluorescence intensity following incubation of beads in 0.1 M KOH for 0, 1, 4, 8, or 24 hrs, followed by P2 gel filtration. The plot indicates that all of the DNA has been released from the beads after ~8 hrs. (e) Scheme showing the finalized assay for quantifying the density of the DNA on the silica beads using the Oligreen reagent. (f) Standard curves of Oligreen fluorescence intensity vs [DNA] from different concentrations of 4 different oligo mixtures. (g) Table showing the # of beads, the measured [DNA], DNA/ μm^2 on the bead surface, and the calculated distance between each oligo on the bead surface. (h) Roughly-to-scale illustration of a 6R-10S bead binding the no spacer G12C target based on the DNA density measurements and literature values for single stranded and double stranded DNA lengths.

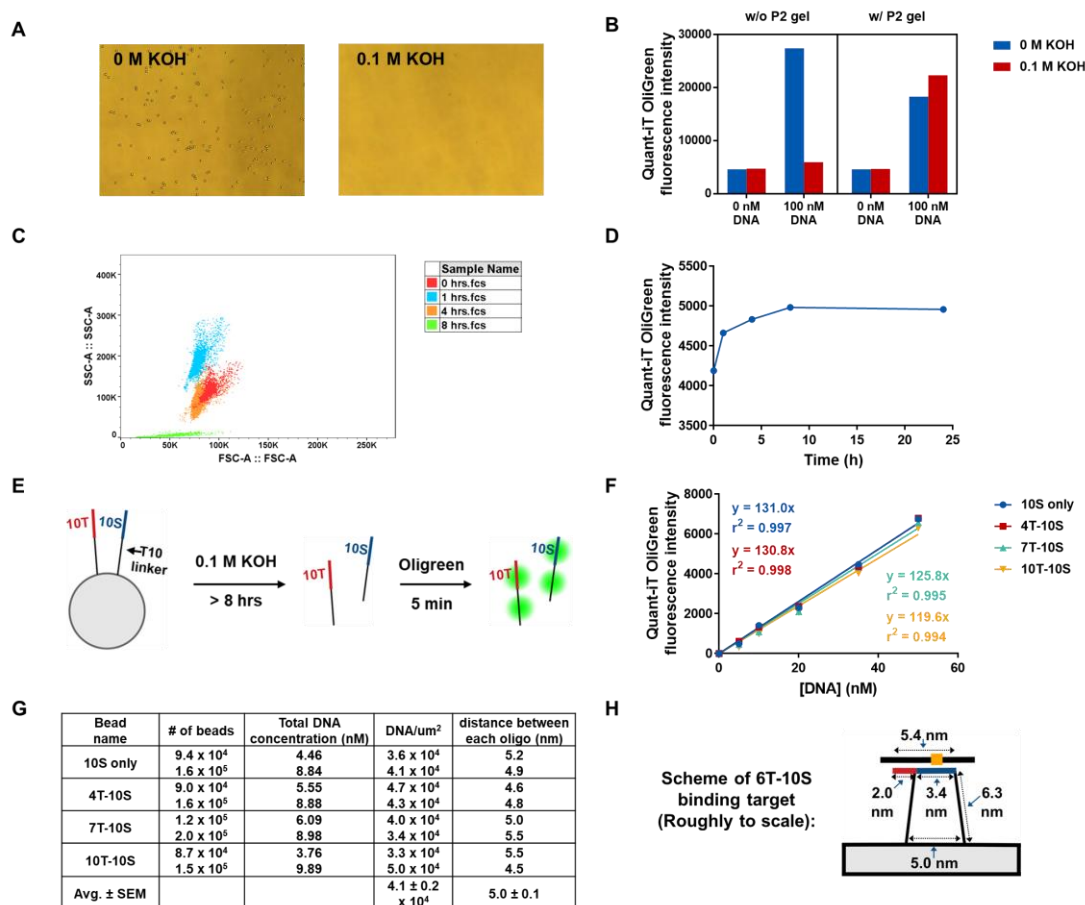


Figure A3.9. Flow cytometry gating strategy to isolate singlet beads for analysis. (a) For each sample, all events are first plotted on a side scatter area vs forward scatter area plot and a “singlets area” gate is drawn to approximately include just the singlet bead population. (b) The cells included in the “singlets area” gate are then plotted on a side scatter height vs forward scatter height plot and a second gate, the “singlets height” gate, is drawn to more accurately include just the singlet bead population. The cells included in the “singlets height” gate are then used as the final singlet bead population shown in the representative histograms and from which the median fluorescence intensity values were calculated.

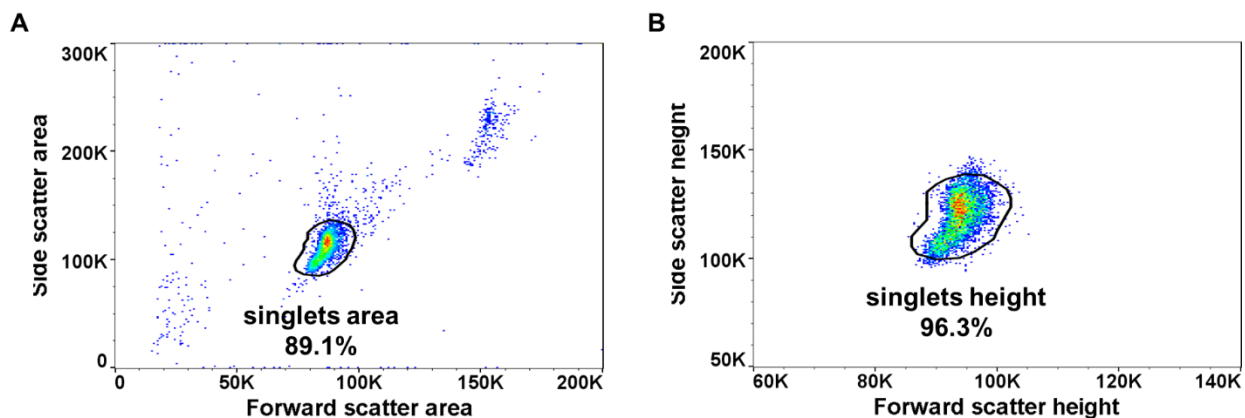


Figure A3.10. Representative histograms for all bead combinations binding the no spacer targets. (a and b) Representative histograms for all bead combinations binding the no spacer G12C target (a) and WT target (b) with one plot for each heatmap column from **Figures 3.2C and 3.2D**.

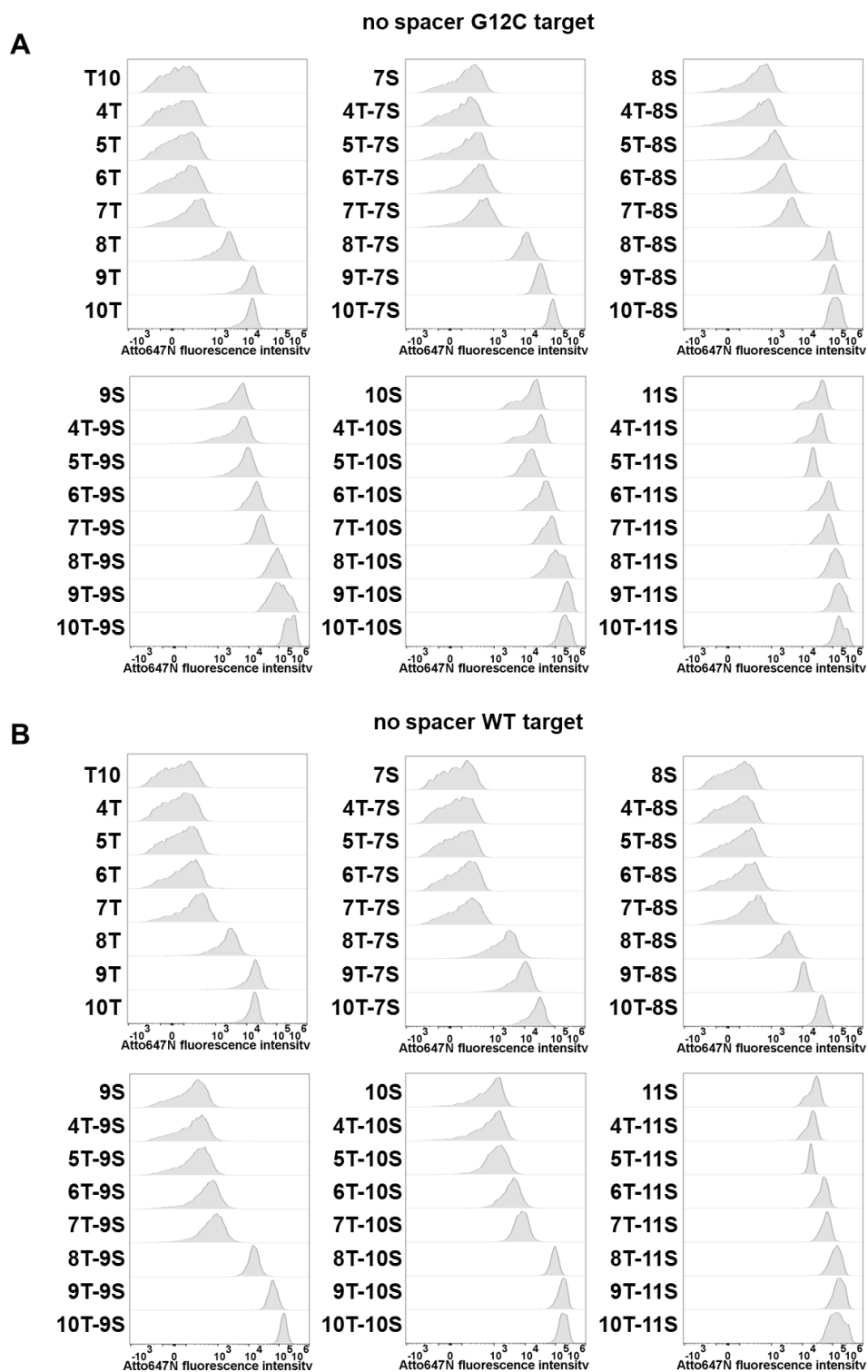


Figure A3.11. Fluorescence microscopy images of beads hybridized to target. Brightfield and fluorescence microscopy images of full-length complement beads hybridized to 1 nM of Atto647N-labeled omicron target or no target.

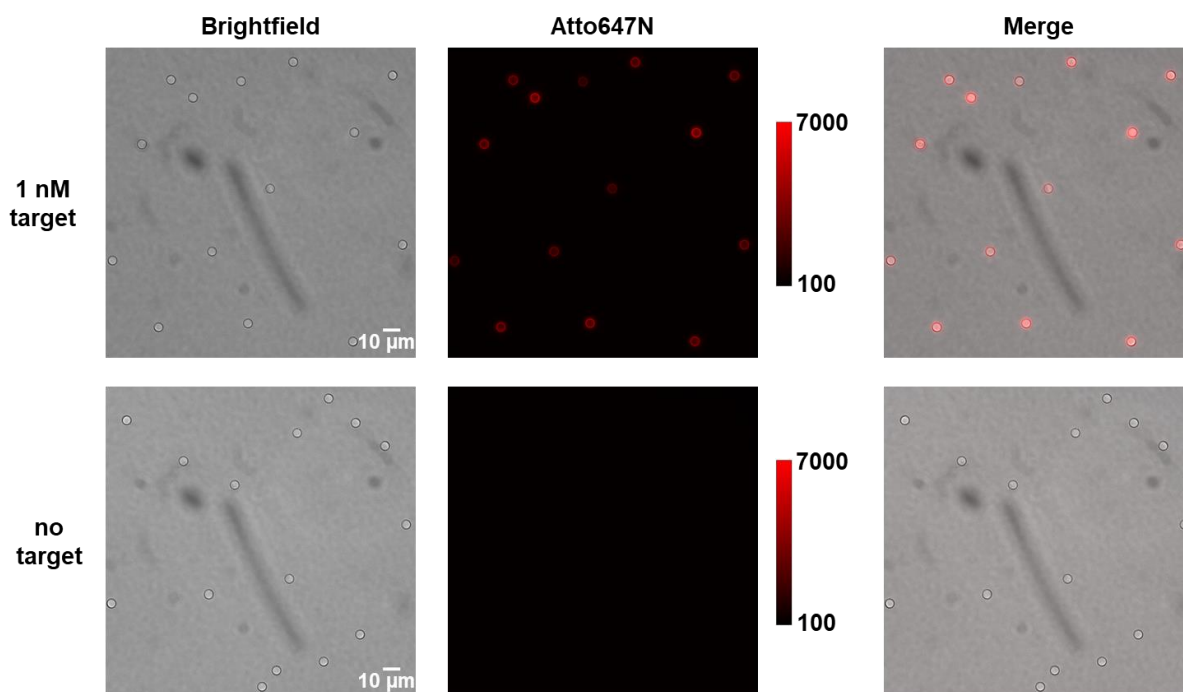


Figure A3.12. Impact of spacer length and type on binding of 8T, 8S, and 8T-8S beads. (a) Representative histograms for the 8T-8S beads binding the WT or G12C version of each of the different spacer length and spacer type targets. (b) Representative histograms for the 8T, 8S, and 8T-8S beads binding the G12C version of each of the different spacer length and spacer type targets. (c and d) A simplified hypothetical illustration showing the 8T (c) and 8S (d) beads binding multivalently to an internal spacer-containing target. (e and f) Scheme showing the possible base pairs formed for the 8T bead binding multivalently to the target (e) and the 8S bead binding multivalently to the target (f). (g-j) Measured median fluorescence intensity values for the 8T (g and i) and 8S (h and j) beads binding the G12C (g and h) or WT (i and j) version of each of the different spacer length and spacer type targets. Error bars represent standard error of the mean.

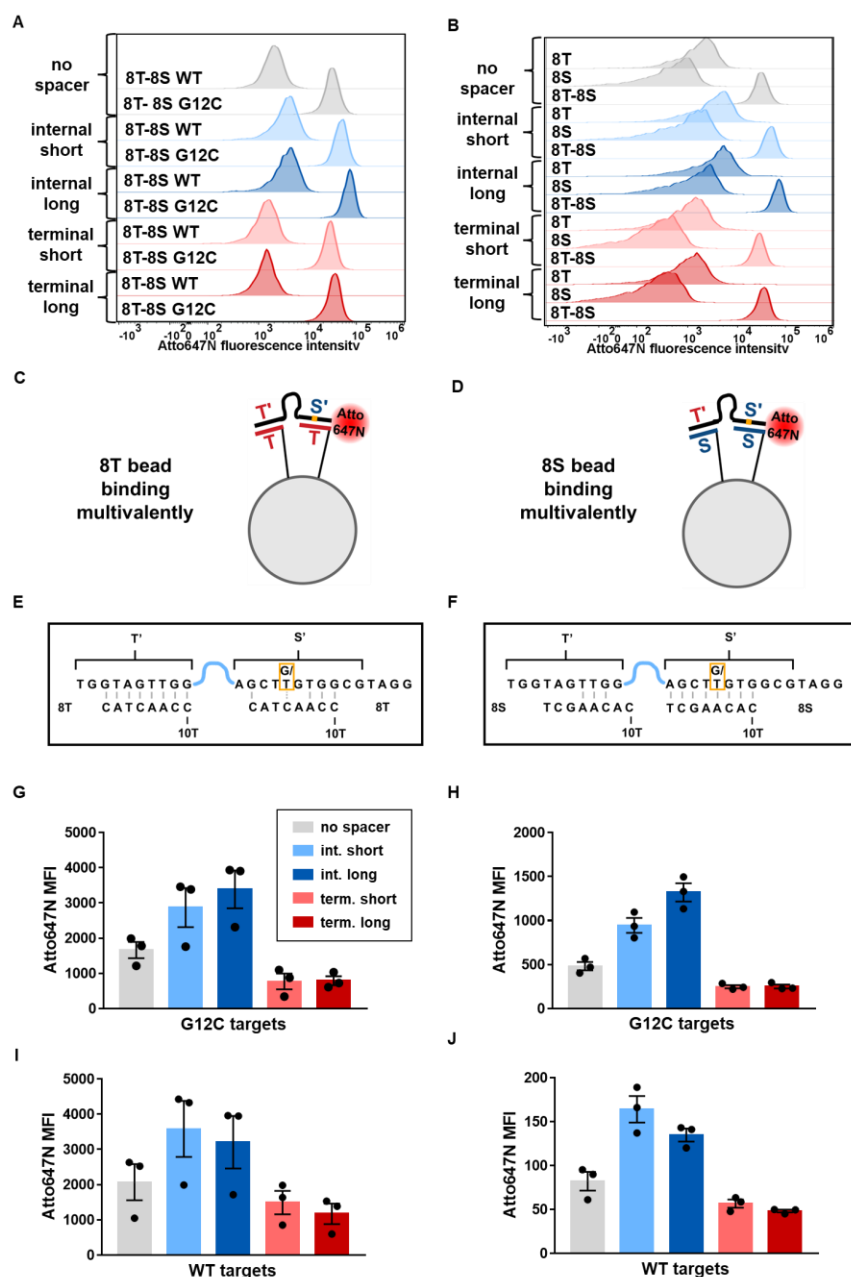


Figure A3.13. Impact of linker orientation on $n=1$ bead binding and representative histograms for $n=2$ beads binding WT targets. (a) Scheme illustrating the possible binding interaction of the 5' 8T, 3' 8T, 5' 8S, and 3' 8S beads binding the no spacer G12C target monovalently. (b) Measured median fluorescence intensity values for the 5' 8T, 3' 8T, 5' 8S, and 3' 8S beads binding the no spacer G12C target. (c) Representative histograms for 8T-8S beads with head-to-tail, head-to-head, or tail-to-tail orientation binding the WT target with no spacer, short spacer, or long spacer. (d) Measured median fluorescence intensity values for 8T-8S beads with head-to-tail, head-to-head, or tail-to-tail orientation binding the WT target with no spacer, short spacer, or long spacer. (e) Representative histograms for 8T-8S beads with head-to-tail, head-to-head, or tail-to-tail orientation binding the G12C and WT no spacer targets. (f) Measured discrimination factors for 8T-8S beads with head-to-tail, head-to-head, or tail-to-tail orientation binding the no spacer, short spacer, or long spacer targets. Error bars represent standard error of the mean. Values were compared using paired one-way ANOVA with multiple comparisons follow-up tests ($^{ns}P > 0.05$, $^{*}P < 0.05$).

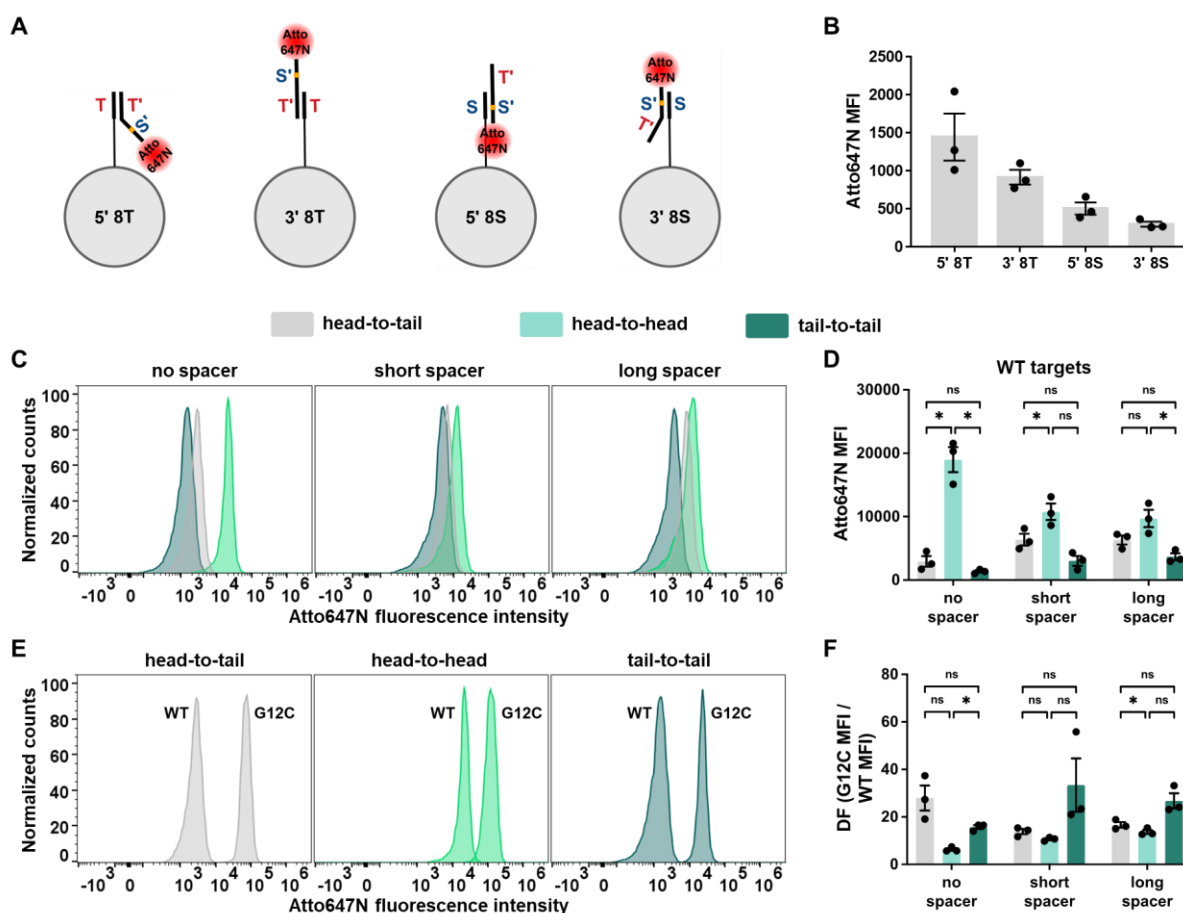


Figure A3.14. Representative histograms and results for all bead combinations binding the SNP₁/SNP₂, WT₁/SNP₂, SNP₁/WT₂, and WT₁/WT₂ targets. (a and b) Scheme showing the sequences, anchor location, and spacer length for each bead combination with the head-to-tail orientation (a) or head-to-head orientation (b) and corresponding representative histograms for each bead combination binding the SNP₁/SNP₂, WT₁/SNP₂, SNP₁/WT₂, and WT₁/WT₂ targets. (c and d) Measured discrimination factors for SNP₁, SNP₂, or SNP₁ + SNP₂ for each bead combination with the head-to-tail orientation (c) or head-to-head orientation (d). Error bars represent standard error of the mean.

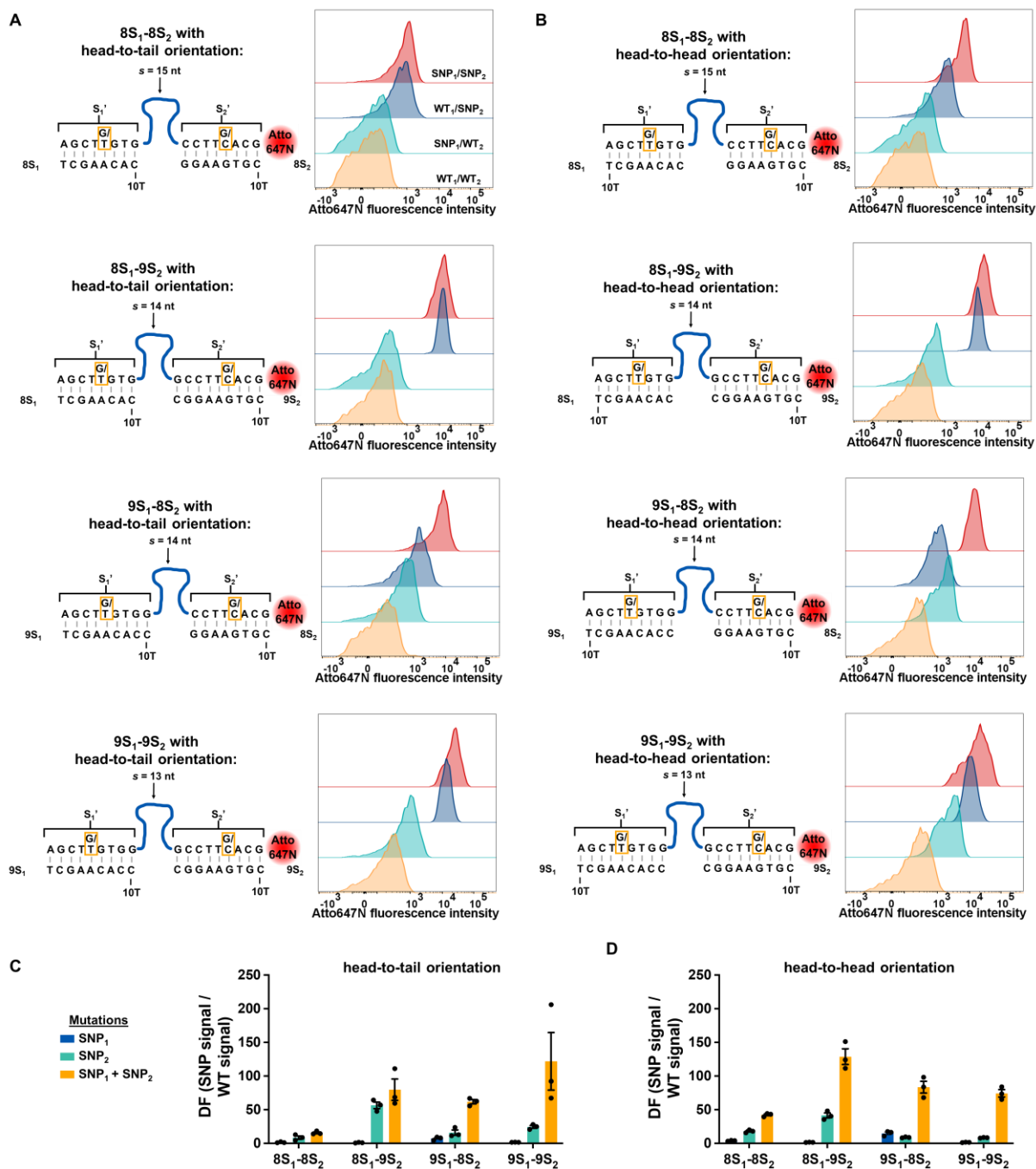


Figure A3.15. Representative histograms and results for all bead combinations binding the model SARS-CoV-2 targets. (a-d) Scheme showing the sequences, anchor location, and spacer length, and corresponding representative histograms for the 8S₁-8S₂ (a), 8S₁-9S₂ (b), 9S₁-8S₂ (c), and 9S₁-9S₂ (d) beads binding the original, alpha, and omicron strain targets. (e) Measured median fluorescence intensity values for each bead combination binding the three targets. (f) Measured discrimination factors for the omicron target versus the original or alpha target for each bead combination. Error bars represent standard error of the mean.

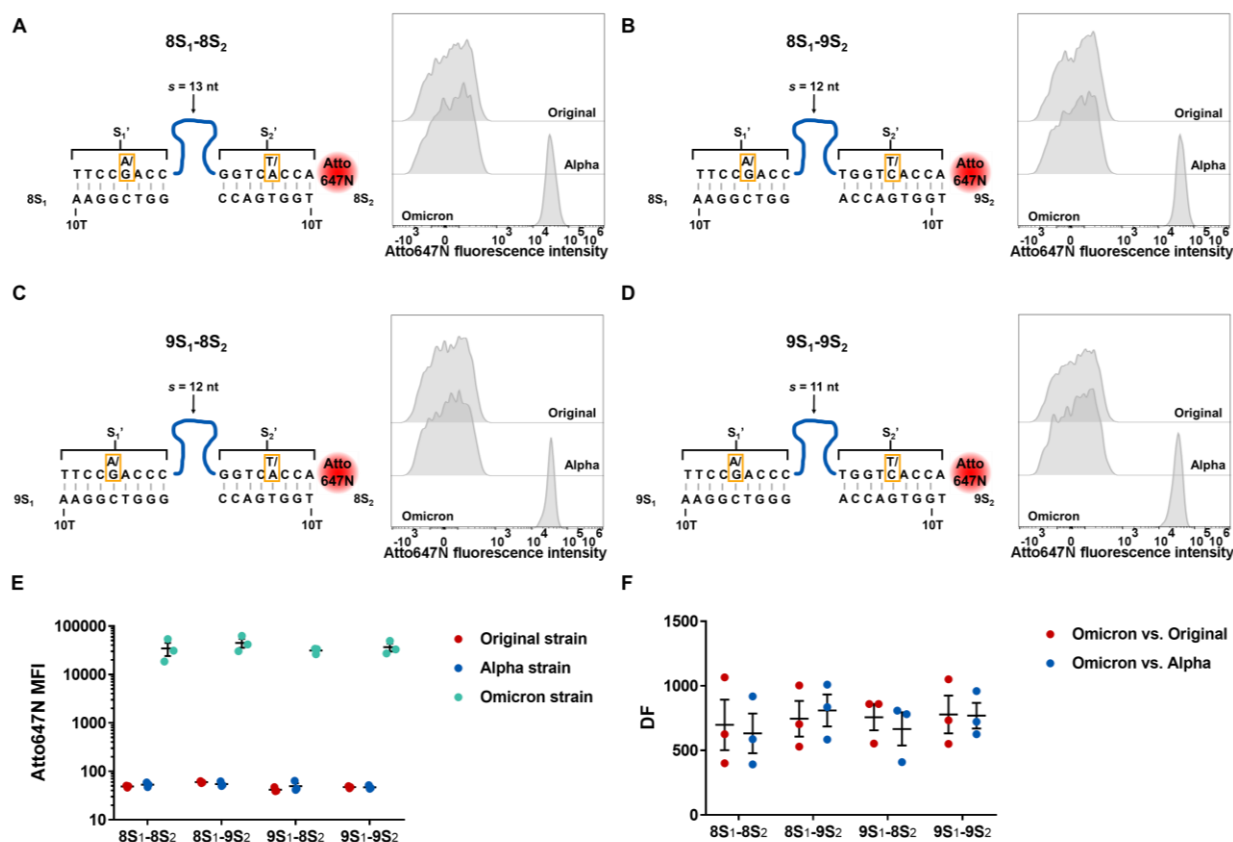


Table A3.2. Average median fluorescence intensity \pm standard error of the mean values for all bead combinations binding no spacer G12C target. The median fluorescence intensity of the no spacer G12C target binding to each bead combination was measured in three independent experiments. The table below shows the calculated average and standard error of the mean for the three median fluorescence intensity values.

	No S	7S	8S	9S	10S	11S
No T	59 \pm 4	154 \pm 13	517 \pm 73	4522 \pm 540	15126 \pm 1789	35194 \pm 935
4T	54 \pm 2	120 \pm 6	472 \pm 33	4939 \pm 328	22647 \pm 423	34573 \pm 1503
5T	93 \pm 10	161 \pm 26	1076 \pm 78	8951 \pm 560	14087 \pm 589	40989 \pm 10285
6T	106 \pm 2	298 \pm 19	1779 \pm 89	15111 \pm 396	42858 \pm 1714	62873 \pm 2816
7T	235 \pm 13	424 \pm 33	3658 \pm 256	20935 \pm 2115	51019 \pm 5841	68290 \pm 1784
8T	2369 \pm 118	10610 \pm 920	53619 \pm 7605	81596 \pm 9674	97022 \pm 8979	125280 \pm 4197
9T	14828 \pm 1224	28731 \pm 5128	76229 \pm 16169	112663 \pm 27240	195151 \pm 22429	154005 \pm 4026
10T	13744 \pm 1450	81537 \pm 4328	148605 \pm 14991	213091 \pm 9045	205227 \pm 5447	176200 \pm 2110

Table A3.3. Average median fluorescence intensity \pm standard error of the mean values for all bead combinations binding no spacer WT target. The median fluorescence intensity of the no spacer WT target binding to each bead combination was measured in three independent experiments. The table below shows the calculated average and standard error of the mean for the three median fluorescence intensity values.

	No S	7S	8S	9S	10S	11S
No T	56 \pm 4	64 \pm 1	72 \pm 3	174 \pm 12	661 \pm 97	24728 \pm 962
4T	61 \pm 7	64 \pm 3	74 \pm 3	213 \pm 20	909 \pm 72	21385 \pm 1218
5T	109 \pm 10	75 \pm 9	113 \pm 4	251 \pm 14	1225 \pm 78	29084 \pm 6095
6T	125 \pm 1	118 \pm 3	170 \pm 5	475 \pm 21	4040 \pm 346	50386 \pm 2148
7T	208 \pm 19	139 \pm 4	277 \pm 11	647 \pm 121	7234 \pm 404	62561 \pm 1675
8T	1955 \pm 635	2262 \pm 117	2826 \pm 58	10898 \pm 2346	81904 \pm 7503	124810 \pm 3137
9T	13597 \pm 2110	8693 \pm 1292	9635 \pm 1436	60413 \pm 8188	159425 \pm 13751	154441 \pm 13439
10T	18205 \pm 1140	25845 \pm 523	38530 \pm 3431	130354 \pm 5038	166468 \pm 18349	166092 \pm 14714

Table A3.4. Average discrimination factor \pm standard error of the mean values for all bead combinations binding no spacer targets. The median fluorescence intensity of the no spacer G12C (Table A3.2) and WT (Table A3.3) targets binding to each bead combination was measured in three independent experiments. The discrimination factor was calculated for each independent replicate by dividing the G12C MFI value by the WT MFI value. The table below shows the calculated average and standard error of the mean for the three discrimination factor values.

	No S	7S	8S	9S	10S	11S
No T	1.0 \pm 0.0	2.4 \pm 0.2	7.2 \pm 0.8	25.9 \pm 1.4	23.2 \pm 2.0	1.4 \pm 0.1
4T	0.9 \pm 0.1	1.9 \pm 0.1	6.4 \pm 0.3	23.3 \pm 0.6	25.2 \pm 2.0	1.6 \pm 0.0
5T	0.8 \pm 0.0	2.1 \pm 0.2	9.5 \pm 0.7	35.6 \pm 1.4	11.5 \pm 0.3	1.4 \pm 0.1
6T	0.8 \pm 0.0	2.5 \pm 0.2	10.5 \pm 0.8	31.8 \pm 0.6	10.7 \pm 0.5	1.2 \pm 0.0
7T	1.2 \pm 0.1	3.1 \pm 0.3	13.2 \pm 0.6	33.9 \pm 4.4	7.1 \pm 0.8	1.1 \pm 0.0
8T	1.8 \pm 1.0	4.7 \pm 0.2	18.9 \pm 2.3	8.0 \pm 1.3	1.2 \pm 0.2	1.0 \pm 0.0
9T	1.1 \pm 0.2	3.3 \pm 0.3	7.9 \pm 1.1	1.8 \pm 0.2	1.2 \pm 0.1	1.0 \pm 0.1
10T	0.8 \pm 0.0	3.2 \pm 0.2	3.9 \pm 0.6	1.6 \pm 0.0	1.3 \pm 0.1	1.1 \pm 0.1

Table A3.5. Average cooperativity factor \pm standard error of the mean values for all bead combinations binding no spacer G12C target. The median fluorescence intensity of the no spacer G12C (Table A3.2) target binding to each bead combination was measured in three independent experiments. The average cooperativity factor was calculated by dividing the average $n=2$ MFI by the average of the average corresponding $n=1$ MFIs. The standard error of the mean was calculated by propagating the SEMs from the three independent MFI measurements for the $n=2$ beads and the $n=1$ beads. The table below shows the calculated average and standard error of the mean cooperativity factor.

	7S	8S	9S	10S	11S
4T	1.2 \pm 0.1	1.7 \pm 0.2	2.2 \pm 0.3	3.0 \pm 0.4	2.0 \pm 0.1
5T	1.3 \pm 0.2	3.5 \pm 0.5	3.9 \pm 0.5	1.9 \pm 0.2	2.3 \pm 0.6
6T	2.3 \pm 0.2	5.7 \pm 0.7	6.5 \pm 0.8	5.6 \pm 0.7	3.6 \pm 0.2
7T	2.2 \pm 0.2	9.7 \pm 1.2	8.8 \pm 1.3	6.6 \pm 1.1	3.9 \pm 0.1
8T	8.4 \pm 0.8	37.2 \pm 5.6	23.7 \pm 3.4	11.1 \pm 1.5	6.7 \pm 0.3
9T	3.8 \pm 0.8	9.9 \pm 2.3	11.6 \pm 2.9	13.0 \pm 1.8	6.2 \pm 0.2
10T	11.7 \pm 1.4	20.8 \pm 3.0	23.3 \pm 2.2	14.2 \pm 1.2	7.2 \pm 0.3

3.6. References

1. Gunderson, K. L.; Steemers, F. J.; Lee, G.; Mendoza, L. G.; Chee, M. S., A genome-wide scalable SNP genotyping assay using microarray technology. *Nat Genet* **2005**, *37* (5), 549-54.
2. Koltai, H.; Weingarten-Baror, C., Specificity of DNA microarray hybridization: characterization, effectors and approaches for data correction. *Nucleic Acids Res* **2008**, *36* (7), 2395-405.
3. Tyagi, S.; Bratu, D. P.; Kramer, F. R., Multicolor molecular beacons for allele discrimination. *Nat Biotechnol* **1998**, *16* (1), 49-53.
4. Tulpan, D.; Andronescu, M.; Chang, S. B.; Shortreed, M. R.; Condon, A.; Hoos, H. H.; Smith, L. M., Thermodynamically based DNA strand design. *Nucleic Acids Res* **2005**, *33* (15), 4951-64.
5. Chen, X.; Liu, N.; Liu, L.; Chen, W.; Chen, N.; Lin, M.; Xu, J.; Zhou, X.; Wang, H.; Zhao, M.; Xiao, X., Thermodynamics and kinetics guided probe design for uniformly sensitive and specific DNA hybridization without optimization. *Nat Commun* **2019**, *10* (1), 4675.
6. Zhang, D. Y.; Chen, S. X.; Yin, P., Optimizing the specificity of nucleic acid hybridization. *Nat Chem* **2012**, *4* (3), 208-14.
7. Wang, J. S.; Zhang, D. Y., Simulation-guided DNA probe design for consistently ultraspecific hybridization. *Nat Chem* **2015**, *7* (7), 545-53.
8. Tyagi, S.; Kramer, F. R., Molecular beacons: probes that fluoresce upon hybridization. *Nat Biotechnol* **1996**, *14* (3), 303-8.
9. Suzuki, S.; Ono, N.; Furusawa, C.; Kashiwagi, A.; Yomo, T., Experimental optimization of probe length to increase the sequence specificity of high-density oligonucleotide microarrays. *BMC Genomics* **2007**, *8*, 373.
10. Kolpashchikov, D. M., Binary probes for nucleic acid analysis. *Chem Rev* **2010**, *110* (8), 4709-23.
11. Taton, T. A.; Mirkin, C. A.; Letsinger, R. L., Scanometric DNA array detection with nanoparticle probes. *Science* **2000**, *289* (5485), 1757-60.
12. Alhasan, A. H.; Kim, D. Y.; Daniel, W. L.; Watson, E.; Meeks, J. J.; Thaxton, C. S.; Mirkin, C. A., Scanometric microRNA array profiling of prostate cancer markers using spherical nucleic acid-gold nanoparticle conjugates. *Anal Chem* **2012**, *84* (9), 4153-60.
13. Diehl, F.; Li, M.; Dressman, D.; He, Y.; Shen, D.; Szabo, S.; Diaz, L. A., Jr.; Goodman, S. N.; David, K. A.; Juhl, H.; Kinzler, K. W.; Vogelstein, B., Detection and quantification of mutations in the plasma of patients with colorectal tumors. *Proc Natl Acad Sci U S A* **2005**, *102* (45), 16368-73.
14. Schena, M.; Shalon, D.; Davis, R. W.; Brown, P. O., Quantitative monitoring of gene expression patterns with a complementary DNA microarray. *Science* **1995**, *270* (5235), 467-70.
15. Curk, T.; Brackley, C. A.; Farrell, J. D.; Xing, Z.; Joshi, D.; Direito, S.; Bren, U.; Angioletti-Uberti, S.; Dobnikar, J.; Eiser, E.; Frenkel, D.; Allen, R. J., Computational design of probes to detect bacterial genomes by multivalent binding. *Proc Natl Acad Sci U S A* **2020**, *117* (16), 8719-8726.
16. Magdalena Estirado, E.; Aleman Garcia, M. A.; Schill, J.; Brunsveld, L., Multivalent Ultrasensitive Interfacing of Supramolecular 1D Nanoplatfoms. *J Am Chem Soc* **2019**, *141* (45), 18030-18037.

17. Deal, B. R.; Ma, R.; Ma, V. P.; Su, H.; Kindt, J. T.; Salaita, K., Engineering DNA-Functionalized Nanostructures to Bind Nucleic Acid Targets Heteromultivalently with Enhanced Avidity. *J Am Chem Soc* **2020**, *142* (21), 9653-9660.
18. Regan, J. F.; Kamitaki, N.; Legler, T.; Cooper, S.; Klitgord, N.; Karlin-Neumann, G.; Wong, C.; Hodges, S.; Koehler, R.; Tzonev, S.; McCarroll, S. A., A rapid molecular approach for chromosomal phasing. *PLoS One* **2015**, *10* (3), e0118270.
19. Zheng, G. X.; Lau, B. T.; Schnall-Levin, M.; Jarosz, M.; Bell, J. M.; Hindson, C. M.; Kyriazopoulou-Panagiotopoulou, S.; Masquelier, D. A.; Merrill, L.; Terry, J. M.; Mudivarti, P. A.; Wyatt, P. W.; Bharadwaj, R.; Makarewicz, A. J.; Li, Y.; Belgrader, P.; Price, A. D.; Lowe, A. J.; Marks, P.; Vurens, G. M.; Hardenbol, P.; Montesclaros, L.; Luo, M.; Greenfield, L.; Wong, A.; Birch, D. E.; Short, S. W.; Bjornson, K. P.; Patel, P.; Hopmans, E. S.; Wood, C.; Kaur, S.; Lockwood, G. K.; Stafford, D.; Delaney, J. P.; Wu, I.; Ordonez, H. S.; Grimes, S. M.; Greer, S.; Lee, J. Y.; Belhocine, K.; Giorda, K. M.; Heaton, W. H.; McDermott, G. P.; Bent, Z. W.; Meschi, F.; Kondov, N. O.; Wilson, R.; Bernate, J. A.; Gauby, S.; Kindwall, A.; Bermejo, C.; Fehr, A. N.; Chan, A.; Saxonov, S.; Ness, K. D.; Hindson, B. J.; Ji, H. P., Haplotyping germline and cancer genomes with high-throughput linked-read sequencing. *Nat Biotechnol* **2016**, *34* (3), 303-11.
20. Song, T.; Eshra, A.; Shah, S.; Bui, H.; Fu, D.; Yang, M.; Mokhtar, R.; Reif, J., Fast and compact DNA logic circuits based on single-stranded gates using strand-displacing polymerase. *Nat Nanotechnol* **2019**, *14* (11), 1075-1081.
21. Schueder, F.; Lara-Gutierrez, J.; Haas, D.; Beckwith, K. S.; Yin, P.; Ellenberg, J.; Jungmann, R., Super-Resolution Spatial Proximity Detection with Proximity-PAINT. *Angew Chem Int Ed Engl* **2021**, *60* (2), 716-720.
22. Chandrasekaran, A. R.; MacIsaac, M.; Dey, P.; Levchenko, O.; Zhou, L.; Andres, M.; Dey, B. K.; Halvorsen, K., Cellular microRNA detection with miRacles: microRNA- activated conditional looping of engineered switches. *Sci Adv* **2019**, *5* (3), eaau9443.
23. Chen, N.; Schrijver, I., Allelic discrimination of cis-trans relationships by digital polymerase chain reaction: GJB2 (p.V27I/p.E114G) and CFTR (p.R117H/5T). *Genet Med* **2011**, *13* (12), 1025-31.
24. Fan, T. W.; Yu, H. L. L.; Hsing, I. M., Conditional Displacement Hybridization Assay for Multiple SNP Phasing. *Anal Chem* **2017**, *89* (18), 9961-9966.
25. Yu, H. A.; Sima, C. S.; Shen, R.; Kass, S.; Gainor, J.; Shaw, A.; Hames, M.; Iams, W.; Aston, J.; Lovly, C. M.; Horn, L.; Lydon, C.; Oxnard, G. R.; Kris, M. G.; Ladanyi, M.; Riely, G. J., Prognostic impact of KRAS mutation subtypes in 677 patients with metastatic lung adenocarcinomas. *J Thorac Oncol* **2015**, *10* (3), 431-7.
26. Bossert, D.; Urban, D. A.; Maceroni, M.; Ackermann-Hirschi, L.; Haeni, L.; Yajan, P.; Spuch-Calvar, M.; Rothen-Rutishauser, B.; Rodriguez-Lorenzo, L.; Petri-Fink, A.; Schwab, F., A hydrofluoric acid-free method to dissolve and quantify silica nanoparticles in aqueous and solid matrices. *Sci Rep* **2019**, *9* (1), 7938.
27. Mammen, M.; Choi, S. K.; Whitesides, G. M., Polyvalent Interactions in Biological Systems: Implications for Design and Use of Multivalent Ligands and Inhibitors. *Angew Chem Int Ed Engl* **1998**, *37* (20), 2754-2794.
28. Kane, R. S., Thermodynamics of multivalent interactions: influence of the linker. *Langmuir* **2010**, *26* (11), 8636-40.
29. Yakovchuk, P.; Protozanova, E.; Frank-Kamenetskii, M. D., Base-stacking and base-pairing contributions into thermal stability of the DNA double helix. *Nucleic Acids Res* **2006**, *34* (2), 564-74.

30. Lane, M. J.; Paner, T.; Kashin, I.; Faldasz, B. D.; Li, B.; Gallo, F. J.; Benight, A. S., The thermodynamic advantage of DNA oligonucleotide 'stacking hybridization' reactions: energetics of a DNA nick. *Nucleic Acids Res* **1997**, *25* (3), 611-7.
31. Maldonado-Rodriguez, R.; Espinosa-Lara, M.; Loyola-Abitia, P.; Beattie, W. G.; Beattie, K. L., Mutation detection by stacking hybridization on genosensor arrays. *Mol Biotechnol* **1999**, *11* (1), 13-25.
32. Walter, A. E.; Turner, D. H.; Kim, J.; Lyttle, M. H.; Muller, P.; Mathews, D. H.; Zuker, M., Coaxial stacking of helices enhances binding of oligoribonucleotides and improves predictions of RNA folding. *Proc Natl Acad Sci U S A* **1994**, *91* (20), 9218-22.
33. Munoz-Maldonado, C.; Zimmer, Y.; Medova, M., A Comparative Analysis of Individual RAS Mutations in Cancer Biology. *Front Oncol* **2019**, *9*, 1088.
34. Lee Yu, H. L.; Fan, T. W.; Hsing, I. M., Oligonucleotide hybridization with magnetic separation assay for multiple SNP phasing. *Anal Chim Acta X* **2020**, *5*, 100050.
35. Zhuang, X.; Lee Yu, H. L.; Hsing, I. M., Toehold probe-based interrogation for haplotype phasing of long nucleic acid strands. *Anal Methods* **2020**, *12* (34), 4185-4190.
36. Chang, W.; Liu, W.; Shen, H.; Chen, S.; Liao, P.; Liu, Y., Molecular AND logic gate for multiple single-nucleotide mutations detection based on CRISPR/Cas9n system-triggered signal amplification. *Anal Chim Acta* **2020**, *1112*, 46-53.
37. Gao, Y.; Wolf, L. K.; Georgiadis, R. M., Secondary structure effects on DNA hybridization kinetics: a solution versus surface comparison. *Nucleic Acids Res* **2006**, *34* (11), 3370-7.
38. Bazrafshan, A.; Kyriazi, M. E.; Holt, B. A.; Deng, W.; Piranej, S.; Su, H.; Hu, Y.; El-Sagheer, A. H.; Brown, T.; Kwong, G. A.; Kanaras, A. G.; Salaita, K., DNA Gold Nanoparticle Motors Demonstrate Processive Motion with Bursts of Speed Up to 50 nm Per Second. *ACS Nano* **2021**, *15* (5), 8427-8438.
39. Huskens, J.; Mulder, A.; Auletta, T.; Nijhuis, C. A.; Ludden, M. J.; Reinhoudt, D. N., A model for describing the thermodynamics of multivalent host-guest interactions at interfaces. *J Am Chem Soc* **2004**, *126* (21), 6784-97.
40. Karadeema, R. J.; Stancescu, M.; Steidl, T. P.; Bertot, S. C.; Kolpashchikov, D. M., The owl sensor: a 'fragile' DNA nanostructure for the analysis of single nucleotide variations. *Nanoscale* **2018**, *10* (21), 10116-10122.
41. Zhou, L.; Hayden, A.; Chandrasekaran, A. R.; Vilcapoma, J.; Cavaliere, C.; Dey, P.; Mao, S.; Sheng, J.; Dey, B. K.; Rangan, P.; Halvorsen, K., Sequence-selective purification of biological RNAs using DNA nanoswitches. *Cell Rep Methods* **2021**, *1* (8).
42. Hail, M.; Elliott, B.; Anderson, K., High Throughput Analysis of Oligonucleotides Using Automated Electrospray Ionization Mass Spectrometry. *Am Biotechnol Lab* **2004**, *12*, 12-14.

Chapter 4

Summary and Future Outlook

4.1. Summary

This dissertation began with an overview of multivalent DNA hybridization, including the fundamental parameters that dictate a successful multivalent interaction and the applications enabled by this concept in the fields of artificial motors, sensing, and biological investigations. To further apply multivalent hybridization towards improving the sensitivity and specificity of binding to single-stranded (ss) nucleic acid targets, we asked whether heteromultivalent (heteroMV) DNA-functionalized structures could hybridize to such targets multivalently with improved binding properties. We hypothesized that engineering heteroMV structures would offer important advantages in applications such as gene regulation, genetic diagnostics, and broadly in nanotechnology.

Based on this question and hypothesis, **Chapter 2** described how we functionalized gold nanoparticles (AuNP) with a heteroMV display of up to six unique DNA oligonucleotide sequences and characterized the properties of their multivalent binding to a ~90 nucleotide ssDNA target. This work began by measuring the melting temperature of the target when it bound to particles that presented a random arrangement of many copies of 1-6 unique DNA sequences (n). We observed increasing melting temperatures as n increased initially, followed by a plateau and subsequent decrease in T_m as n increased further. We hypothesized that the random arrangement of the sequences limited the overall binding valency and T_m increase. To further increase the overall binding avidity of the heteroMV particles, we developed a DNA-templating method to control the relative position of each unique oligo sequence on the particle, yielding patterned heteroMV particles. Using the van't Hoff relationship we further quantified the thermodynamic parameters of the patterned particles and compared them to particles with random oligo arrangement. Significantly, we found that $n=6$ patterned particles bound the target with an ~15 order-of-

magnitude higher binding avidity than $n=6$ random particles. Moreover, based on mathematical modeling and experimental results, we concluded that when n is lower the spatial arrangement of the oligos on the particle is less significant and that random particles should still effectively bind multivalently.

Continuing our investigation into multivalent DNA hybridization, **Chapter 3** presented our findings regarding the specificity and cooperativity of heteroMV binding. In this work, we explored the design of heteroMV particles that bivalently bound to targets that contained 1 or 2 single nucleotide polymorphisms (SNPs). Through modeling, we predicted that tuning the affinity of the two oligos would impact the ability of the particles to detect the presence of a single mutation, to only bind when both ligand-receptor pairs are hybridizing cooperatively, or to bind specifically to targets when two mutations are present. To support these findings with experimental data, we synthesized DNA-functionalized 5 μm silica particles and measured relative binding of each particle-target combination using flow cytometry. We found that hetero-bivalent binding can be used to precisely tune discrimination for a single SNP when a short, 5 nt tuning oligo accompanies a 9 nt SNP-binding oligo on the particle and to enable highly cooperative binding when a pair of 8 nt oligos are used. Furthermore, we investigated how increasing the distance between the two target binding regions would impact the binding properties. These experiments demonstrated that heteroMV hybridization binding cooperativity can actually be enhanced when spacers are added to the target. We hypothesize that is likely due to the target being able to access more ligands on the particle surface, thus increasing the effective concentration. It was also identified that altering the relative binding orientation of the two oligos immobilized on the particle can further tune binding affinity and cooperativity. Ultimately, we revealed that heteroMV binding can be used to detect the presence of two mutations on a single target, even when separated by over 20 nt. This

finding suggests that heteroMV hybridization has significant potential in diagnostics as it offers the ability to determine if two heterozygous mutations are in the cis or trans orientation and to improve detection of rapidly mutating viral strains.

Overall, the experimental findings presented in this dissertation provide a useful guide for future efforts to design DNA-functionalized structures that hybridize heteromultivalently to single-stranded nucleic acid targets. Several important capabilities of heteroMV-hybridizing particles were also described. For example, heteroMV particles can bind to long targets with enhanced avidity through avoiding the harmful effects of ligand secondary structure formation and without increasing the size of the particle. Moreover, heteroMV particles can bind with highly tunable affinity, resulting in high binding specificity and cooperativity, to any biologically relevant target. Due to these capabilities, we envision that heteroMV DNA hybridization has many promising applications in therapeutics, diagnostics, and throughout the field of nanotechnology.

4.2. Future Outlook for Multivalent DNA Hybridization

4.2.1. Further Applications for Multivalent DNA Hybridization in Diagnostics

All the work described in **Chapters 2 and 3** involved measuring binding of fluorophore-labeled synthetic target oligonucleotides. However, to apply multivalent DNA hybridization in diagnostics, it will be necessary to establish a sensitive readout method to allow detection of unlabeled biological targets. For this purpose, we have tested several techniques thus far. The simplest approach that we have explored is to use DNA intercalating dyes, such as SybrGreen and EvaGreen, that become fluorescent upon interaction with double-stranded DNA. We hypothesized that we could simply incubate our DNA-functionalized microparticles that are bound to unlabeled

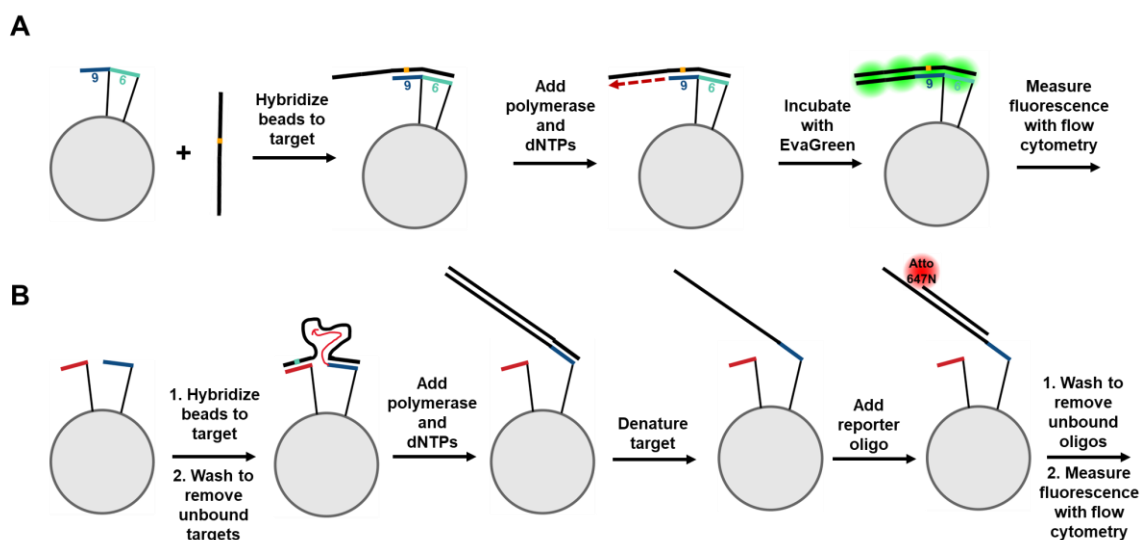


Figure 4.1. Polymerase-mediated methods to detect unlabeled targets. Schemes describing approaches that we tested to detect unlabeled targets more sensitively by using a polymerase to (a) generate a longer duplex with the target and boost EvaGreen signal or (b) to extend the particle-linked oligo and create a region for a fluorescent complement to bind.

targets with these dyes and then measure the fluorescence increase using flow cytometry to quantify the number of targets bound to each particle.

While experimentally simple and fast, we found that the sensitivity of these dyes was too low for our experiments. Specifically, we observed a minimal fluorescence increase with flow cytometry when EvaGreen was incubated with particles with high concentrations of unlabeled targets compared to no targets. However, when using ligands that could form up to 21 bp duplexes with the target, we did observe >10-fold increases in fluorescence compared to when no target was added. In general, we found that the EvaGreen signal was sensitive to the length of the particle-target duplex, as the fluorescence signal correlated with duplex length even when the same number of duplexes were present on each particle. Based on this observation, we tested whether we could use Klenow Fragment polymerase, which is active at room temperature and is compatible with short primer sequences, to increase the length of the particle-target duplex following binding

(**Figure 4.1A**). This approach is possible whenever the target is longer than the particle-linked oligos. We did confirm that the polymerase could extend the length of the duplex in our assay conditions, even with primers less than 10 nt, though the EvaGreen fluorescence signals remained relatively low despite the longer duplexes.

An alternative approach to detecting unlabeled targets that we explored was to couple the polymerase method with fluorescent reporter strands that bound to the particles following successful polymerization. While it is straightforward to simply bind a fluorescent oligonucleotide to an adjacent unbound region of the target, this technique results in loss of fluorescent signal when the target dehybridizes. This was a concern in our case, as we were interested in detecting SNPs and thus the binding affinity for the target was relatively weak to ensure high specificity. Therefore, rather than binding a fluorescent oligo to the target after it bound the particle, we hypothesized that we could bind a fluorescent oligo directly to the particle by hybridizing with a polymerase-extended region of the oligo immobilized on the particle (**Figure 4.1B**). This approach proved to be much more sensitive than EvaGreen as we could detect low concentrations of unlabeled targets with fluorescent signals that were ~50% as high as what we obtained when measuring the binding of the same concentration of labeled targets. Yet, this procedure significantly increased the assay time due to additional washing steps and incubation times and requires the use of enzymes. We expect that this polymerase-mediated sensing method can also be coupled with signal amplification strategies such as common Cas13 and horse radish peroxidase (HRP) readout techniques. Specifically, either a Cas13 guide RNA or an HRP-linked oligo could bind to the polymerase-extended oligo region generated following target binding and perform catalytic signal amplification to allow sensitive detection of label-free targets.

Chapter 3 discussed an approach to precisely tune the binding specificity for single SNP-containing targets but did not demonstrate overall enhancements in binding specificity. Alternatively, we hypothesize that a couple of approaches have the potential to significantly enhance binding specificity for a single mutation using heteroMV hybridization. The first approach is to hybridize several repeats of a short SNP-containing target on a “capture” strand with the SNP-region of each target presented as a ssDNA overhang that can then bind multivalently to a homoMV DNA-functionalized particle (**Figure 4.2A**). By binding multivalently to several copies of the same SNP-containing target, the overall binding specificity can be significantly enhanced as was observed in **Chapter 3** when detecting targets with two mutations. Our modeling data suggests that the specificity can increase by several fold every time the binding valency is increased (**Figure 4.2B**). However, this approach relies on carefully tuning the affinity and spacing of the oligos on the particle. This proposed method does offer the ability to detect label-free targets as the capture oligo can be modified with a fluorophore. Moreover, by coupling this technique with PCR, each primer can be designed to have a 5' overhanging region with the same sequence that can bind to the capture strand. This would allow the same fluorescent capture strand to be used for every SNP being detected, making the readout cheaper and easier.

A second approach is inspired by the biological concept of kinetic proofreading, which has been hypothesized to increase the specificity of biological processes such as T-cell triggering and endocytosis.¹⁻² One variety of kinetic proofreading that was described by Galstyan *et al.* is spatial proofreading. In this case, specificity is enhanced by physically separating the location of two events that are required to yield a biological function or generate a signal (**Figure 4.2C**).³ We hypothesize that this concept can be applied in heteroMV hybridization-based SNP detection. First, two ligands that bind a target multivalently can be spatially separated on a fluid substrate. Then,

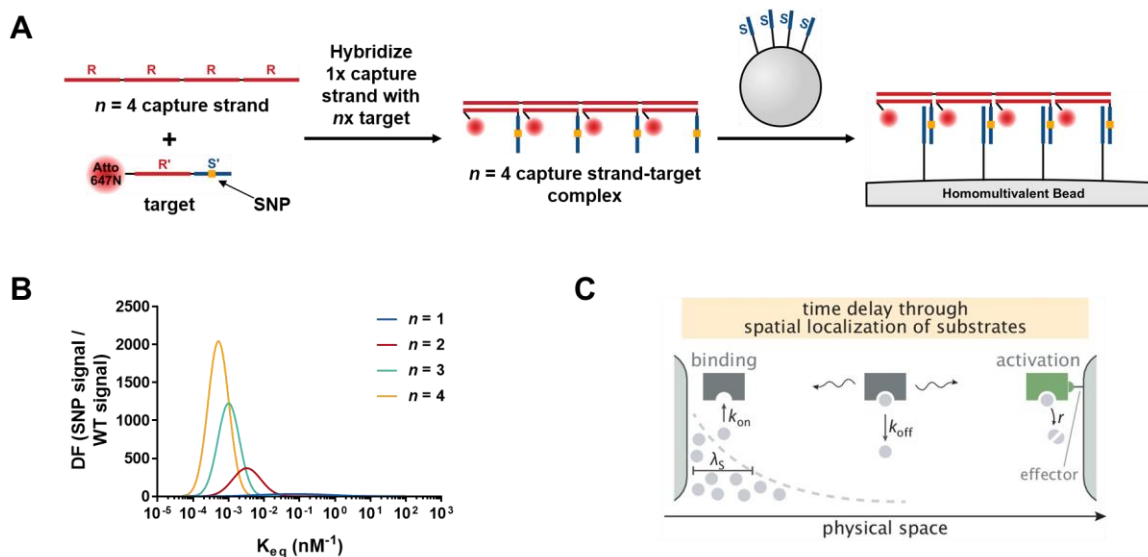


Figure 4.2. Potential methods to enhance specificity for a target with a single SNP using multivalent hybridization. (a) Scheme describing an approach to use a capture strand to hybridize to multiple copies of a SNP-containing target to allow multivalent hybridization to a homoMV particle. (b) Preliminary modeling data showing that increasing the binding valency by increasing the number of targets bound to a capture strand results in dramatic enhancements in discrimination factors when the affinity of the oligo is tuned to an appropriate strength for each value of n . (C) A scheme describing the concept of spatial proofreading where the location that two events occur, such as binding and activation, are separated by a physical space to generate a time delay between the occurrence of the events. During this time delay, off-target binding events are discarded at a faster rate than on-target binding events due to higher k_{off} values.

after a target binds one ligand monovalently it must diffuse from one location to another. During this diffusion, any mismatched targets will dehybridize from the surface due to increased K_{off} , while targets containing the SNP will be able to diffuse across the surface and reach the second oligo to form a stable multivalent interaction and generate a fluorescent readout. We envision that microfluidic channels coated with supported lipid bilayers (SLBs) could be used to separate the two ligands and allow diffusion.

4.2.2. Investigating HeteroMV DNA Hybridization on a Lipid Surface

One concept that we have not explored in our investigations of heteroMV DNA hybridization to ssDNA targets is anchoring the binding oligos to lipid surfaces. As discussed in **Chapter 1**, displaying ligands on a fluid substrate like a lipid bilayer can allow for more effective multivalent hybridization that is less sensitive to ligand spacing and arrangement. Specifically, when the ligands are attached to fluid substrates they can move laterally and rearrange to form higher valency and more energetically favorable interactions with the target. Therefore, we envision that heteroMV DNA-functionalized liposomes or SLB coated particles can be used to bind with high valency to ssDNA targets without the need to control the ligand positioning. In this case, lipids with low transition temperatures that are fluid at the assay temperature must be used.

Alternatively, in some instances it might be desirable to use specific lipids with high transition temperatures that are in the gel phase at the assay temperature. For these applications, we hypothesize that the spatial arrangement of the oligos can be controlled in several ways. One way is identical to the method described in **Chapter 2**, where the oligos are first hybridized to a template before mixing with the liposome or SLB-coated bead (**Figure 4.3A**). While the oligos are still bound to the template, they can either covalently attach to the lipid surface or insert into the membrane using a cholesterol-anchoring modification. Finally, the template can be dehybridized by reducing the salt concentration or adding denaturing chemicals, leaving behind the oligos in a patterned spatial arrangement. A second potential approach involves synthesizing a heteroMV particle with a random oligo arrangement, heating the particle to above the lipid phase transition temperature to allow for oligo diffusion, and then hybridize the particles to a template that can drive the patterning of the oligos as described above (**Figure 4.3B**). Finally, the particle can be cooled back down and then the template can be dehybridized using non-heat-based methods.

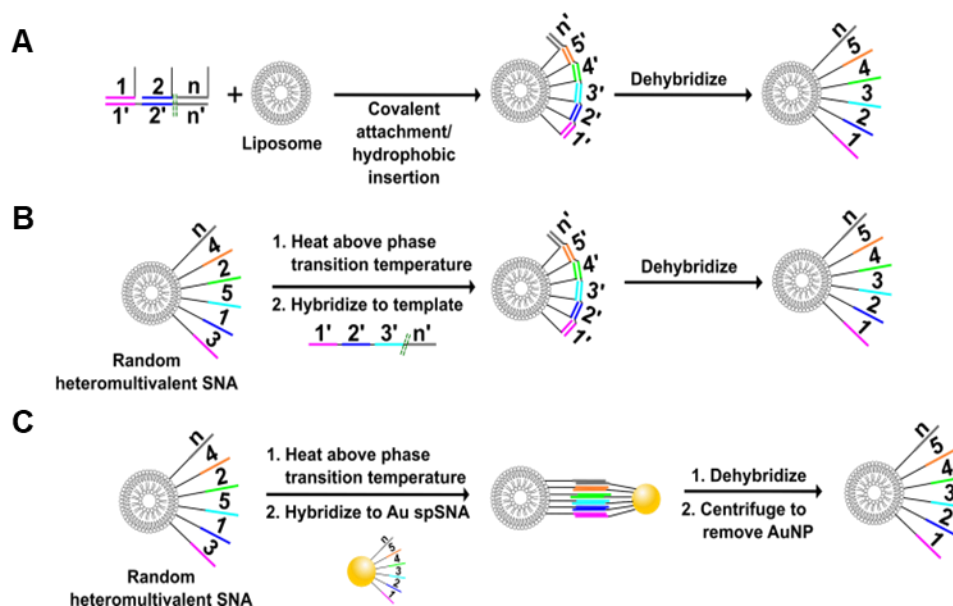


Figure 4.3. Three potential approaches to create patterned heteroMV lipid particles. (a) The binding oligos can be pre-hybridized to a template, conjugated to the lipid particle through covalent attachment or hydrophobic insertion, and then dehybridized from the template using a non-heat-based dehybridization method. (b) A heteroMV lipid particle with a random oligo arrangement can be heated above its phase transition temperature, hybridized to a template and allowed to reach equilibrium, cooled back down, and then dehybridized from the template using a non-heat-based dehybridization method. (c) A heteroMV lipid particle with a random oligo arrangement can be heated above its phase transition temperature, hybridized to a patterned heteroMV AuNP and allowed to reach equilibrium, cooled back down, and then dehybridized and separated from the AuNP.

Furthermore, we hypothesize that a DNA-functionalized AuNP that already has a patterned spatial arrangement can drive the patterning of a random heteroMV particle (**Figure 4.3C**). Similar to the second approach, the random lipid particle can be heated, hybridized to the template particle, cooled back down, and then dehybridized to create a patterned lipid particle. On the other hand, if two random heteroMV lipid particles functionalized with complementary oligos are mixed, it is possible that they can pattern each other. This patterning can occur through a thermodynamic driven process as the most energetically favorable outcome is to form as many duplexes as possible with the complementary particle. Thus, to accomplish this outcome, the oligos on each particle will rearrange in a specific order to maximize the binding valency and avidity of the multivalent

hybridization interaction with the complementary particle. Following rearrangement and hybridization the particles can be cooled down and dehybridized to store the spatial arrangement. By chemically locking the pattern, the patterned particles can then be used to further pattern other particles to “amplify” the pattern. If successful, this approach can be used to engineer self-replicating patterned DNA-functionalized lipid particles without a template.

4.2.3. Potential Advantages and Obstacles for Use of HeteroMV DNA Hybridization in Therapeutic Applications

I began my Ph.D. studies by investigating the potential to use DNA-functionalized particles in therapeutic applications, such as regulating the expression of specific genes through binding and cleaving mRNA targets. Thus, one of the initial goals for designing heteroMV DNA particles was to use them to improve the effectiveness of gene regulation. We hypothesize that heteroMV binding would allow for higher avidity binding to mRNA targets which would yield a more potent therapeutic agent. Moreover, by binding many short oligos to long mRNA targets the harmful effects of secondary structure, both with the particle-linked oligos and the target, can be overcome. Specifically, we envision that by binding to many sites of the target, the naturally occurring secondary structure in the mRNA sequence can be gradually removed as each oligo binds. Furthermore, each additional duplex formed offers another potential site for RNase H-mediated target cleavage.

Despite these potential advantages, there are a couple of possible obstacles that can limit the effectiveness of heteroMV DNA-functionalized nanoparticles in therapeutic applications. Firstly, a common limitation in most nanoparticle-based therapeutics is the ability of the particle to escape endosomal compartments and reach the cytoplasm. Moreover, multivalent binding to the

mRNA target requires oligos to be still attached to the nanoparticle once it reaches the cytoplasm. Currently, it is not known what percentage of particles stay intact as they are trafficked into the cell through endocytosis. As a result, it is unclear whether the observed gene regulation capabilities of DNA-functionalized particles are mediated by DNA attached to or released from the particle surface. However, many efforts are underway to improve the endosomal escape capabilities of nanoparticle therapeutics or instead deliver the nanoparticles directly into the cell cytoplasm. If successful, these findings could greatly improve the therapeutic potential for heteroMV DNA-functionalized nanoparticles.

4.3. References

1. Chakraborty, A. K.; Weiss, A., Insights into the initiation of TCR signaling. *Nat Immunol* **2014**, *15* (9), 798-807.
2. Wu, M.; Wu, X., A kinetic view of clathrin assembly and endocytic cargo sorting. *Curr Opin Cell Biol* **2021**, *71*, 130-138.
3. Galstyan, V.; Husain, K.; Xiao, F.; Murugan, A.; Phillips, R., Proofreading through spatial gradients. *Elife* **2020**, *9*.